Developing a new generation of neuro-prosthetic interfaces: structure- function correlates of viable retina-CNT biohybrids

Cyril G. Eleftheriou

Institute of Neuroscience

Newcastle University

Thesis submitted for the degree of Doctor of Philosophy at Newcastle University

January 2013

Abstract

One of the many challenges in the development of neural prosthetic devices is the choice of electrode material. Electrodes must be biocompatible, and at the same time, they must be able to sustain repetitive current injections in a highly corrosive physiological environment. We investigated the suitability of carbon nanotube (CNT) electrodes for retinal prosthetics by studying prolonged exposure to retinal tissue and repetitive electrical stimulation of retinal ganglion cells (RGCs).

Experiments were performed on retinal wholemounts isolated from the Cone rod homeobox (CRX) knockout mouse, a model of Leber congenital amaurosis. Retinas were interfaced at the vitreo-retinal juncture with CNT assemblies and maintained in physiological conditions for up to three days to investigate any anatomical (immunohistochemistry and electron microscopy) and electrophysiological changes (multielectrode array stimulation and recordings; electrodes were made of CNTs or commercial titanium nitride).

Anatomical characterisation of the inner retina, including RGCs, astrocytes and Müller cells as well as cellular matrix and inner retinal vasculature, provide strong evidence of a gradual remodelling of the retina to incorporate CNT assemblies, with very little indication of an immune response. Prolonged electrophysiological recordings, performed over the course of three days, demonstrate a gradual increase in signal amplitudes, lowering of stimulation thresholds and an increase in cellular recruitment for RGCs interfaced with CNT electrodes, but not with titanium nitride electrodes.

These results provide for the first time electrophysiological, ultrastructural and cellular evidence of the time-dependent formation of strong and viable bio-hybrids between the RGC layer and CNT arrays in intact retinas. We conclude that CNTs are a promising material for inclusion in retinal prosthetic devices.

Acknowledgements

I could never have accomplished the work described in this thesis nor written it without a whole lot of support, advice and help. First of all, I have to thank Dr Evelyne Sernagor, my primary supervisor. Evelyne has always been very helpful, providing direction, scientific advice, lively debates, introduction to some great scientists and of course delicious meals in fine company. Dr Miles Whittington, my secondary supervisor was always available for a chat, a good night out and extra support when needed. I would also like to thank my internal assessment team: Drs Adrian Rees and Andy Jackson. Both were incredibly helpful throughout the PhD. I also got the chance to know Andy outside the assessment process and thank him for great times and many chats about neuroprosthetics and life in general. I will never forget about the Druids!!

This project wouldn't have been possible without the contribution of Dr Yael Hanein, Moshe David-Pur and Lilach Bareket who designed, fabricated and optimised the CNT arrays. I had the chance to visit their laboratory and enjoyed myself tremendously. I would like to give a great big thank you to Nitzan Herzog, Noah Levine-Small and Gur Lubin who were fantastic hosts in Israel.

The neurobiology corridor has been a prolific environment for research with many wise and enlightening personalities. Of these, I have to mention Tracey Davey, Vivian Thompson and Kath White for support and amazing training in Electron Microscopy; Gavin Clowry for teaching me immunohistochemistry and helping with TEM interpretation; Claudia Racca for supplying us with yummy cakes as well as advice on cooking and immunohistochemistry; John Wraith for electronics; Fiona LeBeau for great nights out and good chats; Mark Cunningham for laughs and organising the enthralling epilepsy conference; Karen Parkin for good banter; Mohammed Shoaib for fun squash games; Andy Trevelyan for career advice.

I was also very lucky to work alongside a group of engaging graduate students and post-docs, always available for advice, a drink, a party or even a bit of help with Matlab. I thank Henrick Kjeldsen for mind-blowing revelations about time-travelling neurons, Jonas Zimmerman for inspirational conversations and gherkin experiments as well as sorting out most of the Matlab package before I did any electrophys, John Barrett for being incredibly talented and a whole lot of fun, Chris Adams for getting me

started in the lab and inspiring me to develop neuroengineering skills, Rolando Berlinguer-Palmini for his contribution with electroporation, Dorcas Eden and Daniel Haggerty for showing us the ropes and how to finish off a thesis. I won't forget the pizza-fuelled all-nighters I had with Stephen Hall while he was experimenting on Cock-fosters, Dorcas while she was writing her thesis and Michael Fisher while he was writing his first year report. I thank Bernadette O'Donovan for great fun on nights out, Lucy Carracedo for the joy of Mice Pies, Claire Gillougley for the best hugs in the world, Matt Ainsworth for bringing back The Squirrel, Samantha Rushforth for being inspirational, Leonie Cunnington for stimulating discussions, Michael Fisher for being the sweetest bloke I know, Felix Chan for checking on me each night while I was writing up, Vasileos Glykos for Greek lessons and chats about fissing, Stefan Jaiser for mind-boggling statistics and painful TMS experiments, Thomas Hall for a medic's view on neuroscience, Anais Thouin for conversations about neurological disorders and philosophy, Ana Simon for advice on life and histology, Georgia Rentesi for her fabulous sense of humour, Emma Robson for being the best at organising events, Katherine Newling for being so nice, Sabine Gretenkord for putting up with a moody Harbi, Bonne Habekost for being brilliant, Claire Schofield for fun debates, Edward Merricks for his in-depth knowledge of posh cocktails, Matt Down for his Trianglets, James Van Copenhagen for his unique sense of style.

My closest friends and colleagues also provided unequivocal support throughout the whole process. I thank Kishore Allam and Holly Kishore for regular escapes to beautiful Scotland, Mahmoud Khazim for intense discussions interspaced by great chilling sessh, Natalie Adams for being there from the start and keeping me in check, Harbaljit Sohal for the epic nights out-the best banter-the rep of being a rep and much much more!

My family have always been there for me, providing Love and support. I consider myself extremely lucky in that respect. Many thanks to Maman et Papa who have encouraged me all my life, to the Goodsells for hosting great Christmases and always providing a helping hand, to the Vinsons for sweet Brazilian delicacies and beautiful weddings, to the Galligos for good entertainment and laughs, to my Yaya for the right amount of sugar and spice.

Finally, I dedicate this work to Saran, my love of always.

Table of Contents

List of figures

List of tables

Glossary of acronyms:

AC	Amacrine Cell
aCSF	artificial Cerebro Spinal Fluid
AMD	Age related Macular Degeneration
ASCI	Application Specific Integrated Circuit
BC	Bipolar Cell
BRB	Blood Retina Barrier
CatCh	Calcium Translocating Channel Rhodopsin
Ch-R2	Channel Rhodopsin
CNS	Central Nervous System
CNT	Carbon Nanotube
CRX	Cone Rod Homeobox
DAB	3,3'-Diaminobenzidine
DMEM	Dulbecco's Modified Eagle Medium
DLP	Digital Light Processing
DPX	Distyrene-tricresyl Phosphate-xylene
EC	Endothelial Cell
ECM	Extra cellular Matrix
FBS	Fetal Bovine Serum
GCL	Ganglion Cell Layer
GFAP	Glial Fibrillary Acidic Protein
GFP	Green Fluorescent Protein
GSL-I	Griffonia Simplicifolia Lectin I
HBSS	Hank's Balanced Salt Solution
HC	Horizontal Cell

HRP	Horse Radish Peroxidase
IHC	Immunohistochemistry
ILM	Inner Limiting Membrane
INL	Inner Nuclear Layer
IPL	Inner Plexiform Layer
LED	Light Emitting Diode
LGN	Lateral Geniculate Nucleus
MEA	Micro Electrode Array
MPDA	Multi-Photodiode Array
MWCNT	Multi Walled Carbon Nanotube
NFL	Nerve Fibre Layer
ONL	Outer Nuclear Layer
OPL	Outer Plexiform Layer
PBS	Phosphate Buffered Saline
PDL	Poly-D-Lysine
PDMS	Polydimethylsyloxane
POS	Photoreceptor Outer Segments
PSN	Penicillin Streptomycin Neomycin
RGC	Retinal Ganglion Cell
RP	Retinitis Pigmentosa
RPE	Retinal Pigment Epithelium
SEM	Scanning Electron Microscope
SV	Side View
SWCNT	Single Walled Carbon Nanotube
TEM	Transmission Electron Microscope/Micrograph
TUNEL	Terminal Deoxynucleotidyl Transferase

Chapter 1: Literature Review

Undoubtedly the most indispensable of all sensory modalities, the visual system is extremely complex and robust. Often taken for granted, the outstanding ability that is vision has allowed us to push our species' existence to the limit of our planet's capacity for population, pollution and resource extraction. The relatively recent introduction of pictography, literature, architecture, video and vehicular transport to our society has continuously enriched our perceptions in a world already wealthy in visual stimuli.

As robust as it is, vision can fail. Damage sustained to the eye, the optic nerve or the brain as well as genetic defects can lead to blindness. Variable in strength, blindness is defined by the World Health Organisation as a visual acuity of less than 20/400 (where 20 is the distance in feet between the subject and a Snellen chart, and 400 is the distance at which a fully sighted individual can read the chart as well), in the best of both eyes with the best possible correction. Many scientists and engineers investigate possible solutions to such a devastating disability afflicting millions worldwide.

Retinal dystrophies such as age related macular degeneration (AMD) and retinitis pigmentosa (RP) have been shown to affect with morbid precision large portions of the population. The mechanisms underlying these conditions have been extensively studied, revealing the prolonged survival of the output cells of the retina. This persistent link between the eye and the brain opens the possibility of rescue strategies. The treatments being investigated, can be distinguished between electronic prosthetic devices, drug based therapies, gene therapies and stem cell therapies.

Visual prosthetic devices have been successfully implanted in the visual cortex (Dobelle 2000) and in the retina (Humayun, Weiland et al. 2003; Wilke, Gabel et al. 2011; Zrenner, Bartz-Schmidt et al. 2011) to elicit artificial visual percepts called phosphenes. Not only have these phenomenal translational experiments defined the axioms and objectives of visual neuro-prosthetics, they have also provided the scientific community with tangible data relating to the challenges presented when interfacing electronic equipment with neural tissue to restore satisfactory visual acuity.

The following report describes an anatomical and physiological account of both the healthy and dystrophic retina as well as the most recent studies on retinal prosthetic devices, with a focus on electrode technology at the vitreo-retinal interface.

1.1 The Vertebrate Retina

Common to all vertebrates, the retina provides the initial steps in the highly complex and hierarchical system that is visual processing. Lining the back of the eye, this specialized organ transduces the light reflected off objects into bio-electrical signals and transmits them to the brain for a series of higher level serial and parallel processing sequences which eventually lead to visual perception. An integral part of the central nervous system (CNS), the retina presents a very strict architectural organisation which is preserved throughout the entire phylum and incorporates an essentially feed-forward neural circuitry dedicated to the processing of raw visual information.

Since the end of the 19th century, when Santiago Ramon y Cajal first investigated and described the CNS cytoarchitecture, a large amount of anatomical and physiological evidence has been accumulated concerning the vertebrate retina.

1.1.1 The healthy retina

The retina lines the back of each eye, receiving beams of light, refracted through the cornea and constantly focused by the crystalline lens which adjusts its curvature with respect to the apparent distance of objects. The iris is the pigmented muscle that controls the size of pupil aperture, determining how much light enters the eye (Figure 1.1). Fed by the choroid and the inner retinal blood vessels, the retina is kept in place by the vitreous humour, a viscous gel composed of water (~99%), salts, sugars, a network of collagen type II fibres bridged by proteoglycans and the mucopolysaccharide hyaluronic acid (HA). The vitreous humour also contains phagocytes which remove cellular debris from the visual field (Swann and Constable 1972; Los, van Luyn et al. 1999).

Completely translucent, the retina provides a feed-forward processing circuitry by which light is transduced into graded neural signals by photoreceptor cells in the outermost layers. These signals are processed in a number of parallel pathways by several layers of interneurons (discussed below) before reaching the retinal ganglion

cells (RGC), the output cells of the retina. Conversely to all the other retinal neurons and receptor cells which use graded potentials to communicate, RGCs fire trains of action potentials. These action potentials travel down RGC axons which converge onto the optic disc before bundling up into the optic nerve. RGCs project onto 7 distinct central targets: the lateral geniculate nucleus (LGN) of the thalamus (Perry, Oehler et al. 1984), the pretectum (Perry and Cowey 1984), the superior colliculus (Bunt, Hendrickson et al. 1975), the pulvinar nuclei (Leventhal, Keens et al. 1980), the accessory optic system (Oyster, Simpson et al. 1980), the pregeniculate nucleus (Bunt, Hendrickson et al. 1975) and the suprachiasmatic nucleus (Hattar, Liao et al. 2002).

In the human retina 1°of the visual scene is projected onto 288 µm of the retina (Drasdo and Fowler 1974). The optic disc is 6° in size blocking the visual field with a significant, yet compensated, physiological blind spot. The blind spot is not usually perceived as the brain interpolates it based on surrounding detail and information from the other eye. High resolution visual detection is done at the fovea, (also known as macula in clinical terms) a ~5° zone, located 11.8° temporally to the optic disc (Polyak 1941). The foveola is located at the centre of the fovea and mediates the highest resolution visual detection of the retina. This zone is free of blood vessels and contains the highest density of photoreceptor cells. The macula is the centre of the visual axis which is the central point for image focus in the visual field.

This chapter describes the multi-layered structure of the retina. This is introduced by a section detailing the neuronal cytoarchitecture of the retina. Another section will describe each type of retinal neuron with its anatomical connections and functional role within retinal processing. Then, there is a review of how the vascular system integrates with the eye to supply the retina with sufficient supplies of oxygen and nutrients. This is followed by a molecular description of the interface between retina and vitreous. The final subdivision is dedicated to describing the support and homeostatic roles played by retinal glia.

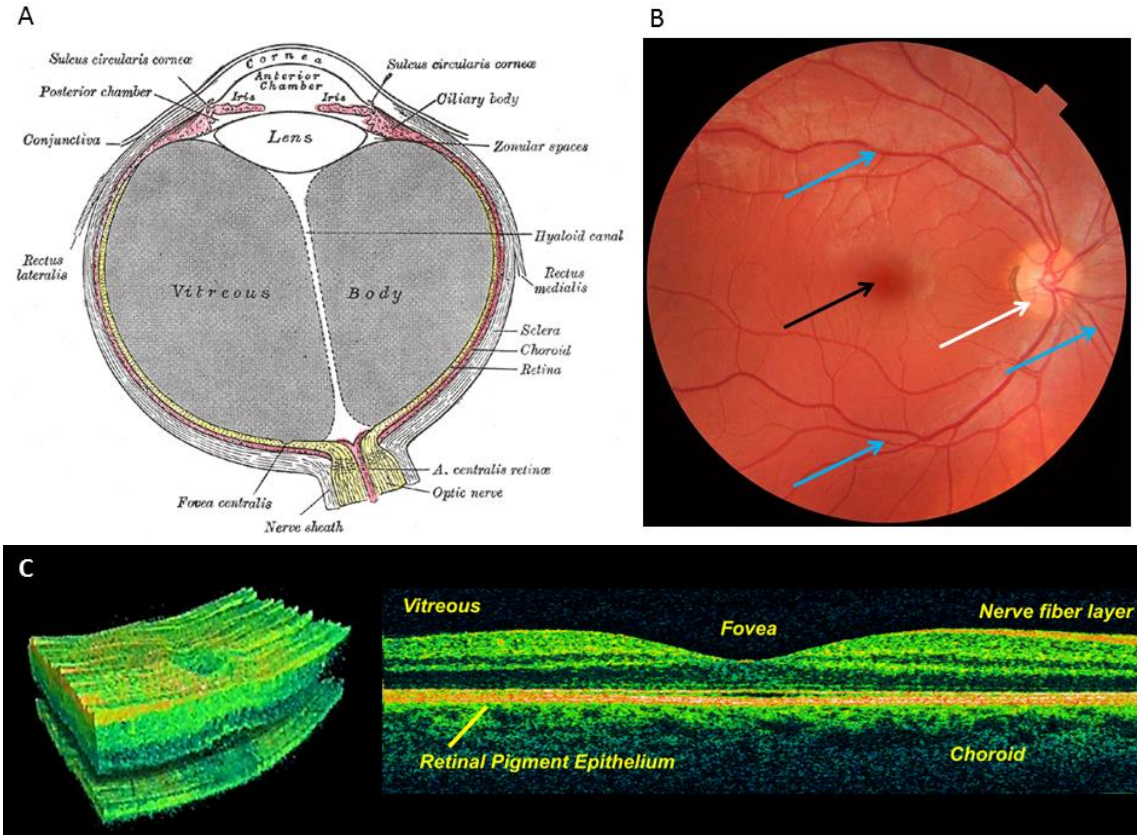

Figure 1.1: Human retina within the eye. A: Diagram taken from Gray's Anatomy (Williams 1995) detailing the gross anatomy of the human eye. B: Fundus image of a human eye displaying the optic disc (white arrow), inner retinal blood vessels (blue arrows) and the macula (black arrow). C: Optical coherence tomographs showing 3 (left) and 2 (right) dimensional portions of the human retina *in vivo*. Adapted from (Wojtkowski, Srinivasan et al. 2005).

1.1.2 Laminar organisation of the healthy retina

Most of the basic anatomical data concerning the retina was accumulated at the end of the 19th century by such anatomists as Santiago Ramon y Cajal and Max Johann Sigismund Schultze (Schultze 1866) using light microscopy and elegant histological staining techniques. Indeed, using the silver nitrate staining technique developed by Camillo Golgi (Golgi 1903) and the nuclear staining technique developed by Franz Nissl (Nissl 1894), these neuro-anatomists methodically characterised the different cell types of the retina (Ramon y Cajal 1911). Although the Golgi staining method only reveals a small percentage of cells within a tissue section, the detail achieved by this technique is exquisite, revealing somata, dendritic trees and axonal projections. The monumental work achieved by Cajal has demonstrated that the laminar organisation of the retina is surprisingly similar throughout the whole vertebrate phylum. Sandwiched between the choroid and vitreous humour, the retina is organised in a number of layers, consisting of alternating cell-body (nuclear) and synaptic (plexiform) layers (Figure 1.2). For an in-depth review of the retina's functional neuro-anatomy, the reader is directed to (Marc 2009).

Light is transduced into electrical signals by photoreceptors (rods and cones) that have their somata in the outer nuclear layer (ONL). They contact second order neurons, namely bipolar and horizontal cells (HC) in the outer plexiform layer (OPL). Bipolar and horizontal cell bodies reside in the inner nuclear layer (INL). Bipolar cells (BC) synapse onto a third kind of interneuron, the amacrine cells (AC) with somata located deeper within the INL. BCs and ACs synapse onto the dendrites of retinal ganglion cells (RGC) within the inner plexiform layer (IPL). The cell bodies of RGCs form the output layer of the retina, the ganglion cell layer (GCL). The axons of RGCs are bundled along the nerve fibre layer (NFL) towards the optic disc. In humans, the retinal thickness varies depending on location. It is thinnest (typically 80 µm) at the *ora serata* (serrated juncture between retina and ciliary body) and thickest (typically 320 µm) at the foveal rim (Sigelman, Ozanics et al. 1982).

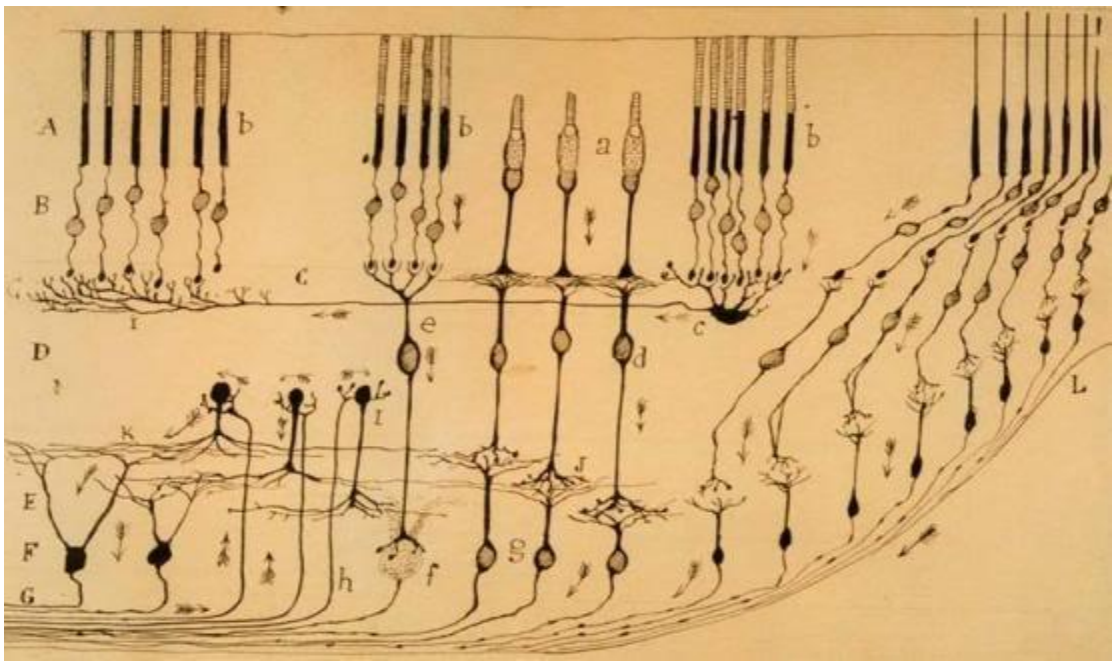

Figure 1.2: Drawing of retinal neurons close to the fovea. A: layer of rods and cones outer(light) and inner (dark) segments. B: outer nuclear layer. C: outer plexiform layer. D: inner nuclear layer. E: inner plexiform layer. F: ganglion cell layer. G: nerve fibre layer; L: fovea, Ramon y Cajal (1911).

1.1.3 Neurons of the healthy retina

The neurons of the retina are among the smallest neurons in the CNS, with a typical RGC having less than 1% the soma-dendritic volume of a cortical pyramidal cell (Masland 2012). There are five major classes of retinal neurons, each providing specialised function to the complex hierarchy of image acquisition and processing in the neural retina: photoreceptors, HCs, BCs, ACs and RGCs. Each of these major classes is further sub-divided into a variety of different types based on morphology, physiology and function, with the total number of cells and the number of different types varying between species. Typically, mammalian retinas are composed of at least 60 different cell types (figure 1.3), with 4 photoreceptor classes (1 rod, 2-3 cones), 4 HC classes (2-3 cones, 1 rod), over 12 BC classes (1 rod and all the other cones), 30 amacrine classes and 12-20 RGC classes (Masland 2001; Ghosh, Bujan et al. 2004; Jurrus, Whitaker et al. 2008).

Retinal cells of the same type are evenly spaced in 2 dimensional mosaics throughout the retina (Rockhill, Euler et al. 2000; Reese, Keeley et al. 2011). This tiling of homotypic retinal neurons ensures a complete yet recurrent coverage of the retinal

surface with dendritic trees from different cell types overlapping at different depths and showing little (e.g. in RGC) to very large overlap (e.g. in ACs). Retinal neurons of different types however appear to be laterally randomly spaced to each other (Rockhill, Euler et al.
2000).

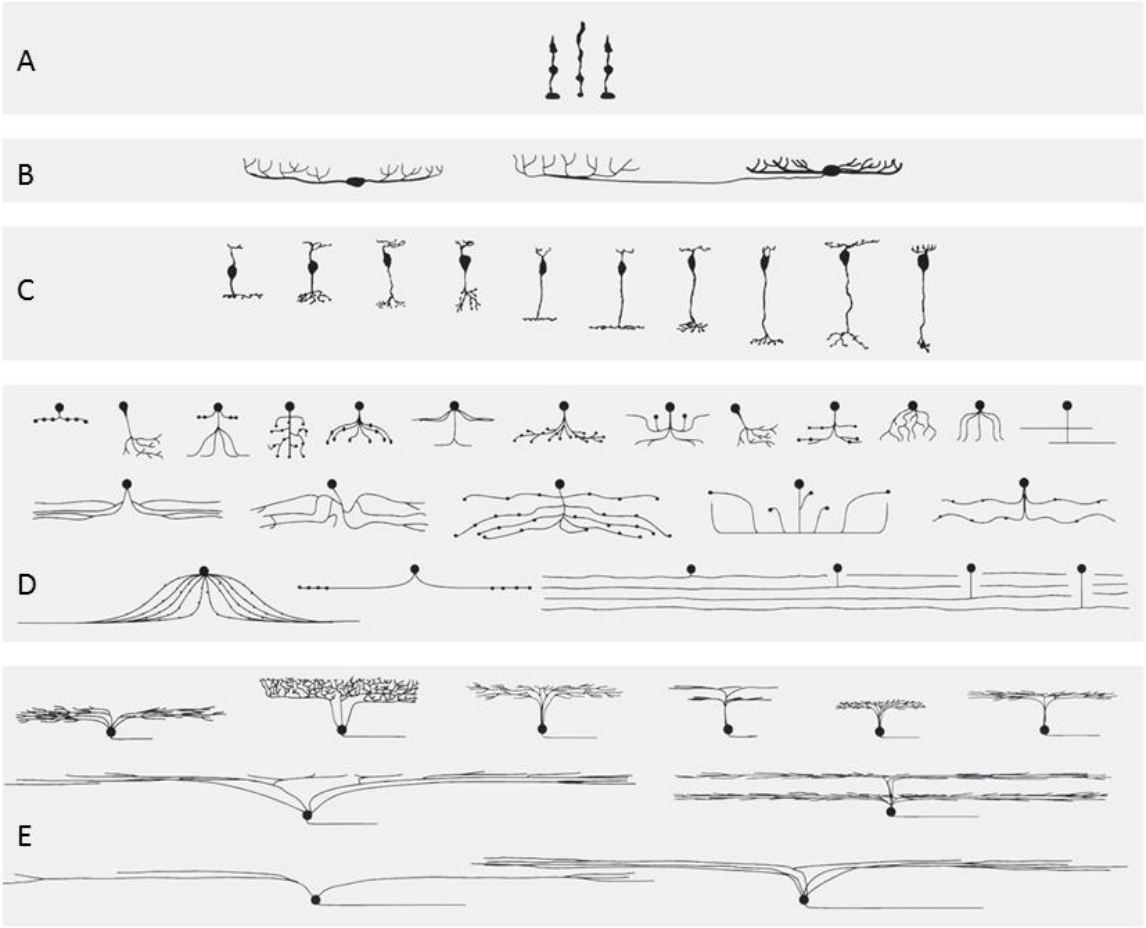

Figure 1.3: Morphological classification of a selection of mammalian retinal neurons. A: photoreceptors, here 2 different cone types and one rod type. B: 2 different types of horizontal cells. C: 10 different types of bipolar cells, projecting to different depths within the IPL. D: amacrine cells. E: retinal ganglion cells. Adapted from (Masland 2001).

Photoreceptors

Photoreceptors are responsible for phototransduction, the conversion of light into neural signals. Phototransduction occurs in discs densely stacked in the outer segments of photoreceptors. The discs are folded membranes expressing

photosensitive proteins (rhodopsin in rods and cone opsins with different spectral absorptions in cones). These discs are formed at the base of the outer segments and shed at the tip where they are phagocyted and recycled by the retinal pigment epithelium (RPE). The inner segments of photoreceptors contain the endoplasmic reticulum, the Golgi apparatus and densely packed mitochondria providing the energy for the high metabolic demands of phototransduction. For thorough reviews on phototransduction, the reader is directed to (Arshavsky, Lamb et al. 2002) and (Fu and Yau 2007).

The vertebrate retina is populated by two complementary types of photoreceptors: rods and cones. Rods are responsible for scotopic (low level of illumination) vision whilst cones are specialized in high resolution colour vision during the day (photopic). Figure 1.5 is a confocal micrograph displaying cones in green.

Mostly present in the periphery and completely absent from the centre of the fovea, rods outnumber cones approximately twenty to one. They are highly sensitive to light, being able to detect single photons (Hecht, Shlaer et al. 1942). Structurally, this is manifested by a longer outer segment (than cones) containing more photopigment and fundamentally, a higher amplification system during phototransduction. As they contain only one type of photopigment (with a maximum spectral sensitivity of around 500 nm (Schnapf, Kraft et al. 1988)), rod-mediated vision is achromatic. One of the characteristics of this system is a slow response time; as in photography, a longer exposure (integration) time is required to detect low levels of light. Another characteristic of rod vision is low acuity, a trade-off intrinsic to the amplification circuitry of rod signals as these connect to multiple RGCs.

Cones complement rods in almost every way. As such, they have a lower sensitivity to changes in luminance and are specialized for photopic vision. They operate over a shorter range of light intensities and have a much faster integration time leading to a high temporal resolution. Concentrated in the fovea, they mediate high acuity vision (discussed below): a human with no cones is legally blind. Chromatic vision is achieved by cones with different spectral sensitivities, three types in primates, and only two in mice. In primates, S-cones detect light with a short wavelength peaking at 420 nm

(blue), M-cones detect light with a medium wavelength peaking at 534 nm (green) and L-cones detect light with a long wavelength peaking at 564 nm (red). Mice have UV- (355 nm) and green-sensitive (508 nm) cones (Szel, Rohlich et al. 1992; Lyubarsky, Falsini et al. 1999).

The innermost portion of photoreceptor cells is dedicated to synaptic transmission with HCs and BCs. Cone pedicules are large processes engulfing the neurites of their postsynaptic partners, contacting them with approximately 30 synaptic ribbons (Ahnelt, Keri et al. 1990). Rod spherules are much smaller processes engulfing the dendritic terminals of 4 second order neurons contacted by 2 synaptic ribbons (Kolb 1970). Constantly releasing glutamate at the ribbon synapses, the photoreceptor response to light is mediated by a metabotropic cascade resulting in a membrane hyperpolarisation in outer segments and followed by a proportional decrease in glutamate release. Photoreceptors are also electrically coupled to each other with cone-cone and cone-rod gap junctions (Raviola and Gilula 1975).

The numbers and topography of rods and cones have been mapped with great precision for most laboratory animals and humans (Collin 2008).

Horizontal Cells

Most vertebrate retinas contain two different types of HCs, A-type HCs have local synaptic arbors and B-type HCs project their output approximately 400 µm away via short axons. These cells have been mapped and quantified across the retinas of most laboratory animal species (Collin 2008). With somata located in the INL and processes connecting to photoreceptor terminals in the OPL, HCs are homotypically connected by gap junctions (Kolb 1977). This mediates the integration of luminance over large areas across the retina and allows experimentalists to visualise large networks of interconnected HCs when filling one cell with a small enough dye molecule (figure 1.4). HCs provide widespread lateral inhibition. This function is thought to mediate initial gain control by averaging the luminance level across an area of the retina and subtracting a proportionate value from the output of photoreceptors. This enhances the edges of objects against background, contributing to centre-surround processing

initially described by visual physiologists (Hartline 1938; Kuffler 1953; Werblin and Dowling 1969).

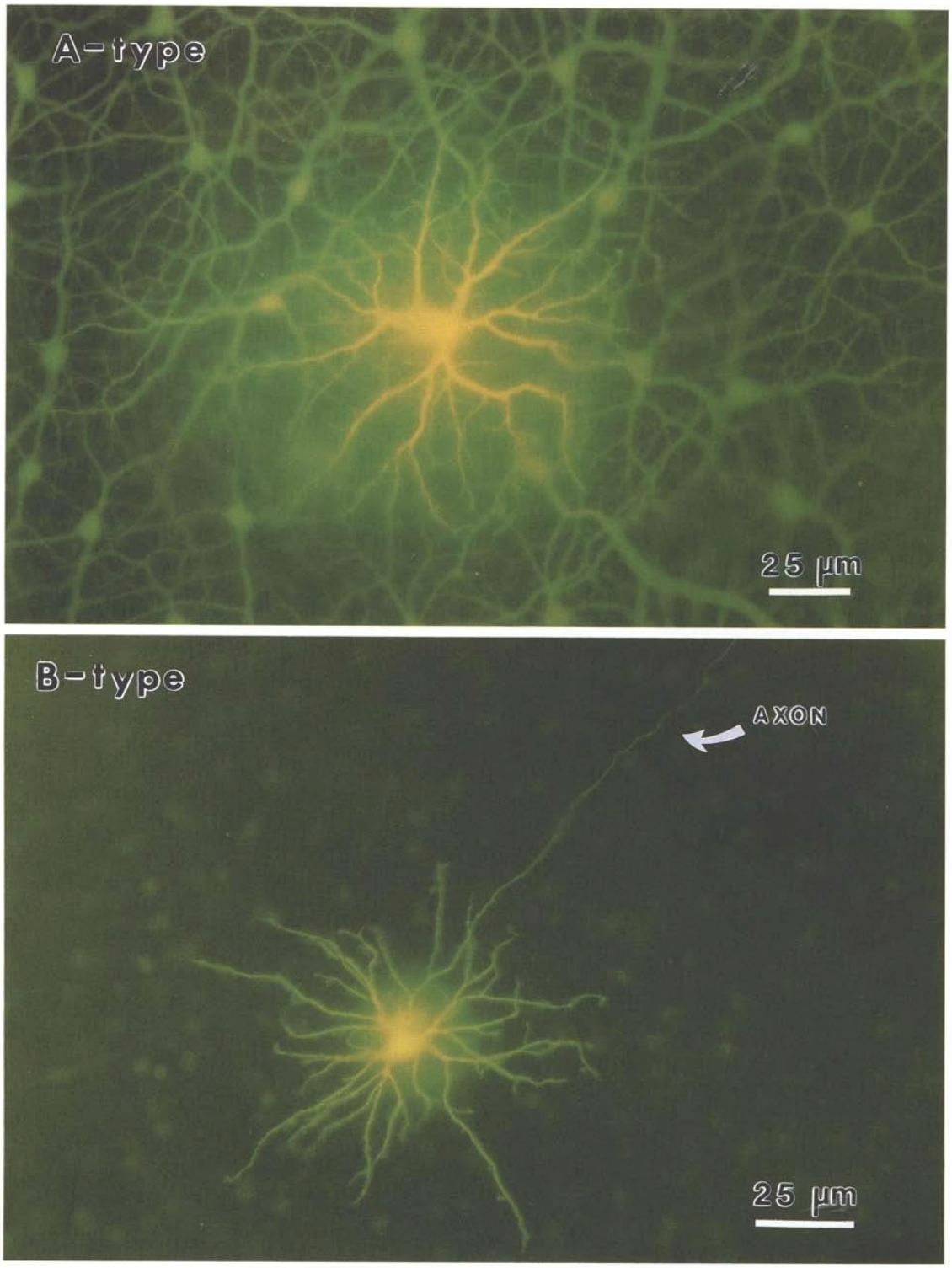

Figure 1.4: Lucifer Yellow filled horizontal cells.
Fluorographs of Lucifer Yellow filled HCs from a rabbit retina. A: A-type HCs. The dye was injected into the central cell's soma and spread to adjacent homeotypic HCs through gap junctions in their processes. B: individual B-type HC showing dendritic tree and axons. Micrographs taken from (Mills and Massey 1994).

Bipolar Cells

Although the exact number of different types of BCs has not been established in all mammals, studies in the rodent retina have revealed one type of rod-connecting BC and 11-12 cone connecting BCs (MacNeil, Heussy et al. 2004; Wassle, Puller et al. 2009). These cells are the main vertical component for information flow in the retina, transmitting input from the OPL to different strata of the IPL (figure 1.5). Functionally, the IPL has been divided into 5 different strata, with the axons of OFF BCs terminating in layers 1-2 and the axons of ON BCs terminating in layers 3-5 (Famiglietti, Kaneko et al. 1977; Nelson, Famiglietti et al. 1978). This functional subdivision of bipolar cells is a result of the synaptic receptors expressed by each of these BCs. OFF BCs express ionotropic glutamate (AMPA and kainate) receptors which hyperpolarise the BC membrane in response to light, physiologically mirroring the photoreceptor responses. ON BCs express a metabotropic receptor (mGluR6) whose activation leads to the closing of cation channels (TRPM1) in response to light, resulting in BC membrane depolarisation, thus physiologically inverting the input signal from photoreceptors (Morgans, Zhang et al. 2009; Shen, Heimel et al. 2009).

Rod BCs have large dendritic trees which connect to rod photoreceptors. One rod BC can be in contact with up to 45 rods. Cone BCs have smaller dendritic trees connecting each cone within that area (Wassle, Puller et al. 2009). The signal generated by any cone is decomposed into a set of different components transmitted in parallel by each of the 11-12 types of cone BC. The segregation of these signals is anatomical (with different BC types projecting to different strata within the IPL) and functional (ON and OFF pathways). In addition, responses of different types of BCs can be sustained, transient or a complex mixture of the two dictated by the kinetics of different glutamate receptors (Wu, Gao et al. 2001). In the macular region of the primate retina, midget bipolars have one-to-one contact with cones, sometimes one cone being in contact with two bipolars (Polyak 1941).

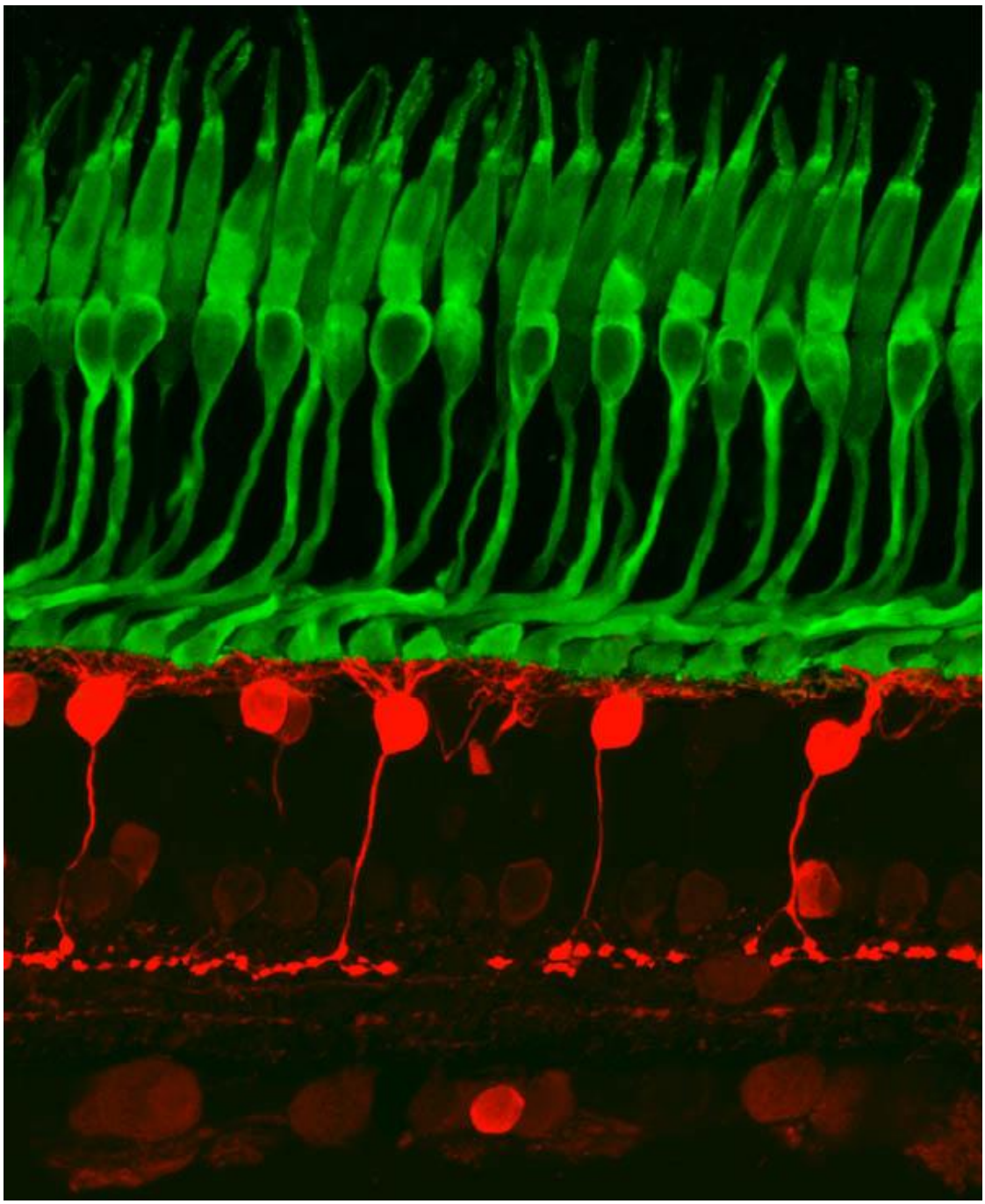

Figure 1.5: Confocal micrograph of cones contacting BCs. Fluorescent confocal micrograph of cones (green) making synaptic contacts with the dendrites of BCs (red) in the monkey retina. Image adapted from www.retinalmicroscopy.com.

Amacrine Cells

Morphological and physiological characterisation of ACs has revealed 29-30 different types (MacNeil and Masland 1998). These have been further subdivided into 3 categories based on the lateral spread of their processes: narrow field, medium field and wide field (figure 1.6). Receiving inputs from BCs in the IPL, ACs provide (mostly) inhibitory connections to BCs, ACs and RGCs in the IPL (Jusuf, Haverkamp et al. 2005; Eggers and Lukasiewicz 2011). Narrow field ACs innervate multiple strata of the IPL, integrating ON and OFF pathways, thus mediating such functions as the linearization of graded input through crossover inhibition or the detection of looming objects. Medium field ACs extend their processes laterally approximately 200 µm and across the ON-OFF boundaries. These promote lateral inhibition and disinhibition of BCs and RGCs, contributing to the centre-surround antagonist receptive field of RGCs. Medium field ACs are mediators of such visual processing functions as directional selectivity, edge enhancement, lateral inhibition and gain control. Wide field ACs extend their processes for up to 1.5 mm within individual strata of the IPL. These cells have fast physiological response times as they are strongly electrically coupled (homotypically) and express voltage gated Na^+ channels (Volgyi, Xin et al. 2001). Wide field ACs receive glycinergic inhibition and release serotonin (Vaney 1986) or dopamine (Dowling and Ehinger 1978).

The lack of polarisation in their processes (inputs or outputs) and their great structural diversity have made ACs hard to conceptualise and incorporate into models of visual function. The segregated pathways transmitted to the IPL by BCs are integrated into more complex signals specific to a set of RGC subtypes. For thorough reviews, the reader is directed to (Gollisch and Meister 2010; Werblin 2011; Masland 2012).

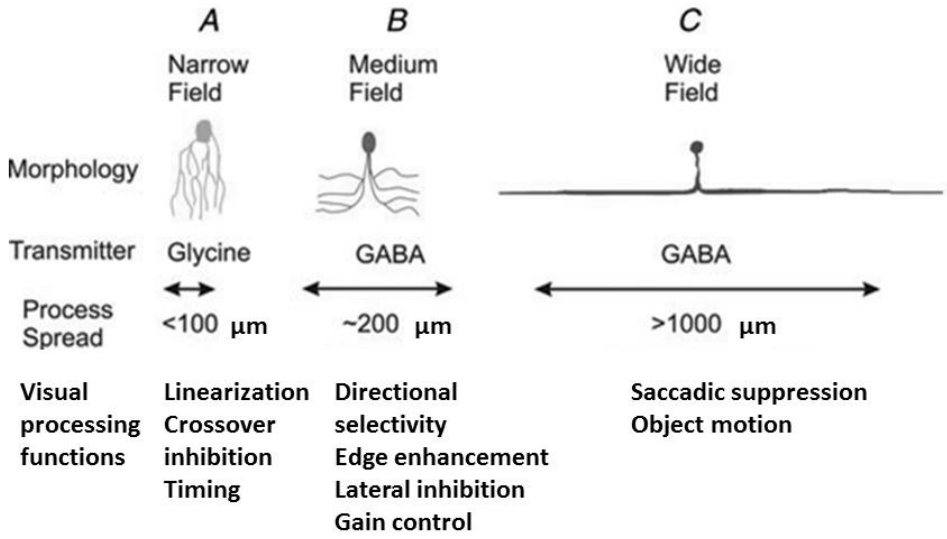

Figure 1.6: 3 major subdivisions of amacrine cells. The ~30 different types of ACs can be subdivided into 3 different groups according to the lateral spread of their processes. Narrow field ACs (A) spread under 100 µm and mediate such complex functions as linearization, crossover inhibition and timing. Medium field ACs (B) spread their processes over approximately 200 µm and mediate such functions as directional selectivity, lateral inhibition and gain control. Wide field ACs (C) spread over 1 mm and mediate such visual functions as saccadic suppression and object motion. Adapted from (Werblin 2011).

One of the most extensively studied AC is the AII AC, which has recently been implicated in the generation of pathological signals in dystrophic retinas (discussed below). Narrow field and bi-stratified (Kolb and Famiglietti 1974), the AII AC has synaptic contacts throughout the entire IPL and is thus involved in vertical signal processing. Glutamatergic inputs are mediated by AMPA and kainate receptors, whilst signals are rapidly transmitted through the cell by spike-like potentials mediated by voltage-gated Na^+ channels (Boos, Schneider et al. 1993). AII ACs are electrically connected to each other and ON-cone BCs through gap junctions (Strettoi, Raviola et al. 1992) in networks ranging from 20 to 300 coupled cells (Vaney, Gynther et al. 1991).

Retinal Ganglion Cells

RGCs extend their dendrites into the IPL where they receive input from BCs and ACs. Providing the only output for the retina, RGC axons converge onto the optic disc (figure 1.7) to become the optic nerve before establishing synaptic contacts in their cortical targets. RGCs from the temporal part of the retina project to the ipsilateral hemisphere and those in the nasal part of the retina project to the contralateral hemisphere. Thus, each brain hemisphere receives input from both eyes and from both the ipsilateral and contralateral visual fields (Stone, Leicester et al. 1973; Cowey and Perry 1979).

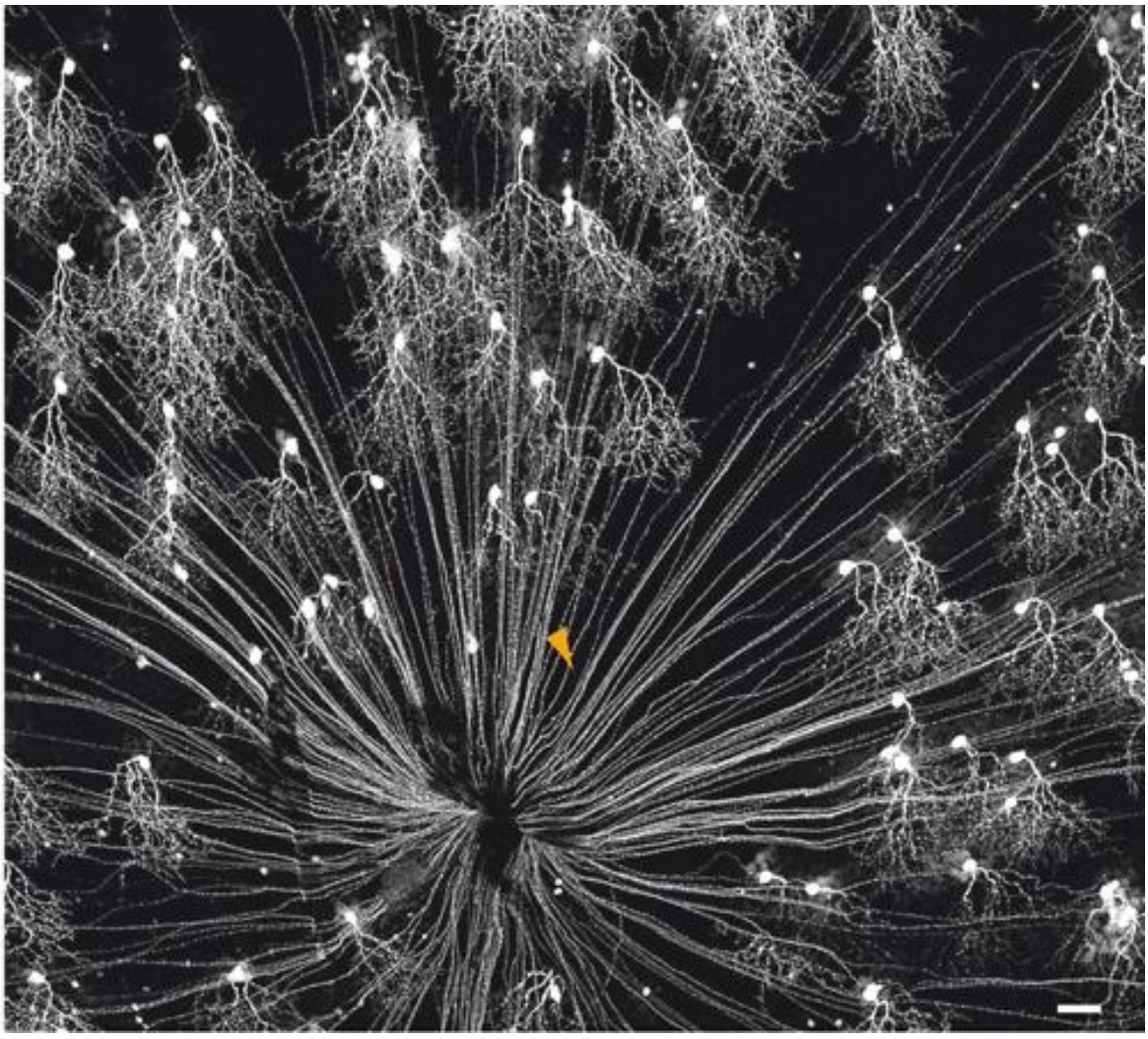

Figure 1.7: RGC axons converge onto the optic disc. Confocal micrograph of a retinal wholemount originating from a mouse genetically modified to express yellow fluorescent protein (YFP) on cells naturally expressing junctional adhesion protein B (JAM-B). This population of OFF-RGCs has been shown to respond to upward motion. The scale bar represents 50 µm and the orange arrow-head points to an RGC axon (Kim, Zhang et al. 2008).

Using Golgi staining, Cajal (1911) characterised RGCs according to size, dendritic morphology and lamination pathways in the IPL. Since then, a number of classification schemes have evolved linking morphology, arborisation and function, some of which include up to twenty three classes (Kolb, Nelson et al. 1981). Seventeen of these can be subdivided according to dendritic tree morphology (figure 1.8), with different dendritic field sizes gathering input from more ACs and BCs as the field gets larger. The size of these fields increases with retinal eccentricity (Dacey 2004).

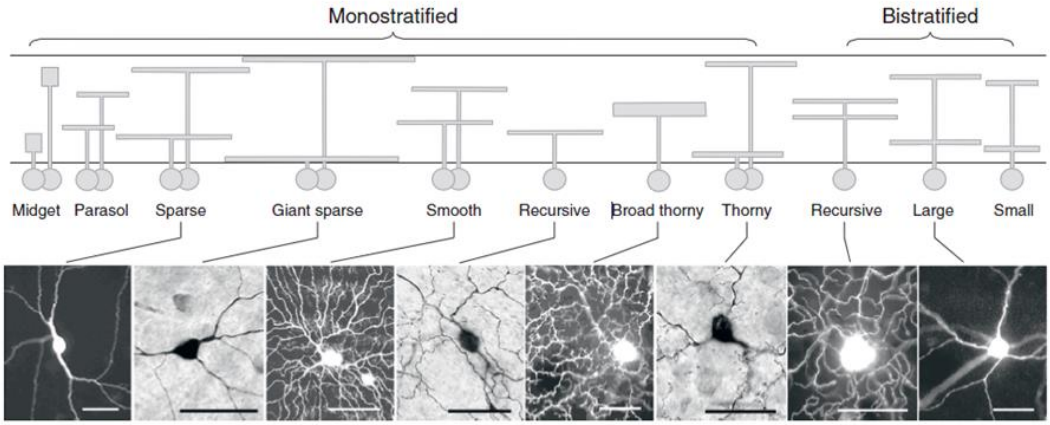

Figure 1.8: Morphological classification of RGCs based on dendritic arbor stratification. The top panel displays schematic representations of 17 different RGC types stratifying at different levels of the IPL with small to wide dendritic fields. Bistratified RGCs receive inputs from both ON and OFF layers within the IPL. The bottom layer displays optical micrographs of 8 different RGCs filled with histological markers. Scale bars are 50 µm (Dacey 2004).

In primates, at least 13 of the different RGC populations project to the LGN, with 90% of these cells being midget, parasol or bistratified RGCs (Schiller and Logothetis 1990). These cell types are understood to form the basis of three anatomically segregated pathways which have been particularly well characterised (figure 1.9) from their photoreceptor inputs to their visual fields in the primary visual cortex (V1). Midget RGCs mediate red-green colour opponency by processing individual ON or OFF signals from L or M cones. In the fovea, this is mediated on a 1-to-1 cell basis. Parasol RGCs integrate the input of many different cones in either ON or OFF sublaminae of the IPL. Bistratified RGCs integrate inputs from L, M and S cones in both the ON and OFF sublaminae of the IPL to mediate blue-ON / yellow-OFF colour opponency (Dacey and Lee 1994). Midget RGCs (green lines in figure 1.9) project to parvocellular layers of the LGN (1,2), parasol RGCs (black lines) project to the magnocellular layers of the LGN (3,

4, 5 and 6) and bistratified RGCs (blue lines) project to koniocellular layers of the LGN. Magno and parvocellular projections from the LGN terminate in layers 4α and 6 of V1. Koniocellular projections from the LGN terminate in layers 1 and cytochrome oxidase blobs of layers 2/3 in V1 (Chatterjee and Callaway 2003). These blobs are cylindrical sections of the visual cortex which are the synaptic target of colour mediating neurons and were first discovered through the use of retrograde tracing with cytochrome oxidase (Wong-Riley 1979).

Characteristics of cells in the parvocellular pathway include small receptive fields, low contrast sensitivity, slow axonal velocities, low temporal frequencies and high spatial frequencies. Conversely, cells of the magnocellular pathway typically have large receptive fields, high contrast sensitivity, fast axonal velocities, high temporal frequencies and low spatial frequencies (Dacey 2000). The koniocellular pathway still remains to be characterised.

The remaining number of RGCs not included in the three pathways described above is (for primates) approximately 200 000, close to the total number of RGCs in a cat retina (Field and Chichilnisky 2007), highlighting the fact that these other RGCs are no doubt performing highly important functions. For example, melanopsin RGCs (~0.2% of RGCs) projecting to the suprachiasmatic nucleus are thought to play a role in circadian rhythms (Hattar, Liao et al. 2002). These remaining classes are hard to characterise due to their small sizes and sparse distributions.

The receptive field of a sensory neuron is defined as a region in space in which the presence of a stimulus will alter the activity pattern of that neuron. RGCs, being the output cells of the retina have complex receptive fields which originate from the responses of photoreceptors and are subject to processing by retinal interneurons. By tiling the retina with each type of RGC, these provide a multimodal representation of the visual field with different receptive fields having different sizes and encoding such complex spatiotemporal functions as local edge detection, directional selectivity or shadow detection. Most of the visual functions encoded have yet to be elucidated, although they are best characterised in the rabbit retina (Amthor, Takahashi et al. 1989).

The most extensively characterised RGC receptive fields are undoubtedly the concentric centre-surround receptive fields (figure 1.10) first discovered by Kuffler in 1953 (Kuffler 1953). ON-centre cells exhibit an increased response when illuminated in the central region of the receptive field and a decreased response when illuminated in the surround region of the receptive field. Conversely, OFF-centre cells exhibit an increased response when illuminated in the surround region of the receptive field and a decreased response when illuminated in the central region of the receptive field. Increased responses can either be sustained or transient. These cells do not exhibit a significant change in spiking when the whole receptive field is illuminated.

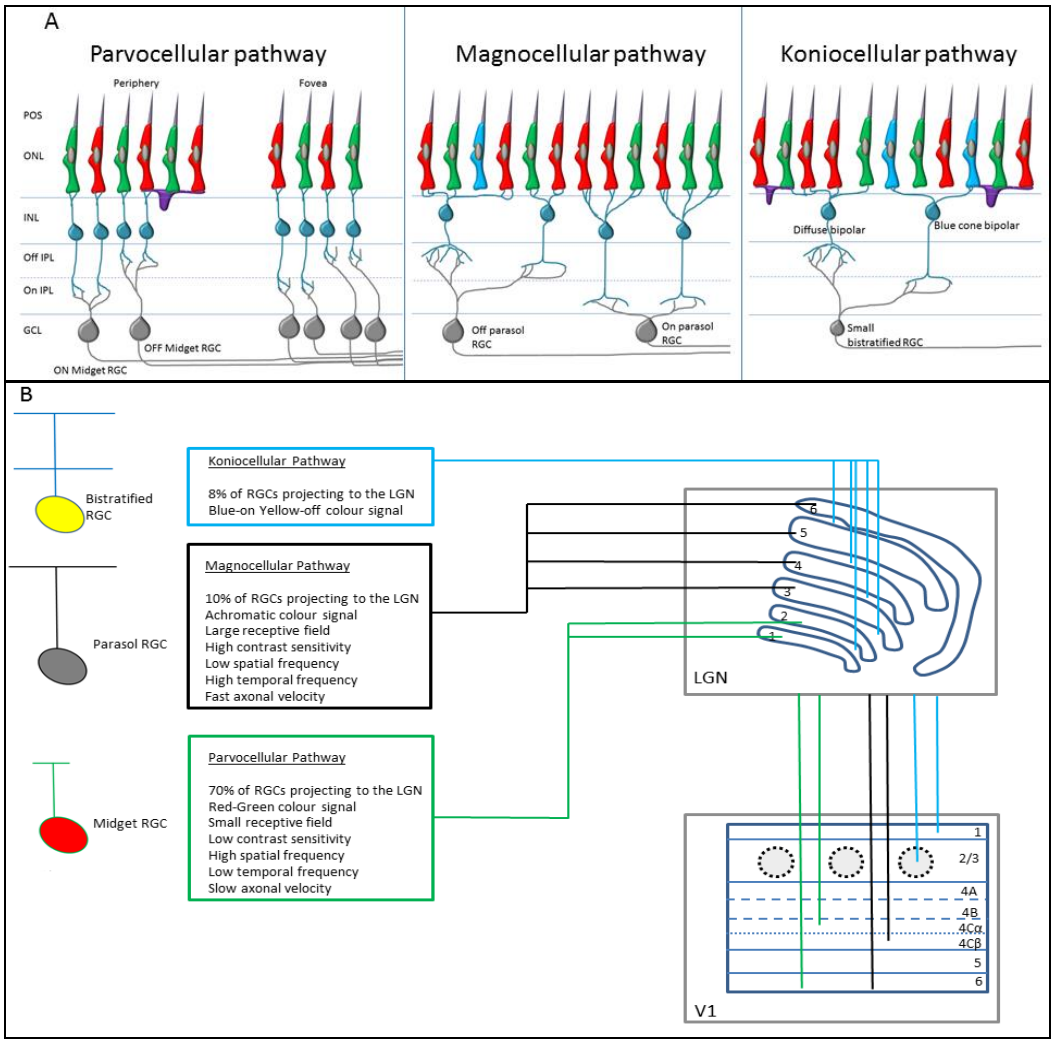

Figure 1.9: Anatomical segregation of magno, parvo and koniocellular pathways in the retina and brain. A: Diagram illustrating the retinal circuitry of the 3 main RGC types in the retina. L (red), S (blue) or M (green) cones contact HCs (purple) and BCs (dark blue) which in turn contact RGCs (grey). B: Diagram illustrating the projections of these separate pathways to the LGN and primary visual cortex (V1). Parvocellular connections: green lines. Magnocellular connections: black lines. Koniocellular connections: blue lines. Grey discs in layer 2/3 of V1: cytochrome oxidase blobs.

Combining the input of ACs and BCs, RGCs respond to much more complex stimuli which they encode with spatiotemporal signals in the form of trains of action potentials transmitted to anatomically segregated retinotopic maps in the LGN. These pathways remain segregated up to the visual cortex where they are integrated and transmitted along the ventral and dorsal streams to form visual perception.

Processing of the visual field by retinal neurons is incredibly complex. Although the literature offers a colossal amount of data, the complete story is still far from being understood. For more complete reviews and models, see (Hennig, Funke et al. 2002; Field, Gauthier et al. 2010).

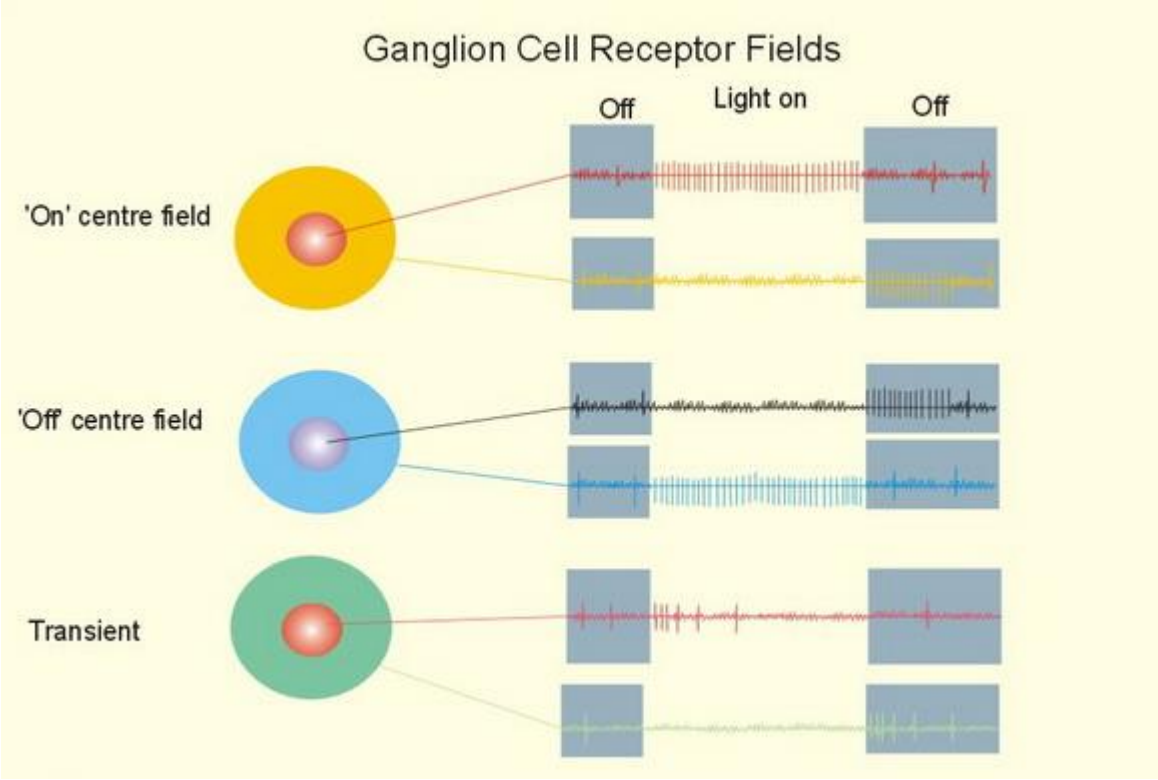

Figure 1.10: RGC centre-surround antagonistic receptive fields. ON-centre cells show an increased response to retinal illumination in the centre of their receptive field. However, when light is shone on the surround region, their firing pattern is inhibited but increases when the light disappears. OFF-centre cells show an increased response to retinal illumination in the surround region of their receptive field and a decrease in firing when light is shone on the receptive field centre. Their activity increases when the light disappears from the centre. When the entire receptive field is illuminated, there is no clear change in firing rate. Adapted from (Kuffler 1953).

1.1.4 Vascularisation of the healthy retina

A thorough understanding of the retinal vasculature is of vital importance to this project. Indeed, it has been demonstrated time and again that the slightest alteration to the retinal metabolic cycle can have disastrous consequences to vision (del Zoppo and Hallenbeck 2000; Antonetti, Barber et al. 2006; Bringmann, Pannicke et al. 2006). As we are proposing to interface electronic devices with this delicate tissue, it has to be established that the permanent introduction of a foreign body will not induce further degeneration. The principle of a retinal prosthesis relies mostly on the fact that RGCs operate flawlessly, making it vital to understand how these cells are maintained in perfect working condition. Location of inner retinal blood vessels and their relationship to RGCs will help in the design of an optimal electrode to interface with the inner retina.

The blood-retinal barrier (BRB) is divided into two distinct regions, the inner BRB and the outer BRB. The inner BRB is composed of specialized, very fine blood vessels below the astrocytic plexus of the ILM (figure 1.10). The tight junctions between the endothelial cells lining these retinal blood vessels provide variable permeability, modulated by endogenous chemical factors (Cunha-Vaz, Shakib et al. 1966; Cunha-Vaz 2004). The outer BRB consists of the RPE outlining the choroid vessels (Cunha-Vaz 2004; Choi and Kim 2008). The RPE is a layer of pigmented hexagonal epithelial cells whose multiple functions include the recycling of bleached photopigments and an interface with the choroid. The BRB contributes to maintaining homeostasis in the retinal microenvironment by limiting fluctuations in plasma composition and preventing blood-borne molecules from disrupting neural function. Small molecules can travel in and between the vitreous body and extracellular fluid of the retina either by diffusion or by bulk flow as there are no diffusional barriers between these two media. Thus, nutrients are delivered to the outer retina by the choroid via the RPE and to the inner retina via retinal blood vessels interfaced with retinal macroglia. Waste diffuses out of the retinal tissue through the extra-cellular medium and is then evacuated by the vitreous humour (Cunha-Vaz 2004). The choroid is much denser, supplying the metabolically hungry photoreceptors (Yu and Cringle 2001). The inner retinal vasculature is composed of a dense superficial vascular plexus, where blood

vessels supply Müller cells and astrocytes (figures 1.12 and 1.13) and less dense intermediate and deep vascular plexuses coupled to Müller cells only at the inner and outer edges of the INL respectively (Provis 2001).

Blood vessels consist of endothelial cells (ECs) supported by accessory mural cells (i.e. pericytes) and ensheathed in a basement membrane (Dorrell and Friedlander 2006). Blood vessel formation is either achieved through vasculogenesis (new vessels formed from precursor angioblasts) or through angiogenesis (vessels forming from existing capillaries) although it is generally agreed that deeper vascular plexuses are formed through angiogenesis (Chan-Ling, McLeod et al. 2004; Dorrell and Friedlander 2006). These involve a complex array of processes (reviewed by Dorrell and Friedlander (2006) as well as Provis (2001)) and can occur pathologically, leading to blindness (Adamis, Aiello et al. 1999).

1.1.5 The inner limiting membrane

The retina is separated from the vitreous humour by a basement membrane: the inner limiting membrane (ILM). Initially, neuro-anatomists thought the ILM was part of the distal retinal macro-glial end-feet (Pedler 1961). Similarly to other basement membranes, the ILM is composed of 3 different layers (figure 1.11): the *lamina rara interna* (adjacent to glial cell endfeet), the *lamina densa* and the *lamina rara externa* (contiguous with the vitreous humour). These layers have the typical molecular constitution of the layers in basement membranes with laminin, collagen IV, collagen I and other proteoglycans. Collagen fibrils of the vitreous are oriented parallel to the *lamina rara externa* rather than penetrating it (Matsumoto, Blanks et al. 1984; Malecaze, Caratero et al. 1985; Russell, Shepherd et al. 1991). The ILM constitutes both a physical and electrostatic barrier between the vitreous and retina. Indeed, it has numerous pores ranging from 10 to 25 nm in diameter (Nishihara 1991) and the *lamina rara externa* contains mostly negatively charged glycosaminoglycans such as hyaluronan, heparin sulfate, chondroitin sulfate and dermatan sulfate (Heegaard, Jensen et al. 1986; Chai and Morris 1994).

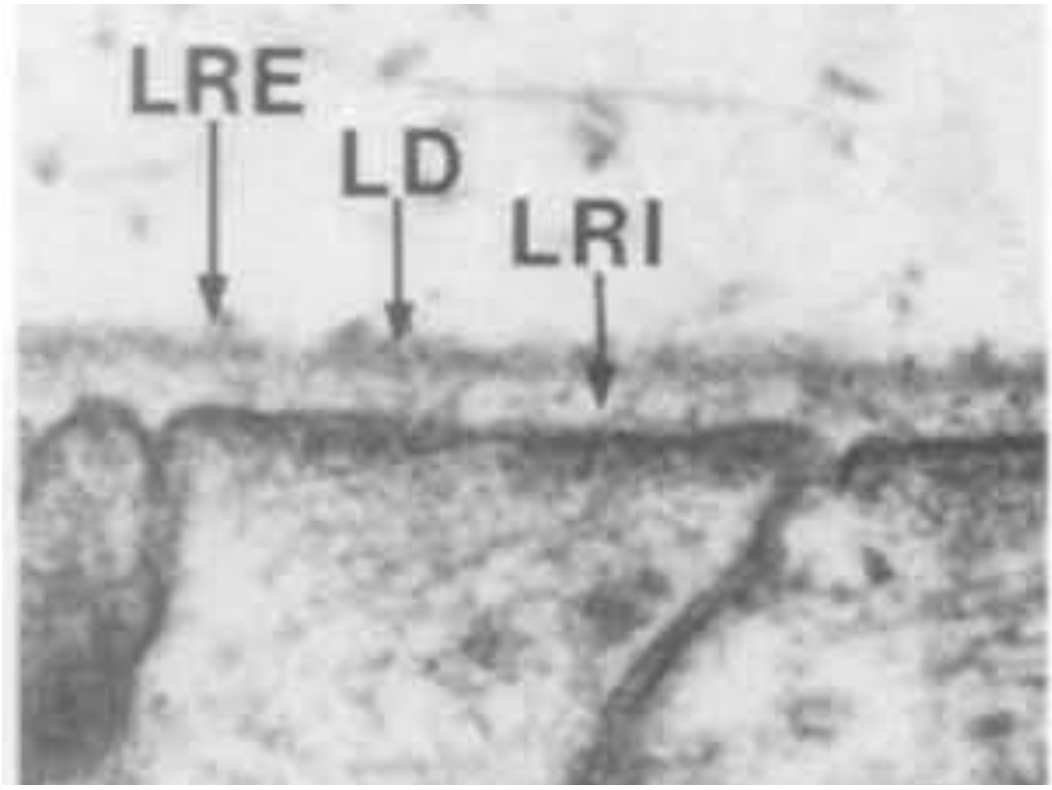

Figure 1.11: Ultrastructure of the ILM. Transmission electron micrograph (TEM) of the ILM from an adult rabbit retina, fixed with Alcian Blue, postfixed with osmium tetroxide and stained with uranyl acetate and lead citrate, detailing the 3 strata of this basement membrane. LRI: *lamina rara interna*, in direct contact with Müller cell cytoplasmic membrane; LD: *lamina densa*; LRE: *lamina rara externa*, in direct contact with the vitreous humour; X 62 000 magnification (Matsumoto, Blanks et al. 1984).

The ILM constitutes both a protective barrier and a delicate interface between the retina and the inner eye. Hence, applying an invasive electronic device to the vitreal side of the retina could have devastating consequences for RGCs. The impairment of Müller cells, astrocytes and retinal blood vessels would impact on the survival of RGCs following implantation of an artificial device as all three are important players in retinal metabolism and homeostasis.

1.1.6 Glial cells in the healthy retina

Glial cells are an important part of the CNS and, in vertebrates, there are 10 to 50 times more glial cells than there are neurons (Kandel, Schwartz et al. 2000). With their name stemming from the Greek word gliok for glue, neuroglia are defined by their architectural support of the nervous system. Although not electrically excitable, glial cells are exquisitely intertwined with neurons in a number of different ways. The vertebrate retina contains three types of glial cells, namely microglia, astrocytes and Müller cells. The next sub-sections review the role of these cells in retinal physiology.

Microglia

Microglia, which populate most layers of the retina (ONL, OPL, INL, IPL, GCL, NFL; (Chen, Yang et al. 2002)) play an important role in the immunological protection of the retina against disease, injury and infection. First seen using the Nissl stain in the 1880s, they were identified as the primary form of immune defence in the CNS (Rio-Hortega 1932; Gehrmann 1996). As the resident macrophages of the brain and spinal cord, their response to microscopic threats include phagocytosis, local proliferation, migration as well as the secretion of cytokines, neurotoxins and chemokines. They have also been implicated in the progression of retinal degeneration diseases (Streit, Walter et al. 1999; Zeiss and Johnson 2004; Langmann 2007).

In their quiescent state, microglia patrol the retina by constantly extending their processes and sensing the environment with an array of proteins expressed at the surface of these processes (Nimmerjahn, Kirchhoff et al. 2005). These proteins include cytokines, chemokines, antibodies, adhesion molecules, purinergic receptors and molecules of the complement system (Langmann 2007). The complement system is a major component of innate immunity and enhances adaptive immunity (Carroll 2004). Microglia activation is triggered by pro-inflammatory cytokines, complement components, thrombin, aggregated insoluble peptides, lipopolysaccharides, gangliosides or heat shock proteins (Schuetz and Thanos 2004). Microglia activation is characterised by migration, proliferation, expression of phagocytic and sulphate receptors, and the release of cytokines, chemokines, neurotoxins, prostaglandins,

nitric oxide, superoxide anions and glutamate. Chronic exposure to these molecules can cause progressive neurodegeneration (Langmann 2007).

Activated microglia have been observed consistently in some models of retinal disease (discussed below) which suggests they may be involved in the initiation or perpetuation of some degenerative processes (Zeiss and Johnson 2004; Zeng, Zhu et al. 2005; Gehrig, Langmann et al. 2007).

Astrocytes

Although they are a ubiquitous feature of the CNS, astrocytes are confined to the inner most layers (NFL, GCL) of vascularised retinal areas (they are absent from the foveal avascular zone). In the NFL, astrocytic processes run parallel to and in between RGC axon bundles, suggesting that these cells provide support to RGCs only (Ogden 1978; Bussow 1980). Believed to immigrate from the optic nerve during development (Watanabe and Raff 1988), retinal astrocytes are heavily connected to both retinal blood vessels and RGC axons (Stone and Dreher 1987), as seen in figure 1.12. During development, immature astrocytes expressing high levels of glial fibrillary acidic protein (GFAP) provide a template for inner retinal vasculature and promote angiogenesis until vascular maturation when they become quiescent (Fruttiger, Calver et al. 1996; Gerhardt, Golding et al. 2003; Dorrell and Friedlander 2006). The maturation of astrocytes is initiated by ECs of the mature inner retinal vascular plexus (Sakimoto, Kidoya et al. 2012).

Contrarily to retinal astrocytes, those resident of the prelaminar optic nerve (portion of the optic nerve located inside the eye) are fibrous and run perpendicularly to axonal bundles (Ogden 1978; Bussow 1980), prolonging the intimate relationship with RGCs established in the retina. Indeed, astrocytes of the optic nerve are deeply implicated in the response to axonal lesions, inducing RGC cell death in amniotes (reptiles, birds and mammals) and mediating neural regeneration in anamniotes (Garcia and Koke 2009). Anamniotes (fish, amphibians) have been extensively studied for their substantial neuro-regeneration capabilities (Rio, Reperant et al. 1989; Nagashima, Sakurai et al. 2009; Duprey-Diaz, Blagburn et al. 2012; Koriyama, Sugitani et al. 2012).

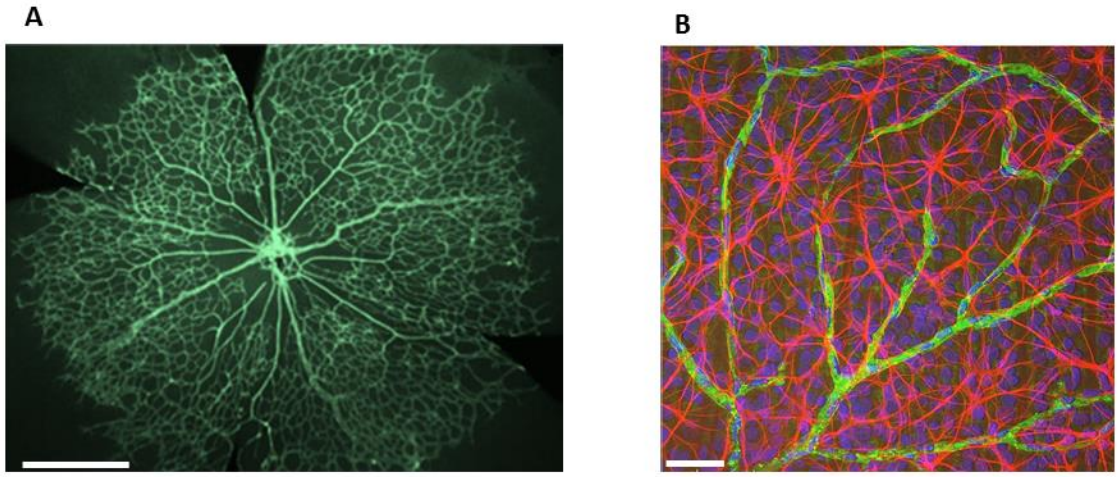

Figure 1.12: Inner retinal vasculature intimately coupled to astrocytes. A: Confocal micrograph of retinal blood vessels stained with PECAM-1, scale bar 40 µm (Sakimoto, Kidoya et al. 2012). B: Confocal micrograph of retinal astrocytes (red) intimately coupled to blood vessels (green, blue nucleus of endothelial cells) and RGCs (purple), scale bar: 40 µm Adapted from www.webvision.med.utah.edu.

Despite their symmetrical appearance, quantitative morphometric studies have helped gather evidence that astroglial cells are in fact polarized, with a number of processes ensheathing synaptic contacts of proximal neurons whilst at least one process is in contact with a blood vessel (del Zoppo and Hallenbeck 2000; Koehler, Roman et al. 2009). Astrocytic end feet are electrically coupled to neurons and other astrocytes via gap junctions (electrical synapses) allowing the propagation of biological signals. This anatomical affiliation has led to the suggestion that integration of neural signals by astrocytes can lead to the constriction of cerebral vessels and thus to the modulation of cerebral blood flow (Harder, Alkayed et al. 1998; Koehler, Roman et al. 2009). Astrocytes can affect the activity of adjacent cells by releasing neurotransmitters (Parpura, Grubisic et al. 2011; Parpura and Verkhratsky 2012). Calcium imaging studies in the retina report the propagation of calcium waves along the astrocytes of the inner vitreo-retinal interface. Although the waves propagate equally between astrocytes and Müller cells, they do not propagate transversely along the bodies of Müller cells (Keirstead and Miller 1995; Newman and Zahs 1997; Newman 2001).

In the brain and spinal cord, astrocytes respond to injury through hypertrophy, hyperplasia and migration to the site of injury as well as fibrotic scar formation (Hatten, Liem et al. 1991; Norenberg 1994; Fitch and Silver 2008). This is accompanied by an up-regulation of GFAP and vimentin. However, retinal astrocytes which form an

interconnected syncytium in the NFL and GCL do not respond to injury in the same way. Instead, they decrease in numbers in response to injury and hypoxia before RGCs start showing any signs of stress (Chan-Ling and Stone 1992; Medana, Chan-Ling et al. 1996; Rungger-Brandle, Dosso et al. 2000). Retinal astrocytes subsequently recolonize the depleted regions (Chan-Ling and Stone 1992; Tailoi, Tout et al. 1992), demonstrating their benign hyperplasic abilities.

In lieu of the hyperplasic and hypertrophic responses of their CNS counterparts, retinal astrocytes have been heavily implicated in the synthesis of nitric oxide synthase in response to mechanical force (intra-ocular pressure) leading to RGC cell death (Neufeld 1999; Liu and Neufeld 2001). It is worth noting that retinal astrocytes have been seen to proliferate in retinal tumour (Khawly, Matthews et al. 1999) and during development (Moshfeghi 2006).

Müller Cells

Müller cells span the entire thickness of the retina (figure 1.12, left) from the ILM to the ONL ensheathing all neurons. Their end-feet, intermingled with those of astrocytes define the vitreo-retinal border. Numerous microvilli ensheath photoreceptor inner segments and mediate nutrient exchanges with the sub-retinal space (Uga and Smelser 1973).

Each Müller cell constitutes the core of a columnar micro-unit of retinal neurons, establishing anatomical links between the neurons they ensheath and the other compartments of the eye, namely, the RPE, the vitreous body and the retinal blood vessels (figure 1.13, right). During development, progenitor cells undergo several divisions, eventually leading to a group of neurons with a Müller cell at its core. In this manner, all the cells in a columnar unit are both clonally and functionally connected (Bringmann, Pannicke et al. 2006).

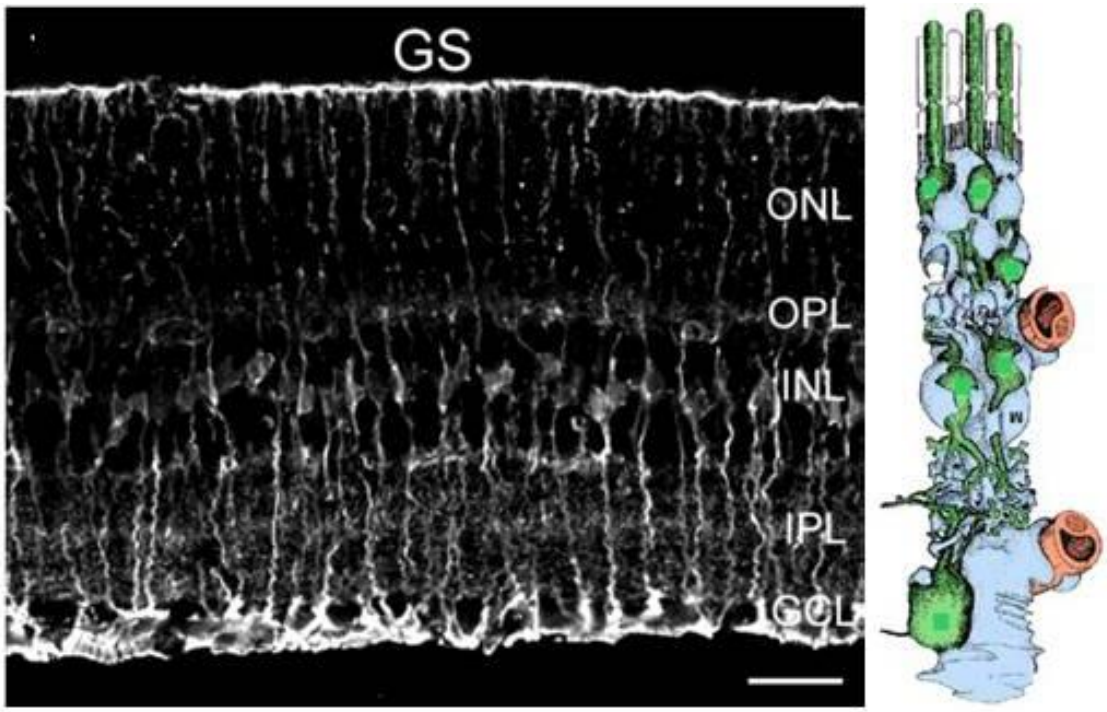

Figure 1.13: Müller cells in the retina. Left: Confocal micrograph of a mouse retinal transverse section stained for glutamine synthetase (GS), an enzyme only expressed by Müller cells (Haverkamp and Wassle 2000), scale bar 25 µm. Right: Diagram of a retinal columnar unit with a Müller cell (blue) ensheathing neurons (green) and capillaries (orange). Adapted from (Bringmann, Pannicke et al. 2006).

The metabolic "ménage a trois" occurring in the cortex between blood capillaries, astrocytes and neurons becomes more complicated in the retina with the addition of Müller cells. With an absence of vasculature in the fovea and the high metabolic demands of photoreceptors, the retina requires a constant supply of energy and a delicate homeostasis. For a thorough review, see (Bringmann, Pannicke et al. 2006).

Müller cells are resistant to anoxia, their metabolism relying mainly on anaerobic glycolysis (Poitry-Yamate, Poitry et al. 1995; Winkler, Arnold et al. 2000) and provide a robust and efficient support to cater for the needs of neurons. The metabolic and nutritional needs of retinal neurons are quenched with the direct delivery of lactate and pyruvate as well as glycogenesis and the storage of glycogen. Potassium homeostasis is achieved by the removal of K^+ ions from the extracellular medium and its release in the vitreous body via Müller cell end-feet. Water homeostasis is maintained by the buffering of CO_2 and the dehydration of the inner retina. The scavenging of free radicals by Müller cells protects retinal neurons from oxidative

stress. The transport of GABA and glutamate complemented by the recycling of glutamate into glutamine by glutamine synthetase assists with the operating of neural signalling. The transport of bleached photopigments to the RPE for recycling purposes is carried out by the Müller microvili around photoreceptor cell outer segments. In addition, Müller cells play an important role in operating delicate control over neural function and retinal blood flow by releasing both neuroactive and vasoactive substances.

As well as maintaining an adequate environment for retinal function, Müller cells play an active role in neural repair (Bringmann and Reichenbach 2001). Following retinal damage, Müller cells activate via up-regulation of intermediary filaments (vimentin and GFAP), hyperplasia, dedifferentiation and hypertrophy (Burke and Smith 1981). Following retinal detachment, their processes invade the outer retinal layers, forming a glial scar and attempting to inhibit photoreceptor death (Anderson, Guerin et al. 1986; Lewis and Fisher 2000). Müller glia mediate both neuronal death (Goureau, Regnier-Ricard et al. 1999; Koeberle and Ball 1999) and rescue (LaVail, Unoki et al. 1992; LaVail, Yasumura et al. 1998; Lewis, Linberg et al. 1999) through the release of cytokines and neurotrophic factors.

1.2 Retinal Dystrophies

Retinal diseases have been characterised extensively and the pathological insults number close to 200 gene defects (http://www.sph.uth.tmc.edu/retnet), with disease loci spanning 23 different genes as well as mitochondrial gene loci. Retinal diseases are subdivided into two main types: optic neuropathies and retinal dystrophies. Optic neuropathies are diseases affecting the RGCs, they can be the result of injury to the optic nerve (Wang, Robertson et al. 2001), toxicity (Kesler and Pianka 2003), intraocular hypertension (Kass, Heuer et al. 2002) or genetic disorders (Newman 1993). As RGCs represent the link between the retina and the brain, restoration of sight cannot be achieved using retinal prostheses (which rely on RGC survival) in optic neuropathies. At the other end of the spectrum, retinal dystrophies affect the photoreceptors. Common retinal dystrophies include Leber congenital Amaurosis (LCA), AMD or RP. LCA and RP are both hereditary (Dryja and Li 1995; Perrault, Rozet et al. 1999; Rivolta, Sharon et al. 2002) whilst the causes of AMD still remain unclear. Defects of the visual field (periphery in RP and central in AMD) are not always as devastating as full-fledged blindness, yet can impair patients in a dramatic way (reading, driving etc). Restoring the ability to perform such activities as driving or reading can be of huge benefits to those who miss them and within the reach of retinal prosthetic devices.

RP is a well characterised inherited dystrophy and has a prevalence of approximately 1 in 4000 with 1 million affected individuals worldwide (Hartong, Berson et al. 2006). Rods deteriorate prior to cones, leaving patients with a progressively diminishing peripheral and scotopic vision.

AMD is far more common and prevalence increases dramatically with age, affecting 0.2% of the combined population of three continents aged 55 to 64 years, then affecting 13% of the population older than 85 (Smith, Assink et al. 2001). Conversely to RP, this disease targets the macula, depriving patients from high resolution vision, thus impairing such tasks as reading or face-recognition. It can occur in either “wet” (choroidal neovascularisation) or “dry” (central geographic atrophy) forms, affecting patients with different timelines, proportion and severity (Chakravarthy, Evans et al. 2010). Dry AMD (90% of all forms of AMD) is caused by atrophy of RPE of the macular

region whilst wet AMD is characterised by an abnormal growth of choroidal blood vessels, leading to leaking of protein and blood in the sub-retinal space. As the macula is devoid of RGCs (cf. section 1.1.1), targeting such cells with an epi-retinal prosthesis has to be achieved in the direct periphery of this region, where RGCs are stacked into multiple layers.

LCA has a prevalence of 1 in 80 000 people, with blindness occurring at birth or in the first few months of life (Maguire, Simonelli et al. 2008).

Defects in retinal dystrophies are numerous, complex and not always well understood, but all lead to oxidative stress and eventual death in the photoreceptor population. This deafferentation was initially thought to spare the neural retina, but research conducted over the last decade has demonstrated heavy remodelling on the molecular, synaptic, cellular and tissue scales for all retinal cell types.

1.2.1 Remodelling of the dystrophic retina

A number of studies, accumulating anatomical evidence from humans and animals with retinal dystrophy reveal drastic remodelling in the neural retina (Marc, Jones et al. 2003; Jones, Kondo et al. 2012). Whatever the cause of photoreceptor death, the retina seems to fall into a typical 3-phase pattern of remodelling (figure 1.14) whose kinetics vary according to the type of retinal dystrophy (Marc 2010).

Phase 1 of retinal remodelling is characterised by photoreceptor stress leading to outer segment truncation and rewiring of their synaptic output. Rods harbouring a rhodopsin defect have been shown to bypass their BC targets and connect directly to RGC dendrites (Marc 2010). Retinal interneurons also display dendritic rewiring, with retargeting to adjacent cone pedicles and a down-regulation of glutamate receptor expression in BCs (Jones, Kondo et al. 2012). This reprogramming in their molecular pharmacology leads to a shift in the functional phenotype of BCs from ON to OFF responses (Marc, Jones et al. 2007; Jones, Kondo et al. 2011). Insults to photoreceptors induced by light damage lead to alteration in the metabolic profiles of Müller cells (Marc, Jones et al. 2008).

Phase 2 of retinal remodelling is characterised by photoreceptor cell death and the formation of a Müller cell seal entombing the neural retina. Depending on the type of disorder, photoreceptor cell death can occur as a widespread phenomenon or in bursts of sporadic apoptosis. Typically, rod death precedes cone death, with some forms of diseases sparing cones, leading to a delay in the onset of phase 3. Phagocytic ablation of the photoreceptor somata by activated microglia and hypertrophic Müller cells lead to a collapse of the distal Müller cell scaffolding and the formation of the Müller cell seal (Jones, Watt et al. 2003; Marc and Jones 2003; Jones and Marc 2005). A complete loss of BC input leads to a change in their morphology as well as aberrant glutamate receptor expression. In cone-sparing forms of retinal degeneration, phase 2 displays BC neurite sprouting to adjacent cones, synaptogenesis and microneuromas (discussed below). The glial seal is formed by hypertrophic and displaced Müller cells linked by adherens junctions. There does not seem to be any evidence suggesting the involvement of astrocytes in this process.

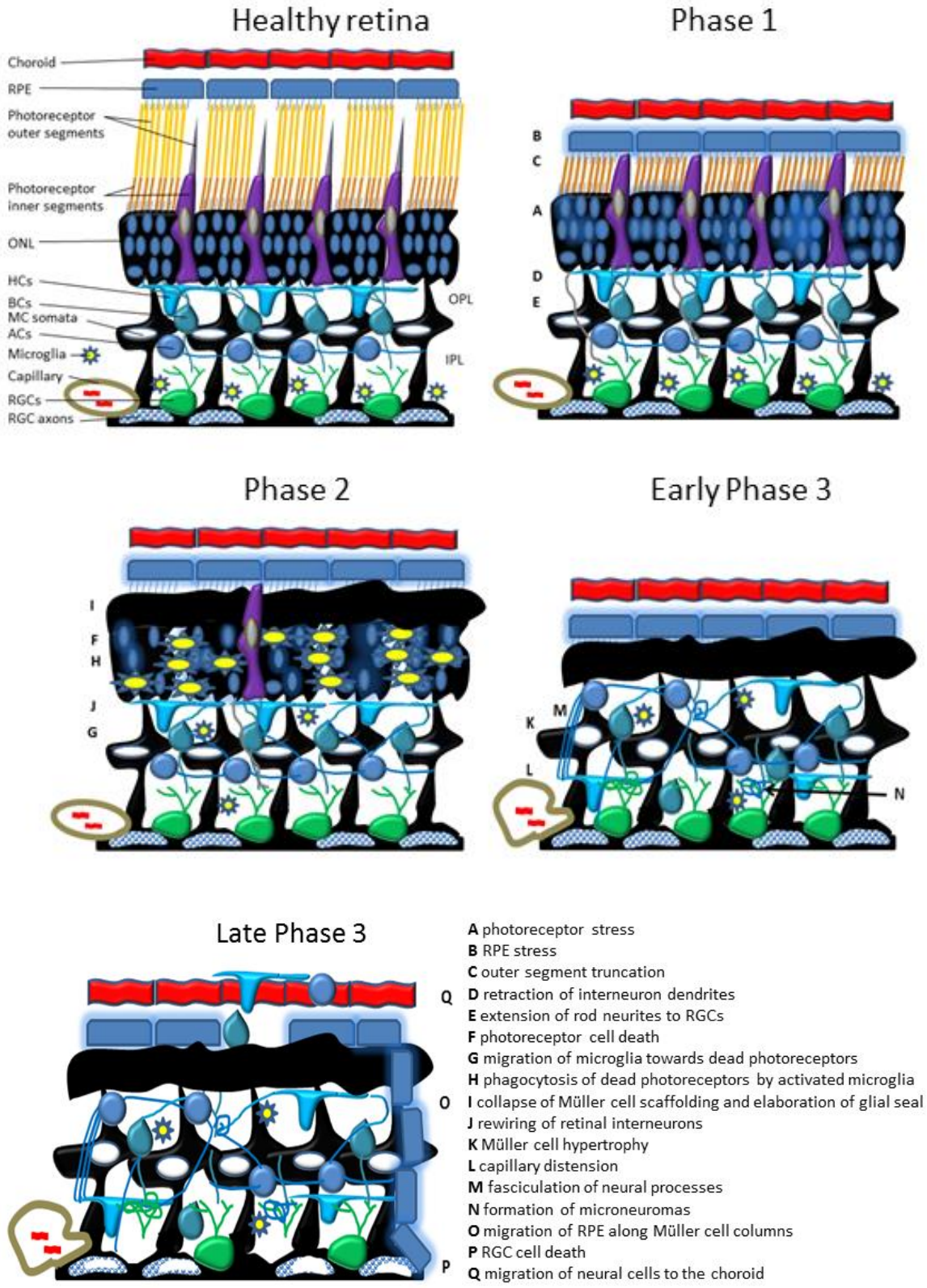

Figure 1.14: Three phases of retinal remodelling. Diagram outlining the 3 typical phases of remodelling during retinal degeneration. Although the kinetics of retinal remodelling differ according to the type of dystrophy, they all follow the same pattern. Not to scale.

Phase 3 occurs when photoreceptor death is complete, highlighting the importance of cone rescue in retinal repair strategies. It is characterised by persistent and continuous remodelling of the retina with a vertical cellular displacement (RGCs invading the INL, ACs and BCs invading the GCL, RPE colonising the vascular retina along Müller cell columns) and sprouting of neurites forming ectopic synapses. These neurites can travel hundreds of microns as bundled fascicules or form tangles of neuropil outside the typical lamination of the IPL as microneuromas (Jones, Watt et al. 2003; Marc, Jones et al. 2003; Jones and Marc 2005; Jones, Marc et al. 2006). The fuctional connectivity of these microneuromas is very complex and can be elucidated through the use of the connectomic approach, where ultra-thin retinal sections are analysed with electron microscopy and reconstructed over several hundreds of microns (Jones and Marc 2005; Anderson, Jones et al. 2009; Anderson, Jones et al. 2011; Marc, Jones et al. 2012). It is worth noting that there does not seem to be an end to retinal remodeling, which can eventually lead to RGC death (Jones, Watt et al. 2003; Jones and Marc 2005; Marc, Jones et al. 2007) and cellular migration (glia and neurons) into the choroid (Jones, Watt et al. 2003; Sullivan, Penfold et al. 2003; Jones and Marc 2005).

In terms of retinal function rescue, scientists and engineers are fighting a moving target, with an ever shifting window of opportunity. Preventing a degenerating retina from going into phase 3 can rescue some of the connectivity as well as save RGCs. As such, preventing photoreceptor death from oxidative stress is a solution which has been investigated in recent years. Such anti-oxidants as saffron have been shown to protect cones from cell death in albino rats after light-induced retinal damage (Maccarone, Di Marco et al. 2008). In this study, Sprague-Dawley rats were pre-fed a saffron supplement before being exposed to bright light for 24 hours. Flash electro retinograms and TUNEL (Terminal deoxynucleotidyl transferase) analysis (to identify apoptotic cells) performed a week after retinal insult provided both functional and anatomical evidence for photoreceptor protection in saffron-treated animals. Further research demonstrated improved flicker sensitivity in early AMD patients following short term (3 months) saffron-based dietary supplement (Falsini, Piccardi et al. 2010; Piccardi, Marangoni et al. 2012). In addition to being a strong antioxidant, saffron appears to affect the expression of dozens of genes involved in cell death,

inflammation and cellular matrix organisation (Natoli, Zhu et al. 2010). Hence its effect is complex, requiring additional investigation.

1.2.2 Models of dystrophic retina

The literature provides ample evidence for different animal models of retinal degeneration in rats (Pavlidis, Fischer et al. 2000; Cuenca, Pinilla et al. 2004; Pinilla, Lund et al. 2005; Machida, Raz-Prag et al. 2008; Garcia-Ayuso, Salinas-Navarro et al. 2010; Li, De La Garza et al. 2012), mice (Bowes, Li et al. 1990; Freund, Gregory-Evans et al. 1997; Furukawa, Morrow et al. 1997; Strettoi, Porciatti et al. 2002; Strettoi, Pignatelli et al. 2003; Morrow, Furukawa et al. 2005; Lin, Masland et al. 2009), rabbit (Jones, Kondo et al. 2011; Zhou, Zhang et al. 2012), pig (Iandiev, Uckermann et al. 2006; Ross, Fernandez de Castro et al. 2012) and cat (Linberg, Lewis et al. 2006).

Retinal degeneration can occur naturally (e.g. Royal College of Surgeons rat), be genetically engineered (e.g. CRX knockout mouse) or be initiated by a physical insult (retinal detachment or strong light exposure in albino animals). The genetically engineered models are typically seen in rodents although recent work resulted in the generation of a P23H porcine model (Ross, Fernandez de Castro et al. 2012). The plethora of data on rodent models (for review, see Marc and Jones 2005) allows researchers to extrapolate the kinetics of retinal degeneration in humans and scheme biological rescue strategies.

As described above, the kinetics of each type of degeneration is different. In this study, we have used the cone rod homeobox (CRX) knockout mouse, a model of LCA. CRX is an important gene for the development of photoreceptor outer segments as well as for the survival of photoreceptors (Freund, Gregory-Evans et al. 1997; Furukawa, Morrow et al. 1997). Consequently, the photoreceptors of CRX -/- mice have atrophied outer segments (Morrow, Furukawa et al. 2005) and therefore they cannot transduce light. Photoreceptors start to die at postnatal day 30 (P30) and the ONL progressively shrinks from 12 rows to 6 at P90, then 3 at P150 and 1 at P210 (Pignatelli, Cepko et al. 2004). The GCL does not appear corrupted until P210, but both BCs and HCs show significant neurite remodelling after 1 and 5 months, respectively.

Consequently, the CRX -/- retina spends most of its adult life (P30 to P210) in phase 2 of retinal remodelling. This study incorporates data collected from retinas harvested between P80 and P200, where RGCs do not show any remodelling, but the ONL is decimated and Müller cells are in an activated state.

1.2.3 Electrophysiological characteristics of the dystrophic retina

The synaptic rewiring and morphological remodelling described above has dramatic consequences on the electrophysiological behaviour of the retina. Without the visual input from photoreceptor cells, surviving neurons need recurrent input for self-activation in order to stay alive. By reconstructing the circuitry of a microneuroma from ultra-thin sections, Jones and Marc (2005) proposed a model in which 4 BCs, 2 GABAergic and 3 glycinergic ACs converge onto a single RGC in a system where any input would produce persistent oscillatory behaviour (figure 1.15 A). In normal wiring, a brief impulse of depolarizing current to a BC will yield a small-signal RGC voltage response (black trace in figure 1.15 B). The response produced by a microneuroma is characterised by a resonant ringing response (gold trace in figure 1.15 B).

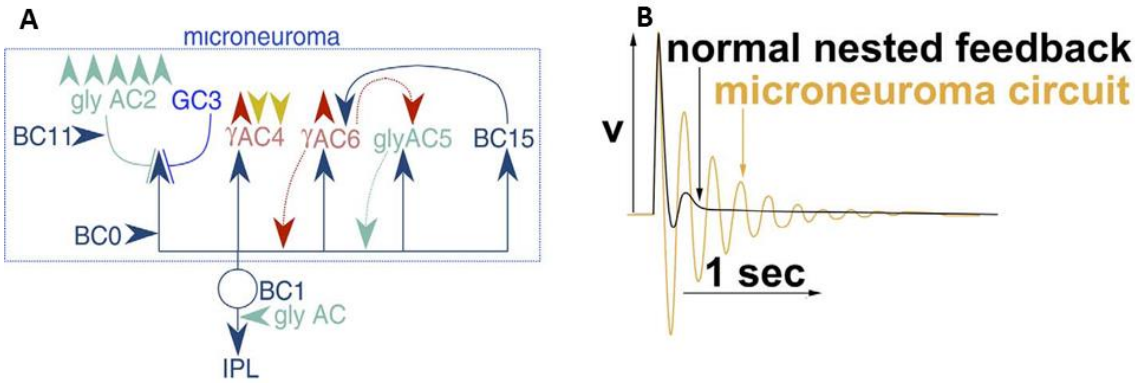

Figure 1.15: Model implicating microneuromas in oscillatory processing of retinal input. A: Diagram of aberrant wiring in microneuroma, with gly: glyceinergic neuron; γ GABAergic neuron; GC: RGC. B: Graph of RGC voltage response to BC depolarisation in normal (black trace) and aberrant (gold trace) wiring (Jones and Marc 2005).

Such oscillations occur spontaneously in adult rd1 mice (Margolis, Newkirk et al. 2008; Stasheff 2008; Menzler and Zeck 2011), P23H rats (Sekirnjak, Hulse et al. 2009) and CRX mice (Adams, Simonotto et al. 2008) *in vitro*. These slow local field potentials (LFP) have a typical ~10 Hz frequency. Extracellular recordings from a multi-transistor array

allowing the simultaneous electrophysiological acquisition over 8192 electrodes of RGCs from isolated rd1 mice retinas showed the rhythmic activity to propagate at a velocity of 8mm/s (Menzler and Zeck 2011). The LFPs were abolished in the presence of either ionotropic glutamate receptor antagonists or gap junction blockers. The authors suggest that these propagating oscillations originate from BCs and are transmitted through electrically coupled ACs.

Whole-cell patch clamp recordings coupled to 2-photon imaging studies in rd1 and wild type mice revealed the oscillations to originate from an electrically coupled network of excitatory ACs (AII ACs) and ON-cone BCs (Borowska, Trenholm et al. 2011; Trenholm, Borowska et al. 2012). These persisted in the presence of pharmacological blocking of inhibitory inputs (including hyperpolarisation-activated currents blocked with Cs^+) but were found to be driven by gap junctions and voltage-gated Na^+ channels (blocked with meclofenamic acid and TTX respectively). These findings clash with those of Menzler and Zeck who could not abolish the oscillations with application of TTX. Pharmacological blockades of photoreceptor inputs induced the oscillations in wild type retinas (Borowska, Trenholm et al. 2011).

1.3 Retinal Prostheses

Retinal prostheses endeavour to restore a degree of vision in patients with photoreceptor degeneration. The principle is to piggyback onto the remaining circuitry of the retina (including RGCs and their axons) to transmit a signal to the brain. There are currently two main approaches to the design and implementation of retinal implants. Sub-retinal prostheses are inserted in the sub-retinal space whilst epi-retinal devices are apposed to the vitreo-retinal juncture.

1.3.1 Sub-retinal prostheses

The concept behind sub-retinal prosthetic devices is to insert an electrode array between the RPE and ONL, in the space normally occupied by photoreceptors in the healthy retina. Focused electrical pulses emanating from this region can stimulate second order neurons (HCs, BCs) that extend their neurites into the OPL. Efforts so far focused on using multi-photodiode arrays (MPDA) as artificial photoreceptor arrays, with stimulating electrodes activated by incoming light. The principle was initially conceived in the 1950s (Tassicker 1956), and has evolved considerably since then with relatively successful clinical trials conducted in the last decade on blind patients (Zrenner, Bartz-Schmidt et al. 2011).

The sub-retinal MPDA concept has a number of advantages. First of all, it stimulates the visual system by replacing the earliest component in the feed-forward pathway (photoreceptors). Thus, the signal would take advantage of normal retinal processing (spatiotemporal processing by retinal interneurons) with no need for external processing devices, keeping the system relatively simple and straight forward. Another advantage is that the fabrication process for MPDAs allows for a very high number of stimulating electrodes (as they do not require to be electronically connected to individual channels), increasing perceptual resolution. Secondly, the device can be fixed robustly in the sub-retinal space without any need for surgical tacks. Thirdly, the device can be surgically implanted in such a way that it moves exactly with the eye, solving such technical issues as object tracking, temporal inhibition and image fading (Klier and Angelaki 2008). Natural eye movements are intrinsic to these processes, as

movements are difficult to reproduce on a head-mounted camera (in the case of epi-retinal devices).

The downsides of this system are not negligible. For one, incident light is not powerful enough to generate supra-threshold stimulation pulses. Retina Implant AG solved this problem by supplying power to the device via a transdermal cable. In the first generation of the device, there were 1500 MPDA elements (72 x 72 µm each) composed of a photodiode controlling a differential amplifier whose output was a titanium nitride (TiN) stimulating electrode (50 x 50 µm). The implantation time was limited to 126 days including pre- implantation and post-explantation procedures due to failure in the transdermal cable (Zrenner, Bartz-Schmidt et al. 2011). Next generation devices are currently being tested in Phase II clinical trials and contain a secondary coil implanted behind the ear and magnetically clipped to the primary coil (Rothermel, Liu et al. 2009). The presence of a sub-retinal implant would limit the nutrition intake from the choroid, but the authors argue that the inner retina is not dependent on choroidal perfusion.

Another approach to powering sub-retinal MPDAs is the use of a near infra-red (880 – 915 nm wavelength) projecting system which transmits data from a visual scene captured by a head-mounted camera and uses a projection system illuminating individual photodiodes (Mathieson, Loudin et al. 2012; Wang, Mathieson et al. 2012; Mandel, Goetz et al. 2013). The electrodes on this array have 3 pn (p-type semiconductor adjacent to an n-type semiconductor) photodiodes in series linked to an active and a concentric return (Iridium oxide) electrode creating pixels 280, 140 and 70 µm in diameter. Each pixel is separated by a 5 µm trench to allow the flow of nutrients from the choroid to the inner retina. Although this system is very promising, it has only been tested in animals and is limited by the mismatch between ocular movements and data acquired by a head mounted camera. Microsaccades are involuntary ocular movements occurring during fixation indispensable to visual perception (Darwin and Darwin 1786). This constant movement of the retina presents an issue to a projection system delivering a constant stream of information to it (also applicable to Optogenetic solutions, see below).

Possibly the biggest failing of sub-retinal prosthesis is the assumption that inner retinal circuitry is intact and available to process visual information in dystrophic retinas. As discussed in the previous section of this chapter, dystrophic retinas undergo severe remodelling, decimating and displacing retinal interneurons as well as creating dysfunctional synapses with aberrant connectivity. Stimulation of the INL with a raw visual signal is unlikely to result in the proper processing of this signal (Jones, Marc et al. 2011).

1.3.2 Epi-retinal prostheses

The concept of an epi-retinal prosthetic device is to stimulate RGCs directly with an array of stimulating electrodes affixed to the vitreo-retinal juncture. The electrodes need to deliver a coherent neural code to the RGCs as the processing achieved by photoreceptors and retinal interneurons has been bypassed. Therefore, the multi electrode array (MEA)'s input is driven by an externally processed feed originating from a video camera (figure 1.15).

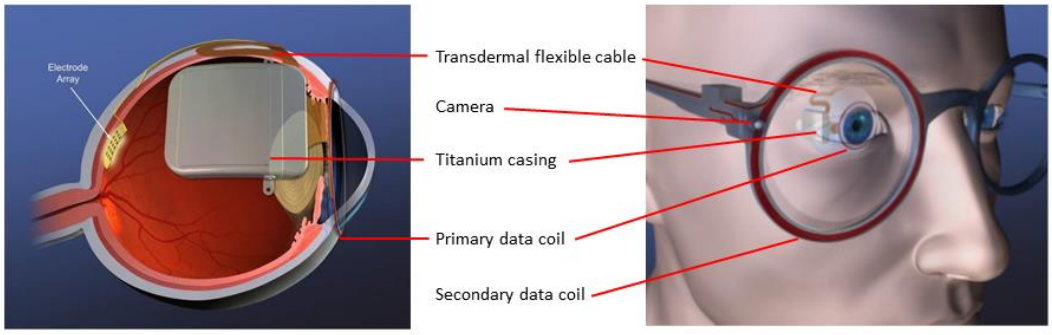

Figure 1.15: Epi-retinal prosthetic device concept. Artist's representation of an epi-retinal prosthetic system (Shire, Kelly et al. 2009). The camera captures a constant video footage of the visual scene which is processed and streamed wirelessly along with power to the secondary data coil, sutured around the cornea. This signal is processed by electronics encapsulated in a titanium casing and transmitted to the MEA via the flexible transdermal cable.

Interestingly, the initial advantages of an epi-retinal electrode lie in the system's complexity. Indeed, as there are multiple components to the system, upgrades and substitutions can be implemented without radical changes to the original configuration (e.g. the components in figure 1.15). The direct stimulation of RGCs provides an additional advantage in that there will be no dissipation of the signal via synaptic propagation through retinal interneurons. By cutting out chemical signalling, the risks

of introducing artefacts mediated by synaptic remodelling are eliminated. Ultimately, the vitreo-retinal interface provides an ideal location for a stimulating electrode array as it is out of the way of retinal nutrient supply by the choroid. Furthermore, heat generated by the electronics can be dissipated in the vitreous without any tissue damage (Margalit, Maia et al. 2002). The major challenge to this approach is that the encoding of complex visual scenes by RGCs into trains of actions potentials is not well understood yet. Furthermore, maintaining MEAs against the vitreo-retinal border is difficult and currently requires the use of retinal tacks, introducing a gap (and thus impedance) between the electrodes and target RGCs (Ahuja, Dorn et al. 2011).

Electrode number and resolution are important factors which need to be established before generating a working prototype. Psychophysical experiments revealed that a 25x25 array is sufficient for reading and mobility if localized around the fovea (Cha, Horch et al. 1992; Cha, Horch et al. 1992). Current epi-retinal strategies use planar stimulating arrays, but the technology exists to manufacture complex 3 dimensional penetrating arrays on the microscopic scales (Gunning, Kenney et al. 2009; Kawano, Harimoto et al. 2010; Gunning, Beggs et al. 2013).

The implanted MEA has to deliver complex patterns of electrical stimuli to the RGCs and each individual electrode has to deliver electrical pulses strong enough to elicit an action potential or train of action potentials in RGCs that are coupled to the same electrode. The threshold value is the minimum amount of charge to be delivered by an electrical pulse required for initiating an action potential. Achieving low threshold values offers a number of advantages. Indeed, lowering the threshold would result in a decrease in the amount of energy required to power the device, reducing the long-term damage to electrodes and tissue. Moreover, lower thresholds would result in less likelihood to cross-activate neighbouring electrodes, therefore enabling the use of denser arrays, with higher spatial resolution. Lowering the power consumption would allow the powering of more channels for the same amount of energy use, thus increasing the number of stimulating electrodes and improving visual perception.

Previously implanted epi-retinal electrodes still have very high activation thresholds (Margalit, Maia et al. 2002). *In-vitro* experiments on isolated retinas display much

lower thresholds than *in vivo* psychophysical experiments (Table 1.1). Indeed, multiple RGCs need to be stimulated in order to elicit phosphene perception in patients.

Direct epi-retinal stimulation of P23H rat RGCs *in vitro* did not show significant differences in thresholds or latency when compared to direct stimulation of WT RGCs (Sekirnjak, Hulse et al. 2009). Conversely, a number of studies activating RGCs with larger more widely spaced electrodes show an increase in threshold when stimulating degenerated retinas (Humayun, Propst et al. 1994; Suzuki, Humayun et al. 2004; Chen, Mahadevappa et al. 2006; O'Hearn, Sadda et al. 2006; Ye, Kim et al. 2008; Jensen, Ziv et al. 2009). However, these may have activated the RGCs synaptically, but could also suggest that the physiological or anatomical changes resulting from retinal degeneration lead to higher impedance between RGCs and stimulating retinal electrodes.

Table 1.1: *In vivo* and *in vitro* thresholds and characteristics of retinal stimulation

Reference	Experimental setup	Species	Electrode placement	Electrode material	Electrode diameter/ spacing (µm)	Pulse Width (µs)	Threshold charge density (mC/cm^2)
(Mahadevappa, Weiland et al. 2005)	*In vivo*	Human	Epi-retinal	Pt	500 and 250/800	1000	0.05-0.57
(Ahuja, Yeoh et al. 2013)	*In vivo*	Human	Epi-retinal	Pt Grey	200/502.5d	450	0.29
(Wilke, Gabel et al. 2011)	*In vivo*	Human	Sub-retinal	TiN	112.83/280 h 396d	2000-3000	0.2-0.6
(Ye, Ryu et al. 2010)	*In vitro*	Mouse	Epi-retinal	TiN	30/200	100-1000	0.069-0.318
(Ye, Ryu et al. 2010)	*In vitro*	Mouse rd1	Epi-retinal	TiN	30/200	100-1000	0.235-0.353
(Jensen, Rizzo et al. 2003)		Rabbit	Epi-retinal	Pt-Ir	3.56/Na	100	5-32.14
(Sekirnjak, Hulse et al. 2009)	*In vitro*	Rat	Epi-retinal	Pt	7-16/60	50/100	0.058
(Sekirnjak, Hulse et al. 2009)	*In vitro*	Rat P23H	Epi-retinal	Pt	7-16/60	50/100	0.049
(Sekirnjak, Hottowy et al. 2008)	*In vitro*	Rhesus monkey	Epi-retinal	Pt	9-15/60	50/100	0.05
(Wang, Mathieson et al. 2012)	*In vitro*	Rat/RCS rat	Sub-retinal	IrO_2	6 0, 40, 20/285, 145, 75	4000	0.26-0.32

Thresholds are highest *in vivo* and in sub-retinal experiments. Underlined numbers were derived from data provided in the referenced papers. Electrode spacing, h: horizontal, d: diagonal.

Epi-retinal stimulation carries the risk of activating RGC axons, which run closer to an epi-retinal stimulating electrode than target cell bodies. Modelling studies demonstrate that RGC somata have lower thresholds than their axons (Greenberg, Velte et al. 1999) owing to the denser distribution of voltage gated sodium channels at the initial segment (Boiko, Van Wart et al. 2003; Schiefer and Grill 2006). This is supported by in vitro stimulation of the rabbit retina (Jensen, Rizzo et al. 2003) with a 10 μm^2 Pt-Ir extra-cellular electrode which yielded somatic RGC thresholds 50% lower than axonal thresholds. In vitro stimulation of rhesus monkey retinas with closely spaced Pt-plated electrodes (60 µm pitch, 9-15 µm diameter) present empirical data suggesting the area most sensitive to epi-retinal stimulation were close to the soma and the proximal portion of the axon (Sekirnjak, Hottowy et al. 2008). Data obtained from patients implanted with the Argus I and II epi-retinal prostheses (Second Sight Medical Products, Inc, Sylmar, CA) show streak-like precepts which contrast with the usual punctate shape of elicited phosphenes and suggest the stimulation of axon bundles. This is to be expected considering the group uses electrodes 200 µm in diameter located ~180 µm from the retina with stimulation thresholds over 90 nC (Ahuja, Yeoh et al. 2013).

A variation on retinal prostheses is the optogenetic approach where populations of retinal neurons are transfected to express light sensitive membrane channels (Boyden, Zhang et al. 2005). Visual information can be acquired from an external camera, processed, and then delivered as strong light pulses focused by the eye's lens onto artificially light-sensitive retinal neurons. There are a number of advantages to this approach, namely the possibility to genetically target sub-populations of retinal neurons and the possibility to elicit either stimulation (using channel rhodopsin (Ch-R2)) or inhibition (using halorhodopsin) in the target neuron. These would allow the use of visual processing by different categories of interneurons as well as channel the centre-surround properties of RGC receptive fields (Greenberg, Pham et al. 2011). This technique has been successfully demonstrated *in vitro* with the use of a digital light processing (DLP) projection system (Nirenberg and Pandarinath 2012) and a micro light emitting diode (LED) array (Grossman, Poher et al. 2010; McGovern, Palmini et al. 2010). Some of the obstacles to this approach include the need to have strong light to

activate photo-sensitive cells and the constant motion of the eye which would need to be mirrored by the photo-stimulation system.

1.3.3 Stimulating electrodes

As the main interface between prosthesis and tissue, electrodes are an important aspect of any neuro-prosthetic system. In the case of an epi-retinal prosthetic device, maximal resolution would involve stimulation of individual RGCs, requiring electrode sizes to match those of their target neurons, ~10 µm for RGC somata (Ramon y Cajal 1911). However, small electrode sizes require higher charge densities to inject enough charge to drive cells above firing threshold. If the charge density is too high, it can damage the tissue or the electrode, rendering the system unusable after a certain number of stimulations. Hence, it is important to estimate safe charge density limits based on electrode and tissue properties, allowing the system to function in the long term. An ideal epi-retinal stimulation system would have very small capacitive electrodes requiring very low amounts of current to depolarise RGCs to threshold.

It is important to distinguish between charge storage capacity and charge injection limit. The charge storage capacity is the amount of charge per unit geometric surface area that an electrode can store at its surface, and thus deliver in the leading phase of a stimulation pulse. The charge injection limit is the value for charge injection capacity at which the electrode would create unsafe reactions (i.e. reach the water electrolysis potential), both are typically given in mC/cm^2 (Cogan 2008). The charge storage capacity is calculated from the integral of a current (generally cathodic when characterising stimulation electrodes) in a slow-sweep-rate cyclic voltammogram over a range of potentials just within the water electrolysis limits. The charge injection limit is determined by measuring the maximum voltage transients delivered when charging stimulation electrodes in current-controlled stimulation pulses, then measuring these maximum potentials against previously established voltage limits.

Neural tissue will suffer damage when the charge density is over 1 mC/cm^2 (McCreery, Agnew et al. 1990). Stimulating electrodes should have higher charge injection capacity than that, to prevent damage to the electrode material when stimulating with high charge densities; target tissue is not always in deirect contact with the stimulating

electrode. Theoretical application of a maximum charge density of 1mC/cm^2 would make the maximum amount of charge that can be applied to neural tissue be 0.196, 0.78 and 1.76 nC for disc electrodes 5, 10 or 15 μm in diameter respectively.

Some materials operate through faradaic reactions to deliver charge to the tissue. Noble metals such as platinum or platinum iridium alloys confine the faradaic reactions to a monolayer at the surface of the electrode, giving them the name of pseudo-capacitive electrodes (Conway 1990). Three dimensional multivalent coatings capable of undergoing reversible redox reactions can be applied to stimulating electrodes. Examples of such coatings are Iridium Oxide (IrO_2) and polyethylenedioxythiophene (PEDOT). Capacitive stimulation is generally more desirable as it does not include exchanges of electroactive species between electrode and tissue, thus minimizing the risk of deterioration to both structures.

As charge density is intrinsically related to the effective surface area of the electrode, the topography of stimulating electrodes strongly affects the charge density limit of the electrode. As such, materials with large effective surface areas make ideal stimulating electrodes. TiN exhibits a rough columnar topography (figure 1.16) and has a charge injection limit estimated between 0.87 (Weiland, Anderson et al. 2002) and 23 mC/cm^2 (Janders, Egert et al. 1996). This value decreases at stimulation frequencies higher than 4 Hz (Weiland, Anderson et al. 2002). IrO_2 has charge injection limits of approximately 4 mC/cm^2, decreasing above stimulation frequencies of 0.5 Hz (Weiland, Anderson et al. 2002). PEDOT is a relatively new material, consisting of an electrically conductive polymer exhibiting both electronic and ionic conductivity. Application of PEDOT to Pt Ir alloy microelectrodes yields a charge injection capacity of 15 mC/cm^2 (Cogan, Peramunage et al. 2007). Conductive polymer technology is still in early days, and it is not known how stable these polymers are in chronic use. Platinum has a charge injection limit of 0.1-0.4 mC/cm^2 (Brummer and Turner 1977). The effective surface area of a platinum electrode can be enhanced by a factor of 76 by laser-roughening the surface and electroplating with platinum black, although the electrochemical properties still remain inferior to those of IrO_2 and TiN (Schuettler 2007). Pt grey is a material developed by Second Sight Medical Products (Sylmar, USA) with the same surface area as Pt black, but with higher resistance to physical stress (US

patent 6974533). They use this material as stimulating electrodes in the Argus II epi-retinal prosthetic implant (Dorn, Ahuja et al. 2012).

Although IrO_2 has a higher charge injection limit than TiN, a number of factors make it inappropriate for use in neuroprosthetic devices. These include the shift in impedance at stimulation frequencies over 0.5 Hz and its delamination during chronic use *in vivo* (Weiland and Anderson 2000). As well as having appropriate electrochemical properties, the materials used in stimulating electrodes need to be stable and biocompatible. Despite a study with retinal cell cultures showing evidence of neurotoxicity (Guenther, Troger et al. 1999), TiN is now widely used in such application as heart pacemakers.

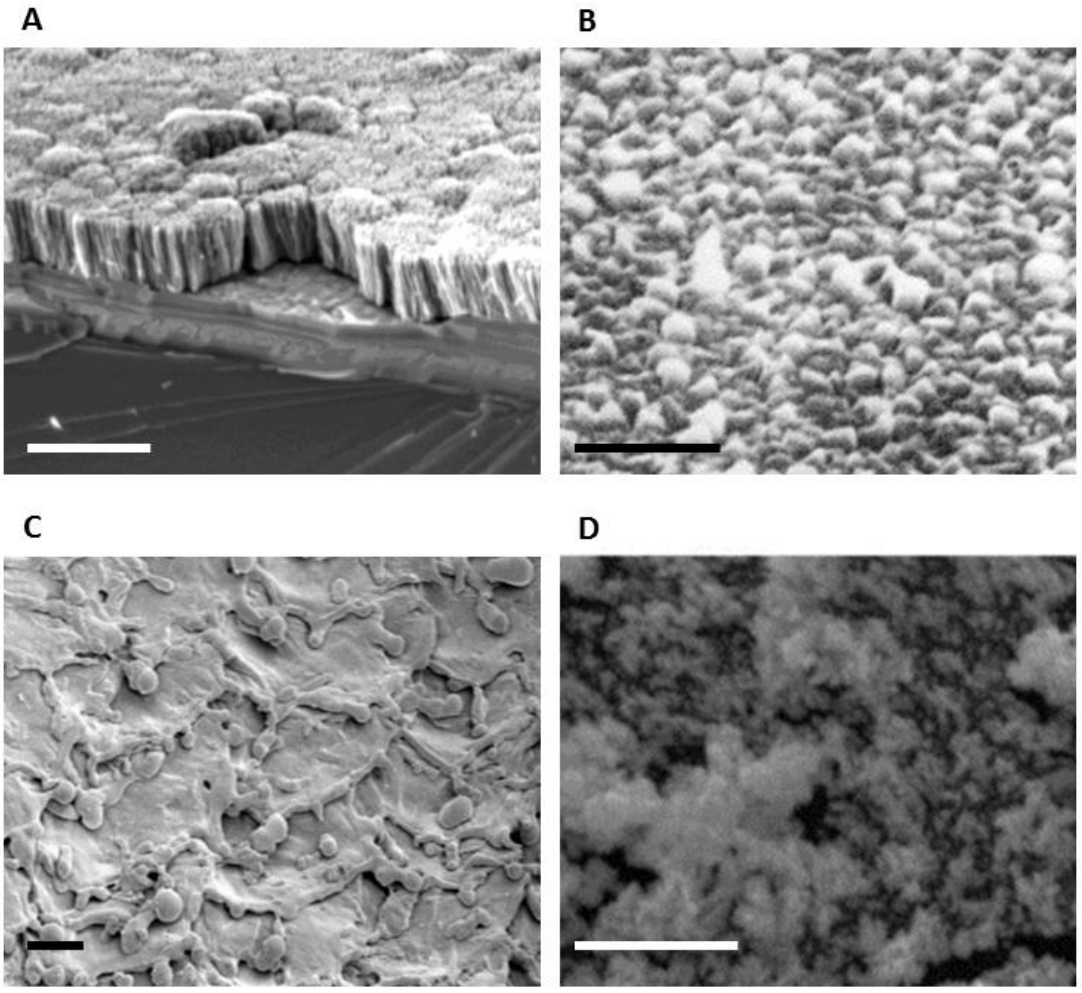

Figure 1.16: Topography of different types of stimulating electrode materials. Scanning electron micrographs of different materials used for neural stimulation. A: TiN, scale bar: 2 µm (Weiland, Anderson et al. 2002). B: IrO_2, scale bar: 1 µm, (El Khakani and Chaker 1998). C: laser-roughened Pt, scale bar: 10 µm, (Schuettler 2007). D: Pt black, scale bar: 1 µm, (Shi, Zhang et al. 2012).

In order to decrease RGC firing thresholds, electrodes need to establish good coupling with the tissue, reducing the distance between RGC and electrode. Also, the stimulation parameters and electrode characteristics have a strong impact on the threshold value. Indeed, there exists an intimate relationship between threshold, current amplitude and pulse duration. As pulse duration increases, current amplitude threshold decreases, and vice versa. This is not true for extreme values; hence the lowest amplitude for a current to elicit an action potential is called the Rheobase. Regardless of how long the pulse is, a current whose amplitude is below the Rheobase cannot depolarize the stimulated cell. The Chronaxie is the duration for which a current equal to twice the Rheobase will elicit an action potential (Ranck 1975). Charge density depends on pulse amplitude and duration of each pulse. Such parameters as pulse number, frequency, shape (e.g. pulsatile vs sinusoidal) and polarity will also affect threshold values.

1.3.4 CNT stimulating electrodes

CNTs are cylindrical carbon allotropes with a nano-sized diameter and a comparatively longer height (up to twenty eight million times longer). The carbon atoms are packed in a hexagonal pattern forming a honey comb lattice rolled into graphene cylinders which have their ends capped with hemispheric fullerene molecules. Single wall carbon nanotubes (SWCNT) are graphene cylinders with a typical diameter of 0.4 to 2 nm. Multi-wall carbon nanotubes (MWCNT) are concentric graphene cylinders with an outer diameter ranging from 2 to 100 nm (figure 1.17). Depending on the hexagonal lattice structure, CNTs can be either conductive or semi-conductive (Charlier, Blase et al. 2007) with some configurations displaying super-conductive properties (Tang, Zhang et al. 2001; Takesue, Haruyama et al. 2006). However, most forms of MWCNTs are conductive.

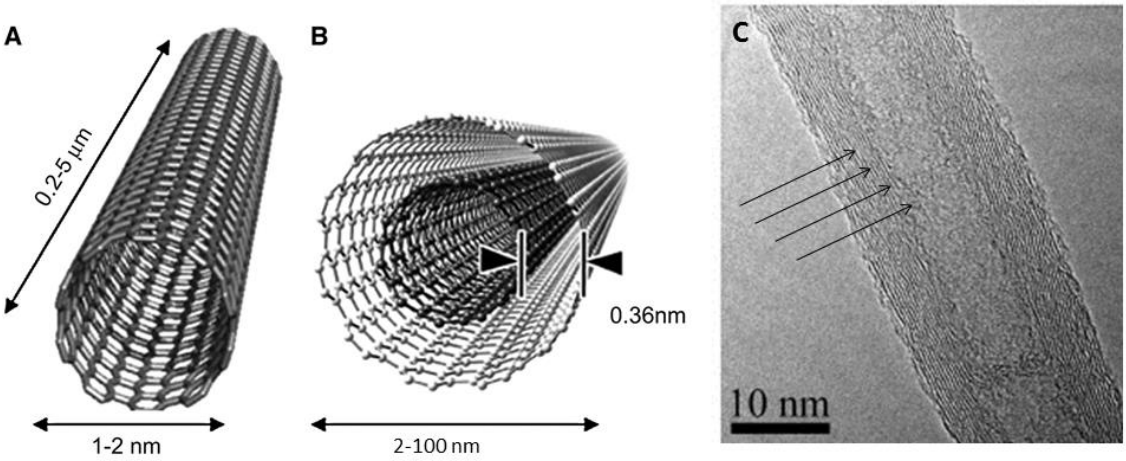

Figure 1.17: Individual CNT shape and dimensions. A, B: artistic representations of SWCNT (A) and MWCNT (B) with typical dimensions (Reilly 2007). C: High resolution transmission electron micrograph of a cross section of individual MWCNT with arrows pointing to concentric cylinders (Koós, Nicholls et al. 2012).

CNTs can be produced in large quantities using such techniques as laser ablation, arc discharge, chemical vapour deposition (CVD) or high pressure carbon monoxide disproportionation (Journet and Bernier 1998). First created in 1952 (Radushkevich and Lukyanovich 1952), they entered the realm of retinal prosthetics 10 years ago, initially because of the micro-fabrication process which could allow the development of penetrating electrodes designed to target specific layers of the IPL (Wang, Loftus et al. 2003).

As an implantable bio-electronic material, CNTs display a number of impressive characteristics. They are very strong, hard and flexible, with multi-walled CNTs displaying tensile strengths over 1 tera Pascal (TPa); they are good thermal and electrical conductors; they are biologically inert and can be coated onto most substrates using relatively cheap methods (Gabriel, Gomez et al. 2009). Structure can be incorporated in the fabrication of CNTs during or after synthesis. High temperature or the application of plasma will coax CNTs to grow vertically (Dai 2002) whilst low temperature CVD will result in "spaghetti" tangles (Gabay, Jakobs et al. 2005). Repetitive network patterns can be created by using the capillary forces of liquids evaporating from films or mats of CNTs (Chakrapani, Wei et al. 2004). Macro-molecular braids and yarns of CNTs have been fabricated and induced orientated neurite outgrowth *in vitro* (Bogdanovich and Bradford 2010; Fan, Feng et al. 2012).

Although heavily hydrophobic, there are a number of methods to increase the solubility of CNTs such as protein treatments, O_2 plasma etching or extended soaking (Wang, Fishman et al. 2006). CNTs can also be chemically modified to increase their solubility or instil bio-mimetic functionality. Etching of the end caps can be achieved with strong acids or plasma as a means to introduce carboxyl groups (Saito, Matsushige et al. 2002). This offers the possibility to covalently link the CNTs to polymers, proteins or other complex molecules.

Composite materials incorporating CNTs and charged polymers have been used as scaffolds and growth substrates for neurons. The different levels of charge in these composites can affect the size and number of neurite outgrowths (Hu, Ni et al. 2004; Hu, Ni et al. 2005). Such neural remodelling was also observed on MWCNTs functionalised with neurotrophic factors (Matsumoto, Sato et al. 2007) demonstrating that biological molecules retain their function when coupled to CNTs, thus expanding the potential of bio-hybrid CNT composites.

For stimulating electrodes, CNT coatings offer a number of substantial advantages over their metal-based counterparts. Mainly, their fractal-like geometry results in a large surface area, significantly increasing the capacitive charge injection capacity and lowering the electrode impedance value (Gabay, Ben-David et al. 2007). High charge injection capacity opens the potential to stimulate at high frequency over long periods of time.

Conventional MEAs can be easily coated with solutions of SWCNTs and used for the recording of action potentials in RGCs (Gabriel, Gomez et al. 2009). Flexible MEAs made of CNTs embedded in Parylene C have been demonstrated to record spikes from *in vitro* crayfish preparations (Lin, Lee et al. 2009).

With respect to an epi-retinal prosthetic MEA, CNT coatings seem an ideal substrate as they have been shown to attract and entangle neurites in dissociated cortical neurons (Sorkin, Greenbaum et al. 2009), improving the coupling between tissue and electrode (Shoval, Adams et al. 2009). The high surface area (figure 1.17, A) confers them charge injection limits of approximately 1.6 mC/cm^2, higher than the charge density damage limit for neural tissue (Wang, Fishman et al. 2006). Further, they can be coated so thin

as to be transparent (Hu, Hecht et al. 2009), a definite advantage in a degenerating retina with a number of photoreceptors still functioning.

MEAs fabricated with MWCNTs by CVD on TiN tracks have been used in acute *in vitro* preparations achieving electrophysiological recordings of RGCs with signal to noise ratios as high as 75 (Shoval, Adams et al. 2009). Spike sizes were shown to increase with time over the course of an hour in these experiments, which was not observed with commercial TiN electrodes. This suggests that the coupling between RGCs and recording electrodes improved with time. In this thesis, we investigate the responses of CRX -/- retinas to interfacing with the CNT electrodes used in this research paper over the course of 3 days (Chapter 3).

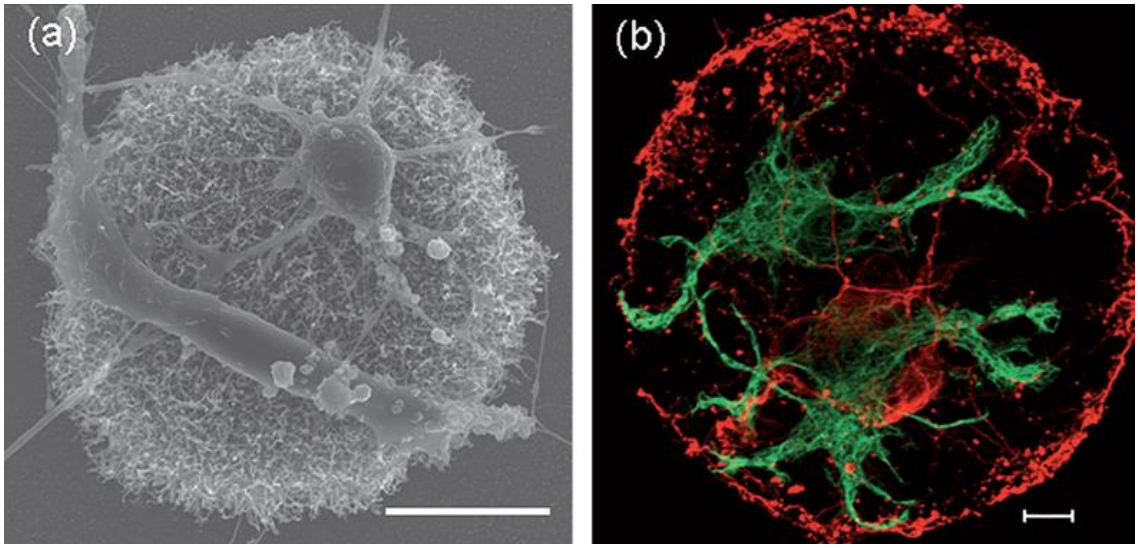

Figure 1.17: Entanglement of neural and glial processes to CNT island. A: High resolution scanning electron micrograph of CNT island with dissociated cells adhering to its surface. B: Confocal micrograph of CNT island with neurons stained for class III β-tubulin (red) and glia stained for GFAP adhering to its surface. Scale bar is 10 µm for both images. Image adapted from (Sorkin, Greenbaum et al. 2009).

1.4 Aims and Objectives

The literature presents the field of retinal prostheses as an interdisciplinary haystack, with a wealth of details influencing every single parameter in the design of a functional, biocompatible and useful device. The ideal material for stimulating electrodes appears to be CNTs, but the lack of experimental data has prompted us to investigate the properties of such a material on degenerated retinas *in vitro*.

Each chapter of this thesis is focused on acquiring data concerning a different set of dimensions in the interactions between isolated retinal tissue and CNT assemblies at the vitreo-retinal juncture.

1. Chapter 2 describes the challenges faced when keeping isolated retinas physiologically stable over several days. Immunohistochemical (IHC) analyses allow the visualisation of CNT assemblies' influence on
    - Retinal vasculature
    - Glial cell populations
    - RGC populations
2. Chapter 3 investigates the electrophysiological characteristics of the coupling between RGCs and CNT electrodes, focusing on
    - Cellular recruitment
    - Activation thresholds
    - Stimulation parameters
3. Chapter 4 investigates the ultrastructure of CNT-retina bio-hybrids over 48 hours, using
    - Transmission electron microscopy (TEM)
    - Scanning electron microscopy (SEM)

Chapter 2: Developing an Organotypic Culture System for the Monitoring of Neural Activity and Immunohistochemical Visualisation of Cell Populations in CNT-CRX Retina Bio-hybrids

2.1 Introduction

Organotypic culture systems aim to maintain populations of cells alive in a three dimensional (3D) organisation. This can be achieved through the seeding of cells onto 3D substrates or by maintaining explants under physiological conditions. The former is still at an early experimental stage with researchers developing novel scaffolds (Cartmell 2009) and elaborating tissue models (Canton, Cole et al. 2010; Koroleva, Gill et al. 2012). The latter has been used in more practical approaches such as the culture of skin (Otto, Nanchahal et al. 1995) or corneal epithelium (Pellegrini, Traverso et al. 1997) to use in grafts as well as the physiological investigation of neural tissue (Gahwiler, Capogna et al. 1997; Egert, Schlosshauer et al. 1998). Organotypic cultures rely on the proliferation of cells to maintain growth of the cultured tissue. As mature neurons cannot proliferate, neural tissue can only be organotypically cultured during developmental stages. This was originally achieved with human foetal brain cells using the roller tube technique in which slices are stuck to a cover slip with a plasma clot or collagen, then rotated in a sealed test tube to provide steady cycles of feeding and aeration (Hogue 1947; Gahwiler 1988). As this technique requires specialised equipment and strict feeding schedules, a simpler organotypic culture (the “Stoppini”) technique was developed where hippocampal slices of neonatal rats (P2-P20) were maintained on semi-permeable membranes covering growth medium and maintained in a CO_2 enriched atmosphere (Stoppini, Buchs et al. 1991).

In both types of culture system, the tissue is maintained above 30°C in a sterile environment (to prevent proliferation of bacteria or fungi) fed by a semi-synthetic medium typically composed of 25% serum, 50% essential basal medium and 25% balanced salt solution enriched with glucose (Gahwiler, Capogna et al. 1997). To perform electrophysiological measurements, the medium has to be switched to aCSF (artificial cerebro-spinal fluid) bubbled with carboxygen (95% O_2, 5% CO_2). Although the tissue maintains its cytoarchitectural organisation, slices tend to flatten with time, eventually forming a monolayer. Also, donor age can influence organisational integrity with young tissue prone to cellular migration and older tissue requiring oxygenation to prevent anoxia (Gahwiler 1988).

Hippocampal slices of neonatal rodents have been cultured on MEAs using the roller tube technique (Egert, Schlosshauer et al. 1998), the “Stoppini” technique by creating MEAs with a porous substrate (Thiebaud, de Rooij et al. 1997) or by using *in situ* microfluidics to supply slices with medium directly onto MEAs (Berdichevsky, Sabolek et al. 2009). As these techniques were developed to investigate the growth of neonatal tissue for up to four weeks *in vitro*, they have not been successfully adapted for the adult retina, with groups recording RGC activity for up to 5 days using the roller tube system (Kohler, Schmid et al. 2005) or an interphase culture system in which medium is constantly agitated below retinas held onto culture inserts (Koizumi, Zeck et al. 2007). The latter has most recently been used in conjunction with particle mediated ballistic gene transfer of Ch-R2 and halorhodopsin to modulate spiking of RGCs in degenerated retinas through light stimulation (Ahuja, Dorn et al. 2011). As isolation of the retina requires the optic nerve to be severed, RGCs inevitably succumb to retrograde degeneration after a few days *in vitro* for amniote retinas (Garcia and Koke 2009).

Previous work performed in our laboratory demonstrates electrophysiological evidence for an increase in coupling between RGCs and CNT electrodes *in vitro* over the course of one hour (Shoval, Adams et al. 2009). In an attempt to elucidate the anatomical and physiological processes involved over longer incubation periods, our initial aim was to develop an organotypic culture system to interface dystrophic retinas with CNT assemblies and to maintain these retinas alive and functional. This would allow us to investigate various physiological and structural changes occurring in the neural retina as well as in glial cells and blood vessels.

Dissociated neurons and glia in culture have been shown to migrate towards and aggregate on CNT islands, elaborating intimate contacts between processes and individual nanotubes (Shein, Greenbaum et al. 2009). In the case of epi-retinal prostheses, the migration of cells within the retina could be either beneficial or detrimental. Migration of RGCs towards CNT electrodes would increase coupling dramatically whilst hyperplasia and aggregation of glial cells onto the electrodes would reduce coupling; damage to blood vessels could lead to neural cell death.

Validation of culture systems was assessed through physiological measurements, discussed in details in Chapter 3. Imaging different cell types in retinas interfaced with CNT constructs was achieved through immunohistochemistry. Other morphological changes were assessed through TEM (discussed in detail in Chapter 4).

This chapter is dedicated to

1. The physiological validation of different incubation systems through
    a. Imaging of structural integrity in retinal slices
    b. Monitoring of electrophysiological activity
    c. Imaging of transfected GFP expression
2. Immunohistochemical imaging of cell populations on retinal wholemounts maintained under different incubation conditions
    a. Macroglial cells: Müller cells and astrocytes
    b. Vascular network
    c. RGCs

The experiments and analyses described in this chapter were performed by Cyril Eleftheriou. CNT constructs were fabricated at Tel Aviv University (Israel).

2.2 Materials and Methods

2.2.1 CNT constructs

CNT assemblies were custom designed and fabricated at Tel Aviv University by Moshe David-Pur and Dr Yael Hanein. Three different types of devices were prepared: MEAs, CNT islands on Si/SiO_2 substrate and CNT islands on a flexible substrate (Figure 2.1). The fabrication process for CNT MEAs is presented in more detail in the literature (Gabay, Ben-David et al. 2007). Individual islands on Si/SiO_2 substrate were fabricated using a similar process involving fewer steps. Briefly, Ni was patterned on Si/SiO_2 substrates by photo-lithography, and then used as a catalyst to grow CNTs by CVD. For MEAs, the CNT islands had a 30 µm diameter and a 200 µm pitch (30/200). Other assemblies had two types of islands. "Small" islands were organised in a central orthogonal lattice with (30/50) whilst "large" islands were organised in an orthogonal lattice concentric to the "small" island lattice with (100/200).

In order to fabricate the flexible devices, polydimethylsiloxane (PDMS) was spin coated and cured onto the islands. PDMS is biocompatible and very flexible, with a Young's modulus of 360-870 KPa (Belanger and Marois 2001). The use of such a material in epi-retinal prosthetic devices is ideal as the device would be able to fit the curvature of the eye. Attempts at making flexible MEAs have been relatively successful, using such materials as graphite (Blau, Murr et al. 2011), CNTs (Lin, Lee et al. 2009) and gold (Kim, Lu et al. 2011) embedded in flexible polymers to generate conducting tracks. Our collaborators have been developing PDMS/CNT MEAs, but the wetting of CNTs by uncured PDMS considerably impedes the conductance of the tracks (unpublished).

The surface roughness of CNT electrodes and CNT islands on Si/SiO_2 substrates is very high (figure 2.1; D, E) whilst the surface of islands on PDMS is significantly smoother (figure 2.1; C, F). However, the CNT islands are intimately coupled to the PDMS whilst they are loosely attached to the Si/SiO_2 substrate. The disparities in substrate flexibility, contact and island surface roughness were exploited in this study to investigate immunohistochemical characteristics of retinas incubated on CNT-PDMS composites and ultrastructural characteristics of retinas incubated on CNT- Si/SiO_2 assemblies (Chapter 4).

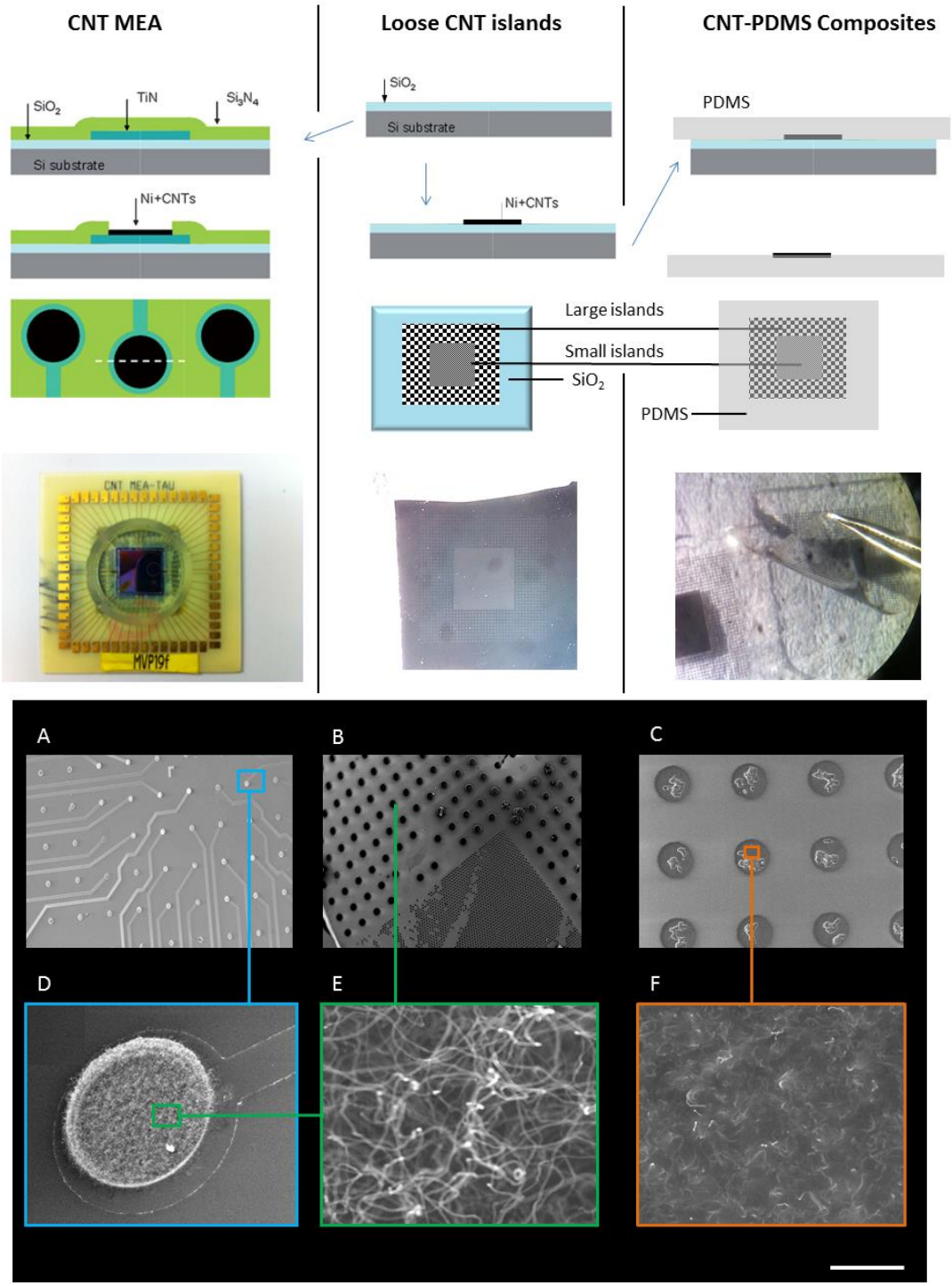

Figure 2.1: Fabrication of CNT constructs. Top two rows: fabrication processes for the three different types of CNT constructs used in this project. Third row: top view of the completed device. Fourth row: photographs of each type of device. Two bottom rows: SEM micrographs of the devices, the top row (A, B, C) showing multiple islands and bottom row (D, E, F) displaying high magnification micrographs of the surface, highlighting the low level of roughness on PDMS devices (C, F) when compared to that of the other devices (D, E). Scale bar is 500 µm (A), 1 mm (B), 250 µm (C), 30 µm (D), 100 nm (E), 2 µm (F). Micrographs acquired on a Cambridge Stereoscan 240.

2.2.2 Animals and surgical procedures

The animals used in this set of experiments were CRX -/- mice, C57 BL6 mice and one rhesus macaque monkey over 10 years old (eye donated by Drs Andrew Jackson and Stuart Baker, Newcastle University). Mice were aged from P90 to P200. This corresponds to the second half of phase 2 in the remodelling process for CRX -/- retinas. Few photoreceptor cell bodies are still present in the ONL, BCs have undergone at least 2 months of synaptic remodelling and both Müller and microglial cells are in an activated state. All animal procedures were conducted under the UK Home Office, Animals (Scientific procedures) Act 1986.

Following cervical dislocation and enucleation, eyes were kept submerged in cold (approximately 2°C, then allowed to warm up during dissection) dissection medium (either oxygenated aCSF or growth medium, discussed below) in a petri dish under a dissection microscope. First, the eye was pierced with a micro-scalpel at the limbus, above the *ora serrata* on the retina. Using this incision as a starting point, the anterior part of the eye was cut out using micro-scissors. The vitreous humour and lens were then removed from the eyecups. The last and most delicate part of the dissection was removing the retina from the eye using two pairs of very fine forceps. The remaining RPE and vitreous humour was then gently teased off using a pair of forceps.

2.2.3 Retinal incubation systems

This section describes four different methods employed to maintain retina function over the course of several days. Each one offered different characteristics, exploited for the different set of features unique to each experiment. These different types of incubation systems can be divided into two categories: submerged and interface incubation (figure 2.2). The former requires the tissue to be submerged in aCSF saturated with carboxygen with gas exchanges occurring by diffusion between dissolved CO_2/O_2 and the cells within the tissue. Interface incubation requires the use of an incubator providing a humid atmosphere, warmth (37 °C) and additional CO_2 (5%), with gas exchanges occurring at the surface of the tissue (figure 2.2).

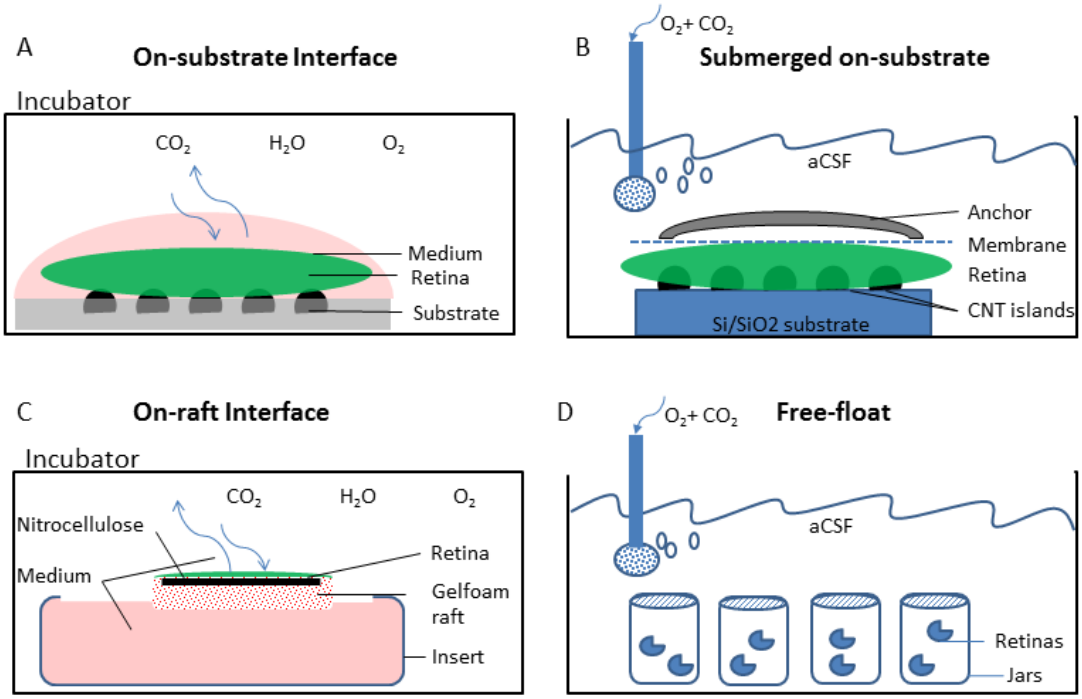

Figure 2.2: Four different incubation conditions. Diagram outlining the four different types of incubation conditions used to maintain physiologically stable retinal explants. A: *On-substrat Interface* system, uses a drop of culture medium, explant kept in an incubator. B: *Submerged on-substrate* system, retina maintained onto substrate by membrane filter and anchor, submerged in carboxygenated aCSF. C: *On-raft Interface* system, retina kept on Gelfoam raft floating in medium. D: *Free-float* system, retinas floating freely in carboxygenated aCSF.

Cultures on CNT- PDMS composites were performed as in the literature (Xin, Yannazzo et al. 2007) with a small amount of culture medium resting on the substrates surface, coating hemi-retinal explants (*On-substrate Interface*, figure 2.2, A). The hydrophobicity of the Si/SiO_2 substrate prevented good covering of tissue by the medium, so for interfacing with Si/SiO_2 substrate, retinas were held down by a stainless steel anchor and submerged in oxygenated aCSF to allow proper gas exchanges (*Submerged on-substrate*, figure 2.2, B, C; figure 3.1; figure 4.4). This approach was used for both retinas incubated on CNT-Si/SiO_2 assemblies and CNT MEAs. This technique is only appropriate for 1 (MEA) to 4 (CNT- Si/SiO_2 assemblies) retinas at a time, so we developed a system in which tens of retinas were kept in glass jars within carboxygenated aCSF (*Free-float*, figure 2.2, D), although without the possibility of interfacing with CNT assemblies. The lid of these jars incorporates a fine meshwork of nylon, allowing liquid and gas exchanges. The *On-raft Interface* system

involved the incubation of retinas on Gelfoam rafts with the RGCs facing up in order to easily transfer retinas from the incubator to MEAs (figure 2.2, C).

In an effort to maintain sterile conditions for *in vitro* incubation, 5% Penicillin–Streptomycin-Neomycin (PSN; Sigma-Aldrich, UK) was added to the aCSF. *Interface* incubation required much more stringent sterile conditions as explants were maintained over much longer periods in an environment prone to bacterial proliferation. Dissections and medium exchange were performed in a laminar flow hood after 20 minutes exposure to UV light and disinfected with 70% ethanol prior to manipulations. Dissection instruments were autoclaved prior to each experiment and flame sterilised during the procedures. Following cervical dislocation, mouse heads were dipped in 70% ethanol.

For *On-substrate Interface* cultures, culture medium consisted of DMEM/F12 (Dulbeco's modified eagle medium; Gibco, Invitrogen, UK) with 5% PSN. The different media used in *On-raft Interface* cultures are detailed in table 2.1. In *On-substrate Interface* culture conditions, retinal explants were planarized with the GCL facing down onto different substrates and allowed to adhere for 1 minute before the addition of 200 µl culture medium. The substrates were glass cover slips, PDMS or CNT-PDMS composites. Substrates were either bare or coated with 20.1 µl Poly-D-Lysine hydrobromide (PDL; Sigma Aldrich UK) and 4.1 µl laminin from Engelbreth-Holm-Swarm murine sarcoma basement membrane (Sigma Aldrich, UK). Culture medium was exchanged daily, at a volume of 200 µl. In *On-raft Interface* culture conditions, retinal explants were planarized with the GCL down onto a glass slide, then lifted off by application of a 2x2 mm^2 piece of nitrocellulose filter (450 nm pores, Sartorius Stedim Biotech, UK) and placed GCL up on a gel-foam (Pfizer, UK) raft in 2 ml of culture medium. The medium was exchanged daily.

For both types of *submerged* conditions, aCSF concentrations are given in mM: 118 NaCl, 25 $NaHCO_3$, 1 NaH_2PO_4, 3 KCl, 1 $MgCl_2$, 2 $CaCl_2$, 10 $C_6H_{12}O_6$. ACSF was perfused at 0.9-1.2 ml/min for *Submerged on-substrate* conditions and 2-3 ml/min for *Free-float* conditions. The purpose of *Free-float* conditions was to maintain a maximum number

of retinas in physiologically stable conditions. These were kept free-floating in glass jars, two retinas per jar and marked by an incision.

Despite many attempts, retinal explants maintained under *On-raft Interface* incubation did not yield any electrophysiological activity. Variables considered included dissection medium composition, culture medium composition, dissection medium temperature, substrate chemistry, substrate coating and dissection technique. Table 2.1 summarizes these parameters. The supplements added to Neurobasal A medium were L-Glutamine (Gibco, Invitrogen, UK), B27 (Invitrogen, UK), N-2 (Invitrogen, UK), NEAA (Non-essential amino acids; Gibco, Invitrogen, UK), PSN and GlutaMAX (Gibco, Invitrogen, UK). Direct retinal isolation refers to the dissection method used in all other experiments (cf. section 2.2.2).

Table 2.1: Parameters of *On-raft Interface* incubation

Culture Medium Composition	Neurobasal A	Neurobasal A + supplements	DMEM + FBS + PSN	DMEM/Ham's F12 + 5% FBS
Dissection medium composition	HBSS	Co_2-O_2 aCSF	DMEM + PSN	
Recording medium composition		Co_2-O_2 aCSF	Neurobasal A + supplements	
Dissection medium temperature	4°C	24°C	35°C	
Substrate	Nitrocellulose filter	Gelfoam + nitrocellulose filter	5µm Polyester membrane	
Substrate coating	No Coating	PDL/Laminin		
Dissection technique	Direct retinal isolation	Retina incubated in eyecups		

Neurobasal A (Invitrogen, UK), HBSS (Hank's balanced salts solution; Invitrogen, UK), DMEM/Ham's F12 (Invitrogen, UK), FBS (Fetal Bovine Serum; Invitrogen, UK).

2.2.4 Histochemical characterisation

Structural integrity of retinal explants was assessed by inspecting Nissl stained transverse sections of these explants. Retinas were peeled off their substrate, fixed for 24 hours in PFA, cryo-protected in a 30% sucrose phosphate buffered saline (PBS) solution for 72 hours, embedded in Tissue-Tek OCT Compound (Sakura, Japan) at -30°C

and sectioned perpendicular to the ILM in 30 µm slices with a cryo-microtome (HM560, Microm International). Sections were gathered on gelatine-coated microscope slides, air-dried for 24 hours, immersed in de-ionised H_2O for 10 minutes to melt the OCT compound, air-dried for 24 hours, immersed for 2 minutes in a solution of 0.1% Cresyl Violet Acetate (MP Biomedicals Inc, USA), dehydrated in increasing concentrations of ethanol (50, 70, 90, 90 + 5% acetic acid, twice 100% for 3 min each), dipped for 3 min in 2 consecutive jars of Histo-clear (Fisher Scientific, UK) and finally covered with a cover slip using distyrene-tricresyl phosphate-xylene (DPX; Sigma Aldrich, UK).

Wholemount and ultrastructural preparations needed different staining procedures: Depending on the substrate onto which they were incubated, explants had to be exposed to specific staining processes. Explants incubated GCL down on substrates adhered to it. Hence, removing the explant caused damage at the tissue-CNT interface. Therefore, explants incubated on PDMS or glass slides were kept in the culture dishes and stained directly on the substrate. Explants incubated onto MEAs were teased off with forceps and a polyethersulfone membrane filter (8 µm pores, Sterlitech, UK) used as a micro shovel. Explants incubated on Si/SiO_2 CNT assemblies were dehydrated by means of removing the aCSF with a pipette before a 2x2 mm^2 piece of nitrocellulose filter was gently pushed down on the tissue and teased off the substrate using forceps and a polyethersulfone membrane filter. Samples prepared for ultrastructural analyses were fixed in 2% glutaraldehyde for 48 hours whilst samples prepared for immunohystochemical analyses were fixed in 4% PFA for 24 hours.

For fluorescent probes, explants were washed in 0.1 M PBS exposed to 0.6% H_2O_2 for 20 min (to remove endogenous peroxidase), exposed to 20% blocking serum (Normal Horse Serum, Vector Labs, UK) for an hour, followed by primary antibodies and 10% blocking serum for 24 hours, secondary antibodies for 3 hours, mounted onto gelatine-coated slides, air-dried for 24 hours and finally coated with a coverslip using hard-setting Vectashield (Vecor Labs, UK).

For 3,3'-Diaminobenzidine (DAB) reactive probes, explants were washed in PBS exposed to 0.6% H_2O_2 for 20 min, followed by 20% blocking serum for an hour, primary

antibodies and 10% blocking serum for 24 hours, secondary antibodies for 3 hours, horseradish peroxidase (HRP)-streptavidin (Vector Labs, UK) for 3 hours, reacted with H_2O_2 and DAB, mounted on gelatine coated slides, air-dried for 12 hours, dehydrated in increasing concentration of ethanol (50, 70, 90, and twice 100% for 3 min each), dipped for 3 min in 2 consecutive jars of Histo-clear (Fisher Scientific, UK) and finally coated with a cover slip using Entellan (Merck Millipore, USA).

Antibodies and reactants were diluted in PBS containing 1% Triton X 100 (Sigma Aldrich, UK). Between each of the steps described above (up to dehydration), samples were washed three times in 0.1 M PBS for 3 minutes. A list of the antibodies and working dilutions are presented in Table 2.2.

Micrographs of DAB-reacted probes were acquired on an Olympus BX60 (Olympus, Japan) microscope with a Zeiss Axiocam HRc camera using Zeiss Axio Vision 3.1 software (Carl Zeiss AG, Germany). Micrographs of fluorescent probes were acquired on a Leica DMRA microscope (Leica Microsystems) with a Hamamatsu Orca-ER camera (Hamamatsu Photonics, Japan) using the Axio Vision 4.8 (Carl Zeiss AG, Germany) software.

Table 2.2 List of antibodies and working dilutions

	Antigen	Antiserum	Source	Working Dilution
Primary Antibodies	GFAP	Mouse anti-GFAP	Sigma-Aldrich, Gillingham, UK	1:200
	GSL-1	Biotyntilated GSL-1	Vector labs, Peterborough, UK	1:200
	Thy-1	Rat anti-Thy-1	Abcam, Cambridge UK	1:1000
Secondary Antibodies	Alexa 488	Rat anti-mouse IgG	Invitrogen, Paisley, Scotland, UK	1:200
	FITC Affini pure	Donkey anti-goat IgG	Stratech Scientific, Newmarket, UK	1:500
	Cy3 Affini pure	Donkey anti-rat IgG	Stratech Scientific, Newmarket, UK	1:500
	Avidin	Biotintilated anti-mouse IgG	Vector labs, Peterborough, UK	1:1000
	HRP-Streptavidin	N/A	Vector labs, Peterborough, UK	1:1000

[1]GSL 1, Griffonia Simplicifolia Lectin I; GFAP, glial fibrillary acidic protein; GS, Glutamine Synthetase; Thy-1, CD-90

The antibodies listed in table 2.2 allowed the identification of various cells in incubated explants. GFAP is a protein expressed in the retina by activated astrocytes and Müller cells (Bringmann and Reichenbach 2001) whilst Griffonia Simplicifolia lectin I (GSL-I) is a protein expressed in the retina by microglia and the endothelial cells (Gehrig, Langmann et al. 2007). Thy-1 is a protein only expressed by RGCs (Nash and Osborne 1999) in the adult retina.

Photomicrographs were edited in Photoshop CS2 (Adobe, USA), Paint.net 3.5.10 (dotPDN LLC, USA), ImageJ 1.45s (National Institute of Health, USA) and PowerPoint 2010 (Microsoft, USA). Distances and areas were measured on micrographs using ImageJ 1.45s and statistical analyses were performed with Sigma Plot 11.0 (Systat Software Inc., USA). Pixel density analysis for vascular and astrocytic networks was carried out by calculating the pixel to area ratio from binary versions of photo-merged images. The algorithm dedicated to pixel density analysis is shown in figure 2.3.

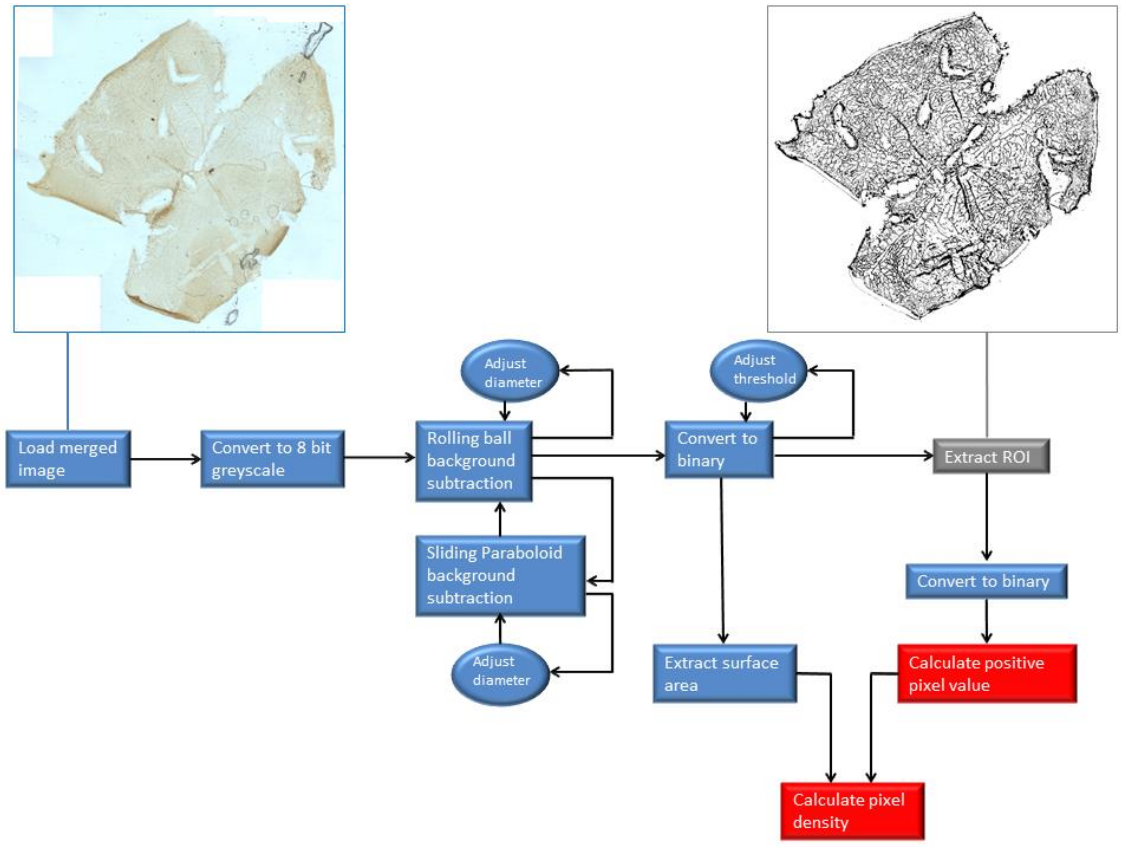

Figure 2.3: Pixel density analysis algorithm diagram. Diagram outlining the steps required to extract the pixel density from optical micrographs of DAB-stained endothelial cells. Blue boxes represent steps undertaken in ImageJ, red boxes represent steps undertaken in Matlab and the grey box represents a step performed in Paint.net. ROI: region of interest.

2.2.5 Electrophysiological measurements

In order to validate neuronal activity after time spent in incubation, electrophysiological activity was monitored with 60-channel MEAs interfaced with a computer running the proprietary software MC_Rac (Multi Channel Systems, Reutlingen, Germany) using an MEA1060INV (Multi Channel Systems, Reutlingen, Germany) amplifier via a PCI (Peripheral Component Interconnect) MC card. 5 minute data files were recorded in MC_Rack and analysed off-line. Briefly, files were imported into Matlab (The MathWorks, USA) using the FIND toolbox (Meier, Egert et al. 2008). Spikes were automatically extracted and sorted by supra-paramagnetic clustering and wavelet analysis using Wave_clus (Quiroga, Nadasdy et al. 2004). These results were later inspected visually and re-clustered using the Wave_clus "temperature" tool.

2.3 Results

This section provides details of the histological and physiological analyses performed on retinal explants incubated using the four different incubation systems. Physiological validation of culture systems included the recording of electrophysiological activity for up to 5 days, observing Nissl stained transverse sections as well as expression of GFP through plasmid mediated transfection. Immunohistochemical analyses of wholemount retinal explants demonstrate changes (or lack thereof) in RGC and macroglial cell populations as well as vasculature in response to interfacing with CNT constructs.

2.3.1 Physiological validation of culture systems

The most direct measure of the functional integrity of the retina is neural activity. Electrophysiological activity recorded from RGCs following incubation of retinas with the GCL facing up *(On-raft Interface* system), free-float (*Free-float* system) or directly onto MEAs (*Submerged on-substrate* system) was easily measured. However, retinas interfaced GCL down could not be placed onto MEAs as they had created an intimate coupling with the substrate. Their structural integrity was assessed through the more

conventional approach of observing their cytoarchitectural integrity through Nissl-stained transverse sections.

Retinas maintained under *interface* conditions kept their integrity across layers as illustrated in figure 2.4. Here, both intact and dystrophic retinas are shown to maintain their typical cytoarchitecture after 9 days in culture. To further validate our *On-substrate Interface* incubation system, a macaque retina was also shown to retain cytoarchitectural integrity after 9 days.

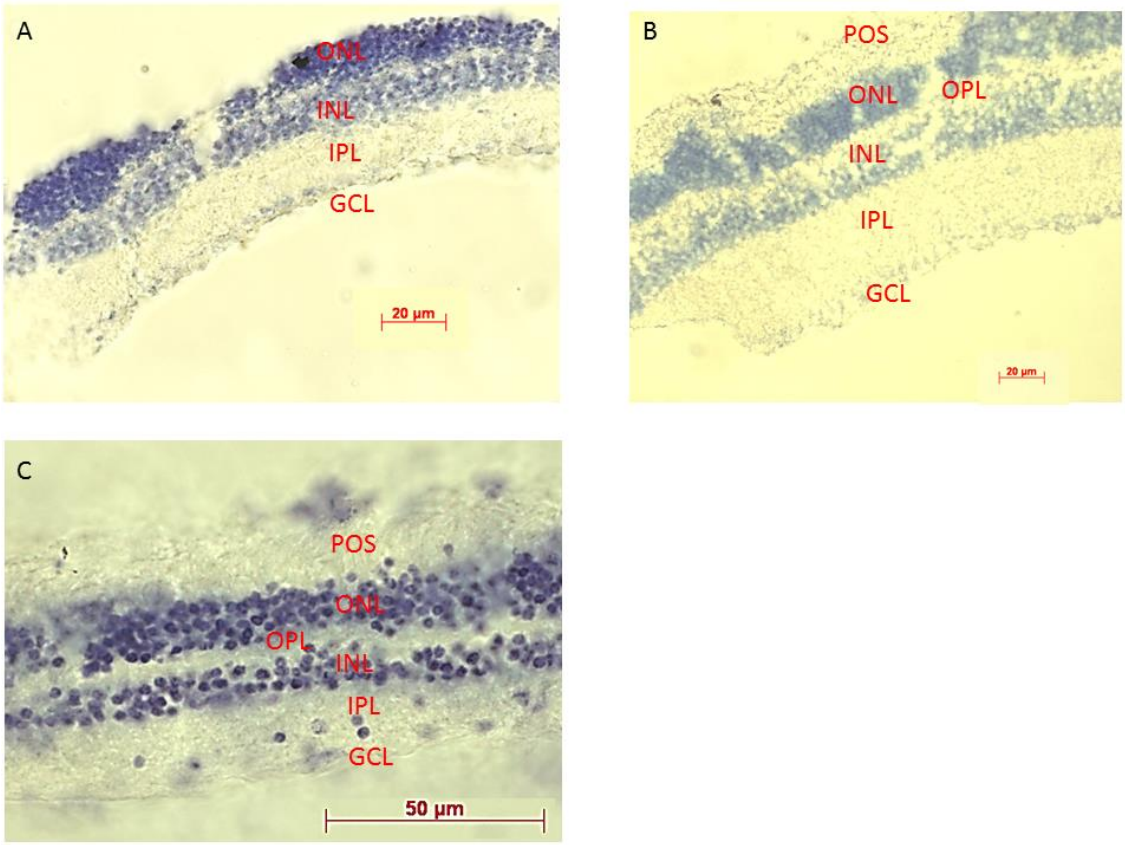

Figure 2.4: Cytoarchitectural integrity of retinas incubated with *On-substrate Interface* system. Photomicrographs of Nissl stained sections of retinas from adult CRX -/- mouse (A), C57-BL6 mouse (B) and macaque (C). These retain their cytoarchitectural integrity after 9 days maintained under *On-substrate Interface* conditions. Although Nissl only stains for somata, semi-transparent plasma membranes in the IPL and POS can be perceived in these micrographs. The adult CRX -/- retina is devoid of POS and has an atrophied OPL and ONL. POS, photoreceptor outer segments; ONL, outer nuclear layer; OPL, outer plexiform layer; INL, inner nuclear layer; IPL, inner plexiform layer; GCL, ganglion cell layer.

Explants incubated under *Submerged on-substrate* conditions yielded stable and consistent electrophysiological recordings for up to three days. These are detailed in chapter 3. The *Free-float* system was developed to maintain multiple retinas under

physiological conditions whilst they underwent remodelling induced by experimental procedures (e.g. interfacing with retinal constructs or genetic transfections).

Explants incubated under *Free-float* conditions yielded electrophysiological recordings for up to five days. One of the drawbacks of this system was the need to handle the tissue between incubation and recording stages (e.g. MEA), which led to degradation of the tissue. Hence, electrophysiological recordings and fluorescence imaging were performed sparingly. As described in Chapter 1, dystrophic retinas are characterised by slow oscillations and vigorous bursting. The slow oscillations disappeared in all explants incubated under *Free-float* conditions after 3 days. However, these same explants retained their capability to fire action potentials (figure 2.5B) and even vigorous bursting (figure 2.5C).

8 CRX -/- retinas aged 92 days were maintained under *Free-float* conditions with no other experimental manipulations (i.e. interfacing with CNT constructs, transfections or planarizing cuts). Of these, 4 displayed physiological activity on Day 5 (96 hours incubation) but not on Day 6 anymore. On Day 5, an average of 18.5 RGCs were firing and in one retina there was firing in 29 RGCs. The average firing rate (over 5 minute recordings) was 3.4 Hz ±0.88 with one RGC firing at 37 Hz.

2.3.2 Immunohistochemical imaging of explants maintained under interface conditions

72 hemi-retinal explants were incubated under *On-substrate Interface* conditions, corresponding to a total of 18 mice aged 95 to 193 days old. Of these, 58 explants were incubated onto CNT-PDMS composites, 10 onto glass cover-slips and 4 onto PDMS only. Time spent in culture was 2 (N = 4), 4 (N=20), 8 (N= 4), 12 (N = 7), 24 (N = 4), 48 (N = 16) or 72 (N = 17) hours. DAB-reaction staining with anti-GFAP only was performed on 32 explants, fluorescent staining with anti-Thy-1 was performed on 8 explants and fluorescent double labelling with both anti-Thy-1 and anti-GFAP was performed on 30 explants (figure 2.6).

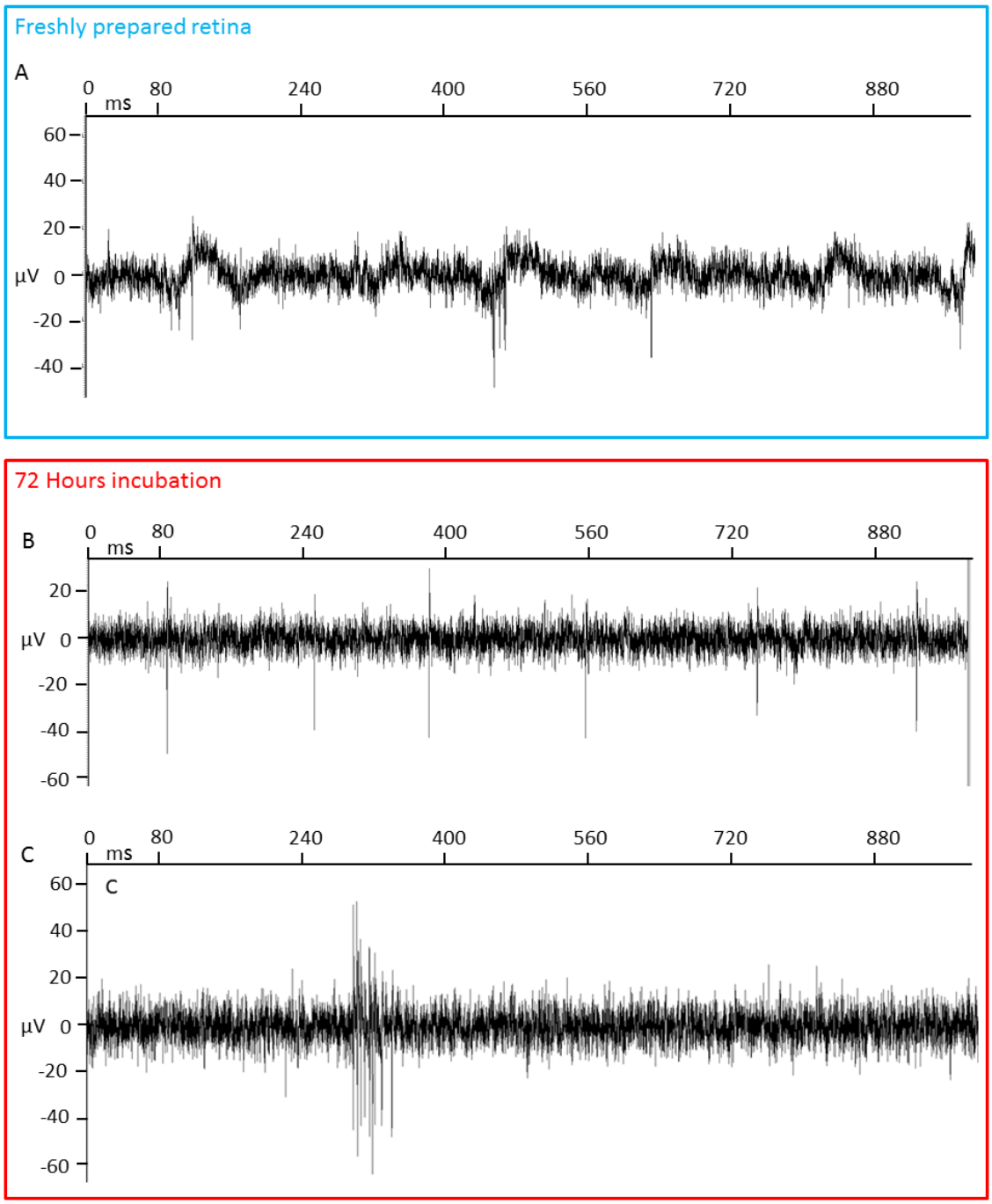

Figure 2.5: Loss of oscillations in isolated retinas after 5 days in culture. Raw trace recordings from single channels showing electrophysiological activity in retinas after 0 (A) and 72 hours in culture (B, C). The freshly dissected retina (A) shows rhythmic local field potentials (LFP) of approximately 12 Hz as well as bursting activity contrasted with no LFPs (B, C), steady 6 Hz firing (B) and high frequency bursting (~180 Hz, C) after 72 hours.

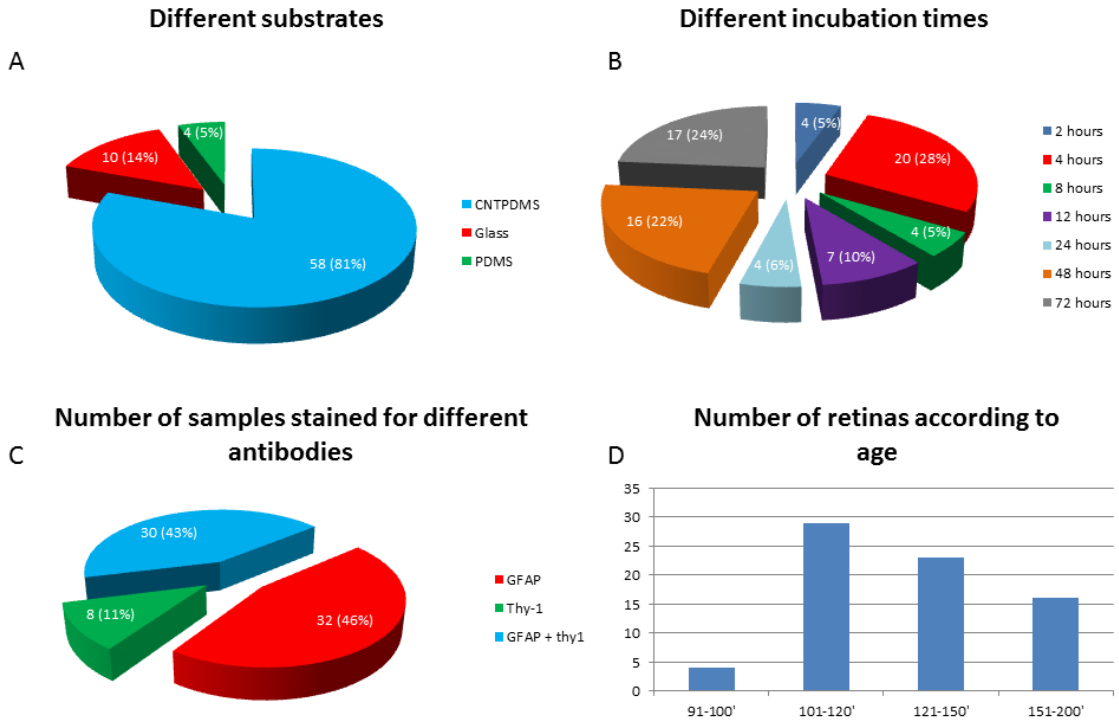

Figure 2.6: Breakdown of the different samples incubated using *On-substrate Interface* incubation. Pie-charts showing numbers and percentages for *On-substrate Interface* incubation samples (A, B, C) as well as a histogram binning for the ages of retinas used in the study (D). Most explants were incubated on CNT-PDMS substrates compared to glass and PDMS controls (A). Explants were maintained in culture for 2 to 72 hours (B) and stained with GFAP, Thy-1 or both (C). Cultures were performed on retinas in phase 2 degeneration, aged 90 to 200 days (D).

Samples stained on glass were all destroyed during the staining and mounting process. Indeed, removing samples from glass cover slips often resulted in broken cover slips with glass shards damaging the explants. Attempts were made to minimise damage by removing the samples prior to staining but were also unsuccessful. Stained explants were more easily removed from PDMS substrates due to their flexibility. This was achieved by carefully shaving the ECM (extra cellular matrix) bond between sample and substrate using a scalpel. Some samples were almost pristine (figure 2.7, A) but in most cases they sustained heavy damage (figure 2.7, B). In control samples (incubated on PDMS only) the regular syncytium of astrocytes coupled at their processes and lining blood vessels was characterised despite damage to the sample (figure 2.7, A). As such, the average density of the astrocytic plexus is 6.14 pixel/μm^2 under control conditions.

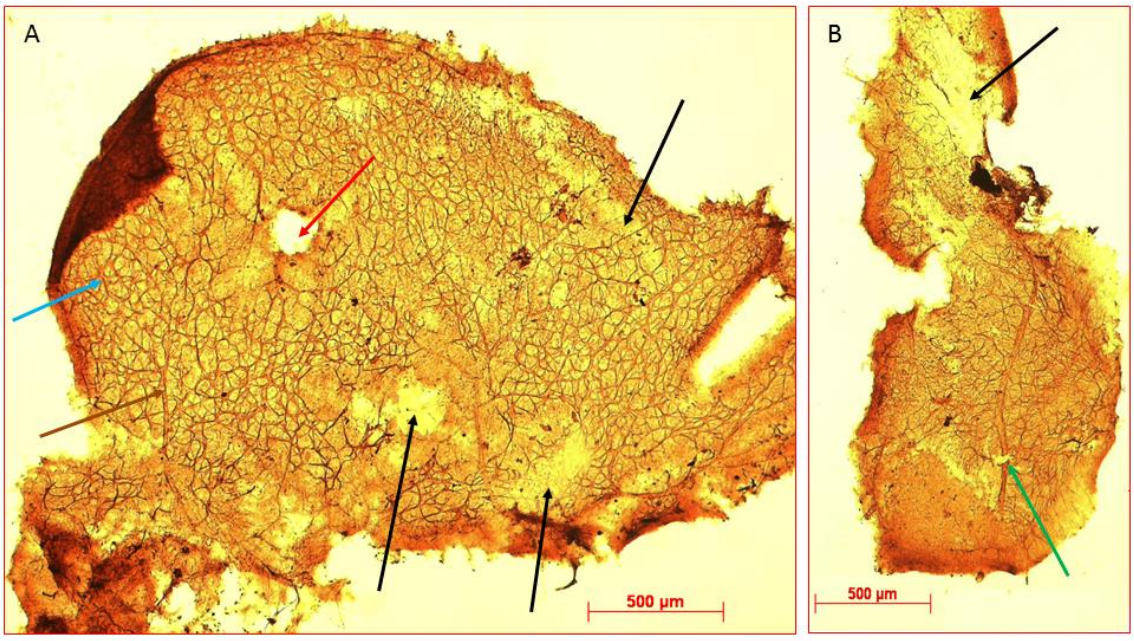

Figure 2.7: Degradation of tissue through staining and mounting process. Micrographs of retinal explants incubated on PDMS substrate and stained with GFAP-DAB. Some of the explants were relatively well preserved (A) despite light damage such as tears in the astrocytic syncytium (black arrows). Other samples were thoroughly damaged (B) and displayed damage to blood vessels (green arrow), tears (black arrow) and a general breakdown of the explant's integrity (much smaller sample). Well preserved explants incubated on control substrates allowed the visualisation of the syncytium created by coupled astrocytes (blue arrow) in the GCL-NFL and their intimate relationship with blood vessels (brown arrow). The red arrow marks the optic disc which sometimes gets ripped out during dissections.

Anti-Thy-1 allowed the visualisation of RGCs and their axons through fluorescence of the Cy3 marker. None of the samples stained for Thy-1 displayed any form of alteration to the RGC population. However, since none of these samples were pristine, anatomical changes could have taken place at the site of damage without being observed (figure 2.8).

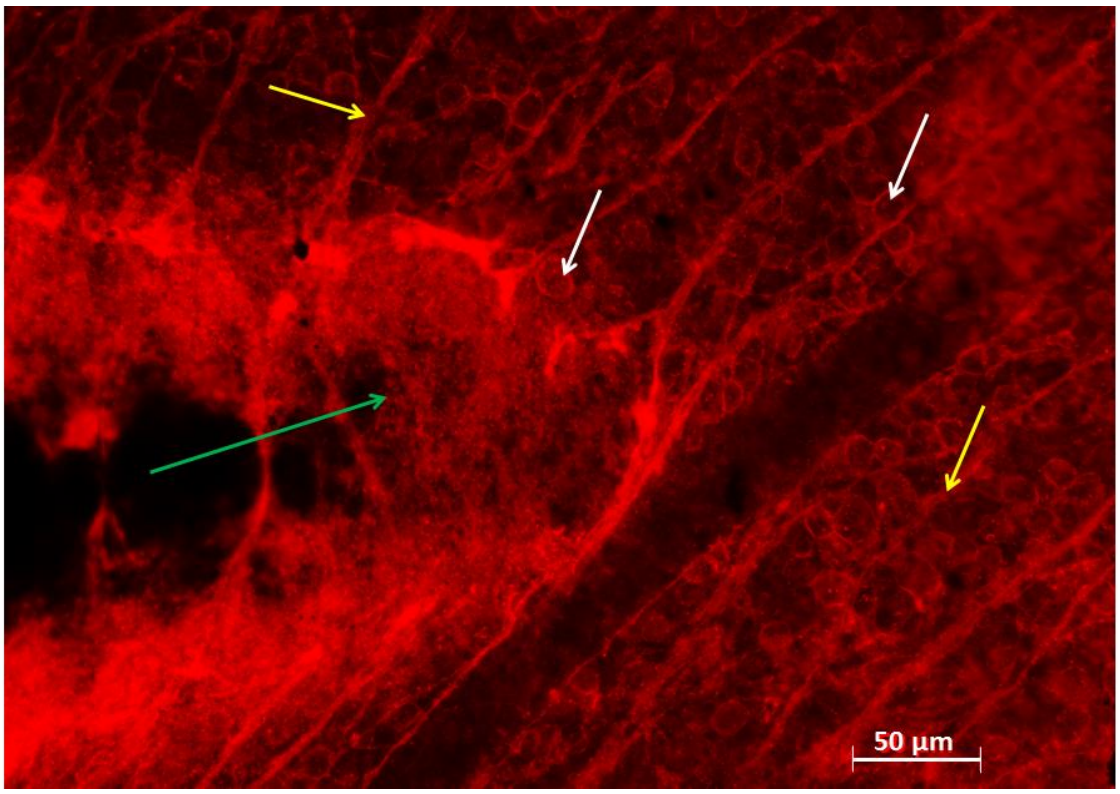

Figure 2.8: Tear in explants stained for Thy-1. High magnification fluorograph of retinal explant stained for Thy-1. Thy-1 staining allowed the visualisation of RGCs (white arrows) and their axons (yellow arrows). Explants stained with fluorescent probes seemed more delicate than samples stained with a DAB reaction, and were prone to large tears (green arrow).

Only 4 retinal explants stained for GFAP showed any sign of changes in the astrocytic plexus. All 4 explants were from a P120 CRX -/-mouse, incubated for 72 hours. On one of the explants, 6 aggregates of GFAP-labelled cells were observed amid a depleted astrocytic syncytium (figure 2.9). The average diameter of these clusters (established as perfect circles encompassing the clusters) was 131.5 ±5.6 µm and the centre-to-centre (of gravity) spacing was 227.2 ±9.3 (figure 2.9, B) which corresponds roughly to the size and spacing of large CNT islands in CNT-PDMS assemblies (100 µm/ 200 µm). The average density of cells present in these clusters (85% GFAP stain) was significantly larger ($p \leq 0.001$, one way ANOVA) than that of the areas between the clusters (27% GFAP stain) as well as that of control explants (61% GFAP stain; figure 2.9 C). Another one of these aggregates was observed on a different explant whose astrocytic syncytium is obliterated at a location where the explant was resting on the border between large and small CNT islands (figure 2.10). This particular aggregate has a diameter of 189.5 µm, which is almost double that of large CNT islands.

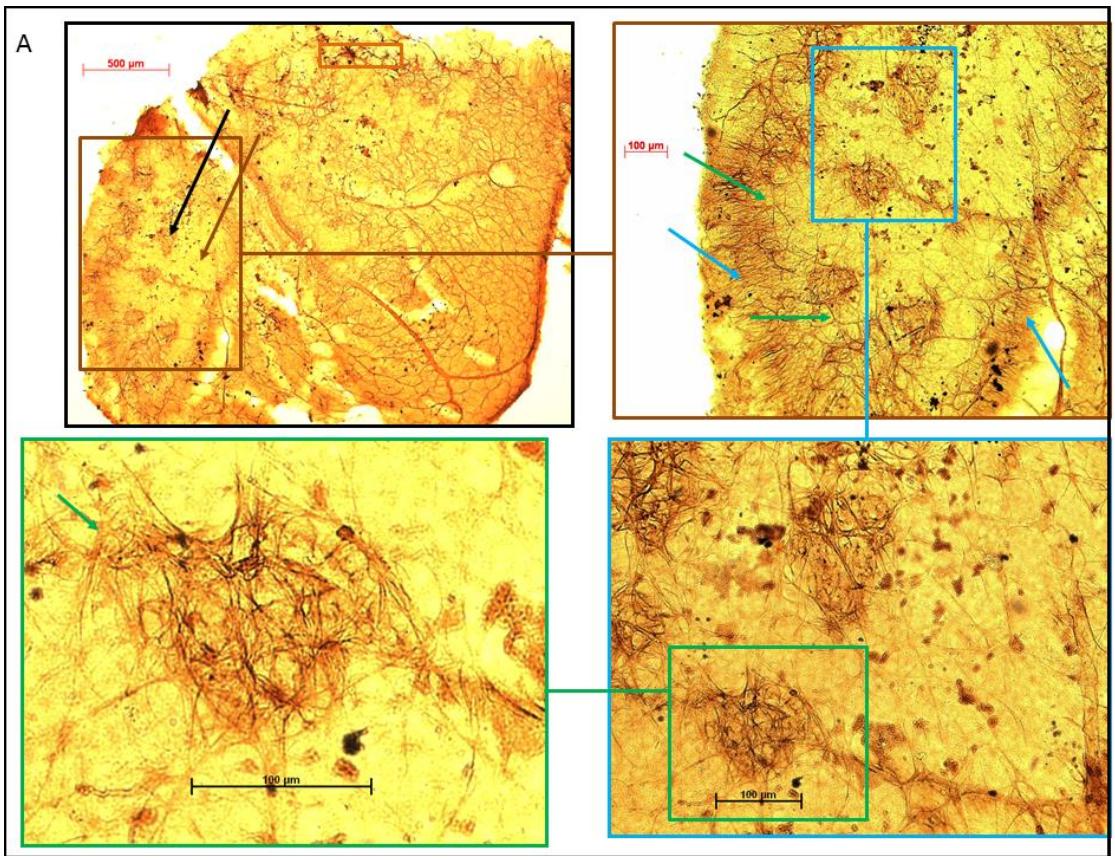

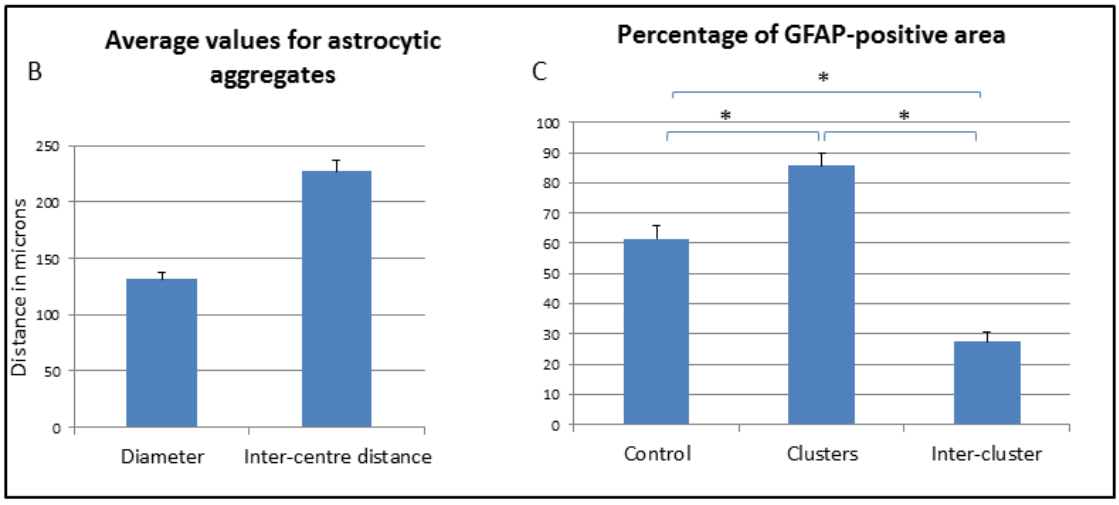

Figure 2.9: Astrocytic aggregates in explant incubated on CNT-PDMS composite. Micrographs (A) and associated values (B, C) of explant displaying GFAP-positive aggregates amid a depleted astrocytic plexus. A: optical micrographs organised in a clockwise fashion, offering a higher magnification of features highlighted in the previous micrograph. Black-lined micrograph: hemi-retinal explant incubated for 72 hours on a CNT-PDMS composite. The brown box highlights 6 astrocytic aggregates (black arrow) amid a depleted astrocytic syncytium (brown arrow). Brown-lined micrograph: magnification allowing the resolution of Müller cells (blue arrow) through their fibrous parallel appearance and astrocytes (green arrows) through their star-shaped morphology (figure 2.9'). B: Average diameter and centre-to-centre values for aggregates. C: Average density of astrocytes at aggregate and inter-aggregate locations.

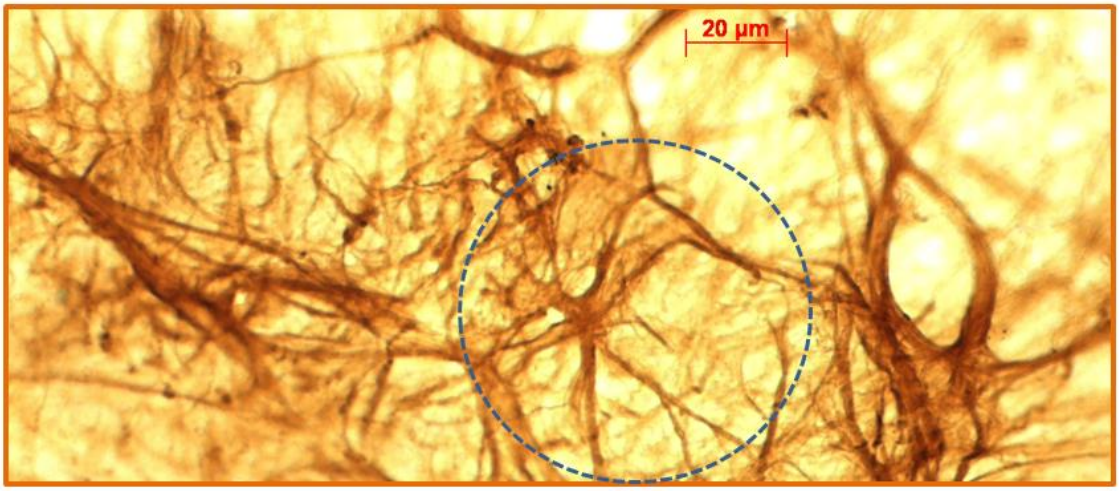

Figure 2.9': High optical magnification of astrocyte. Micrograph depicting a clearer view of an astrocyte from the orange box in the black-lined panel of figure 2.9A.

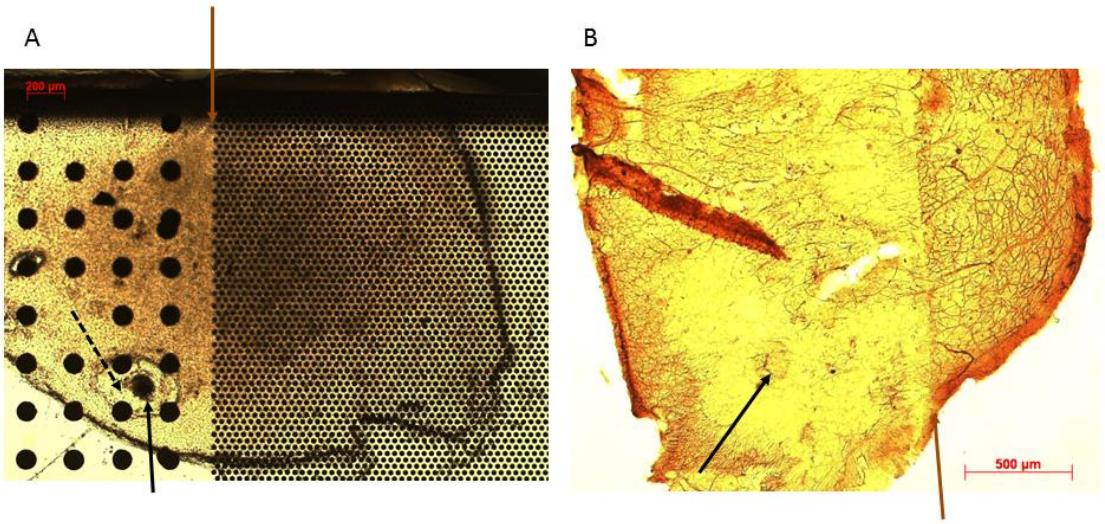

Figure 2.10: Focal obliteration of astrocytic syncytium in retinal explant incubated on CNT-PDMS composite. Micrographs of retinal explant incubated under the same conditions as the one displayed in figure 2.10. Micrograph A displays the retinal explant sitting on the CNT-PDMS composite following culture and fixation, but before the immunohystochemical staining process. The black arrow points to displaced CNT island (A) and a GFAP positive aggregate (B) in a similar location. The dashed arrow describes the displacing trajectory of that CNT island and the brown arrow points to the area separating the large from the small CNT islands on the substrate. Micrograph B displays the same retina stained with DAB for GFAP. The black arrow points to a GFAP positive aggregate surrounded by a depleted astrocytic plexus and the brown arrow points to a straight line separating an intact astrocytic plexus from a depleted one. During staining and mounting, the retinal tissue experiences shrinking, tool inflicted damage and is compressed between two layers of glass. This can explain the different shape of the tissue in both micrographs.

2.3.3 Immunohistochemical imaging of explants maintained under submerged conditions

Following incubation under *Submerged on-substrate* conditions and acquisition of electrophysiological activity (detailed in chapter 3), the retinal explants were lifted off MEAs (either CNT or TiN), stained for Thy-1 or GFAP and then imaged. Of the 26 retinas isolated, only 13 resulted in positive staining. Figures 2.11 and 2.12 display two sets of montages of low magnification micrographs of these 13 retinas. Figure 2.11 displays the control retinas (free-float) whilst figure 2.11 displays the retinas kept on CNT MEAs. A striking difference can be observed between control and MEA-incubated retinas. Indeed, the control retinas appear to have maintained morphological integrity whilst those maintained on CNT MEAs have undergone severe damage. Indeed, these retinas were maintained onto protruding electrodes for 48 hours before being removed from them. The process of removing the retinas from CNT electrodes was quite like that of removing two pieces of Velcro which most likely resulted in the damage observed here. This may be problematic in implanting and removing prosthetic devices. Further investigations may be required as to these processes. The retinal tissue appears to secrete extracellular matrix which creates a strong adhesive bond between retina and substrate. When retinas are removed from MEAs, this bond is destroyed as bits of tissue remain stuck onto the electrode. Removal of the retinas from Si/SiO2 substrates with loose CNT islands allows preservation of the contact between tissue and CNT island. This interface is investigated through electron microscopy in Chapter 4.

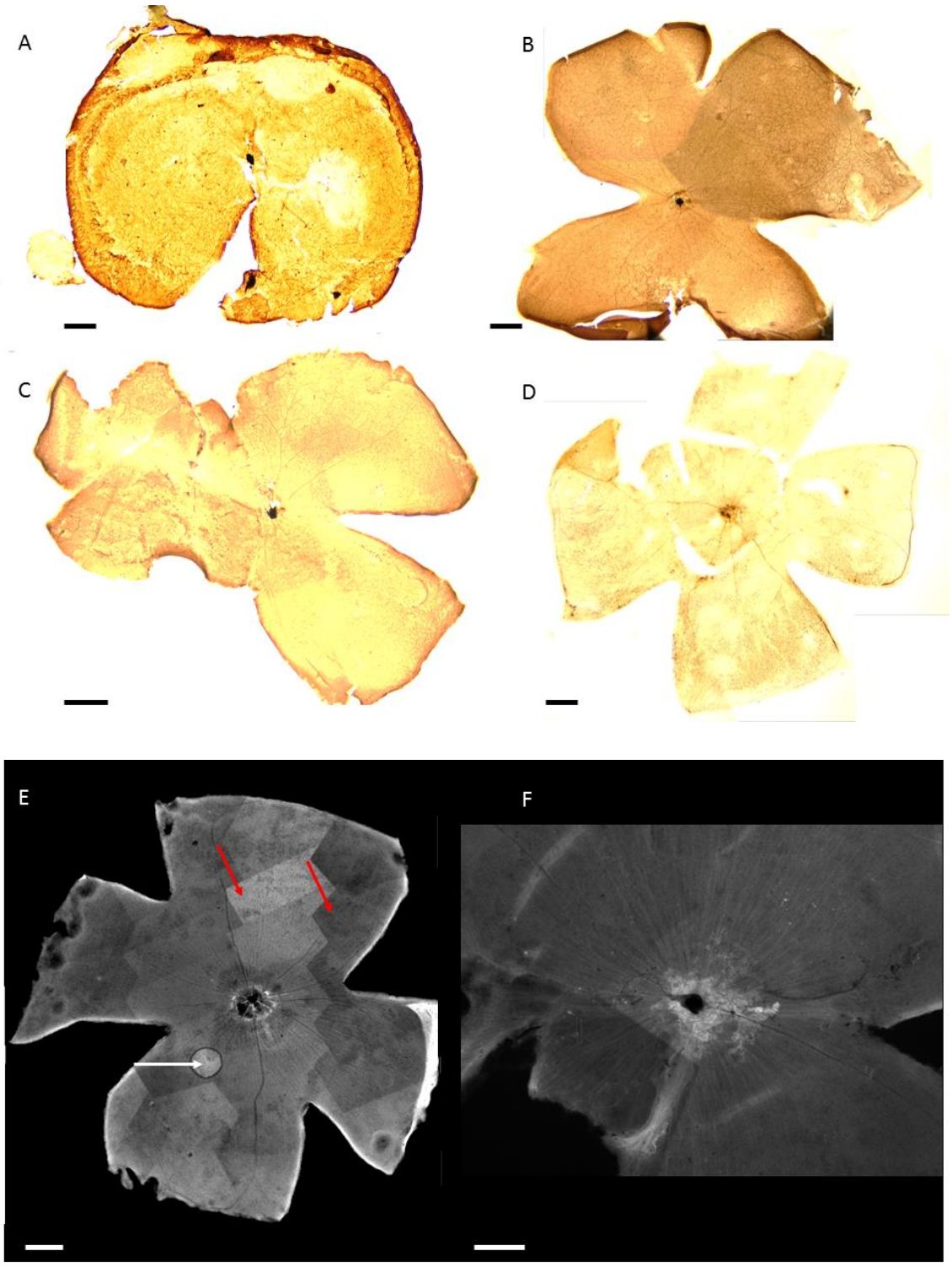

Figure 2.11: Control retinas incubated under *Free-float* conditions. Low magnification reconstruction montages of retinas incubated under *Free-float* conditions for 48 hours and stained for GFAP (A, B, C), GSL-I (D) and Thy-1 (E, F). The retinas appear to have kept their integrity. Retina C has a few unstained areas, presumably due to folding during free-float *in vitro* and retina E displays two obvious imaging artefacts: a bubble insinuated during the mounting stage (white arrow) and differences in contrast of the original images (red arrows). Scale bars are 200 µm for each panel.

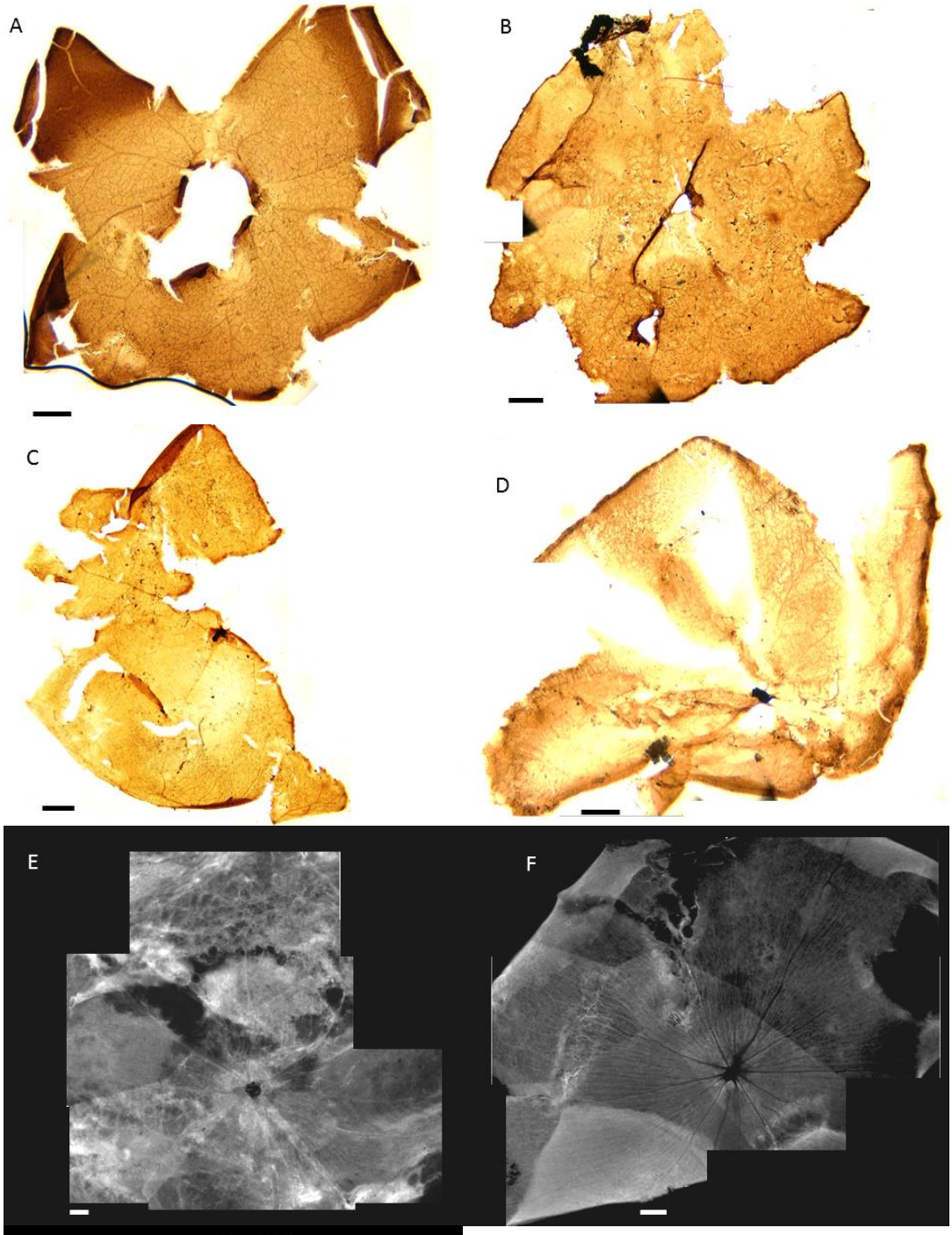

Figure 2.12: Retinas incubated under *Submerged on-substrate* conditions on CNT MEAs. Low magnification reconstruction montages of retinas incubated under *Submerged on-substrate* conditions for 48 hours on a CNT MEA and stained for GFAP (A, B, C, D) and Thy-1 (E, F, G). All these retinas have undergone severe damage, rendering the characterisation of global cell populations impossible. Scale

Much larger GFAP-positive aggregates were observed on two explants kept on CNT MEAs. Figure 2.13 displays low to high magnification of one of these explants with particular focus on one of the aggregates (dashed ellipses). The average diameter of these clusters is 174.9 ±9.4 μm, which is approximately 6 times the diameter of CNT electrodes on the MEA. Whilst the aggregates described in figures 2.9 and 2.10 appear to consist of astrocytic cells, the ones observed here appear to consist of Müller cells. Indeed, the cells are elongated and seem to form radial spokes (e.g. dashed box in green-lined panel). Also, there does not appear to be an astrocytic syncytium surrounding them. Only one portion of the explant (red box) appears to have an astrocytic plexus. Once again, these results are mitigated by the fact that most of the samples sustained heavy damage during the culture, staining and mounting processes.

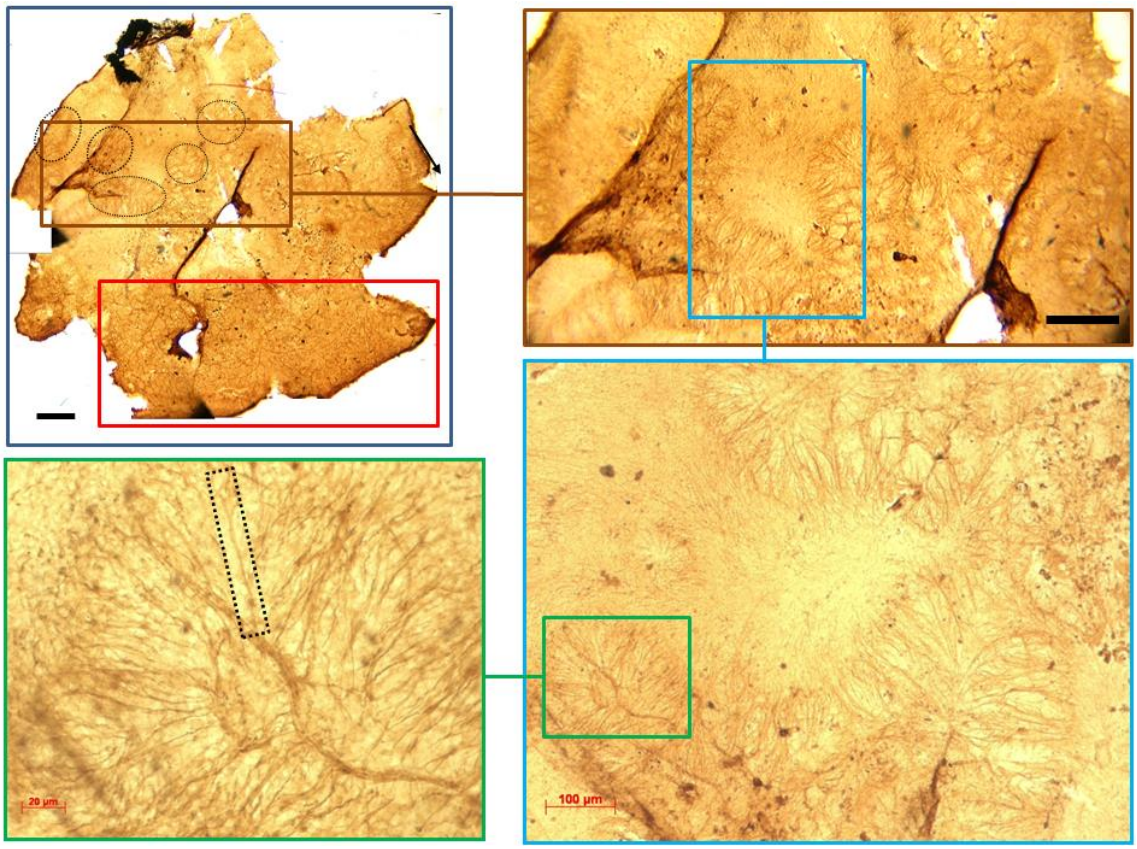

Figure 2.13: Müller aggregates on retinal explants kept on CNT MEA. Micrographs of GFAP stained retina after culture on CNT MEA under *Submerged on-substrate* conditions. Micrographs are organised in a clockwise fashion, offering a higher magnification of features highlighted in the previous micrograph. The black-lined panel displays the wholemount retina, with dashed ellipses encircling GFAP-positive aggregates. The red box highlights the only area on the explant with an astrocytic plexus and the brown box displays a different area with 5 aggregates. The brown, blue and green lined panels display higher magnifications of these aggregates, offering the possibility to resolve individual cells. The elongated morphology of these cells suggests they are Müller cells as opposed to astrocytes. Scale bars are 200, 200, 100 and 20 µm (clockwise from the top left corner).

Figures 2.14 and 2.15 display micrographs of retinal wholemounts maintained for 48 hours under *submerged* conditions and stained for GSL-I. The retina in figure 2.14 was kept free-float whilst those in figure 2.15 were interfaced with CNT-PDMS constructs. Although GSL-I is a typical marker for reactive microglia (Streit, Walter et al. 1999), it did not allow the visualisation of microglial cells in CRX -/- retinas but instead that of endothelial cells and bacteria (figure 2.14). This allowed the investigation of vascular remodelling and damage in response to epi-retinal interfacing with CNT islands. Since retinal blood vessels are located deeper than astrocytes and RGCs within the retina, they are less prone to damage inflicted during removal of explants from the culture substrate. Figure 2.18 displays binary images of reconstructed montages from 4 retinas interfaced for 48 hours onto CNT-PDMS substrates. These had vascular densities of 1.6 (A), 5.0 (B), 4.3 (C) and 4.9 (D) pixels / μm^2 which is consistently lower than the control value of 6.45 pixels / μm^2. Unfortunately, the low quality of the tissue samples prevents these values from being directly linked to the presence of CNT assemblies.

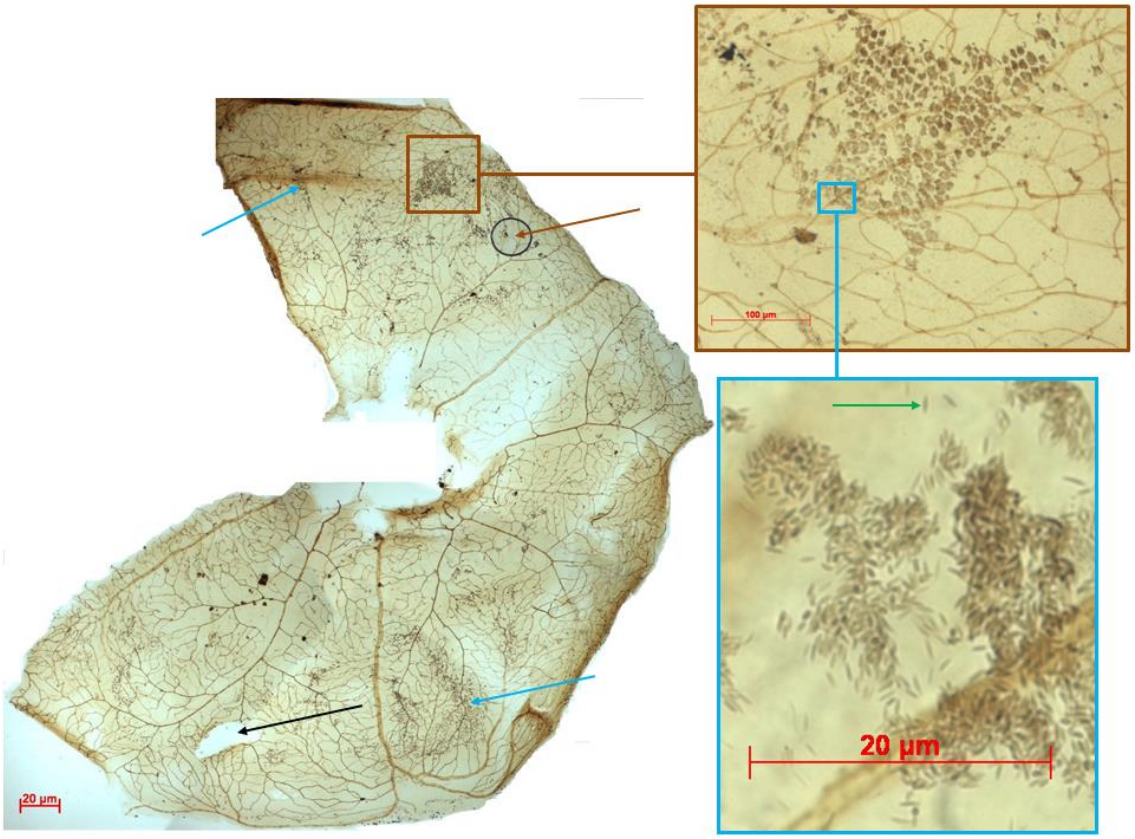

Figure 2.14: GSL-I stained control CRX -/- retina. Micrographs of planarized P147 CRX -/- mouse retinal wholemount stained with GSL-I/DAB after culture under *Free-float* conditions for 48 hours. Micrographs are organised in a clockwise fashion, offering a higher magnification of features highlighted in the previous micrograph. Although the retina sustained some processing-induced damage (black arrow), the vascular network is relatively well preserved. The brown arrow points to a bubble trapped below the coverslip, the blue arrows point to aggregates of microscopic dimensions appearing to have the morphological characteristics of bacteria (green arrow) at 100x magnification (blue-lined panel). Scale bars are 20, 100 and 20 µm (clockwise from the left micrograph).

GSL-I has also appeared to bind to bacteria (figure 2.14, n =6). This highlighted a major drawback in the *submerged* culture systems in that explants are exposed to bacterial infection.

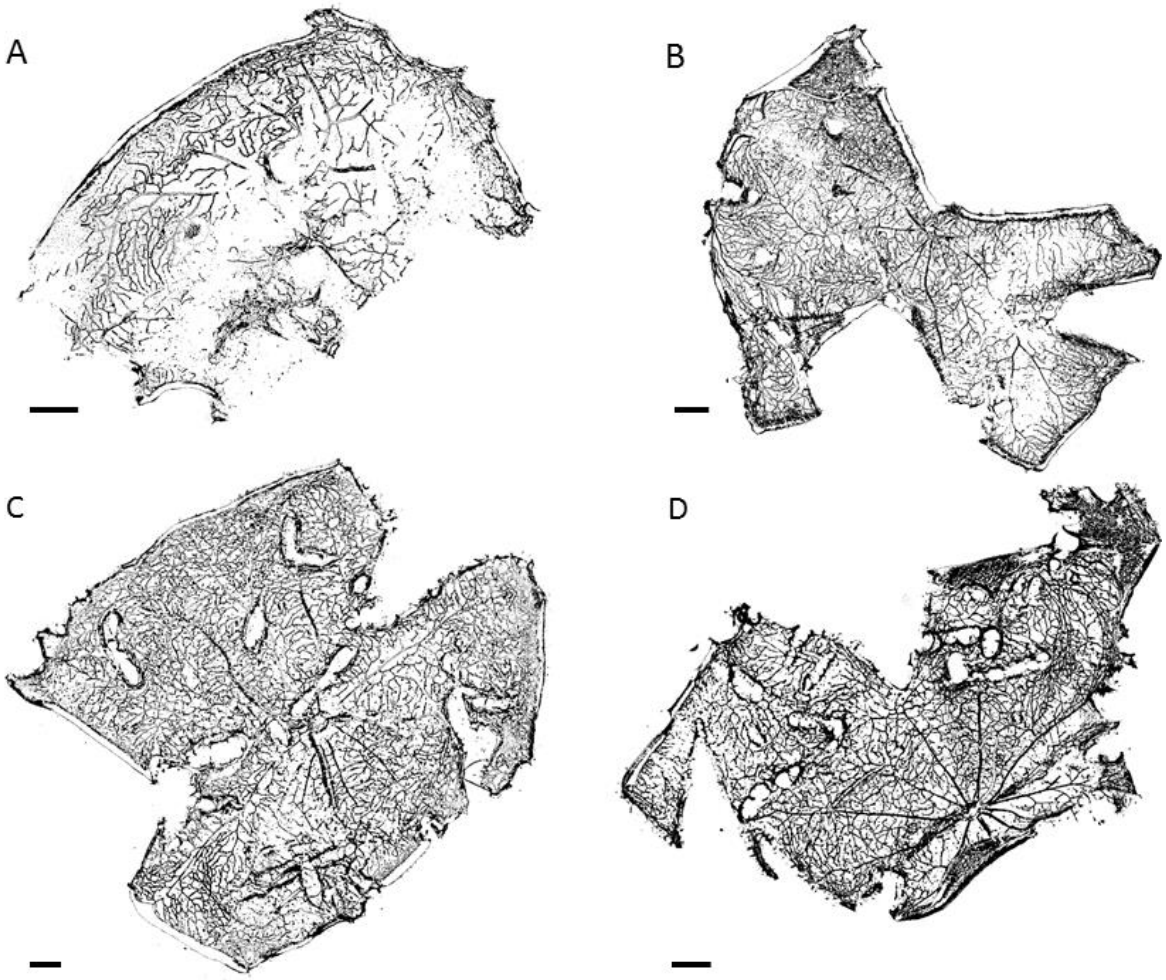

Figure 2.15: GSL-I stained CRX -/- retinas after interfacing with CNT-PDMS composites. Low magnification reconstruction montages of planarized P147 CRX -/- mouse retinal explants. These were stained with GSL-I/DAB after culture under *Submerged on-substrate* conditions for 48 hours whilst interfaced with CNT-PDMS composites. Observation of high magnification photomicrographs did not reveal any focused damage to retinal blood vessels or aggregation of activated microglia. Scale bars are 200 µm in each panel.

2.4 Discussion

As retinal rescue strategies from degenerative diseases is an expanding field, it is important to develop methods to investigate degeneration and repair in whole retinas maintained *in vitro*. Indeed, organotypic retinal culture systems would allow the step-by-step monitoring of retinal function following time-dependent rescue strategies such as genetic transfection, protein up-regulation, stem cell integration or implant incorporation. Although there exist a number of rodent models for retinal degeneration, maintaining these retinas *in vitro* remains a major technical challenge.

Immature normal rodent retinas have been shown to stay alive in organotypic culture systems for up to 4 weeks (Ogilvie, Speck et al. 1999; Fischer, Kneussel et al. 2000; Rohrer and Ogilvie 2003) but adult retinas are notoriously hard to maintain due to the high metabolic demands of photoreceptors. The tissue's gross anatomy is well preserved and readily characterised; cells display physiological changes in response to transfection but neural activity can only be recorded for a few days in culture (Cogan, Peramunage et al. 2007; Moritoh, Tanaka et al. 2010).

The adult CRX -/- retina does not contain active photoreceptors, yet we were unable to maintain RGC populations active for more than a few hours using typical *ex vivo* conditions. However, we demonstrated in this chapter the use of a hybrid long term-acute system in which the electrophysiological activity of CRX-/- RGC populations can be monitored for up to 5 days. This also allowed the imaging of GFP transfected retinal cells. The electrophysiological measurements acquired over three days on CNT MEAs are discussed in detail in the next chapter.

The advantages and drawbacks of the culture systems developed are discussed below, as well as ways of improving them.

2.4.1 Glial response to inner-retinal interfacing with CNT islands

In the brain and spinal cord, glial response is characterised by activation, hypertrophy and hyperplasia of both microglia and astrocytes (Hatten, Liem et al. 1991; Norenberg 1994; Fitch and Silver 2008). The retinal immune response is mediated by Müller cells (Bringmann and Reichenbach 2001) and microglia (Gehrig, Langmann et al. 2007). Retinal astrocytes for their part play a major role in the homeostatic support of RGCs and their axons, as well as angiogenesis (Stone and Dreher 1987; Fruttiger, Calver et al. 1996; Otani, Kinder et al. 2002). Modification of astrocytic behaviour would translate as changes in the astrocytic plexus of the NFL, changes in RGC populations (as astrocytes provide homeostatic support to RGCs, cf. section 1.1.5), and changes in retinal vasculature. Reactive gliosis would be characterised by changes in the microglial and Müller cell populations.

Astrocytic aggregates observed in figure 2.9 contain significantly more cells than the control astrocytic networks as well as the depleted areas surrounding them. However, there is no significant difference between the density of cells in the depleted areas and the control plexus. This surprising result rules-out the possibility that cells died in areas with no CNTs to latch onto and suggests hyperplasia at the islands rather than migration to the islands. Conversely, the depleted area in figure 2.10 contains only one astrocytic aggregate, which does not explain the disappearance of astrocytes over the area containing large CNT islands. We suggest that in this particular scenario, astrocytes migrated onto large CNT islands and were ripped off from the retina during the stage in which it was separated from the substrate. It has to be emphasised that this phenomenon occurred on 4 explants part of one same experiment of explants incubated on CNT-PDMS composites, the overall significance of these results is weak. Moreover, organotypic cultures of that nature tend to flatten with time without the assistance of anchors. Hippocampal slices cultured using the “Stoppini” method thinned from 450 µm to 150 µm over the course of 1 week (Stoppini, Buchs et al. 1991).

The radial clusters of Müller cells observed in figure 2.13 do not correspond in any way to the size and location of CNT electrodes on which the retina was placed. Müller cells become activated and re-enter the cell cycle within 24 hours following retinal injury

(Dyer and Cepko 2000). This timeline fits with the trauma of dissection and culture onto an MEA sustained by the retina. However, these clusters appear more like focal compression of the retina than hyperplasic cells. Indeed, the retina was forced down by weights during its time on the MEA. This could compromise its structural integrity and lead to flattening of the Müller cells in a manner similar to that observed in figure 2.16.

Imaging of microglial cells was not observed using the GSL-I marker despite it being extensively documented as a marker for activated microglia in mice (Ashwell 1990; Medana, Hunt et al. 1997; Frautschy, Yang et al. 1998). This could be either because microglial cells were not activated in these preparations or because it does not bind to retinal microglia. No scientific research papers were found to refute this theory. According to the manufacturers, GSL-I is a mixture of five different isolectins each expressing two types of subunits, A and B. A-rich lectins are specific for a-N-acetylgalactosamine whilst B-rich lectins are specific for a-galactose residues. GSL-I has been used to detect endothelial cells in murine retinas (Zayed, Yuan et al. 2007) and immunoreactive proliferating cell nuclear antigens (Haskal and Brennecke 1999). It has also been demonstrated to be reactive to both perfused and non-perfused microvessels (Greene, Lombard et al. 1990). Ways of assuring the observation of microglia in future experiments would be to use macrophage-specific antigens (e.g. F4/80 or FcIgG1/2b), type-three complement (Mac-1) receptors (Perry, Hume et al. 1985; Suzumura, Mezitis et al. 1987) or breed our CRX -/- mice with GFP positive microglia transgenic mice (e.g. CX3CR1$^{+/GFP}$ mice) as used by Lee et al. (Lee, Liang et al. 2008).
Severe damage sustained by the retinal tissue also prevented the correct interpretation of the effect of CNT islands on retinal vasculature. The literature suggests that damage to astrocytes or retinal blood vessels is followed by repair and replenishment (Chan-Ling and Stone 1992).

One of the major caveats of this study was the low surface area of CNT-PDMS composites (figure 2.1) as well as their unpredictable nature. Differences in fabrication between batches are most likely the reason for the low yield of astrocytic clusters. Improving the fabrication of CNT-PDMS composites would allow the correct evaluation

of the impact of CNT islands on retinal histo-morphology. One approach would be the creation of vertically aligned CNT pillars as described by (Wang, Fishman et al. 2006) or by plasma-enhanced CVD, then embedding these pillars in PDMS, cure it and finally etch the structure containing the trench from whence the CNT pillars grew. This would create protruding CNT islands from a PDMS substrate. However, the PDMS might wet the CNT pillars throughout, modifying the CNT architecture.

Bio-molecular techniques can be used to minimise glial proliferation in response to mechanical damage inflicted by epi-retinal electrodes. For example, electrodes could be deployed in a set of hydrogels releasing molecules in a controlled manner. Hydrogels have been used in neural implants for regeneration and repair (Lesny, De Croos et al. 2002). These polymers can be engineered to release molecules in response to PH changes or to specific antigens (Miyata, Asami et al. 1999; Gerhardt, Golding et al. 2003). As such, a primary layer could release vitreous digesting enzymes (hyaluronidase and collagenase). Once this layer was consumed, the apex of the electrodes would be in direct contact with the ILM. A secondary layer of hydrogel could then release antimitotic agents and cytokines (e.g. nitric oxide inhibitors) to inhibit glial activation and proliferation. Once this layer is consumed, the electrode would be integrated with the retina and a tertiary hydrogel layer would then be able to release support molecules for RGCs (e.g. neurotrophic factors).

2.4.2 Optimisation of interface incubation systems

Although the *interface* incubation systems allowed the observation of specific cell types following epi-retinal interfacing with CNT constructs, damage to the retina did not allow a thorough investigation of these populations. Approximately half as thin as wild type retinas, degenerated retinas are extremely delicate and susceptible to processing induced damage. Most of the damage incurred by the retinas happened during three key stages of the experimental process: retinal dissection, removal of the retinas from the substrates and mounting of the stained retinas onto slides.

As experimentalists grow accustomed to the technique, damage inflicted during retinal dissection can be minimised. However, there is still room for technological

improvement. We propose the use of three different types of forceps during dissection. A forceps which has been polished using a miniature drilling tool to keep hold of ocular tissue without damaging the retina, a forceps which has been coated with a smooth and flexible polymer (possibly PDMS) to hold neural tissue without inflicting damage and a forceps whose interior has been roughened to grab collagen fibrils of the vitreous cortex still adhering to the ILM. In primates and humans, the vitreous humour is significantly denser and forces vitreo-retinal surgeons to use molecular (Gandorfer, Ulbig et al. 2002) or mechanical (Fujii, de Juan et al. 2002) probes to detach it from the ILM.

Isolated retinas secrete adhesive ECM at the vitreo-retinal juncture, creating an intimate bond with the substrate unto which they are interfaced. Dissociation of this bond inevitably leads to damage of the tissue. A group investigating the ultrastructural integration of dissociated cells onto micro-fabricated constructs embedded the cells into Agar and dissolved the glass substrate using fluoric acid (Spira, Kamber et al. 2007). Such an approach could be used on future CNT-PDMS composites although the non-transparent CNT islands would still be present in the explant.

Recent work on embryonic stem cell culture has led to the full differentiation of a 3D eye-cup in a viscous culture substrate: Matrigel (Eiraku and Sasai 2011). Such a substrate could be used as a support for both CNT islands and retinal explants, allowing incubation, staining and mounting with minimised handling.

Chapter 3: Electrical Stimulation of the CRX -/- Retina over Three Days *In Vitro*

3.1 Introduction

This chapter is dedicated to the investigation of coupling at the CNT-retina interface through electrophysiological characterisation. CRX -/- retinas at an advanced stage of degeneration were isolated and placed on CNT and TiN MEAs. Spontaneous and evoked activity were recorded and monitored over 3 days as the retina was maintained under *in vitro* physiological (*Submerged on-substrate*) conditions directly onto the MEA. Changes in spike amplitude, number of cells evoked through a single electrical stimulation pulse (cellular recruitment) and threshold are indications of change in coupling at the retina-electrode interface.

Electrophysiological characterisation over 3 days led to the following results

1. Spontaneous activity
    a. A small but steady decrease in the number of active channels for both CNT and TiN electrodes
    b. A dramatic decrease in the oscillations for both CNT and TiN electrodes
    c. Gradual increase in spike sizes for CNT electrodes but not TiN electrodes
2. Different responses
    a. Mostly early, single spike responses for both types of electrodes
    b. Cathodic first, with asymmetric waveform stimulation pulses yielded lower thresholds for both types of electrodes
3. Number of evoked responses
    a. Increase in direct cellular recruitment on Day 2 for CNT electrodes
    b. Increase in direct cellular recruitment on Day 2 for TiN electrodes
    c. No significant increase in indirect cellular recruitment on Day 2 for TiN electrodes
    d. Increase in indirect cellular recruitment on Day 2 for CNT electrodes
4. Response thresholds
    a. Gradual decrease in threshold for early responses on CNT electrodes
    b. No significant variations in thresholds for TiN electrodes

The experiments and analyses described in this chapter were performed by Cyril Eleftheriou. CNT MEAs were fabricated at Tel Aviv University (Israel). The Ruby code used to generate stimulation trials was generated by Dr Jonas Zimmerman, as a Masters student in Dr Evelyne Sernagor's laboratory. The Matlab code (The Mathworks, USA) used to extract the data, remove the artefact and generate raster plots was generated by Dr Jonas Zimmermann, and then subsequently optimised by Henrik Kjeldsen and John Barrett as Master's students in Dr Sernagor's laboratory.

3.2 Methods

3.2.1 Maintenance of retinal explants

A total of 15 CRX -/- mice (aged 84 to 111 day) yielded 30 retinas, 15 of which were used for the electrophysiological part of this project. Retinas were isolated as described in Chapter 2 and mounted onto MEAs with the GCL facing down onto the electrodes and the optic disc to the side (not in contact with electrodes) as this part of the retina has no RGC somata. To improve the coupling, a polyester membrane filter (5µm pores) held the retina in place whilst being weighed down by two stainless steel anchors (0.75g each) bearing a framework of parallel glass capillaries (Figure 3.1, insert). Thirteen of the isolated retinas were mounted onto CNT MEAs and two onto TiN MEAs.

To preserve physiological conditions, the tissue was perfused with oxygenated aCSF at 1 ml/minute over the course of 72 hours using a peristaltic pump (SCI400, Watson Marlow, UK). During the recording of electrophysiological activity, retinal explants were maintained at 32˚C using a Universal Serial Bus (USB) temperature controller (TC02, Multi Channel Systems, Reutlingen, Germany) regulating a metallic chamber below the MEA (MEA1060 INV, Multi Channel Systems, Reutlingen, Germany) and an inline heater for the inflow of aCSF (Ph01, Multi Channel Systems, Reutlingen, Germany). In order to increase the amount of oxygen dissolved in aCSF between periods of recording, the temperature controller was shut off overnight, and the retina maintained at room temperature (Hennig et al., 2011).

Although CRX -/- mice do not develop photoreceptor-mediated vision, melanopsin

induced phototransduction occurs in a population of RGCs in the presence of blue light (Hattar, Liao et al. 2002). This is characterised by firing of melanopsin expressing RGCs (Adams, Simonotto et al. 2008). To avoid this phenomenon, all experiments were carried out in darkness.

3.2.2 Recording and stimulation equipment

Electrophysiological signals were recorded using 60-channel MEAs interfaced with a computer running the proprietary software MC_Rack (Multi Channel Systems, Reutlingen, Germany) using an MEA1060INV (Multi Channel Systems, Reutlingen, Germany) amplifier via a PCI (Peripheral Component Interconnect) MC card.

Electrodes had a 30 µm diameter and were spaced at 200 µm on a square grid. The control MEAs were 60MEA200/30-Ti-gr (Multi Channel Systems, Reutlingen, Germany) with typical impedance values of 30-50 kΩ at 1 kHz. CNT MEAs were fabricated by Moshe David-Pur and Dr Yael Hanein (Tel Aviv University, Israel) with typical impedance values of 10 kΩ (Gabay, Ben-David et al. 2007).

Recordings were made at 25 kHz sampling frequency during the acquisition of both spontaneous and evoked activity. Spontaneous activity was recorded during 10 minutes before and after each stimulation run, totalling 15 stimulation runs and 15 spontaneous activity files per retina. Malfunctioning channels were grounded (figure 3.3) as the noise level was affecting the signal on nearby electrodes, sometimes saturating them. This level of noise was often due to a bubble on the electrode, etching of the passivation layer or damage to the electrode contact.

Electrical stimulation of retinal tissue was achieved via individual electrodes on MEAs connected to an STG2002 stimulator (Multi Channel Systems, Reutlingen, Germany) controlled by a computer running the proprietary software MC_Stim (Multi Channel Systems, Reutlingen, Germany) via a USB connection. The stimulator was also connected to the recording equipment's PCI acquisition card via a Bayonet Neill–Concelman (BNC) cable for synchronised recordings. Acquisition of electrophysiological signals during stimulation runs included 100 ms before and 200 ms after the stimulus.

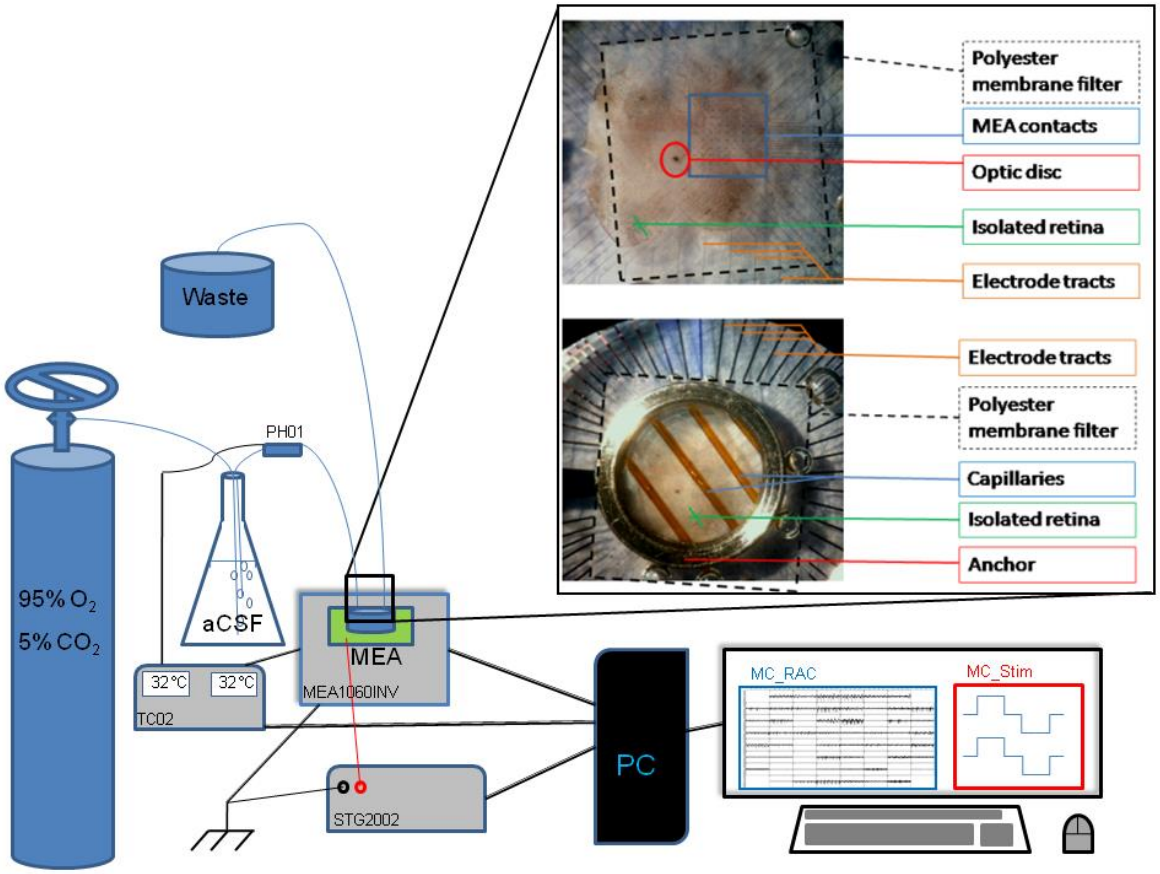

Figure 3.1: Diagram outlining the experimental setup for maintenance of isolated retinas, electrical stimulation and recording of spontaneous and evoked activity. Retinas were maintained in physiological conditions with a constant flow of heated oxygenated aCSF and kept at 32˚C by heating a copper plate below the recording chamber (MEA 1060INV) and an inline heater (PH01). Injection of charge through individual electrodes of the MEA was achieved by connecting the PC controlled STG2002 stimulator to the corresponding external contact on the recording chamber. Insert in the top right hand corner shows photographs of a retina planarized on a TiN MEA (top) and held down by a stainless steel anchor (bottom). The optic disc is slightly to the left of the MEA's contacts to avoid recording from that region.

3.2.3 Stimulation parameters

Previous work in several groups, including our own, has demonstrated that the choice of stimulation parameters influence the threshold level to induce action potentials. Work by Chichilnisky and colleagues (Sekirnjak, Hottowy et al. 2006) has shown that the polarity, inter-phase interval and ratio between current intensity and pulse width (i.e. duration) all have an effect on how electrical stimuli can elicit a response in RGCs. All electrical stimuli were rectangular charge-balanced biphasic pulses with a 30 µs

inter-phase interval. Previous work in our laboratory (Zimmermann 2009) suggested that a 30 µs interval resulted in lower thresholds. Variations were made to the current intensity, the phase duration, the ratio between current intensity and phase width between both phases as well as the polarity of the first phase to determine which combination was most effective (figure 3.2). The pulses were charge-balanced to prevent electrolysis at the tissue-electrode interface.

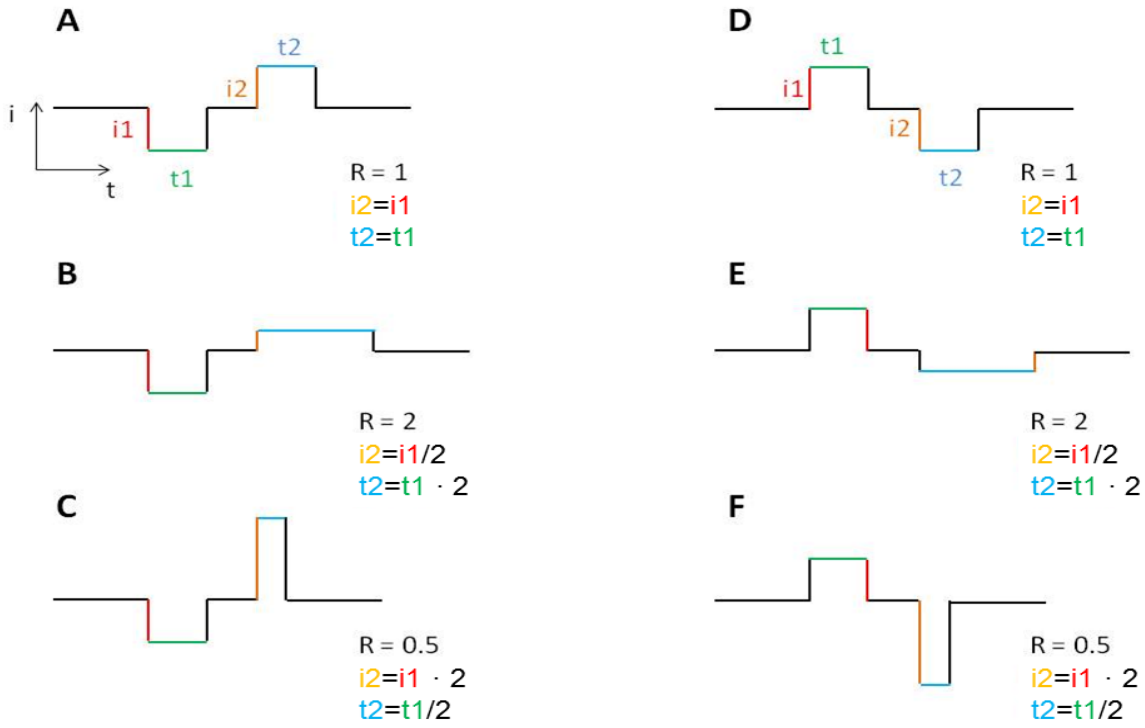

Figure 3.2: Different stimulation parameters. These parameters comprise the negative phase first (A, B, C), positive phase first (D, E, F), symmetric phases (A, D), a longer width for the second pulse (B, E) or a higher current intensity for the second pulse (C, F). All stimuli were charged balanced, satisfying the relationship t1·i1 = t2·i2

The amount of charge (q) in each phase of a pulse injected into the retina via an individual electrode on an MEA is equal to the phase duration (t) multiplied by the current intensity (i).

$$q = i \cdot t$$

As a charge balanced pulse, the first phase's total charge (Q1 = t1 · i1) must equate that of the second phase (Q2 = t2 · i2). Thus, an asymmetrical stimulus will still be charge-balanced, provided

$$Q1 = Q2$$

$$t1 \cdot i1 = t2 \cdot i2$$

To change the ratio (r) between the width of the first and second phase, the current intensity of the second phase must be divided by that ratio to preserve the charge balance.

$$Q2 = (t1 \cdot r) \cdot (i1 / r)$$

Three different waveforms were used, one where r = 1 (symmetrical), one where r = 0.5 and one where r = 2 (figure 3.2). Each waveform was also presented with positive or negative polarity first, resulting in a total of 6 different stimulus combinations. The use of asymmetrical stimuli will help us establish which type of waveform is most effective at stimulating RGCs.

Stimulus intensities ranged from 10 to 100 µA, with pulse durations lasting from 20 to 100 µs for each phase. Intervals between individual stimuli were varied randomly from 1 to 2 seconds, averaging 0.67 Hz to avoid such artefacts as low frequency potentiation or resonance with intrinsic oscillations of the RGC as seen in degenerated retinas (Margolis, Newkirk et al. 2008; Stasheff 2008; Menzler and Zeck 2011), see also (figures 2.5 and 3.3). Once the preparation had settled (typically 1 hour after the tissue was placed onto the MEA), threshold was established in a systematic fashion by stimulating with increasing values of charge per pulse until obtaining an online (whilst performing the experiment) response, then decreasing the charge per pulse value in steps of 0.1 nC until a response is obtained in 50% of cases. Online thresholds were determined visually and thus unreliably which is why the value was only a guideline in generating a set of appropriate stimulation parameters. A set of conditions was selected which included sub and supra-threshold charge values obtained by a combination of diverse current intensities and pulse widths. The stimuli were delivered randomly, with either 10 or 30 different trials recorded per condition. Consequently, each stimulation-run lasted approximately one hour.

3.2.4 Data analysis

MCD files were imported into Matlab (The MathWorks, USA) using the FIND toolbox (Meier, Egert et al. 2008). The artefact introduced by applying electrical stimulation was removed using the SALPA algorithm (Wagenaar and Potter 2002). Spikes were automatically extracted and sorted by supra-paramagnetic clustering and wavelet analysis using Wave_clus (Quiroga, Nadasdy et al. 2004). These results were later inspected visually and re-clustered using the Wave_clus "temperature" tool.

Epochs containing sorted spikes for each electrode were mapped to the different stimulus conditions and organized as raster plots with the ordinates divided into the different charge injected values in ascending order. Consequently, the results for a single stimulation run consisted of a set of six (the number of different stimulating combinations) raster plots for each spike cluster on each recording electrode.

Thresholds were determined by visual inspection of the raster plots: evoked spikes would disappear below a certain threshold (figure 3.12). Spike sizes were measured by peak-to-peak amplitude of each extracted spike. Statistical analyses and graph plotting were carried out using Sigma Plot (Systat Software Inc., San Jose, California, USA) and Excel (Microsoft, USA) respectively. Statistical significance was measured using non-parametric analyses (ANOVA coupled to 1 or 2 tailed Wilcoxon, Tukey or Mann-Whitney test) with a significance limit of $p \leq 0.05$.

The values are normalised to percentages for quantitative measures displayed in most of the figures of this chapter. Indeed, the number of recruited cells and their individual thresholds cannot be expected to be the same for each different experiment. Some of the variables are hard to account for, such as the exact location of the electrodes on the retina, the electrochemical characteristics of each single electrode on each single MEA (which change after each experiment (Wagenaar, Pine et al. 2004)) and the actual level of remodelling in each one of these degenerated retinas.

Matlab scripts and Sigma Plot analysis reports are included in Appendices i and ii respectively.

3.3 Results

3.3.1 Spontaneous activity

Spontaneous activity patterns indicate whether the retina is physiologically sound during an experiment. The total number of active channels and those exhibiting rhythmic activity indicate whether synaptic networks are still functioning whilst measures of spike sizes offer an indication of the quality of the coupling at the tissue-electrode interface.

3.3.2 Spontaneous activity: active channels

If the retina is in direct contact with an electrode on the MEA, that channel will display spontaneous activity. In dystrophic retinas, this consists of vigorous RGC bursting and slow oscillations (Stasheff 2008). As the activity of the retina stabilises at the onset of an experiment, gradually more channels will display oscillatory bursting activity with time. However when the retina is maintained *in vitro* for a prolonged time (2-3 days), gradually fewer channels exhibit spontaneous activity (although RGCs are still alive as demonstrated by their ability to generate action potentials). Figure 3.3 displays an example of this process with three screen shots of the spontaneous activity recorded from the GCL on Day 1, 2, 3.

In order to quantify this phenomenon over time, the number of active electrodes was counted for each recording of spontaneous activity (before and after each stimulation run). Thus, we obtain a total of 15 temporal points per experiment (five/day) with an average interval of one hour during the same day and 15 hours in between days (points 5 to 6 and 10 to 11).

Figure 3.4 (A, B) shows the percentage of active electrodes from all live channels (grounded and noisy removed) on the MEA for all experiments over 6 of the 15 time points. On the abscissa, 1.1 corresponds to the first time point of Day 1, 1.5 corresponds to the last time point of Day 1, 2.1 corresponds to the first time point of Day 2 and so on. Of the 11 CNT experiments that lasted three days, 7 (64%) had over 40% of active channels on Day 1 and 6 (56%) on Day 3, indicating only a slight deterioration in the viability of these preparations. The 40% mark was chosen here

because it highlights a clear divide in the number of experiments with high and low levels of activity on Figure 3.4 (A). It is also worth noting that for 10 of those experiments, the number of active channels was higher by the end of Day 1, indicating an increase in tissue-electrode coupling and stable physiological conditions. For TiN experiments (of which only two were carried out over 3 days), both display an increase in active channels during Day 1, and only one shows a decrease in activity on Day 3. Previous work in our laboratory has demonstrated retinas maintained under physiological conditions for 2 days (Hennig, Maccione et al. 2011).

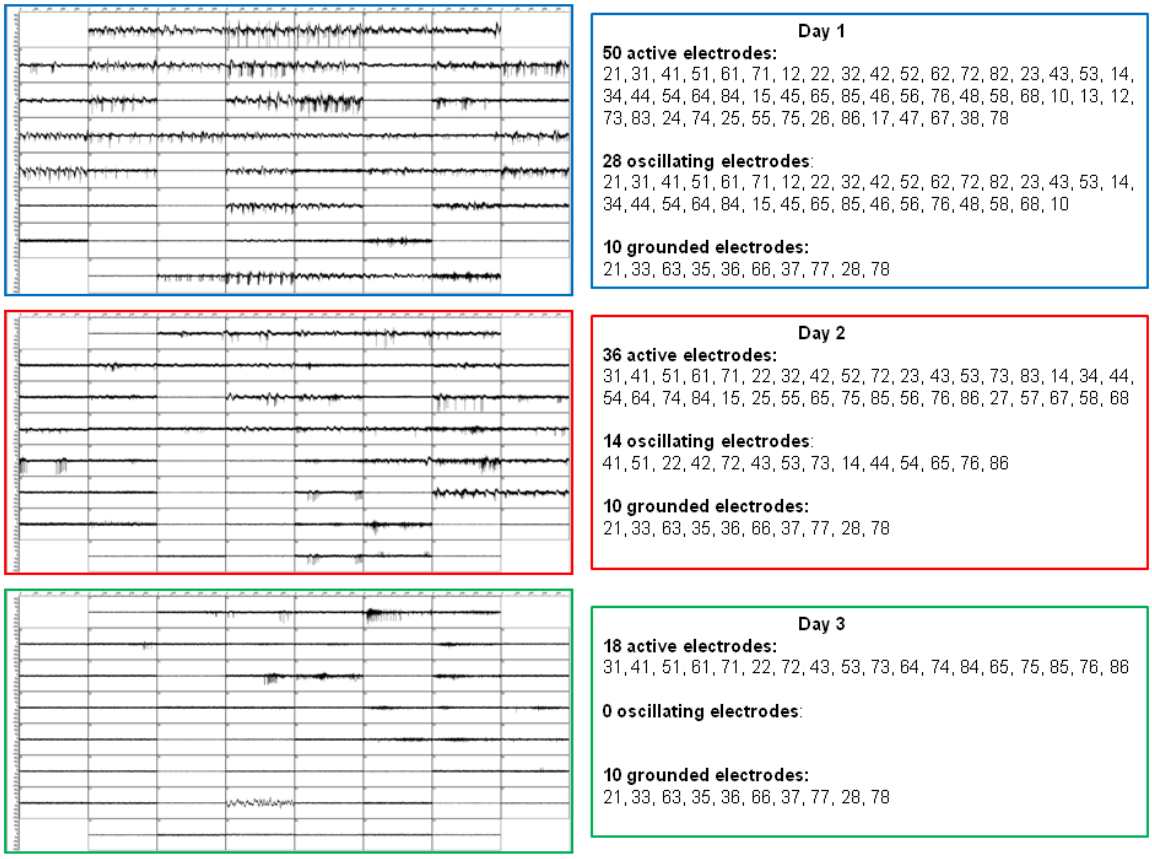

Figure 3.3: Screenshots of retinal spontaneous activity. Screenshots of electrophysiological recordings (left) grabbed from MC_Rack on Day 1 (blue), Day 2 (red) and Day 3 (green) for experiment CE0027. The numbers of active and grounded channels, as well as those displaying oscillatory activity are displayed on the right for Day 1 (blue), Day 2 (red) and Day 3 (green).

3.3.3 Spontaneous rhythmic activity

The dystrophic retina is characterised by spontaneous oscillations, resulting in the synchronicity of local field potentials (LFP) that can be recorded from the RGC layer on MEAs (Stasheff 2008). In our experiments, 10 out of 12 CNT MEAs exhibited spontaneous oscillations on over 40% of the channels on Day 1, but then the incidence decreased to 1 out of 12 over 40% of the channels on Day 3 (figure 3.4, C). As for TiN MEAs, both showed over 60% of oscillating channels on Day 1, but not on Day 3. These results indicate that the networks involved in generating these oscillations begin to fail after maintaining the retina *in vitro* over prolonged periods (but RGCs are still capable of generating spikes, see below). At the same time, 8 out of 14 of all experiments (both TiN and CNT) show a rise in the number of oscillating electrodes between the beginning and end of Day 1 (figure 3.4 D), indicating that networks keep their functional integrity for many hours, and up to 2 days (Hennig et al. 2012). Over all experiments, there was a statistically significant decline in oscillating channels (figure 3.6 E; $p \leq 0.02$ from time point 2.2 onwards; one way ANOVA), yet no statistical difference in the number of active channels (figure 3.6 F; $p = 0.128$; Kruskal-Wallis one way ANOVA).

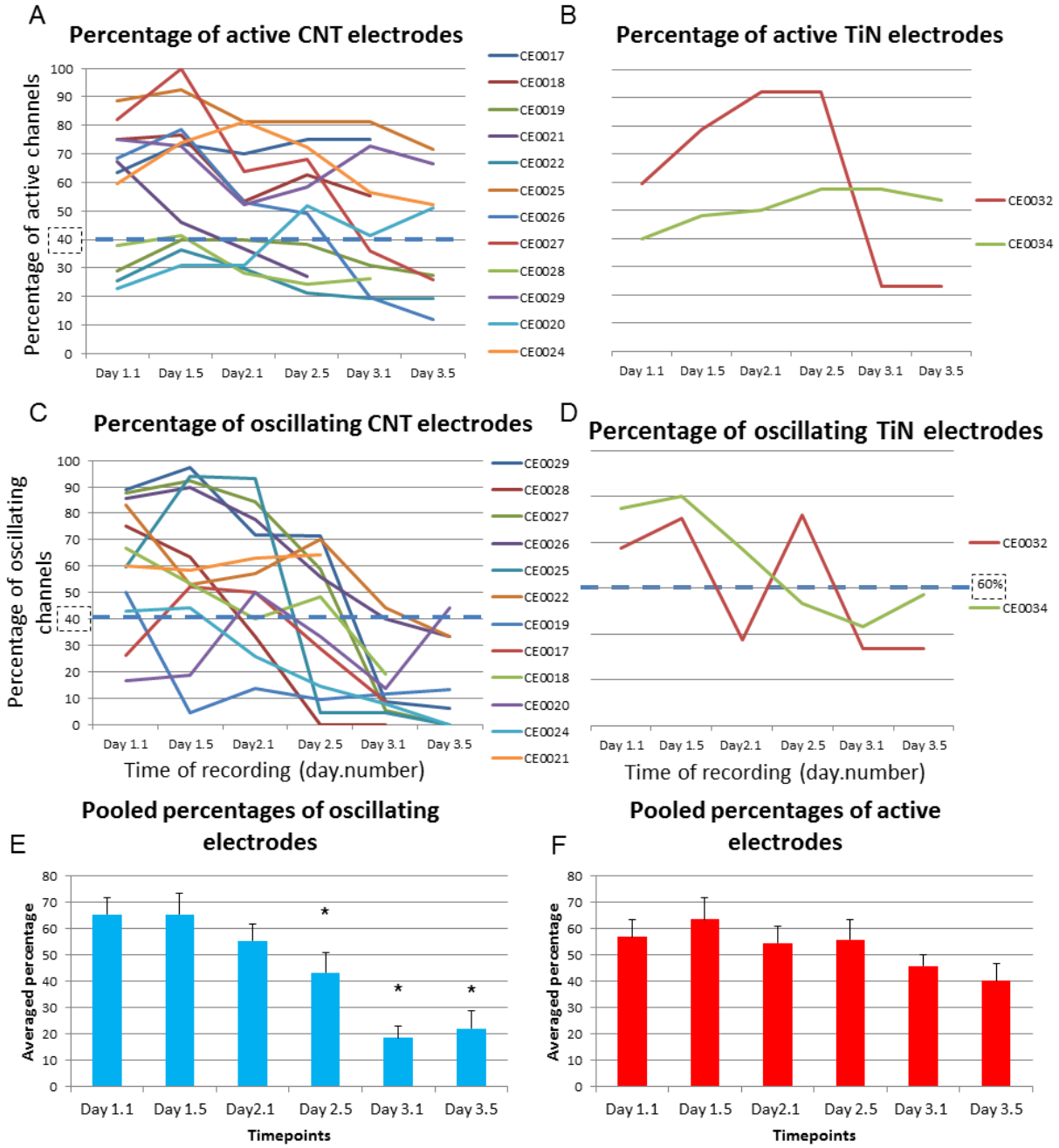

Figure 3.4: Percentage of active and oscillating channels. A, B: Number of active channels as a percentage of the total number of live channels. C, D: number of channels showing rhythmic activity as a percentage of all active channels over a three day period *in vitro*. A, C: CNT experiments. B, D: TiN experiments. Ordinates for B and D are the same as A and C respectively. E, F: Percentage of oscillating (blue, E) and active (red, F) channels over all experiments. Error bars: S.E.M.; asterisks: statistical significance.

3.3.4 Spontaneous activity: inverted spikes

Most of the action potentials recorded had the typical shape characteristic of extracellular recordings: a biphasic waveform with a sharp negative phase followed by a smaller and slower positive phase as shown in figure 3.5 B. However, a number of our recordings display occurrences of “inverted” spikes, with a sharp positive phase followed by a negative phase with similar kinetics to the first phase, as shown in figure 3.5 C.

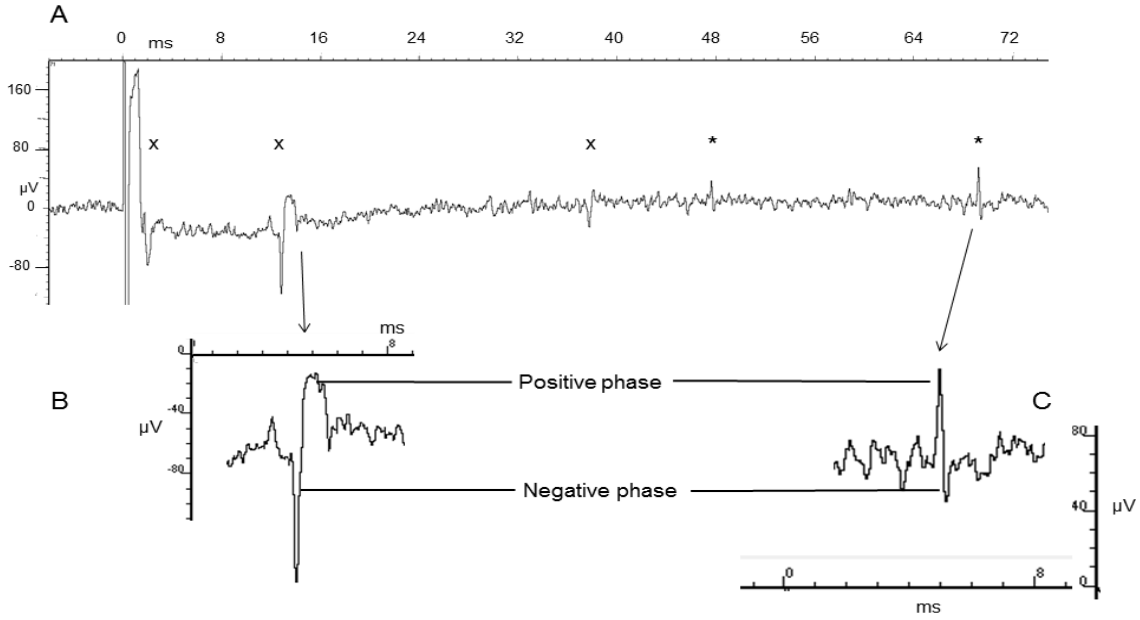

Figure 3.5: Example of “inverted” spontaneous spikes recorded following electrical stimulation. A: 72 ms of spontaneous activity following electrical stimulation on a distal electrode showing three conventionally shaped spikes (crosses) and two “inverted” spikes (asterisks). B: Conventional spikes are characterised by a sharp negative phase followed by a smaller and slower positive phase. C: “Inverted” spikes are characterised by a sharp positive phase followed by a smaller negative phase.

Of the 15 retinas investigated, 13 displayed this type of activity, with a total of 60 electrodes recording “inverted” spikes. This represents ~5 % of the 1224 electrodes having recorded spontaneous activity. The number of electrodes displaying “inverted” spikes varies with the number of days *in vitro* for each individual retina. Figure 3.6 shows the total number of occurrences over all retinas for each day as well as a value for the average number of electrodes showing “inverted” spikes for each retina. There is a significant increase between the average number of electrodes showing these

events on Day 1 and Day 2 and decrease between Day 2 and Day 3 (p =0.002, Kruskal-Wallis one way ANOVA coupled to Tukey test).

The maximum number of electrodes with “inverted” spikes per experiment is 6 and always occurs on Day 2, for both TiN and CNT MEAs. It is worth noting that both TiN experiments showed no “inverted” spikes on Day 1, but a higher average number on Day 2 and Day 3 (figure 3.6, C). Not significant (t test, p = 0.574 for Day 2 and p = 0.160 for Day 3).

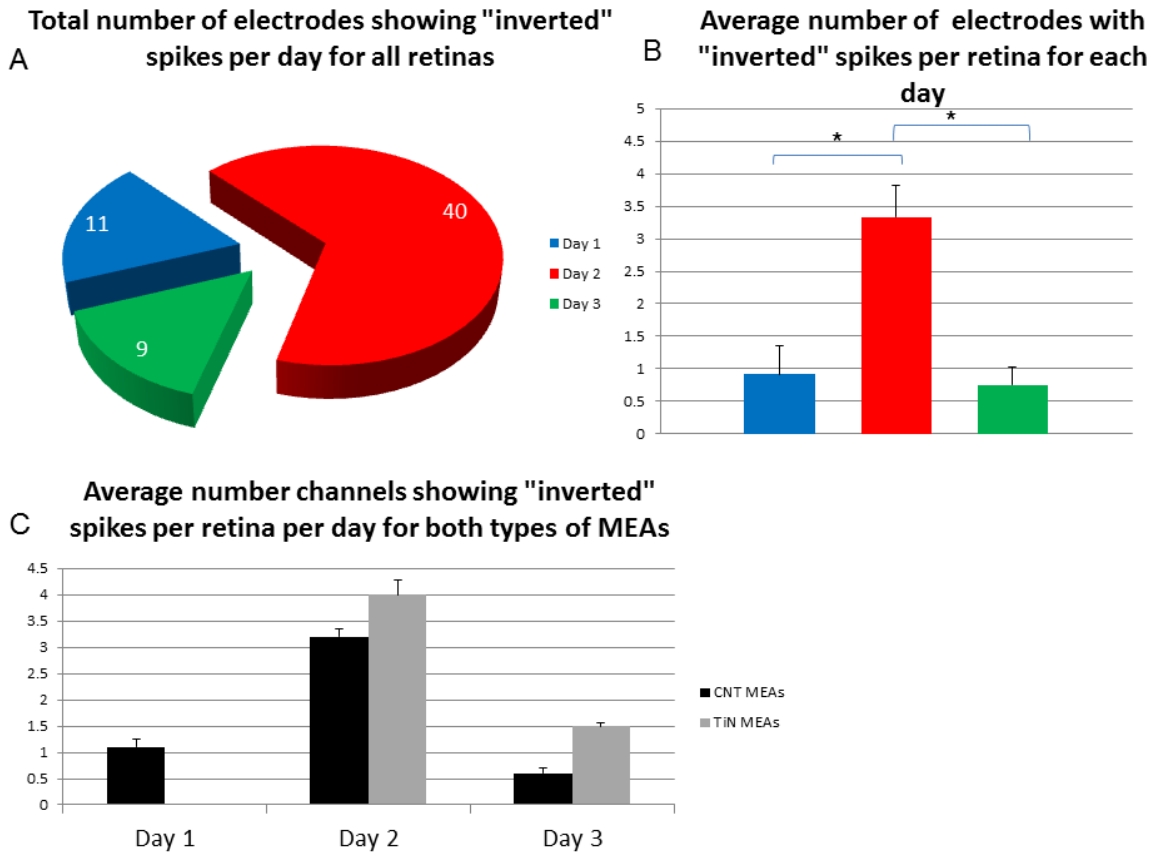

Figure 3.6: Statistics of “inverted” spikes. A: Pie chart displaying the number of channels recording “inverted” spikes as a grand total for each day. B: Column plot of the average number of “inverted” spikes per retina for each day. C: Column plot displaying average number of channels recording inverted spikes for each day according to electrode type. Error bars: S.E.M. Asterisk: statistical significance. Colour code: blue, Day 1; red, Day 2; green, Day 3; black, CNT MEA; grey, TiN MEA.

3.3.5 Spontaneous activity: spike size

Spike sizes were calculated by taking the peak-to-peak value of all extracted action potentials above 3 standard deviations of the noise level on each channel for a

particular experiment. Figure 3.7 and 3.8 display these values as histograms showing the number of spikes according to their size. Figure 3.7 displays the number of spikes and their sizes for experiments performed on TiN experiments. In both experiments, there is no gradual change in spike size. However, experiment CE0032 displays a decrease in spike amplitude on Day 2 followed by an increase on Day 3 although the largest spikes were only observed on Day 1.The largest spike size for TiN experiments is 135 µV, occurring on experiment CE0034.

Figure 3.8 displays the distribution of spike amplitudes for experiments performed on CNT MEAs. All these distributions display larger spikes on Day 2 and/or Day 3 than on Day 1, suggesting a time-dependent spike increase with spikes nearing 400 µV in 3 experiments, a value almost triple the size of the largest spikes on TiN MEAs. Of the 9 experiments with values on all 3 days, 22% display a gradual increase in spike sizes from Day 1 to Day 3 (CE0018, CE0029), 44% display a decrease in spike size on Day 2 (CE0019, CE0025, CE0027, CE0028) and 33% display a decrease in spike size on Day 3 (CE0020, CE0024, CE0026). In a subset of experiments (CE0017, CE0018 and CE0027) a separate population of larger spikes seem to appear in later days. These changes suggest that there is a gradual increase in coupling between the retina and the CNT electrodes.

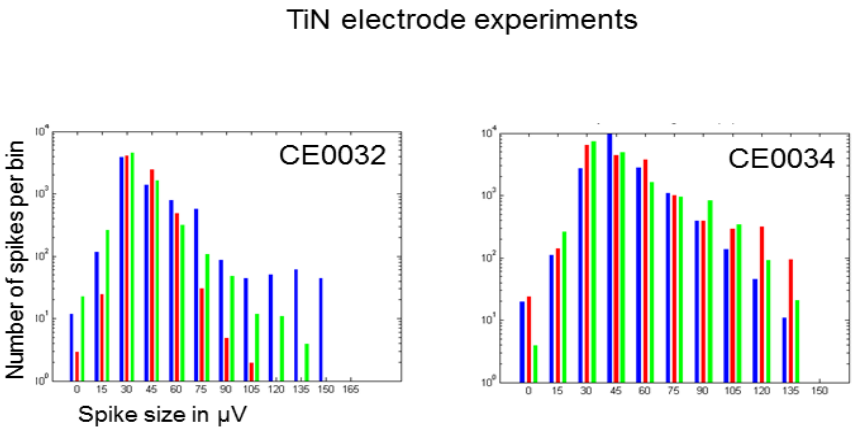

Figure 3.7: TiN spike size histograms. Histograms of spontaneous spike sizes for two TiN experiments (CE0032, CE0034) colour coded by day with Day 1, blue; Day 2, red; Day 3, green. The abscissae represent spike size (µV) and the ordinates represent the number of spikes on a logarithmic scale.

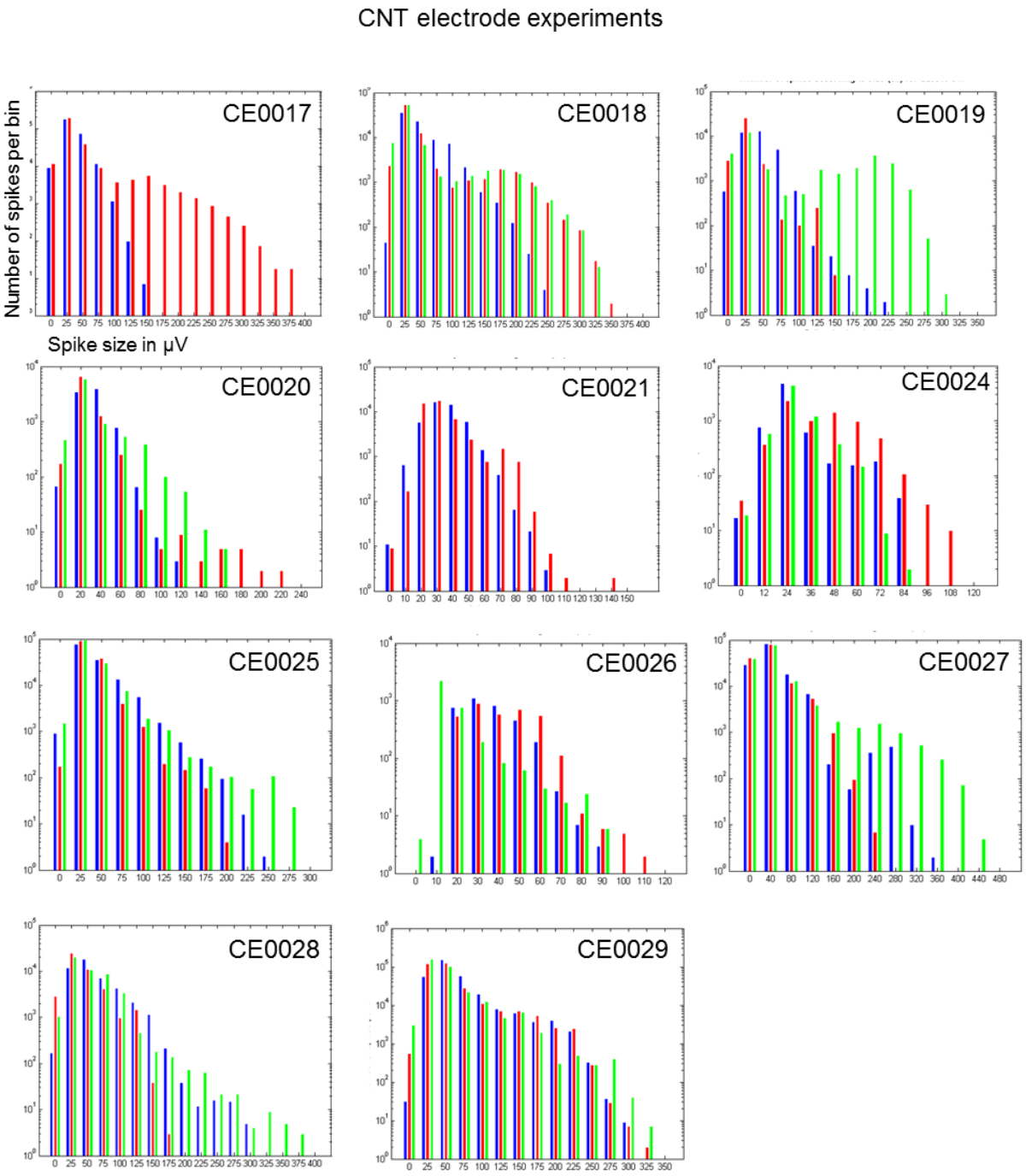

Figure 3.8: CNT spike size histograms. Histograms of spontaneous spike sizes for all CNT experiments (CE0017-CE0029) colour coded by day with Day 1, blue; Day 2, red; Day 3, green. The abscissae represent spike size (µV) and the ordinates represent the number of spikes on a logarithmic scale.

3.3.6 Electrically evoked responses: number of spikes

As described above, fifteen retinas were experimented on over a period of three days, stimulating the same four individual electrodes (for each retina) on each day, generating a theoretical total of 180 stimulation runs. However, some experiments did not yield data for various reasons (artefacts too strong to remove, tissue deterioration on Day 3, human error during experimental procedure) leading to a total of 133 stimulation runs with 109 being CNT and 24 being TiN electrode experiments.

For each stimulation run, a stimulating electrode would stimulate the retina, resulting in RGC action potentials recorded on other electrodes of the MEA (unfortunately, the system does not allow us to record from the stimulating electrode). The total number of different clustered evoked responses for CNT experiments, is 1015, with 327 (32%) on Day 1, 480 (47%) on Day 2 and 208 (20%) on Day 3 (figure 3.9, A). For TiN experiments, the total number of clustered responses is 312, with 113 on Day 1 (36%), 132 (42%) on Day 2 and 67 (22%) on Day 3 (figure 3.9, B). Hence, as in the case of spontaneous oscillations, both types of MEAs display most responses on Day 2 and significantly less on Day 3, with a stronger increase on Day 2 for CNT MEAs.

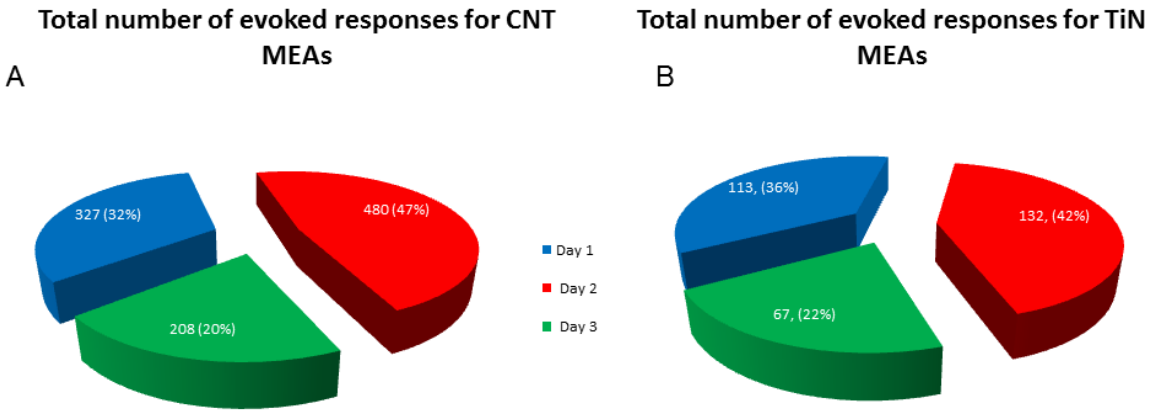

Figure 3.9: Total number of evoked responses. Pie charts displaying the total number of evoked responses on each of the 3 days for CNT (A) and TiN (B) experiments. Colour code: blue, Day 1; red, Day 2; green, Day 3.

Figure 3.10 and 3.11 display the total number of RGCs firing evoked spikes on each day (A) and these values normalised as percentages (B) for experiments performed on CNT and TiN MEAs respectively. The maximum number of stimulus-evoked firing cells in a retina was 190 for CNT MEAs, while it was slightly lower, 163, for both TiN MEAs. Furthermore, the majority of experiments performed with CNT MEAs (63.63%) display a rise in cellular recruitment on Day 2, whilst this was only observed in 50% of experiments performed on TiN MEAs. The results indicate a stronger time-dependent increase in coupling for CNT MEAs than for TiN MEAs. It is worth noting that 20% of experiments performed on CNT MEAs displayed a higher cellular recruitment on Day 3 than on Day 1 and Day 2. This was not observed with TiN MEAs.

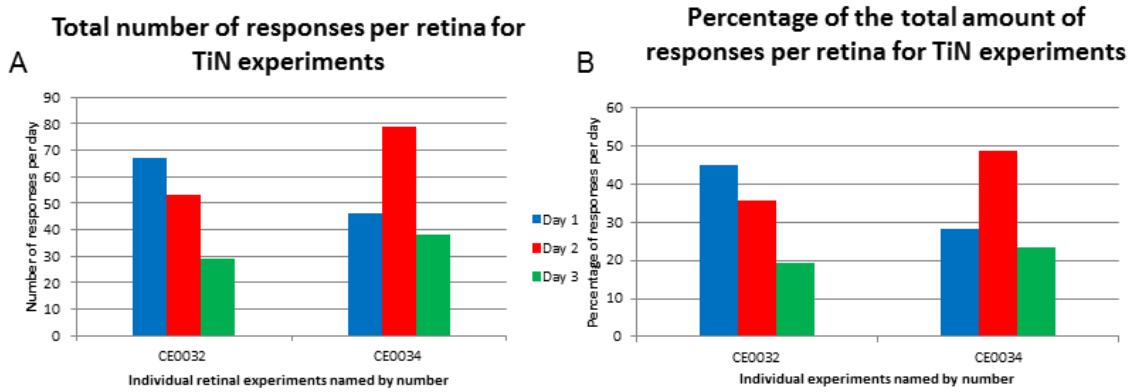

Figure 3.10: Number of responses per retina per day for TiN experiments. A: Column plot displaying the number of responding cells on each day for each retina on TiN MEAs. B: Column plot displaying the percentage of cells (normalised to the value on Day 1) evoked on each day for each retina on TiN MEAs. In both plots, the abscissa display MEA serial numbers. Colour code: blue, Day 1; red, Day 2; green, Day 3.

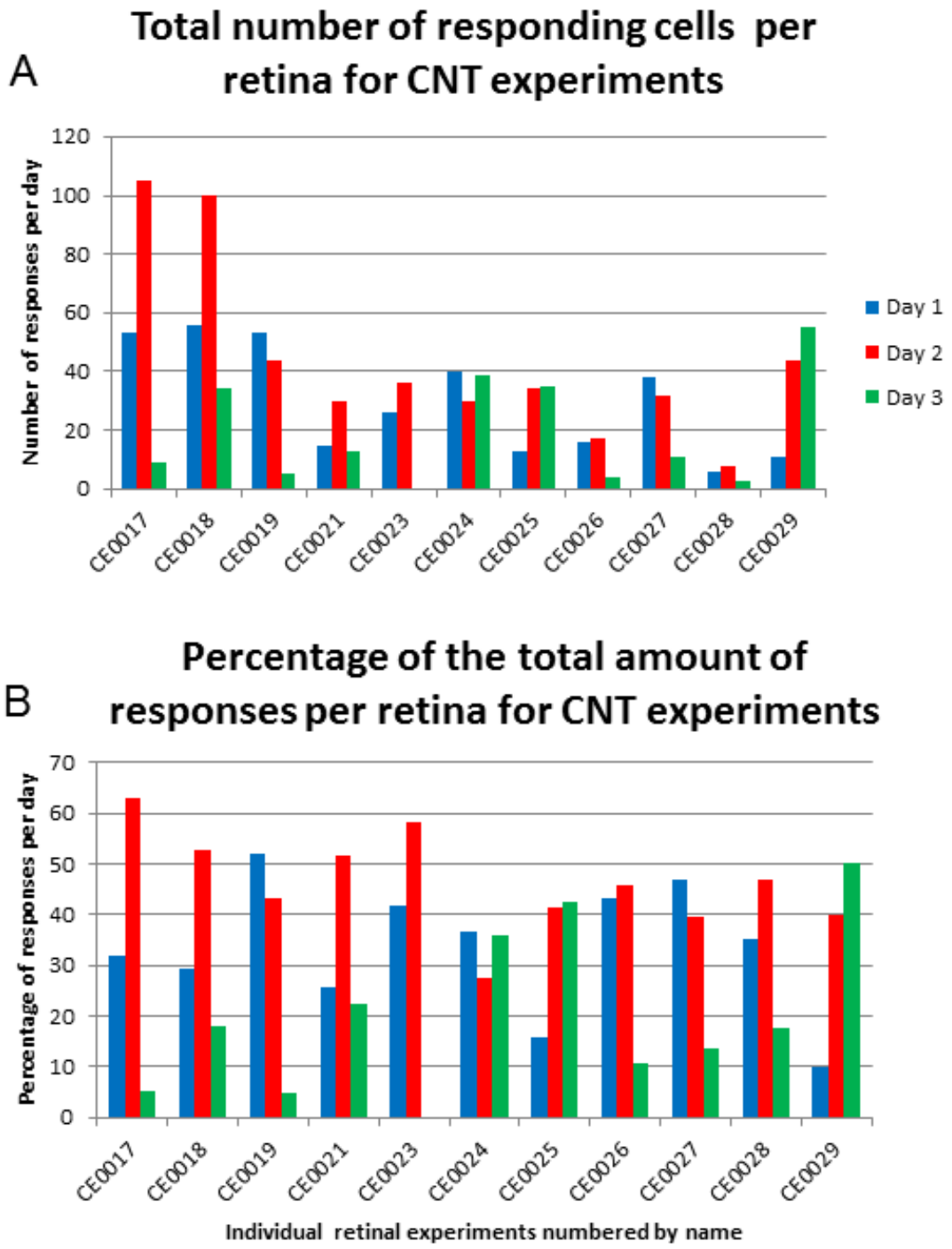

Figure 3.11: Number of responses per retina per day for CNT experiments. A: Column plot displaying the number of responding cells on each day for each retina on CNT MEAs. B: Column plot displaying the percentage of cells (normalised to the value on Day 1) evoked on each day for each retina on CNT MEAs. Graph conventions as for Figure 3.10.

3.3.7 Different types of electrically evoked responses

Evoked responses were identified by their synchronicity and similarity with regards to other responses to the same stimulus condition. Raster plots allow the visualisation of hundreds of trials by stacking them in ascending order of stimulus charge value. Figure 3.12 displays example raster plots of all the different types of responses encountered, with early responses displayed in the left hand side panels and late responses displayed in the panels on the right hand side. These plots show the spike times for all trials conditions (different charge values), 100 ms before and after the stimulus (represented here as a grey vertical line). These plots were used to identify the threshold values for responses as they provide an overall view of all the responses for a single RGC for a particular set of conditions. Electrical stimulation (grey bar at time 0) evoked early (A, C, E, G) or late (B, C, G, D, F) responses which were synchronous (A, B, C, D, G) or not (F, G, H). These responses were expressed as single spikes (A, B, D), double/triple spikes (C), bursts (E), stereotypical trains (G), increased non-synchronised activity (F) or inhibition (H). The examples displayed in C and G show two distinct responses of the same cell (but elicited at different thresholds), one early and one late. These were classed as two distinct responses.

Table 3.1 details all the different responses identified for CNT and TiN experiments whilst figures 3.13 and 3.14 classifies their frequencies in pie charts.

Table 3.1: different responses identified for CNT and TiN experiments

Different Evoked Responses	TiN experiments	CNT experiments
Single synchronised spike	176	490
Single uncoordinated spike	18	149
Single synchronised late spike	13	51
Single uncoordinated late spike	2	12
Increased spike rate	5	32
late increased spike rate	68	86
Uncoordinated burst	7	16
Late uncoordinated burst	3	37
Double synchronised spike	2	20
Inhibition	4	34
Late train	1	1
Total	299	28

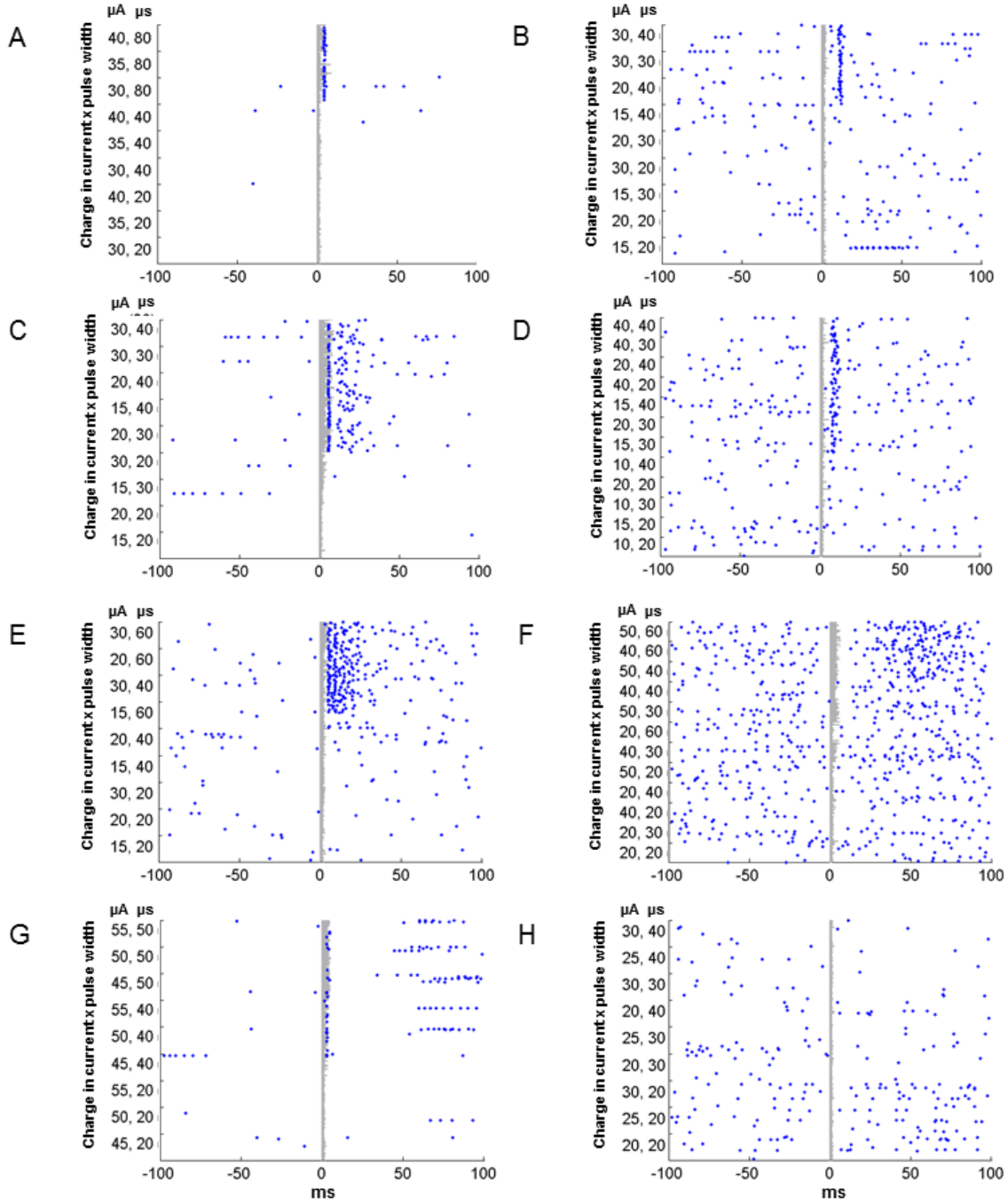

Figure 3.12: Raster plots of different evoked responses. The ordinates represent the amount of charge injected per phase (current intensity in µA, phase duration in µs) and the abscissae represent time (ms). Responses were classified as early (A, C, E, G), late (B, D, G, F), synchronous (A, B, C, D, G) or asynchronous (F, G, H). The abscissae represent time in milliseconds and the ordinates represent the amount of charge injected per phase (current intensity in µA, phase duration in µs, number of conditions per charge value).

For CNT experiments, with regards to post-stimulus delay, 82 % of all responses had short latencies (<10 ms) following electrical stimulation and 17% were classed as late responses (>10 ms following stimulation). Single spikes accounted for 76% of all

responses, double spikes for 3%, bursts (>3 consecutive spikes) for 7%, an increase in the cell firing rate for 12%, an inhibition of the cell firing for 1% and stereotypical trains of spikes (a specifically timed pattern of more than 3 spikes) for 0.1%.

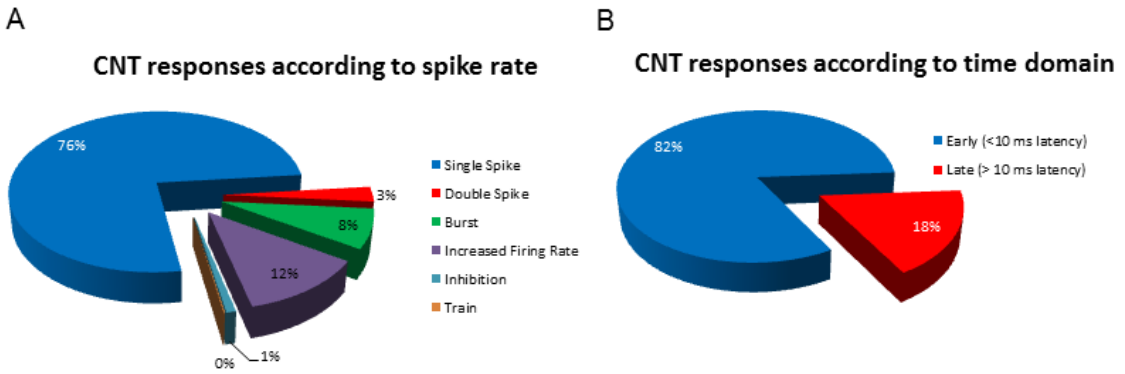

Figure 3.13: Different evoked responses for CNT experiments. A: Pie chart displaying the percentage of responses according to number of spikes. B: Pie chart displaying the percentage of responses according to the time domain in which they occurred.

Firing behaviour was very similar for TiN experiments. With regards to post-stimulus delay, 71% of all responses had short latencies following electrical stimulation (<10 ms) and 29% were classed as late responses (>10 ms following stimulation). Single spikes accounted for 70 % of all responses, double spikes for 1%, bursts (> than 3 consecutive spikes) for 3%, an increase in the cell firing rate for 25%, inhibition of the cell firing for 1% and trains of spikes (a specifically timed pattern of over 3 spikes) for 0.1%. Essentially, the differences highlighted here are an increase in indirect responses, with more late responses and increases in firing rate.

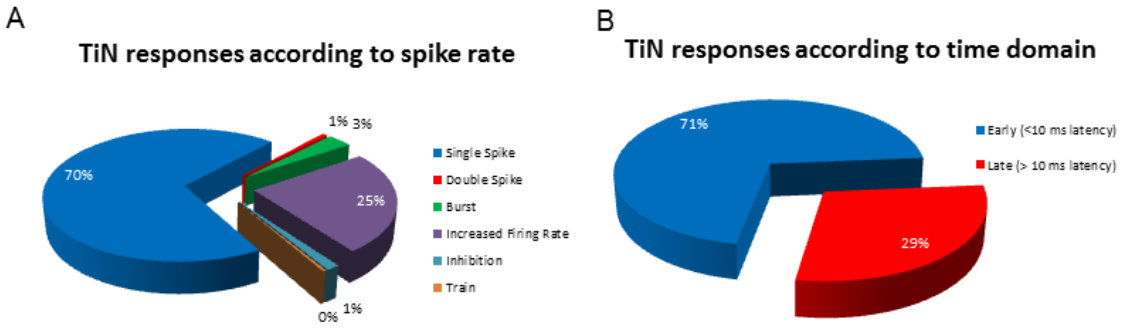

Figure 3.14: Different evoked responses for TiN experiments. A: Pie chart displaying the percentage of responses according to number of spikes. B: Pie chart displaying the percentage of responses according to the time domain in which they occurred.

3.3.8 Electrically evoked responses: effect of stimulation parameters

As mentioned in the Methods section of this chapter (figure 3.2), different conditions for a given amount of charge injected varied in two fundamentally distinct ways: polarity (positive phase first or negative phase first) and waveform (r = 1, 0.5 or 2). Figure 3.18 displays a summary of the parameters that evoked a response with the lowest charge injected (i.e. threshold) as a percentage of the total amount of responses for both CNT and TiN experiments.

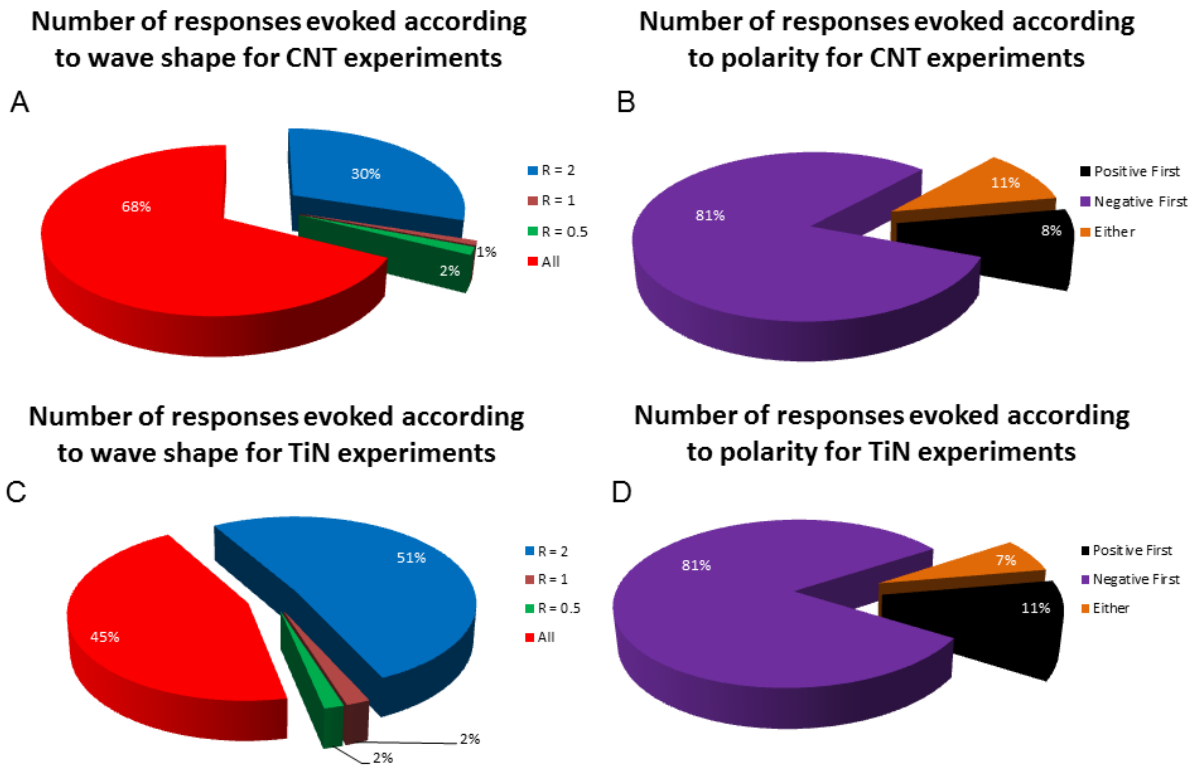

Figure 3.15: Number of responses according to different stimulation parameters. Pie charts outlining the preferred stimulation parameters for electrical stimulation with CNT (A, B) or TiN (C, D) electrodes. The optimal parameters according to waveform (A, C) included different ratios where r = 2 (blue), r = 0.5 (green), r = 1 (pink) or when the shape did not exert an influence on threshold (red). The optimal parameters according to polarity (B, D) varied according to whether the first phase was negative (purple), positive (black) or whether the polarity did not affect threshold (orange).

When considering waveform for stimulation by CNT electrodes, 68% of all responses did not display any preference whilst 30% preferred a waveform where r =2, 1% where r = 1 and 2% where r = 0.5. Stimulation by TiN experiments show a higher sensitivity to waveform with 51% of responses having lower thresholds when using R = 2 but similar values for r = 1 and 0.5.

When considering polarity, both types of electrodes evoked lower thresholds when the pulse had a negative first phase first (81% of all responses). However, slightly fewer cells stimulated with CNT electrodes (8%) had a preference for positive-phase first stimuli than cells stimulated with TiN electrodes (11%).

3.3.9 Electrically evoked responses: stimulation thresholds

A stimulation threshold is the minimum amount of charge required to evoke a response to electrical stimulation of a defined charge in 50% of the trials. With the framework of an epi-retinal prosthetic device in mind, direct stimulation of RGCs is considered to be the ideal scenario. However, very short latency spikes (<2ms) cannot be identified due to the large artefact introduced by the electrical stimuli in our system. *In vitro* studies in mammalian retinas reveal that most directly evoked spikes are followed by another spike 5-7 ms later (Sekirnjak, Hottowy et al. 2006), which is consistent with the intrinsic firing properties of RGCs (Devries and Baylor 1997).

Our system does not offer the possibility to record responses of cells coupled with the stimulating electrodes. Hence, the closest distance between stimulating and recording electrode is limited by the electrode pitch, which is 200 µm in our arrays. A smaller electrode pitch would mean a lower charge to elicit a response, thus a smaller artefact as well as the possibility of observing one RGC response over multiple electrodes (Sekirnjak, Hulse et al. 2009). Therefore, we have to make a number of assumptions concerning the responses we observe. Firstly, that action potentials recorded by an electrode correspond to the activity of RGCs in the vicinity of that electrode. Secondly, that late responses (occurring over 10 ms after the stimulus) correspond to cells indirectly activated through synaptic pathways. Thirdly, that a transient decrease in activity corresponds to synaptic inhibition. Consequently, the responses to stimulation observed here have been classified as either being direct (single spikes or bursts occurring within 10 ms of stimulation) or indirect (activity occurring 10 ms after stimulation, a decrease in the cell's activity or asynchronous spiking).

Table 3.2 displays all the average threshold values (in nC) obtained each day over all experiments, subdivided according to whether they correspond to direct or indirect

responses. The rest of the chapter investigates these values in detail, down to individual recording electrodes with the first part dedicated to direct thresholds and the second part dedicated to indirect thresholds.

Table 3.2: Average threshold values (in nC) for all cells according to the electrode material, response type and number of days *in vitro*.

	Direct (<10 ms latency)		**Indirect (>10 ms latency)**	
	CNT Threshold (nC) ±SEM, n	**TiN** Threshold (nC) ±SEM, n	**CNT** Threshold (nC) ±SEM, n	**TiN** Threshold (nC) ±SEM, n
Day 1	1.83 ±0.04, 241	1.95 ±0.06, 83	2.23 ±0.08, 81	1.49 ±0.05, 48
Day 2	1.50 ±0.03, 389	1.78 ±0.06, 96	1.63 ±0.07, 116	1.59 ±0.08, 45
Day 3	1.35 ±0.05, 156	2.02 ±0.09, 50	1.49 ±0.09, 75	1.79 ±0.14, 20

3.3.10 Electrically evoked responses: direct response thresholds

In the following section, we investigate the direct threshold value as it evolves over three days of stimulation *in-vitro*. As there is variability in the quality of the coupling between retinas and MEAs, it is important to make a distinction between average thresholds and the values obtained for each recording electrode for every experiment.

Direct response thresholds for individual recording electrodes

The firing threshold value of individual RGCs cells is identified and followed in time according to their location on the MEA (e.g. electrode location) and according to their action potential waveform signature. For the 15 retinas investigated in this study, the direct responses of 161 cells were tracked between Day 1 and Day 2 and only 100 cells could be tracked between Day 2 and Day 3 as well. Variations in the threshold value (vT) were calculated as percentages using the following formula

$$vT = (-(T1-T2)/T1)*100$$

with T1 corresponding to the threshold on the first day and T2 corresponding to the threshold on the second day. Figure 3.28 shows an example of a cell which has been tracked over three days on a CNT electrode. The cell was identified according to its electrode location, response pattern (raster plots, top row) and waveform (spike traces, bottom row). In this example, the increase in coupling between cell and electrode is characterised by an increase in spike size and a decrease in threshold. On Day 1, the threshold value is 2.25 nC and the average peak-to-peak spike size is 32 µV. On Day 2, the threshold is 1.88 nC and the average peak-to-peak spike size is 41 µV. On Day 3 the threshold is 1.6 nC and the average peak-to-peak spike size is 58 µV. This cell did not display any spontaneous bursting on either of the days.

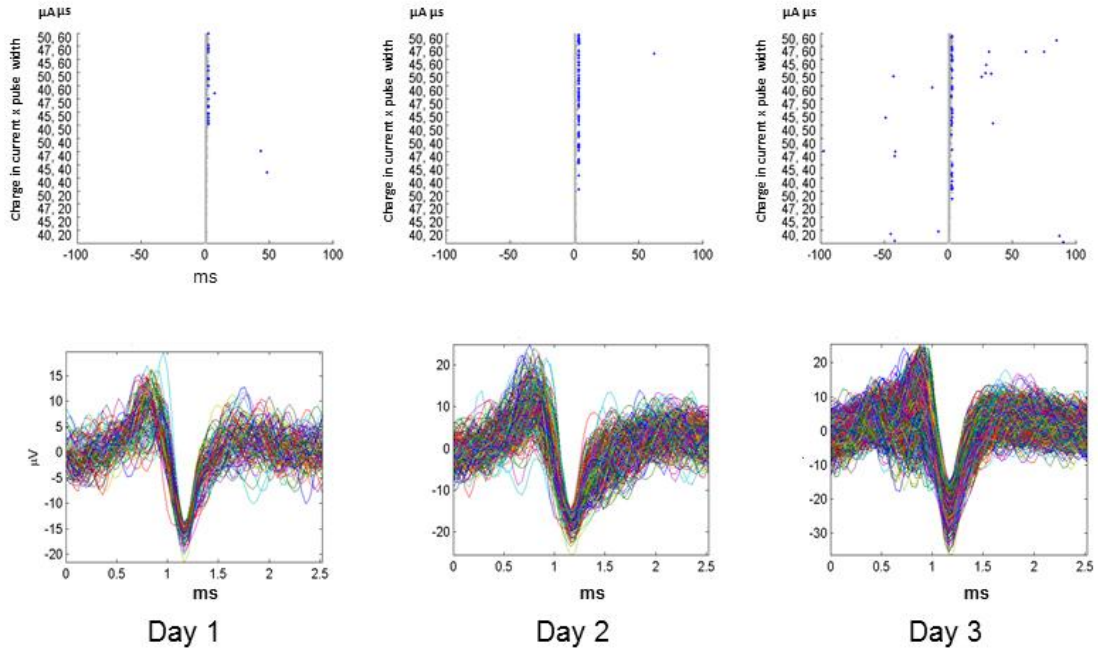

Figure 3.16: Example of direct response tracked over 3 days. Raster plots (top row) and associated Wave_Clus spike traces (bottom row) of a cell tracked over three days outlining the decrease in threshold and increase in spike size. For raster plots, the abscissa represent time (ms) and the ordinates represent the amount of charge injected per phase (current intensity in µA, phase duration in µs, number of trials per condition). For spike traces, the abscissa represent time in ms and the ordinates represent voltage in µV.

For CNT experiments (figure 3.17), the direct threshold values of 123 cells were tracked over Day 1 and Day 2 whereas those of 70 cells were tracked over Day 2 and Day 3. Between Day 1 and Day 2, 43% of cells showed a decrease (of 34.18% on average) in threshold. 37% of cells had a further decrease (of 30.02% on average) between Day 2 and Day 3. Fewer cells (27%) had a 40% increase in threshold between

Day 1 and Day 2; and 14% had a 61.30% increase in threshold between Day 2 and Day 3.

For TiN experiments (figure 3.18), the direct threshold values of 32 cells were tracked over Day 1 and Day 2 whereas those of 30 cells were tracked over Day 2 and Day 3. Between Day 1 and Day 2, 61% of cells showed a decrease (of 33. % on average) in threshold. 25% of cells had a decrease (of 24% on average) between Day 2 and Day 3. Fewer cells (17%) had a 43% increase in threshold between Day 2 and Day 1; and 31% had a 70% increase in threshold between Day 2 and Day 3.

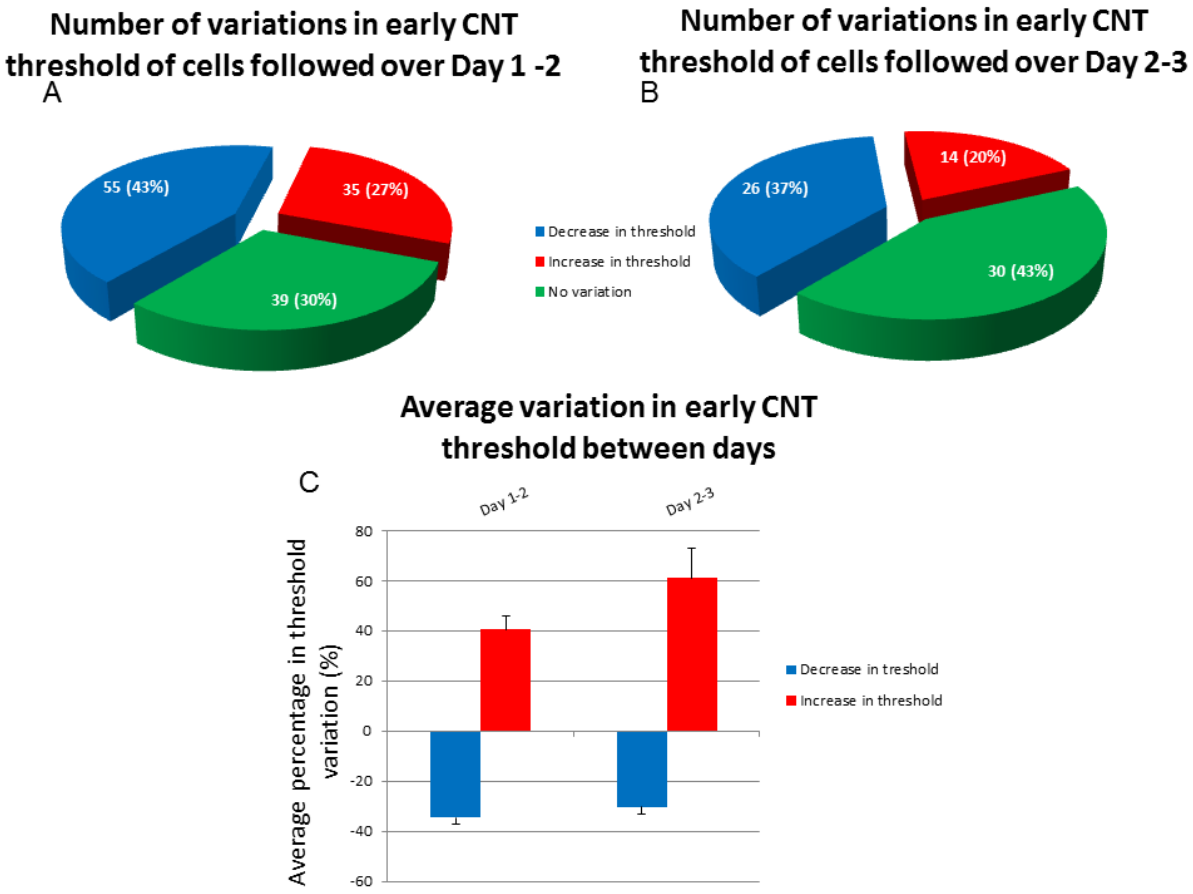

Figure 3.17: Changes in number and thresholds of direct responses for CNT experiments. A: Number of cells showing changes in threshold between Day 1 and Day 2. B: Number of cells showing changes in threshold between Day 2 and Day 3. C: Average change in threshold as a percentage of the value on Day 1. Colour code: blue, decrease; red, increase; green, no change. Error bars: SEM.

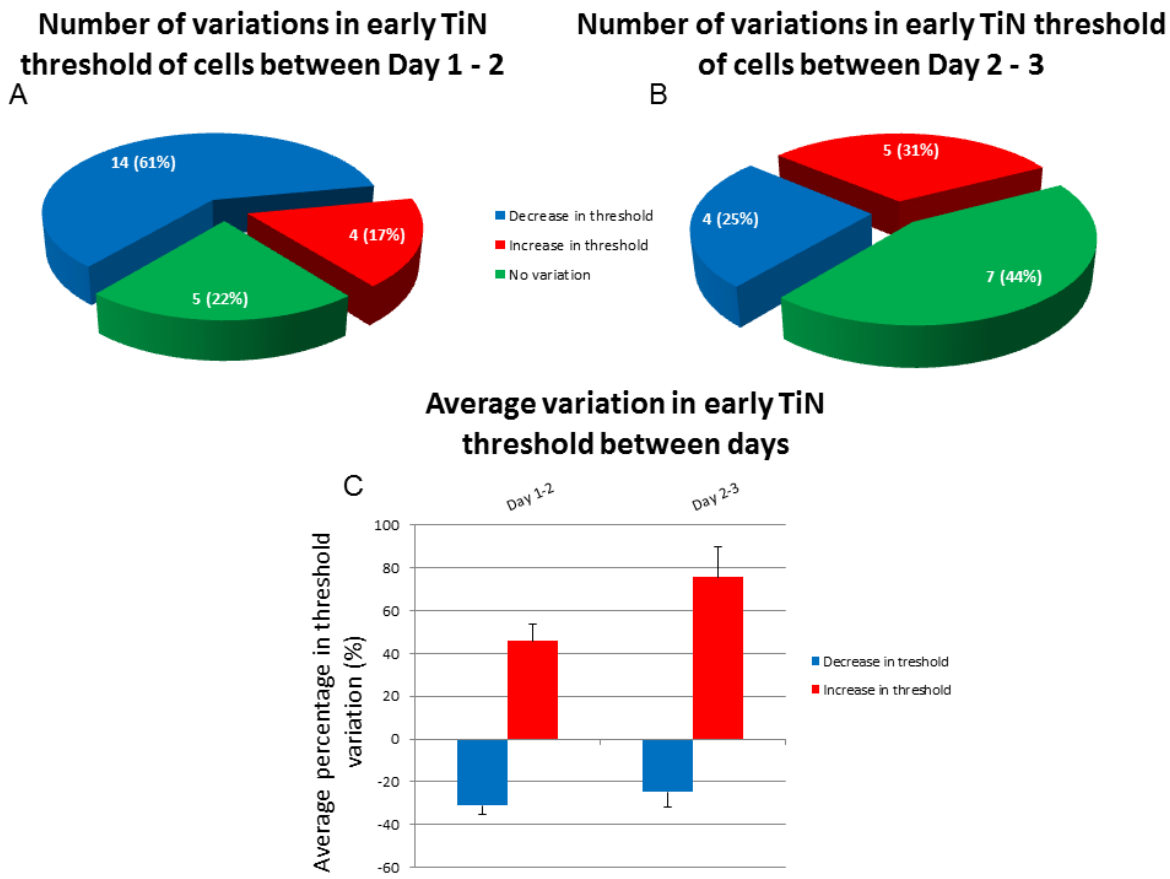

Figure 3.18: Changes in number and thresholds of direct responses for TiN experiments. A: Number of cells showing changes in threshold between Day 1 and Day 2. B: Number of cells showing changes in threshold between Day 2 and Day 3. C: Average change in threshold as a percentage of the value on Day 1. Colour code: blue, decrease; red, increase; green, no change. Error bars: SEM.

Pooled direct response thresholds

For CNT electrodes, direct stimulation thresholds calculated over 3 days were 1.56±0.02 nC. These values were significantly higher for TiN electrodes; 1.89±0.04 nC ($P \leq 0.001$, Mann-Whitney rank sum t-test).

The total number of early responses to electrical stimulation is 786 for CNT electrodes, with 241 (31%) on Day 1, 389 (49%) on Day 2 and 156 (20%) on Day 3 (figure 3.19, A). For TiN electrodes, the total number of early responses is 229, with 83 (36%) on Day 1, 96 (42%) on Day 2 and 50 (22%) on Day 3 (figure 3.19, C).

In CNT experiments, the mean value for all thresholds decreased consistently over three days of experimentation (figure 3.19, B) from 1.83 nC on Day 1 to 1.55 nC on Day

2 and 1.35 nC for Day 3. The differences between these values are significant ($P \leq 0.001$, Kruskal-Wallis one way ANOVA on ranks).

In TiN experiments, the mean value for all thresholds did not decrease significantly (figure 3.19, D) with the average value for Day 1 corresponding to 1.95 nC, 1.78 nC for Day 2 and 2.02 nC for Day 3 ($P = 0.069$, Kruskal-Wallis one way ANOVA on ranks).

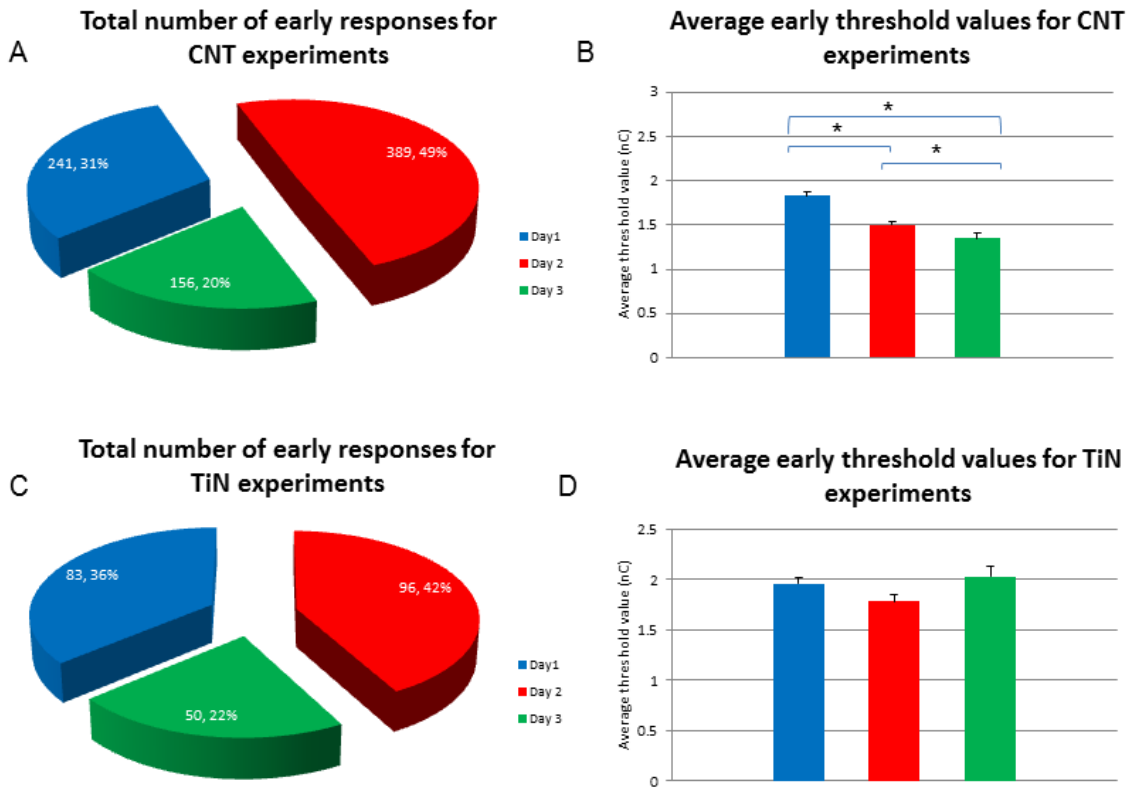

Figure 3.19: Pooled number of direct responses and average threshold values. A, C: The total number of direct responses are shown as pie charts for CNT experiments (A) and TiN experiments (C). B, D: Column plots of average direct thresholds for CNT (B) and TiN (D) experiments. Colour code: blue, Day 1; red, Day 2; green, Day 3. Error bars: S.E.M. Asterisks: statistical significance.

Direct response thresholds per retina

Each isolated retina is a separate entity subject to biological variability. Here, we investigate the threshold values as an average of all the responses obtained for all four

stimulation electrodes in an individual retina and how this value varies over three days *in vitro*.

Figure 3.20 illustrates column plots of average number of responses (A, C) and threshold values (B, D) for CNT (A, B) and TiN (C, D) electrodes. For both types of electrode, the highest and lowest numbers of responses obtained per retina were Day 2 and Day 3, respectively. The difference between the number of responses obtained on Day 2 and Day 3 was statistically significant for CNT electrodes (P = 0.024, one way repeated measures ANOVA and Tukey test) but not for TiN electrodes (P = 0.50, one way repeated measures ANOVA and Tukey test). For CNT electrodes, the threshold values diminished gradually with time without any statistical significance (P = 0.175, one way repeated measures ANOVA). For thresholds obtained with TiN electrodes, the average value per retina decreased on Day 2 before increasing on Day 3 with no significant difference (P = 0.067, Kruskal-Wallis one way ANOVA).

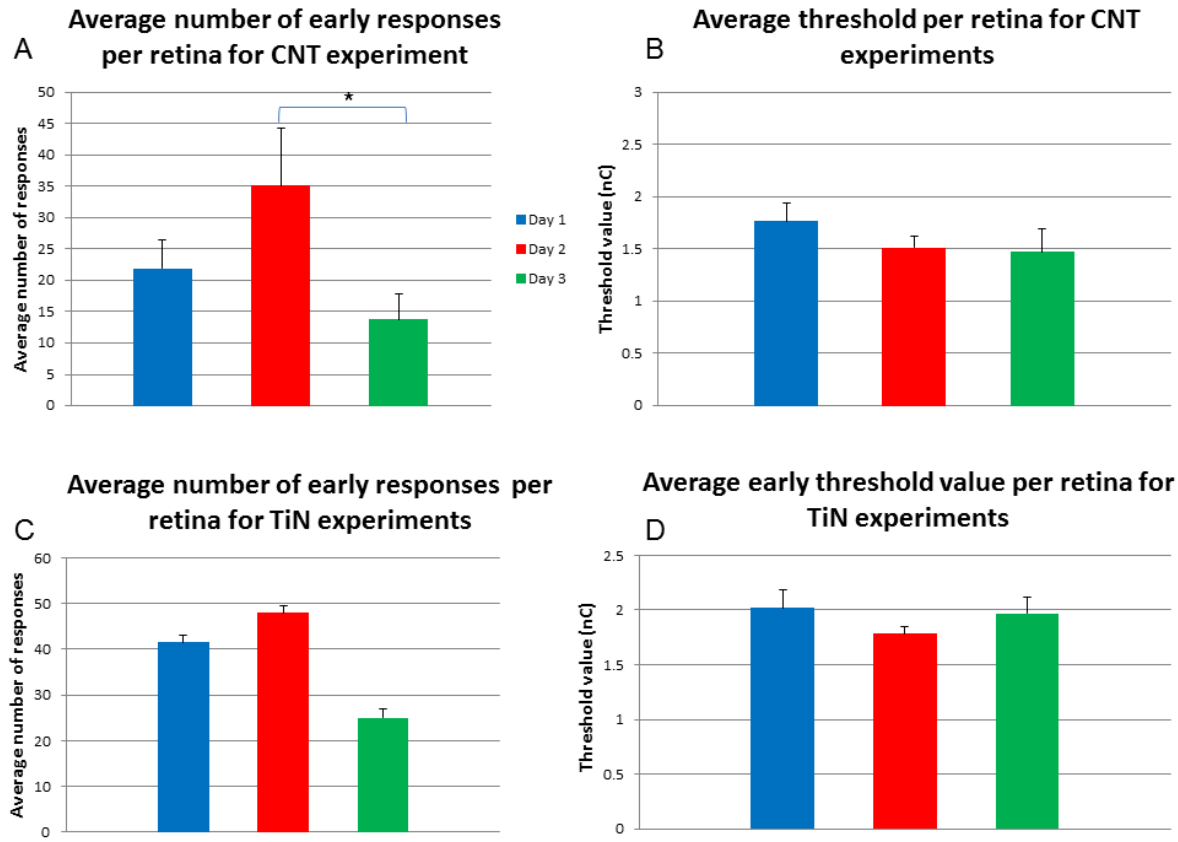

Figure 3.20: Average number of direct responses and thresholds per retina. Column plots of average number of responses (A, C) and thresholds (B, D) for CNT (A, B) and TiN (C, D) electrodes colour-coded according to days (Day 1, blue; Day 2, red; Day 3, green). Error bars: SEM. Asterisk: statistical significance.

For CNT experiments, the number of direct responses obtained for each retina is displayed in figure 3.21 with values ranging from 5 to 45 on Day 1, 5 to 98 on Day 2 and 2 to 37 on day 3. In most cases (72%), Day 2 yielded more responses than Day 1. In 70% of cases, Day 2 yielded more responses than Day 3 and Day 1 yielded more responses than Day 3 (figure 3.22, A).

There is also high variability in the thresholds within and between days, with values ranging from 0.9 to 2.05 on Day 1, 0.92 to 2.26 on Day 2 and 0.8 to 3.33 on Day 3 (figure 3.21, B). The prevalence is that most RGCs have lower thresholds on Day 2 and higher thresholds on Day 3 (figure 3.22, B). Although 75% of all experiments indicate that RGCs have lower thresholds on Day 2 than Day 1, only 6 out of 12 retinas show a statistically significant difference. Of these, 3 show Day 2 average thresholds to be lower than Day 1, 2 that Day 2 thresholds are lower than Day 3 and three that Day 3 thresholds are lower than Day 1. Statistical tests were Kruskal-Wallis one way ANOVAs except for CE0021 which did not have values for Day 3 (Mann-Whitney rank sum t-test). $P \leq 0.001$ for CE0017 and CE0018; $P = 0.126$ for CE0019; $P = 0.022$ for CE0020; $P = 0.246$ for CE0021; $P = 0.022$ for CE0024; $P = 0.392$ for CE0025; $P = 0.01$ for CE0026; $P = 0.006$ for CE0027; $P = 0.181$ for CE0028; $P = 0.671$ for CE0029).

In an effort to summarize these results, figure 3.22 displays the incidence of retinas showing an increase (red) or decrease (blue) for a particular day of stimulation (white text). For example, the first column in figure 3.22 A compares the number of retinas showing an increase in number of responses between Day 1 and Day 2. 72% of retinas showed more responses on Day 2 when only 27% of retinas showed more responses on Day 1.

Similar values are shown for the experiments performed with TiN electrodes in figure 3.23. Both experiments show a similar number of direct responses and only one shows an increase in the number of responses on Day 2. There is no significant change for the stimulation thresholds between days. $P = 0.669$ for CE0032 and $p = 0.678$ for CE0034, Kruskal-Wallis one way ANOVA.

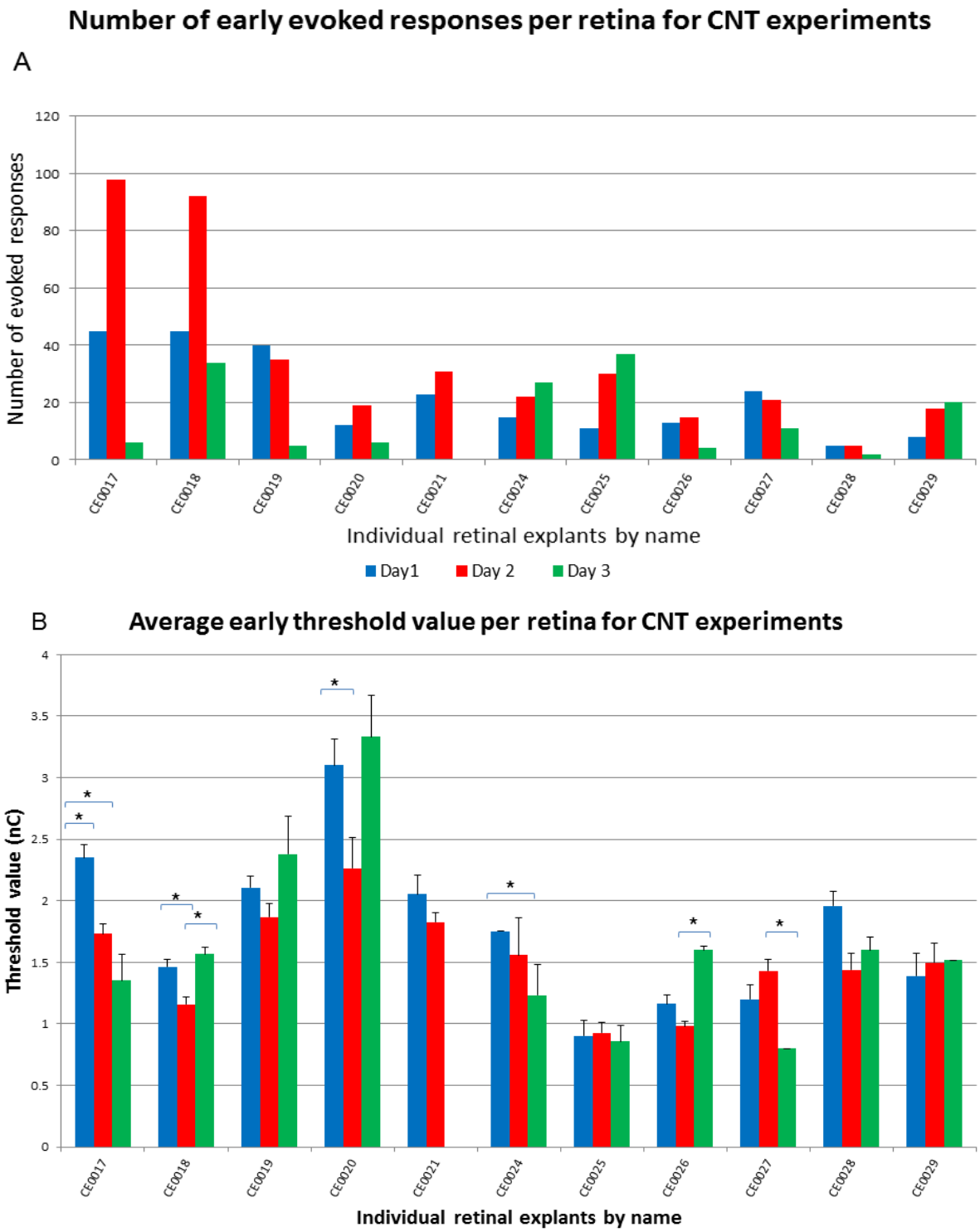

Figure 3.21: Average number of direct responses and thresholds for each retina on CNT electrodes. Column plots of total number of responses (A) and average thresholds (B) for CNT electrodes colour-coded according to days (Day 1, blue; Day 2, red; Day 3, green). Error bars: SEM. Asterisks: statistical significance.

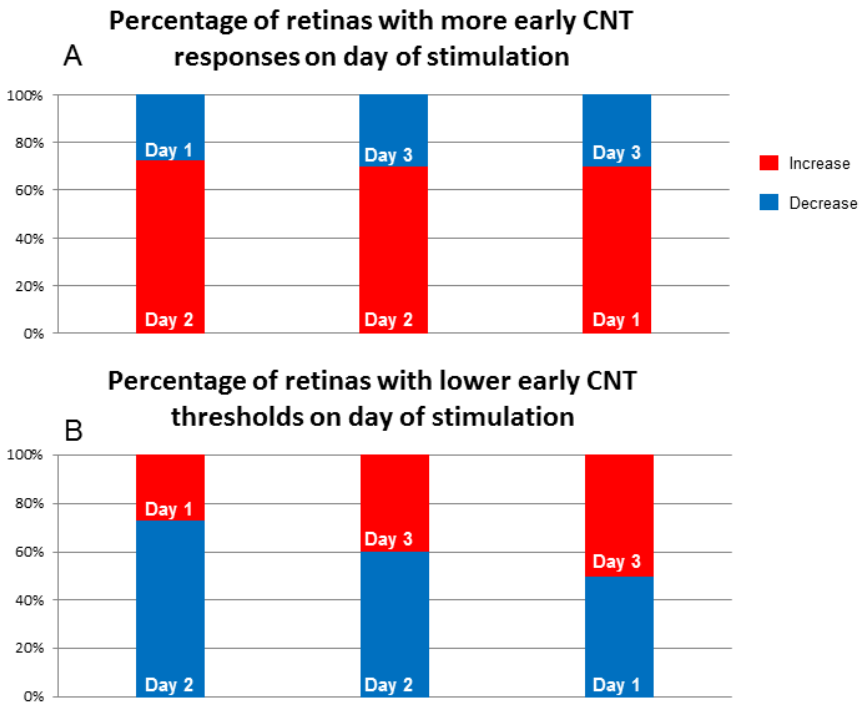

Figure 3.22: Incidence of direct responses and their threshold differences over days. Incidence of direct responses (A) and their threshold differences (B) over days (white text) is shown as blocks with the percentage of the number of retinas showing an increase (red) or decrease (blue) in the relevant value.

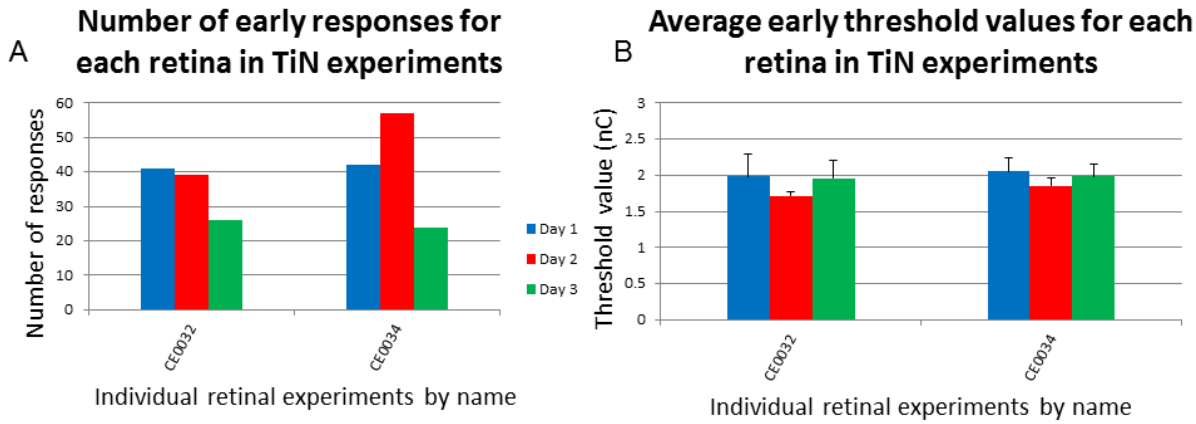

Figure 3.23: Average number of direct responses and thresholds for each retina for TiN electrodes. Column plots of total number of responses (A) and average thresholds (B) for TiN electrodes colour-coded according to days (Day 1, blue; Day 2, red; Day 3, green). Error bars: SEM.

3.3.11 Electrically evoked responses: indirect response thresholds

Indirect response thresholds for individual recording electrodes

Figure 3.24 shows an example of a cell which has been tracked over three days during a CNT experiment. The cell was identified according to its location, response pattern (raster plots, top row) and waveform (spike traces, bottom row). In this example, there is variation in the threshold value, a decrease in spike size and a change in firing rate. On Day 1, the threshold value is 1.2 nC and the average peak-to-peak spike size is 78 µV. On Day 2, the threshold is 0.8 nC and the average peak-to-peak spike size is 56 µV. On Day 3 the threshold is 0.9 nC and the average peak-to-peak spike size is 44 µV. On Day 3, there is a decrease in spontaneous firing and an increase in evoked firing.

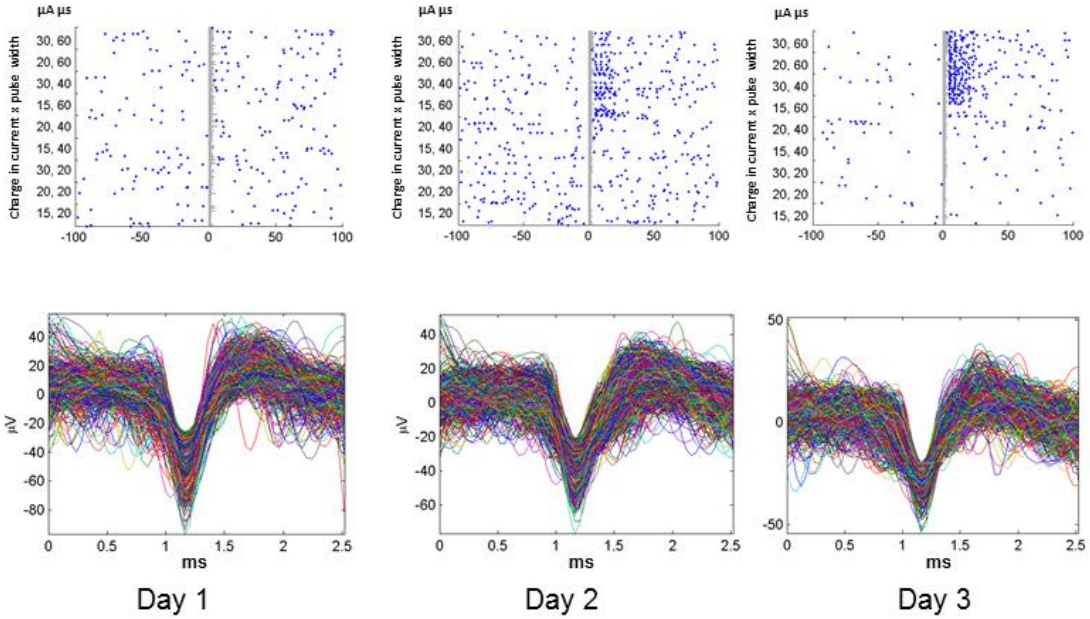

Figure 3.24: Example of indirect response tracked over 3 days. Raster plots (top row) and associated Wave_Clus spike traces (bottom row) of a cell tracked over three days highlighting a decrease in spike size but an increase in frequency. For raster plots, the abscissa represent time (ms) and the ordinates represent the amount of charge injected per phase (current intensity in µA, phase duration in µs, number of trials per condition). For spike traces, the abscissa represent time in ms and the ordinates represent voltage in µV.

For CNT experiments (figure 3.25), the indirect threshold values of 23 cells were tracked over Day 1 and Day 2; those of 16 cells over Day 2 and Day 3. Between Day 1 and Day 2, 50% of cells showed a 33% decrease in threshold. A further 50% of cells displayed a 24% decrease in threshold between Day 2 and Day 3. Fewer cells (14%) had

a 45% increase in threshold between Day 2 and Day 1; and 35% had a 75% increase in threshold between Day 2 and Day 3.

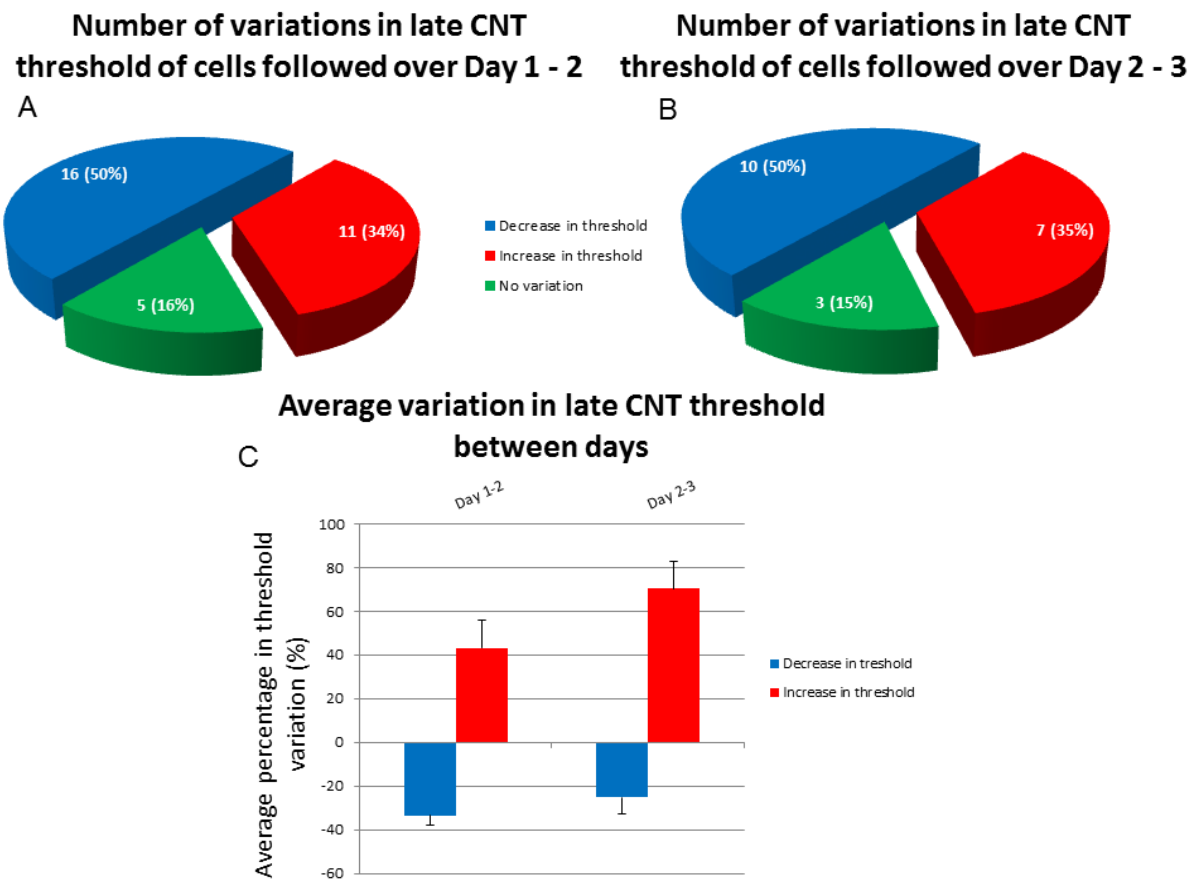

Figure 3.25: Changes in number and thresholds of indirect responses for CNT experiments. A: Number of cells showing changes in threshold between Day 1 and Day 2. B: Number of cells showing changes in threshold between Day 2 and Day 3. C: Average change in threshold as a percentage of the value on Day 1. Colour code: blue, decrease; red, increase; green, no change.

For TiN experiments (figure 3.26), indirect threshold values of 19 cells were tracked over Day 1 and Day 2; those of 10 over Day 2 and Day 3. Between Day 1 and Day 2, 48% of cells showed 38% decrease in threshold. A further 25% of these cells had an additional 42% decrease between Day 2 and Day 3. Fewer cells (34%) had a 24% increase in threshold between Day 2 and Day 1; and 35% had a 97% increase in threshold between Day 2 and Day 3.

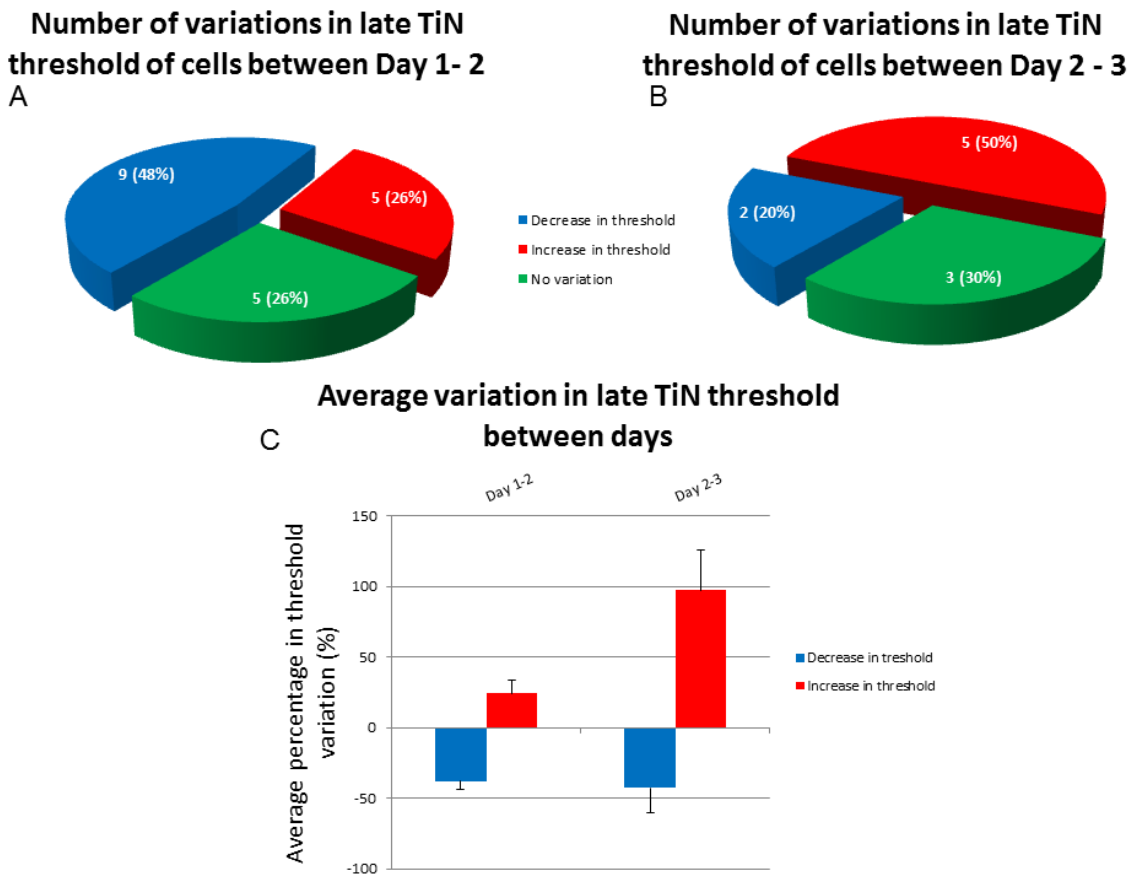

Figure 3.26: Changes in number and thresholds of indirect responses for TiN experiments. A: Number of cells showing changes in threshold between Day 1 and Day 2. B: Number of cells showing changes in threshold between Day 2 and Day 3. C: Average change in threshold as a percentage of the value on Day 1. Colour code: blue, decrease; red, increase; green, no change.

Pooled indirect response thresholds

The average value for late stimulation thresholds over all 3 days was not significantly different between CNT (1.59 ±0.04 nC) and TiN (1.59 ±0.04) electrodes (P = 0.198, Mann-Whitney rank sum t-test).

The total number of different clustered indirect evoked action potential responses for CNT experiments is 172, with 81 (30%) on Day 1, 116 (43%) on Day 2 and 75 (20%) on Day 3 (figure 3.27, A). For TiN experiments, the total number of clustered responses is 111, with 48 (42%) on Day 1, 45 (43%) on Day 2 and 20 (18%) on Day 3 (figure 3.27, C).

In CNT experiments, the mean value for all late thresholds decreased gradually yet insignificantly over three days of experimentation (figure 3.27, B) from 2.23 to 1.63

and 1.49 nC for Day 1, 2 and 3 respectively (P = 0.220, Kruskal-Wallis one way ANOVA on ranks). In TiN experiments, the mean value for all late thresholds increased gradually yet insignificantly (figure 3.27, D) from 1.49 to 1.59 and 1.79 nC for Day 1, 2 and 3 respectively (P = 0.084, Kruskal-Wallis one way ANOVA on ranks).

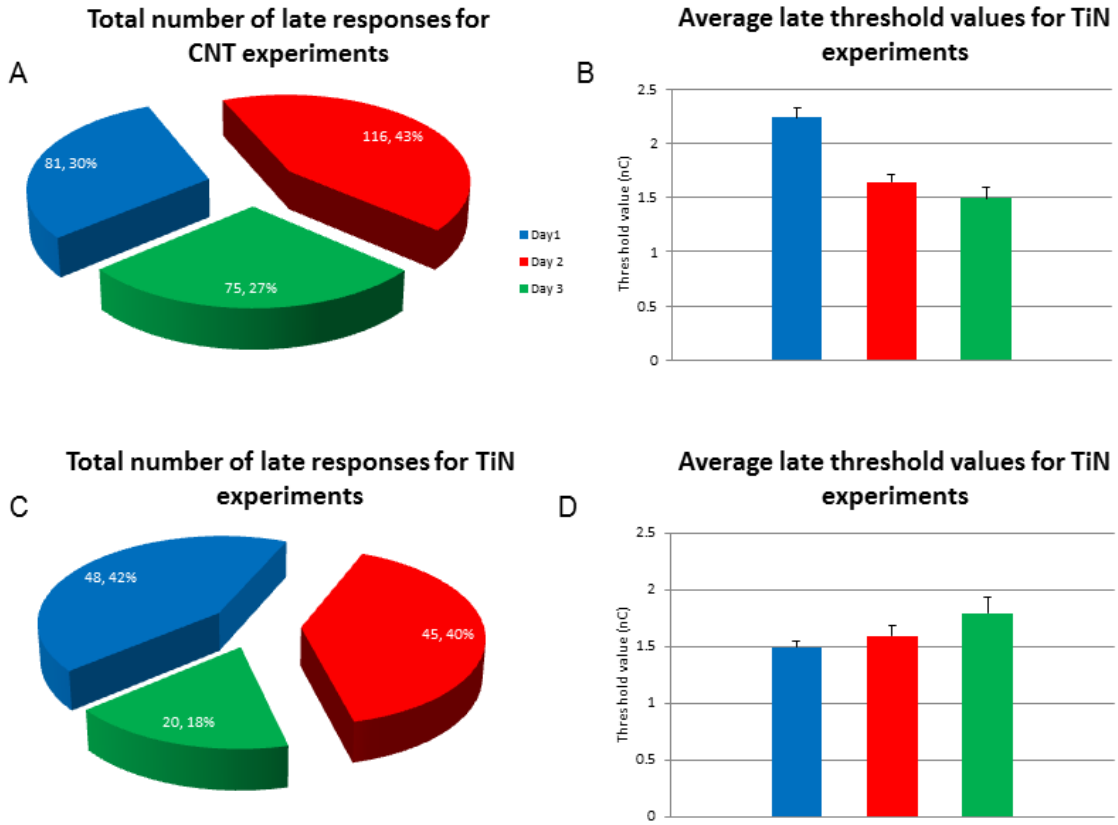

Figure 3.27: Pooled number of late responses and average threshold values. A, C: The total number of indirect responses are shown as pie charts for CNT experiments (A) and TiN experiments (C). B, D: Column plots of average direct thresholds for CNT (B) and TiN (D) experiments. Colour code: blue, Day 1; red, Day 2; green, Day 3. Error bars: S.E.M.

Indirect response thresholds per retina

Figure 3.28 illustrates column plots of average number of responses (A, C) and threshold values (B, D) for CNT (A, B) and TiN (C, D) electrodes. For CNT electrodes, the highest and lowest values (number of responses and threshold) obtained per retina were Day 2 and Day 3, respectively. (P = 0.167, one way repeated measures ANOVA). For TiN electrodes, the average number of responses decreased with time (with a dramatic decrease between Days 2 and 3) conversely to the average threshold value

which increased with time. None of these values were significantly different within each set of measurements. The corresponding p values per plot are 0.584 (A), 0.202 (B), 0.500 (C) and 0. 833 (D), Friedman repeated measures ANOVA on ranks.

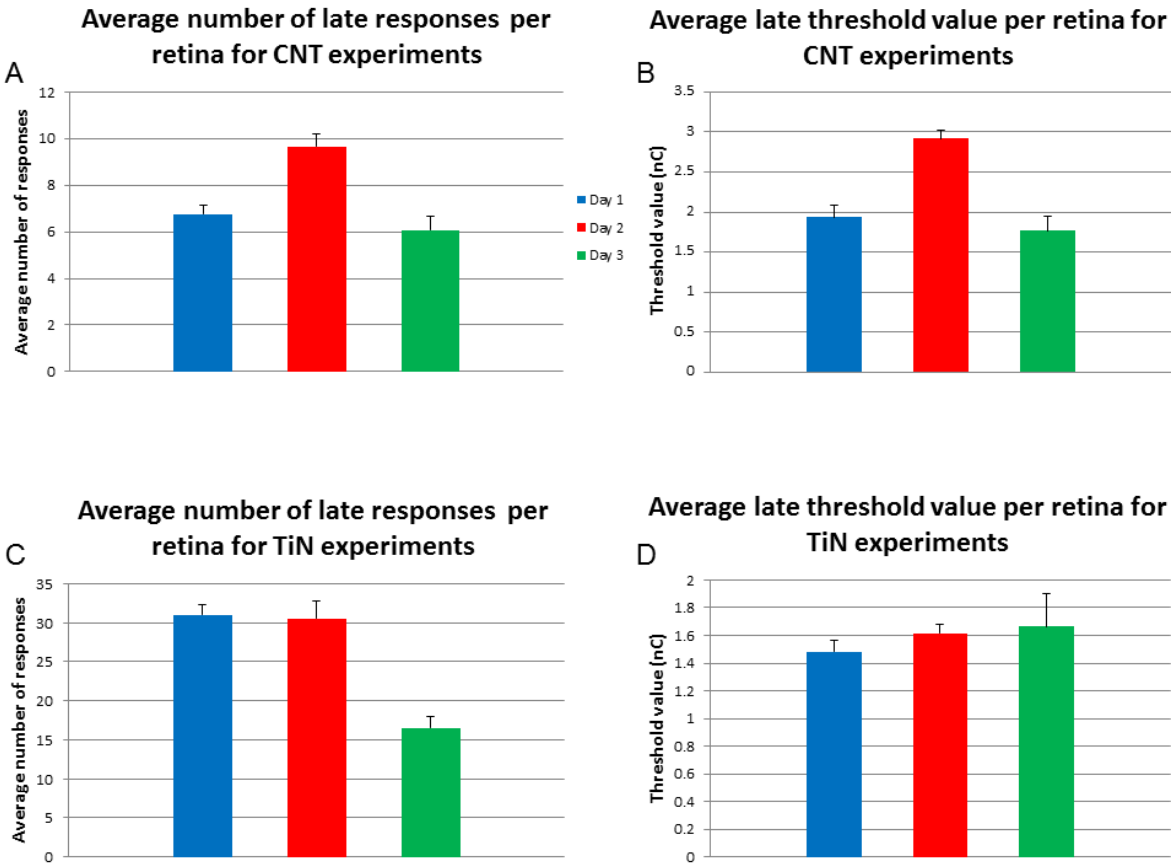

Figure 3.28: Average number of late responses and thresholds per retina. Column plots of average number of responses (A, C) and thresholds (B, D) for CNT (A, B) and TiN (C, D) electrodes, colour-coded according to days (Day 1, blue; Day 2, red; Day 3, green). Error bars: SEM.

For CNT experiments, the number of late responses obtained for each retina is displayed in figure 3.30 with values ranging from 2 to 16 on Day 1, 1 to 27 on Day 2 and 1 to 35 on Day 3. In most cases (75%), Day 2 yielded more responses than Day 3. In 58% of cases, Day 2 yielded more responses than Day 1 and Day 1 yielded more responses than Day 3. As is the variability in the number of responses for this set of samples, so is the variability in the thresholds between days (figure 3.29, B) with average values ranging from 0.52 to 3.1 on Day 1, 0.6 to 2.08 on Day 2 and 0.6 to 3.35 on Day 3. For each retina, none of the values obtained between days had a statistically significant difference. Kruskal-Wallis one way ANOVAs except for CE0017, CE0021,

CE0022, CE0024, CE0026 and CE0028 which did not have enough responses on each day to perform any statistical tests. The p values for the other experiments are given as p = 0.507 (CE0018), 0.773 (CE0019), 0.263 (CE0020), 0.181 (CE0025), 0.322 (CE0027) and 0.061 (CE0029).

Similar values are shown for the experiments performed with TiN electrodes in figure 3.29. Although both experiments show a similar number of indirect responses, only one shows an increase in the number of responses for Day 2. For both experiments there was no significant change in threshold on Day 2. P = 0.325 for CE0032 and 0.271 for CE0034, Kruskal-Wallis one way ANOVA.

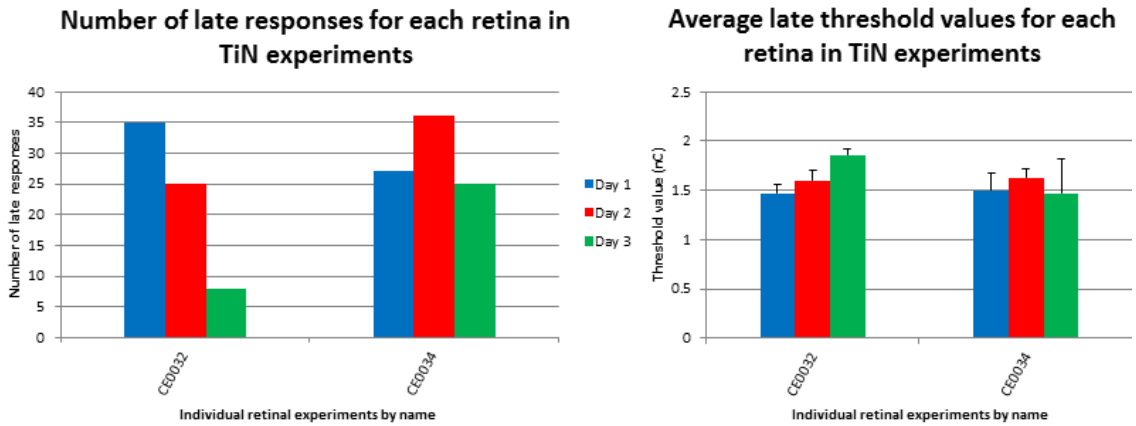

Figure 3.29: Average number of late responses and thresholds for each retina for TiN electrodes. Column plots of total number of responses (A) and average thresholds (B) for TiN electrodes colour-coded according to days (Day 1, blue; Day 2, red; Day 3, green). Error bars: S.E.M.

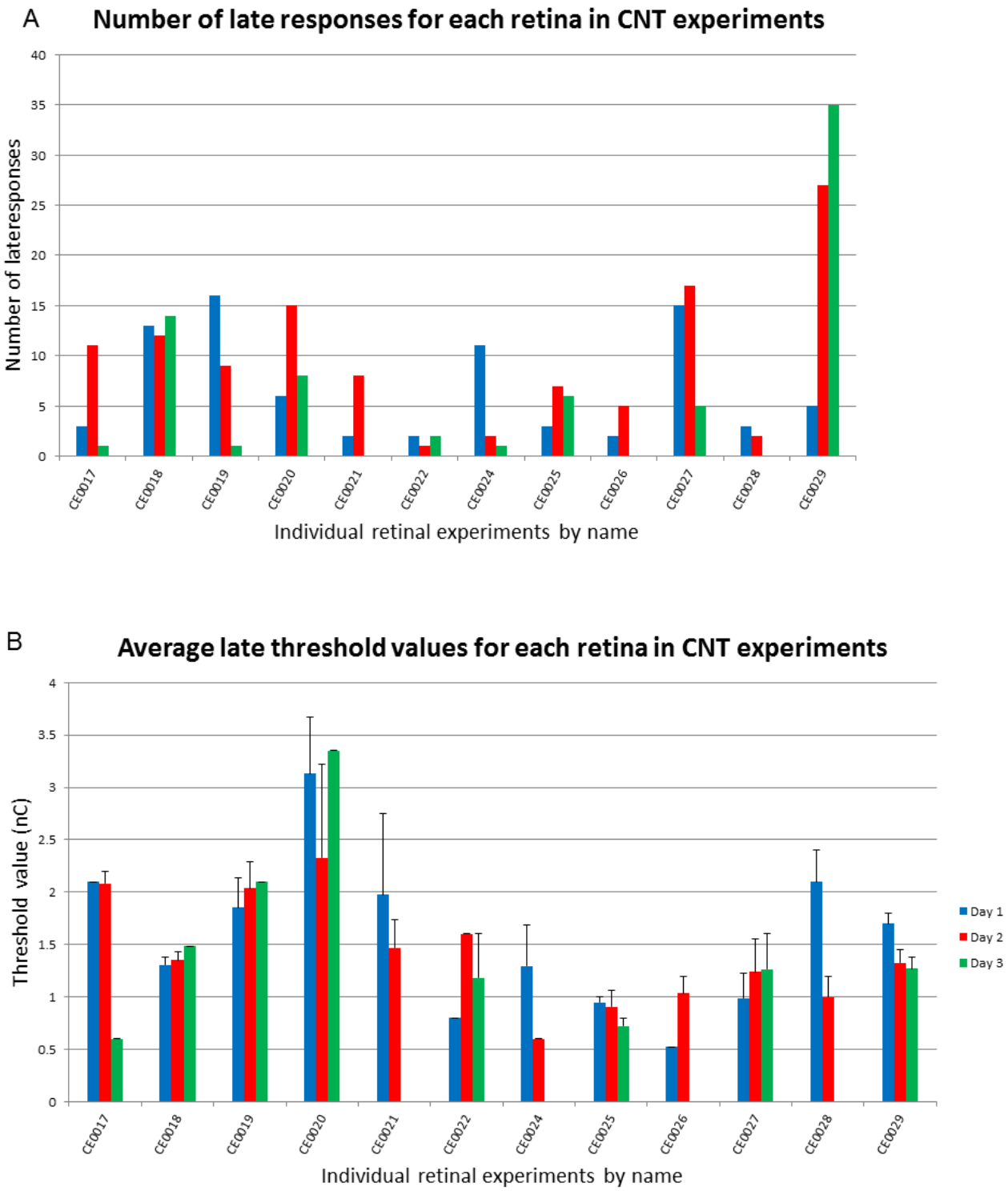

Figure 3.30: Average number of late responses and thresholds for each retina using CNT electrodes. Column plots of total number of responses (A) and average thresholds (B) for CNT electrodes, colour-coded according to days (Day 1, blue; Day 2, red; Day 3, green). Error bars: S.E.M.

3.4 Discussion

3.4.1 Electrophysiological evidence of time-dependent coupling for CNT electrodes

This chapter has presented an indication from electrophysiological evidence that coupling between CNT electrodes and the retina increases with time. The first line of evidence stems from spontaneous activity recordings showing a time-dependent increase in signal-to-noise ratio. Indeed, CNT electrodes recorded larger spontaneous spikes on Day 2 and Day 3 than on Day 1. Such time-dependent increase in signal amplitude was not observed on TiN electrodes. Further, cellular recruitment of directly activated RGCs was much higher on Day 2 than Day 1 for CNT electrodes but only slightly higher for TiN electrodes. Cellular recruitment of indirectly activated RGCs was higher on Day 2 than Day 1 for CNT electrodes but lower for TiN electrodes. Cellular recruitment of both direct and indirect evoked responses were lower with both types of electrodes on Day 3, which can be accounted for by the state of the tissue's health after so much time *in vitro* (discussed below). An increase in signal amplitude is an indication of the quality of the coupling between the retinal tissue and the recording electrode, as the propagation of such signals through resistive biological tissue is attenuated with increasing distance between the two.

Our data also indicates a time-dependent decrease in direct and indirect thresholds when stimulating with CNT electrodes. The average direct threshold values were consistently and significantly lower on Day 3 than on Day 2 and Day 1 as well as lower on Day 2 than on Day 1 (*cf.* section 1.3.3.1). Conversely, this phenomenon was not observed with TiN electrodes and even inverted in the case of thresholds for indirectly evoked responses. These results indicate that smaller amounts of current are required to depolarise RGCs past their firing threshold as the resistivity of the ILM-CNT electrode interface decreases with time, suggesting that the retina becomes gradually more intimately coupled to the CNTs.

The data collected here is consistent with the results obtained in a previous study (Shoval, Adams et al. 2009). In that research paper, the authors observed a time-dependent increase in coupling for CNT MEAs and thoroughly investigated the spike

size and associated spiking probability over an hour, a time frame which we have managed to multiply 48 fold. The technical difficulties associated with keeping spiking physiologically stable retinal explants (discussed in chapter 2) were detrimental to our aim, making results obtained on Day 3 inconsistent and untrustworthy.

The group led by Micha Spira in Jerusalem provided evidence of a substantial increase in coupling following the partial engulfment of electrodes by different types of dissociated cells in culture. In the initial study (Spira, Kamber et al. 2007), they coated mushroom-shaped gold electrodes (1.56 µm height, 1.84 µm peak diameter and 850 nm at the base) with a phagocytosis promoting peptide which later allowed the recording, stimulation and investigating the kinetics of electroporation of *Aplysia* neurons (Hai, Dormann et al. 2009; Hai, Shappir et al. 2010; Hai and Spira 2012). When coating the electrodes with standard ECM proteins such as laminin and Poly-L-Lysine, individual *cells* would still partially engulf the electrodes, but not to the same extent as with the engulfment promoting peptide, although the electrophysiological characteristics did not differ significantly (Hai, Dormann et al. 2009). After culturing mammalian hippocampal cells (Fendyur, Mazurski et al. 2011) and cardiomyocytes (Fendyur and Spira 2012) onto these electrodes, the group realised that standard ECM proteins where preferential for these types of cells; the engulfment promoting peptide causing cells to aggregate and eventually collapsing the network.

This highlights the notion that the size, shape, texture and coating of individual electrodes is of great importance to the interfacing of such devices with neural tissue. In the case of the retina, the target neurons are protected by a negatively charged basement membrane (the ILM) and surrounded by collateral tissue (Müller cells, astrocytes, glial scars, blood vessels). An ideal epi-retinal electrode would penetrate the ILM, pass the glial cells without provoking unspecific reactive gliosis and promote intimate contact with RGCs.

3.4.2 Health of tissue by the third day

Preparations on both TiN and CNT MEAs showed a decline in the percentage of active and oscillating channels on the third day *in-vitro* (*cf.* sections 3.3.2 and 3.3.3).

Moreover, cellular recruitment analysis (*cf.* sections 3.3.6, 3.3.10 and 3.3.11) consistently revealed significantly fewer evoked responses on Day 3. Furthermore, TiN electrode experiments revealed higher thresholds for both direct and indirect responses (*cf.* sections 3.3.10 and 3.3.11) although without any statistical significance. These results suggest an increase in resistivity between tissue and electrode which could be due to astroglial scarring in response to the presence of the electrodes at the ILM (Edell, Toi et al. 1992; Turner, Shain et al. 1999; Cui, Wiler et al. 2003). However, TiN experiments showed no trend in the spike size analysis, which is inconsistent with this theory as recordings on Day 3 would show smaller amplitude action potentials (*cf.* section 3.3.5). Experiments with CNT electrodes revealed larger amplitude spikes on both Day 2 and Day 3, which further discredits this theory. CNT electrode experiments showed lower firing thresholds on Day 3 for both direct and indirect responses (*cf.* sections 3.3.10 and 3.3.11), although only the values for the direct response thresholds were significant. This data is incompatible with the hypothesis of a glial scar at the tissue electrode interface as an increased resistivity would lead to higher direct threshold values and smaller amplitude spikes on Day 3. Another possible explanation is metabolic stress leading to reduced synaptic transmission, caused by lack of neurotransmitter precursors or ionic pump failure, resulting in the collapse of ionic gradients and membrane potentials.

Loss of activity in the remodelled INL of these degenerated retinas (*cf.* Chapter 1) would account for these results. Indeed, the oscillations observed in the extracellular field are a combination of the activity of every single excitable membrane in the vicinity (Buzsaki, Anastassiou et al. 2012), from slow astrocytic calcium waves to vigorous bursting of RGCs and activity in BCs and ACs. As activity from these cells decreases with metabolic stress, rhythmic LFPs will disappear. Metabolic stress would also affect RGCs, leading to a lower cellular recruitment. Fewer active BCs and ACs in the INL would lead to fewer indirect responses and higher indirect thresholds as these cells provide the pre-synaptic drive for indirect activation.

As in all *in vitro* preparations, our method of retinal isolation is a very harsh process in which the optic nerve is severed and relatively large parts (given the size of murine retinas) of the retina are sheared, leaving the tissue open to a plethora of noxious

responses mediated by Müller cells, astrocytes, microglia and the RGCs themselves. Indeed, some of the mechanisms involved in RGC apoptosis are neurotrophin deprivation (neurotrophins delivered from the brain via retrograde transport along RGC axons) (Eggers and Lukasiewicz 2011), astrocytic synthesised nitric oxide (Neufeld 1999), elimination of severed neurons by microglia (Thanos, Mey et al. 1993) and cytokine secretion by Müller cells following retinal detachment (Nakazawa, Matsubara et al. 2006). Nevertheless, our *submerged* system is very proficient, allowing us to observe spontaneous electrophysiological activity for up to five days by protecting retinal cells from anoxia (*cf.* Chapter 2).

In order to rule out the possibility of glial scarring in response to the presence of CNT assemblies, the retinas were fixed in PFA and stained for GFAP (discussed in Chapter 2). In retrospect, it might have been ideal to section the retinas into 4 lobes, use the lobe placed on electrodes for GFAP labelling (as performed in this study) and probe the remaining lobes for apoptotic cells and markers of metabolic stress.

As discussed in the previous chapter, physiologically stable incubation of adult vascularised retinas over extended periods is challenging. Although a number of research groups have developed systems in which morphology and anatomy are uncorrupted for weeks on end, electrophysiological signals seem to disappear after a day or two. The use of an interphase culture system in which medium was constantly agitated below retinas held on culture inserts allowed the recording of electrophysiological signals from rabbit (un-vascularised retina) and rat (vascularised retina) RGCs. In the rabbit retina, where transport of glucose and oxygen is achieved by diffusion through the choroid (Ames, Li et al. 1992), MEA recordings confirmed the presence of RGC populations after 3 days *in vitro* while patch clamp recordings confirmed electrophysiological measurements after 6 days *in vitro* (Koizumi, Zeck et al. 2007). In the rat retina, patch clamp and trans-field recordings confirmed electrophysiological activity after 4 days *in vitro* (Koizumi and Jouhou 2009). The fundamental advantage of our technique is the steady perfusion of carboxygenated aCSF, without recycling, which evacuates noxious secretions from the tissue.

3.4.3 Indirect responses

In section 3.3.9, we defined synaptically driven (indirect) responses as those occurring at least 10 ms after the stimulation, leading to firing suppression or producing spikes that are not time-locked to the stimulus. In healthy adult mammalian retinas, BCs and ACs connect to RGCs in the IPL. RGCs in turn project to brain visual areas (*cf.* Chapter 1). However, retinas with photoreceptor degeneration undergo severe remodelling (Jones, Watt et al. 2003; Jones and Marc 2005) characterised by RGCs migrating away from the GCL, ACs and BCs migrating to the GCL and synaptic terminals being subject to fascicular rewiring. Thus, epi-retinal electrical stimulation of CRX -/- retinas at an advanced stage of degeneration is likely to directly activate neurons synapsing onto RGCs as well, giving rise to complex late responses in RGCs.

As described in section 3.3.7, there are fewer indirect responses than direct responses, 18% of all responses for CNT electrodes and 29% for TiN electrodes. Also, the threshold value for indirect responses is significantly lower than for direct responses for TiN electrodes ($p \leq 0.001$), but not for CNT electrodes ($p = 0.979$) although the average threshold value for direct responses is significantly lower with CNT electrodes than with TiN electrodes (*cf.* section 1.3.3.1 and figure 3.41; $p \leq 0.001$). Figure 3.41 demonstrates that the average direct threshold value obtained for every experiment on every day for TiN electrodes is significantly larger than for late thresholds ($p < 0.001$, Mann-Whitney rank sum t-test). In addition, direct threshold values for CNT electrodes are significantly lower than for TiN electrodes ($p < 0.001$, Mann-Whitney rank sum t-test). These complementary data suggest that the epi-retinal activation of RGCs by CNT electrodes requires less current than the activation of retinal interneurons. This corroborates findings using calcium imaging and patch clamp recordings in isolated retinas (Margalit, Babai et al. 2011).

In support, there is a time-dependent decrease in threshold values for direct RGC activation with CNT electrodes (*cf.* section 3.3.10) but not for indirect RGC activation (*cf.* section 3.3.11). Indeed, more RGCs are being directly activated, with lower charge on Day 2 and Day 3, but the same number of interneurons (on average) is being activated with the same charge (on average). Time-dependent morphological changes in the retina induced by the shape, topography and material composition of electrodes

may account for the ease with which RGCs are excited after *in-vitro* interfacing, an important issue that will be addressed in Chapter 4. For example, planar CNT electrodes do not penetrate deep enough within the tissue to reach most interneurons. Hence, the effect is more pronounced on direct responses.

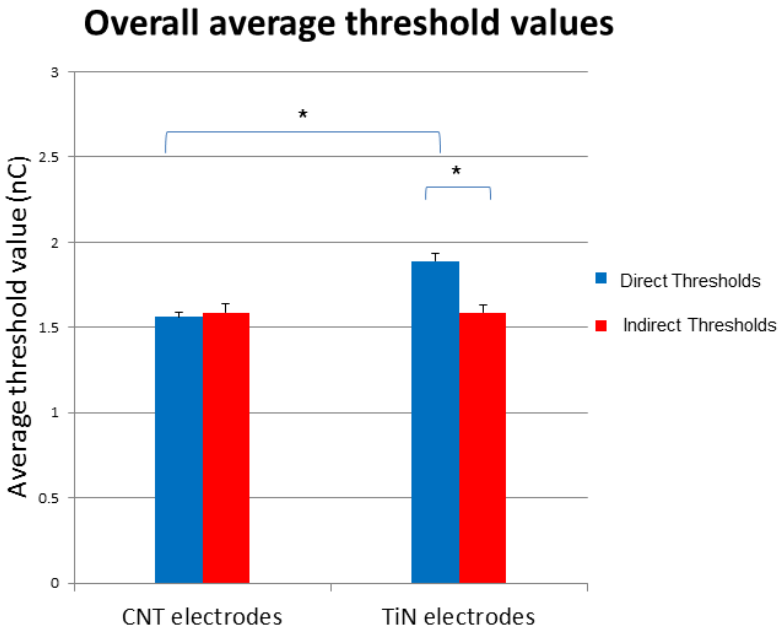

Figure 3.31: Pooled average threshold values of direct and indirect RGC activation obtained with CNT and TiN electrodes. Column plots displaying average threshold values for CNT and TiN MEAs when comparing direct to indirect responses. Colour code: blue, direct threshold; red, indirect threshold. Error bars: S.E.M. Asterisks: statistical significance.

3.4.4 Stimulation parameters

Data acquired using both TiN and CNT electrodes indicate that a cathodic phase first stimulus is more likely to elicit a response in RGCs. Our analysis of the stimulus waveform shows that the R2 shape, where the duration of the second phase is double that of the first and the current intensity of the first phase is double that of the second yielded lower thresholds in 30% and 51% of the responses for CNT and TiN electrodes respectively. This indicates that had we used cathodic first R2 waveforms only, we would have obtained the lowest possible thresholds for 98% of the CNT evoked responses and 96% of the TiN evoked responses.

Recent work in the field has revealed that pulse width is one of the characteristics most likely to affect the shape of the excitation area within retinal tissue, allowing for

more targeted stimulation of RGCs, irrespective of the electrode size (Jensen, Rizzo et al. 2003; Jensen, Ziv et al. 2005; Behrend, Ahuja et al. 2011). Further interpretation of our results indicates that stimulation pulses with the R2 shape yielded similar types of responses as those seen with all different stimulus waveforms, with a preference for single direct spikes. Figure 3.32 displays a set of pie charts indicating the number of responses to R2 stimulation according to spike rate and time-domain. When comparing figure 3.32 to figures 3.13 and 3.14, we notice a higher percentage of single spikes (7 percentage points increase for CNT and 6 for TiN electrodes), a reduction in the percentage of bursts (3 percentage points decrease for CNT and 1 for TiN electrodes) and an increase of 6 percentage points for direct responses on TiN electrodes.

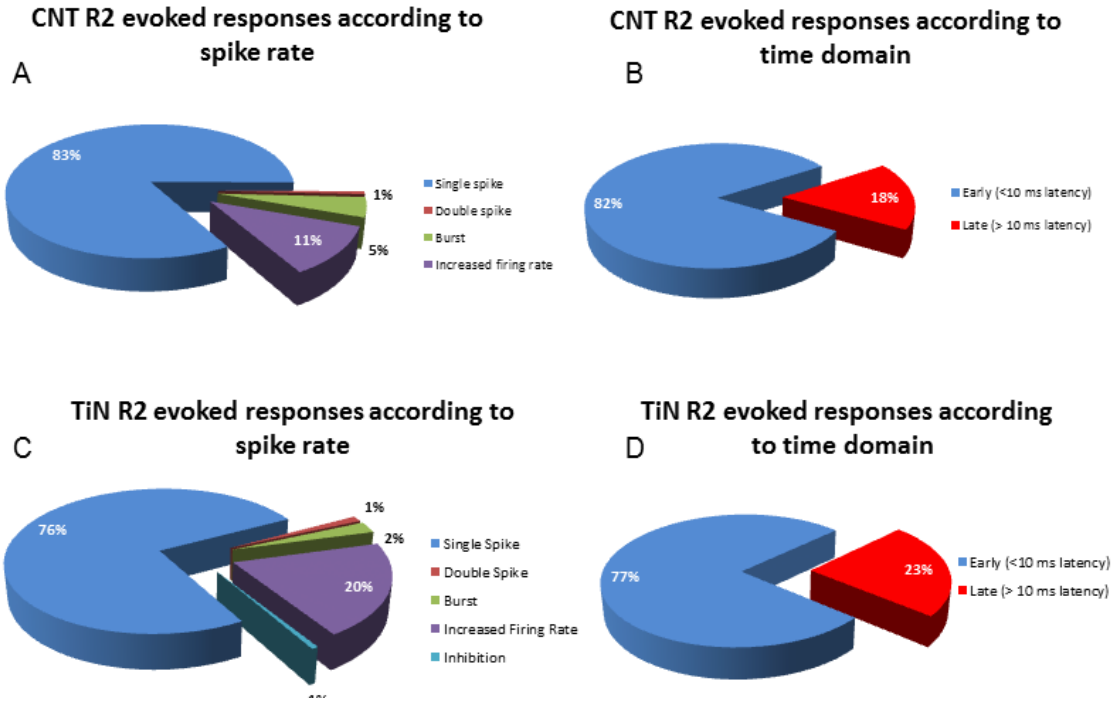

Figure 3.32: Temporal and spike rate dissection of responses evoked with R2 stimulus waveform. Pie charts indicating the percentage of responses according to spike rate (A, C) and time domain (B, D) for responses evoked using the R2 stimulus waveform with CNT (A, B) or TiN (C, D) electrodes.

Previous work performed in our laboratory on 30 retinas of young CRX -/- mice (~P20-P50) with CNT MEAs and Hexa MEAs (Multi Channel Systems, Germany) with TiN electrodes 10, 20 and 30 µm diameter revealed that the best inter-pulse interval for stimulation was 40 µs (Zimmermann 2009). Table 3.3 displays data from a variety of research groups having performed epi-retinal stimulation on transgenic rodents

presenting dystrophic retinas. The lowest thresholds obtained were by Sekirnjak, Hulse *et al.* (2009) which are the only group presenting very clear direct stimulation of RGCs with latencies well below 1 ms. They discuss the use of long pulses to provide deeper stimulation of the tissue, thus targeting retinal interneurons and generating synaptically driven long latency responses. This is supported by data provided by Ye, Ryu *et al.* (2010) who obtained responses over 400 ms following stimulation of pulses up to 1 s in duration.

Table 3.3: Epi-retinal *in vitro* stimulation of dystrophic rodents by various research groups.

Reference	Degeneration Model	Stimulus Shape	Pulse Width (µs)	Pulse amplitude (µA)	Electrode diameter /spacing (µm)/ material	Threshold (nC)	Threshold (mC/cm^2)	Response Latency (ms)
(O'Hearn, Sadda et al. 2006)	Mouse rd1	Cb,N1,3000,r1	1000	10-60	125	50	0.111	2.69
(Cartmell 2009)	Mouse rd1	Cb,P1,0,r1	60-1000	2-60	30/200 /TiN	2.5-3.1	0.35-0.42	<2
(Garcia-Ayuso, Salinas-Navarro et al. 2010)	Mouse rd1	Cb,P1,0,r1	100-1000	2-60	30/200/ /TiN	2.5-3.3	0.235-0.353	100
(Sekirnjak, Hulse et al. 2009)	Rat P23H	Cb,N1,0,r2	50/100	<5	7-16/60 /Pt	0.018 – 0.098	0.049	0.24
This work	Mouse CRX	Cb, N1, 40, r2	10-100	1-100	30/200 /CNT	1.56	0.22	<10
This work	Mouse CRX	Cb, N1, 40, r2	10-100	1-100	30/200 /TiN	1.89	0.27	<10

The lowest threshold was seen by Sekirnjak, Hulse et al. who used similar stimulation parameters to those used in this study. Underlined numbers were calculated from data provided in paper. In the "stimulation shape" column: Cb, charge balanced; N1, negative pulse first; P1, positive pulse first; inter-pulse interval in µs (here 0, 40, 3000); waveform shape (here r1 or r2).

Similarly to Ye, Kim et al. (2008), we were unable to confirm that very short latency spikes were not part of the stimulation artefact. The very short latencies observed by Sekirnjak, Hulse *et al.* (2009) was helped by the superior equipment and analysis methods. Moreover, smaller diameter (7-16 µm) and shorter spacing of electrodes (60 µm) evoked responses with significantly lower charge values, resulting in much smaller stimulation artefacts. The pigmented P23H rats used by this group responded to light up to P500 despite severe retinal degeneration, allowing them to map RGC receptive fields with light driven stimuli. The small electrode pitch allowed the mapping of RGC from their spontaneous and light driven activity over multiple electrodes, further

amplifying the chance of obtaining a clear response (visible on several electrodes). In the paper, they do not provide the threshold charge or an accurate current stimulation value (<5 µA). Instead, they provide the charge density value (0.049), calculated according to the electrode diameter which they claim "varied between 7 and 16 µm". This allows a back-calculation of the threshold values (underlined in Table 3.2) to vary between 0.018 and 0.098 nC or 0.098 to 1.9 µA, depending on the actual electrode size.

The use of cathodic first pulse waveforms generating the lowest possible charge to stimulate RGCs is physiologically counterintuitive. Indeed, lowering the cell membrane potential brings it further from its action potential generating threshold.

A study of stimulation parameters on dissociated neurons in culture (Wagenaar, Pine et al. 2004) found that negative pulses were most likely to directly depolarise neurons. The authors propose that negative capacitive currents would lower the potential of the medium near the electrode, charging the membrane capacitance and depolarising the membrane potential closer to threshold. Although the study does not shed light on the origin of the signals recorded (axon or soma), the authors suggest that the spiking originates from antidromically activated somata. They also propose that voltage-controlled pulses where least likely to cause Faradaic currents without the necessity of closely monitoring results or electrode impedance. Indeed, current-controlled pulses run the risk of generating sharp voltage transients leading to faradaic reactions. Ye, Ryu et al. (2010) found that stimulating using voltage (as opposed to current) yielded lower thresholds in both degenerated and wild type mice whilst (Suzuki, Humayun et al. 2004) found that a 1 kHz sinusoidal waveform was more efficient at stimulating wild type retinas (but not degenerated rd1 mice retinas) than a biphasic current pulse of 500 µs/phase *in vivo*.

In all of their recent retinal stimulation experiments, the group led by E.J. Chichilnisky use the cathodic first R2 waveform (Sekirnjak, Hottowy et al. 2006; Sekirnjak, Hottowy et al. 2008; Sekirnjak, Hulse et al. 2009). It may be worth noting that the R2 stimulus waveform resembles in shape that of an extracellular single unit with its sharp negative phase preceding its blunt positive phase (figure 3.33). The reason action

potentials exhibit this particular waveform is due to the kinetics of the voltage-gated ion channels along the axon. Indeed, Na^+ voltage-gated channels which mark the sharp depolarisation of the membrane potential open fast, about 1-2ms before the K^+ voltage-gated channel (delayed rectifier) open (Hodgkin and Huxley 1952). The transient charging and discharging of the extracellular medium along timelines mapping the kinetics of these two channels may coax the axon hillock into action potential generation and propagation.

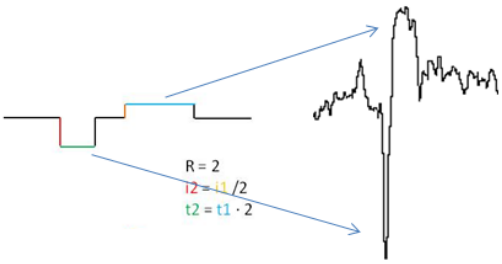

Figure 3.33: Resemblance of R2 stimulation waveform to extracellular spike. Not to scale, stimuli were ~100 – 250 µs whilst spikes are ~1ms.

Another application of different stimulation waveforms is to reduce the stimulation artefact, which can be much larger than neuronal spikes. The experiments described above as well as those of this thesis have made use of offline analysis techniques to remove most of the artefact whilst still losing the first few millisecond to the artefact. Recent advances in integrated circuit design have led to the Stimchip, an application specific integrated circuit (ASIC) able to produce complex patterns of tri-phasic stimulation pulses (Hottowy, Skoczen et al. 2012). These produce very low artefacts, allowing the recording of evoked spikes on the stimulation electrode itself as well as the reproduction of visually evoked spiking activity.

3.4.5 Inverted spikes

Individual CNTs have mechanical and electrical properties that would make them ideal for intracellular electrodes. Indeed, they are incredibly strong, robust, inert, and conductive, and they have a very small diameter. The surface of individual CNT electrodes on our MEA as seen by S.E.M. (*cf.* Chapter 2) allows us to identify a myriad of protruding individual CNTs, representing as many intracellular electrode tips. The appearance of “inverted spikes” amid conventionally shaped extracellular potentials in

the recordings performed with CNT electrodes prompted the suggestion of having inadvertently recorded intracellular spikes. However, these were also seen when using TiN electrodes. Also, the amplitude of these events is smaller than those of regular extracellular spikes. Experiments led by György Buzsàki predict that an extracellular spike corresponds to the negative of the first derivative of the recordings obtained from an intracellular electrode and that the size of the extracellular signal is smaller and decreases as the electrode tip is moved away from the soma (Henze, Borhegyi et al. 2000). Further work by this group reveals that the extracellular field recording of action potentials shifts with the position of the recording electrode, emphasising different phases of the action potential corresponding to different ionic currents. At the genesis of an action potential, the positive capacitive current is the largest membrane current and is the dominant potential recorded from electrodes along the apical dendritic trunk, some distance from the soma (Gold, Henze et al. 2006). RGCs have dendritic arbors infiltrating the IPL and axonal initial segments in the NFL. An electrode located sufficiently close to the dendritic arbor could potentially record a potential with a positive capacitive-dominant phase.

We note that most of these signals were recorded on Day 2, and that when recorded on Day 1, they occurred only after the tissue had been in contact with the electrodes for a few hours. Flattening of the tissue with time, induced by dispersion of the HA component of the ILM by perfused aCSF and pressure by the anchors placed above the retina could possibly allow dendritic arbors to move relatively closer to the recording electrode resulting in the recording of dendritic currents. Figure 3.34 illustrates how this phenomenon could occur. Modelling studies inspired by data acquired in the hippocampus have led to an understanding of how an action potential is detected in the extracellular space around a pyramidal cell, illustrated by the diagram in panel A (Buzsaki, Anastassiou et al. 2012). In our system, we observe similar events as those observed in the distal basal dendrites after the tissue has been in contact with the electrodes for a few hours. The electrode detects the depolarisation of firing RGCs within a certain volume (grey ellipse, Bi). As time goes by, the tissue flattens (dissolution of hyaluronic component of ILM, flopping of RGC dendrites with pressure of anchors on tissue) encompassing dendritic arbors into the elliptic volume (Bii).

Signals recorded from gold mushroom electrodes partially engulphed by Aplysia neurons after 48 hours presented the same characteristics (shape and size) as the signals recorded from an intracellular glass electrode (Hai, Shappir et al. 2010). When investigating two gold mushroom microelectrodes with different levels of coupling, the authors found that both signals presented the characteristic intracellular shape but the signal from the low-seal electrode was much lower (~0.5 mV) than that presented on the high-seal electrode (~3 mV). By optimizing the size and shape of the CNT electrodes, future experiments will allow the multisite partial engulfment of CNTs with the promise of higher quality recordings and lower stimulation thresholds.

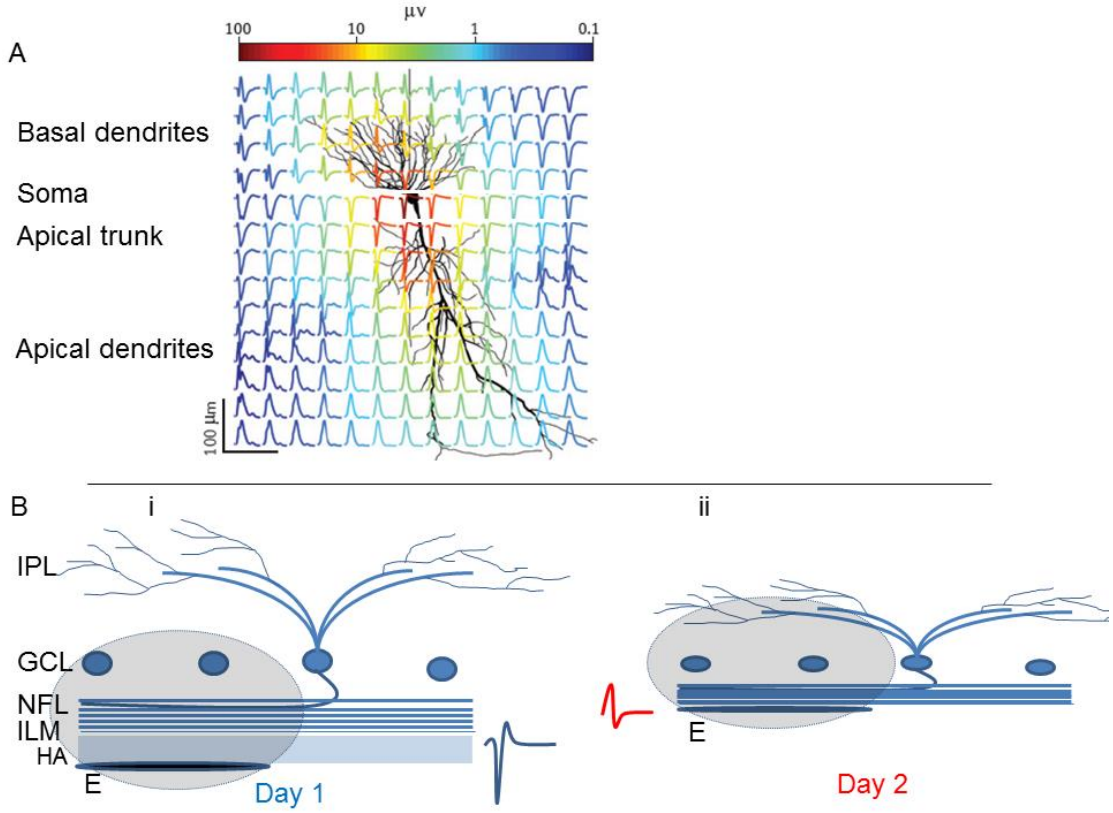

Figure 3.34: Inverted spikes could be the detection of dendritic currents due to flattening of the retina with time. A: Diagram adapted from (Buzsaki, Anastassiou et al. 2012) illustrating the extracellular signals detected around a hippocampal pyramidal cell. B: diagram illustrating the ability of planar epi-retinal electrodes to record somatic spikes in acute preparations (i) then dendritic spikes following flattening of the retina after 2 days *in vitro* (ii). E, electrode; IPL, inner plexiform layer; GCL, ganglion cell layer; NFL, nerve fibre layer; ILM, inner limiting membrane; HA, hyaluronic acid component of the ILM.

3.1.1 Future work

Although the results presented in this chapter have uncovered some of the electrophysiological processes involved during *in vitro* stimulation and recording of RGCs in degenerated retinas with CNT MEAs, further experimentation and analyses would provide complimentary data useful to the field.

Capacitive stimulation of RGCs using more complex stimulation parameters such as high temporal resolution trains or staggered pulses (e.g. multiple steps within each phase of a biphasic pulse) can potentially lower threshold values as well as influence RGC spiking in a more predictable way.

When using large spacing between electrodes, stimulation charges need to be high enough to activate RGCs several hundred microns away. This led to the observation of indirect responses in every single experiment performed. Further investigation of these responses requires longer post-stimulus acquisition (Garcia-Ayuso, Salinas-Navarro et al. 2010), which would also allow analyses of the mechanisms involved in pathological slow oscillations and how these can be abolished by electrical stimulation.

The superior time-dependent coupling between CNT electrodes and RGCs has great potential in a retinal prosthetic device where minimal amounts of charge need to be applied. Future investigation of this coupling is necessary to translate these findings to biomedical applications.

Creation of MEAs with closer spacing and smaller electrodes would allow the detection of directly activated RGCs in the direct vicinity of stimulating electrodes (Sekirnjak, Hulse et al. 2009). Optimisation of the tissue culture system would allow the maintenance of retinal explants for longer amounts of time and further investigate the tissue reaction to CNT electrodes. Fabrication of CNT electrodes with different designs (e.g. orthogonally aligned, invaginated or evaginated) would allow us to gain more insight about how the retina reacts to different electrode morphologies, investigating strategies to further increase the coupling between electrode and target RGC.

Chapter 4: Ultrastructural Study of the Interface Between the Inner Retina and Carbon Nanotube Assemblies

4.1 Introduction

Electrophysiological measurements taken over three days suggest a time-dependent increase in the coupling between CNT electrodes and RGCs in CRX-/- retinas. In order to elucidate the anatomical correlate of this phenomenon, we have interfaced passive CNT islands with CRX retinas *in vitro* before sectioning them and visualising the sections in a TEM. Initial light microscopy analysis revealed a time dependent shortening of the distance between the ILM and CNT islands, until the islands became fully integrated to the ILM after 48 hours. Analysis of SEM and TEM data provided us with an ultrastructural insight into the interactions between CNT assemblies and the retinas, specifically components of the ILM.

This chapter is focused on investigating the CNT-retina interactions at the vitreo-retinal interface by observing

1. Low magnification optic micrographs of transverse retinal sections incubated on loose CNT assemblies
    a. These show a gradual integration between 4 and 48 hours
    b. More islands adhere with time between 4 and 48 hours
2. High magnification TEM and SEM micrographs display
    a. The retina's immune response to the presence of CNT islands
    b. A structural modification in the shape of the retina to accommodate large CNT islands at the ILM
    c. The anchoring of individual nanotubes into collagen fibrils of the ILM
    d. Production of an adhesive matrix by the retina which grapples CNTs

The experiments and analyses described in this chapter were performed by Cyril Eleftheriou. CNT MEAs were fabricated at Tel Aviv University (Israel).

4.2 Materials and Methods

4.2.1 Loose CNT assemblies

Loose CNT island assemblies were prepared by our collaborators in Tel Aviv University. A nickel (Ni) layer was evaporated (E-beam, VST) onto an Si/SiO_2 substrate using a self-aligned process. The size and thickness of Ni islands determined the CNT site dimension and the surface packing of CNT assemblies. As such, "large" CNT islands, 80 - 100 µm in diameter, were fabricated using a 100 µm Ni disc 2.5 nm thick. "Small" CNT islands, 20 µm in diameter, were fabricated using 20 µm Ni discs 2.5 nm thick.

Similarly to the CNT MEAs used for the electrophysiological experiments detailed in Chapter 3, loose CNT assemblies were synthesized by CVD onto a Si/SiO_2 substrate using Ni as a catalyst (Fig. 4.1). The crucial difference in the fabrication of these islands with the electrodes of CNT MEAs is the necessity to have them lift off easily from the substrate. As such, TiN was omitted from the process because it normally provides the conducting tracks of the MEA, as well as a strong base for the CNTs to protrude from. Indeed, during the CVD process, the patterned Nickel is heated up to 900°C, melting into droplets which penetrate deep into the porous TiN before producing CNTs. Without the strong TiN base, the CNT islands can easily detach from the substrate (Fig 4.2, C). This is important because the goal of these experiments was to verify whether CNTs become entangled with the retina strongly enough to be lifted off the Si/SiO_2 substrate together with the tissue.

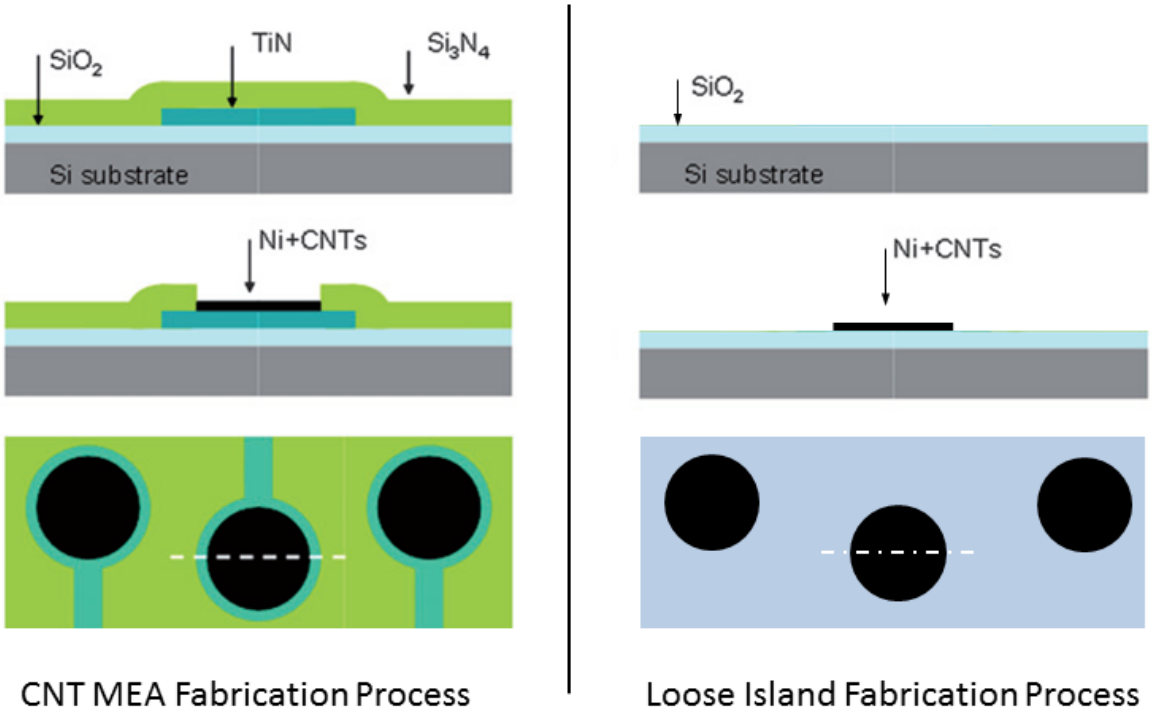

Figure 4.1: MEA and loose CNT island fabrication. Diagram outlining the fabrication steps required to produce CNT MEAs (left) and loose CNT islands (right). TiN acts both as the conducting material for the MEA's tracks and a fixed base for the CNT electrodes.

The self-aligned process mentioned above allowed for a precise topographical arrangement of the islands onto the Si/SiO_2 substrate, with "large" islands pitched at 200 µm centre-to centre (fig 4.2, A) and "small" islands pitched at 50 µm centre-to-centre (fig 4.2, B). As these assemblies are inherently loosely bonded to the substrate, they can easily be lifted off. The brown arrow indicates a location where multiple dislodged "large" islands have randomly congregated. Although the CNTs were grown to produce islands approximately 5 µm in height, some were found to measure only 1 µm in TEM micrographs (figure 4.21 and 4.22), possibly due to processing or fabrication artefacts.

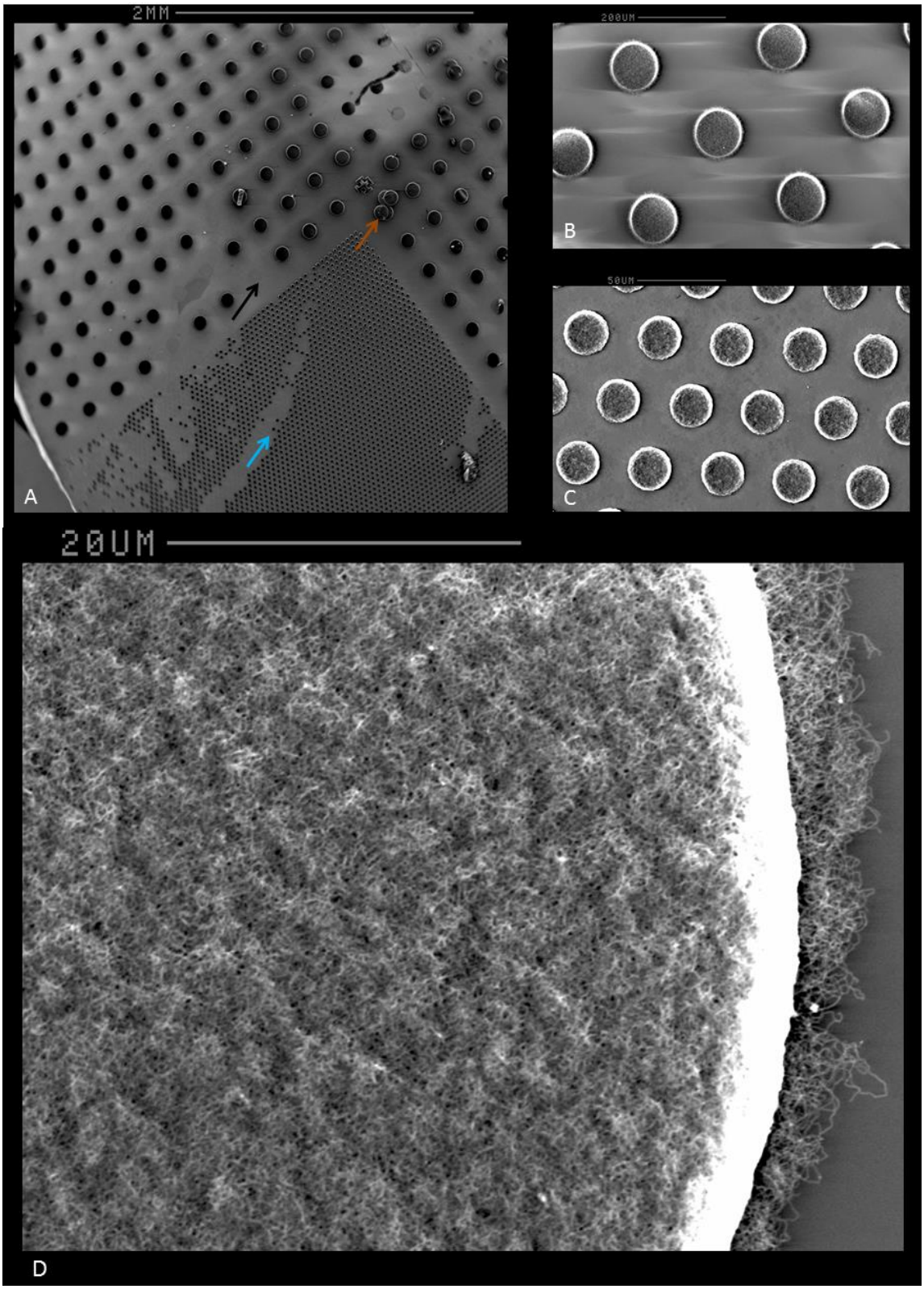

Figure 4.2: Scanning electron micrograph of "large" and "small" CNT islands on SiO_2 substrate. A: low magnification micrograph of both types of CNT islands on substrate. The black arrow indicates a location where a "large" island is missing. The blue arrow indicates a location where a streak of "small" islands are missing. B: Micrograph of "large" CNT islands. C: Micrograph of "small" CNT islands. B: High magnification micrograph of "large" CNT islands. Micrographs were taken on a Cambridge Stereoscan 240.

4.2.2 Maintenance of retinal explants

A total of six CRX -/- mice (aged 90 to 150 days old) yielded twelve retinas, eleven of which were used for the ultrastructural investigation of this project. Retinas were isolated as described in Chapter 2 and mounted onto loose CNT islands with the GCL facing down onto the islands. To improve the coupling, a polyester membrane filter (5µm pores) held the retina in place whilst being weighed down by two stainless steel anchors (0.75g each) bearing a framework of parallel glass capillaries (Figure 4.4, insert). To maintain physiological conditions, the tissue was perfused with aCSF at 1.2 ml/minute over the course of 4, 12, 24 and 48 hours using a peristaltic pump (SCI400, Watson Marlow, UK), like in electrophysiological experiments. The aCSF was directly oxygenated (95% O_2 and 5% CO_2) in a large chamber containing up to 4 samples (figure 4.3).

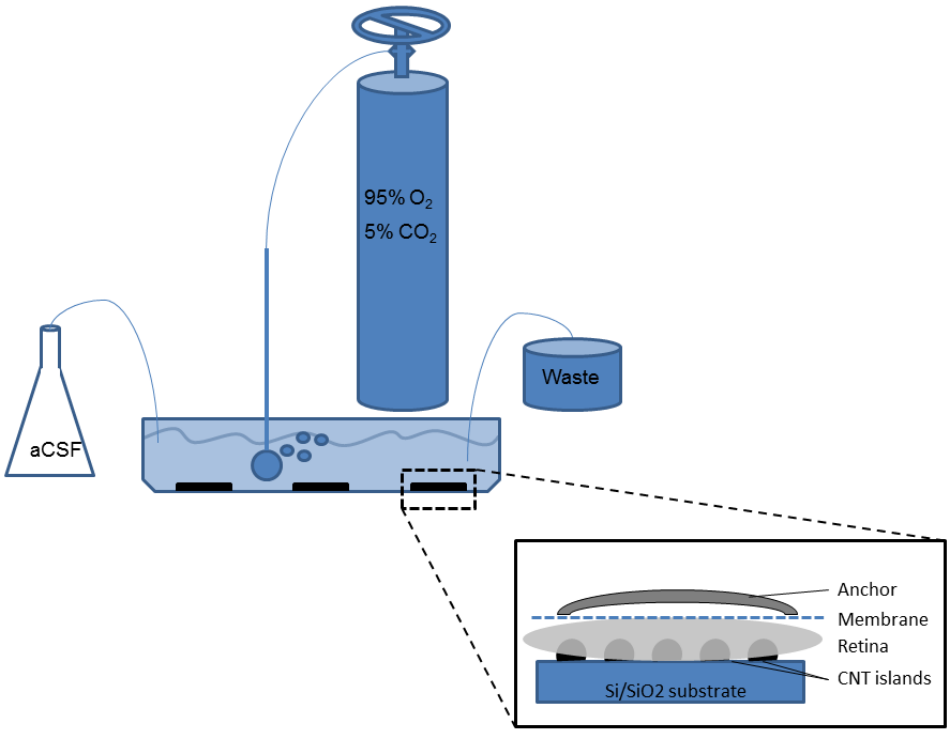

Figure 4.3: *In vitro* experimental setup. Isolated retinas were kept alive on loose CNT islands by perfusing aCSF at 1.2 ml/min and oxygenating it in the dish.

4.2.3 Processing for electron microscopy

Transmission electron microscopy

The retinas were lifted off from the SiO_2 substrate with nitrocellulose membrane filter, halved along the optic disc, then fixed in 2% Glutaraldehyde (Cacodylate buffered), postfixed in osmium tetroxide, dehydrated in acetone, and embedded in epoxy resin (TAAB, UK). Semi-thin (2 µm thick) and ultra-thin (70-90 nm thick) sections were cut perpendicular to the surface of the retina on a Ultracut E ultra-microtome (Reichert-Jung, Austria, now Leica Microsystems) then stained with either Toluidine Blue (semi-thin sections) or uranyl acetate and lead citrate (ultra-thin section). Semi-thin sections were obtained in levels of 3 series comprising 6 sections to be used for staining to locate the CNT islands in the tissue. Thus, each one of these levels corresponded to a 36 µm-long segment of tissue, preventing the inadvertent full sectioning of a "large" CNT island. Each level was composed of 3 series to avoid aggregation of semi-thin islands as they dried on microscope slides. This process is illustrated in figure 4.4.

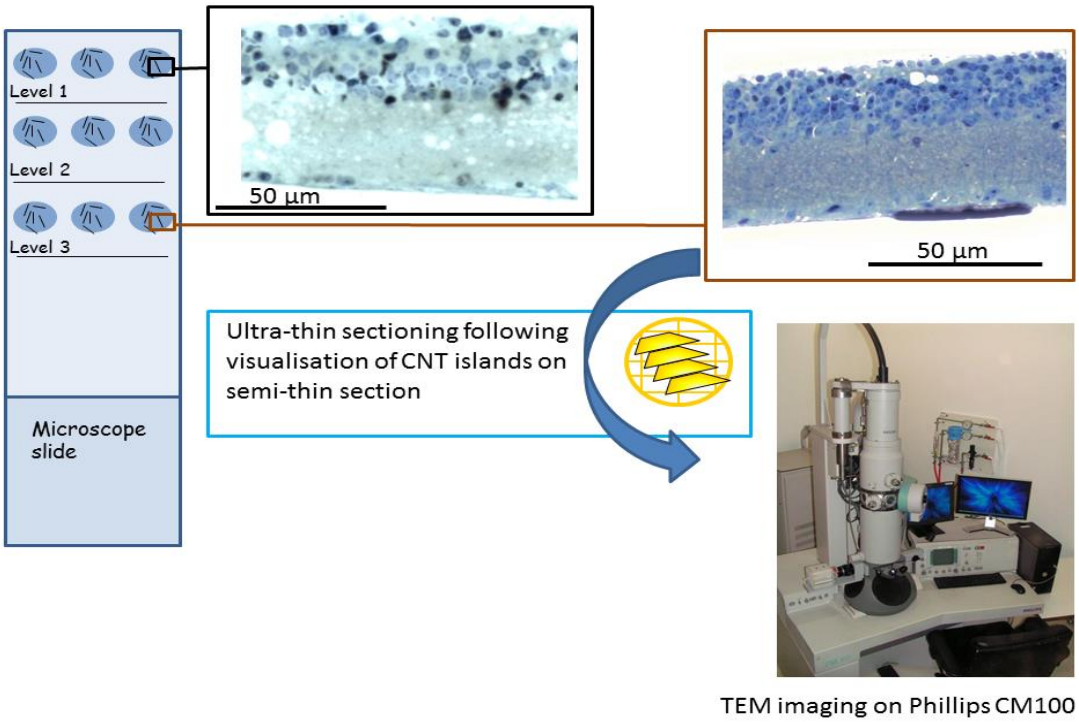

Figure 4.4: Ultra-thin sectioning of CNT-retina bio-hybrids following visualisation of CNT islands on semi-thin sections. Embedded retinas were sectioned in 36 µm levels of 18 semi-thin sections before being stained with Toluidine Blue and observed for the potential presence of CNT islands under an optical microscope. If CNT islands were observed (brown-lined panel), the block was sectioned in 70-90 nm sections and collected on copper grids to visualise under the TEM.

Scanning electron microscopy

After fixing in 2% Gluteraldehyde (Sorensons buffered), dehydrating in increasing concentrations of ethanol and critical point drying (CPD 030, Bal-Tec, Lichtenstein, now Leica Microsystems), the samples were coated with a 15 nm gold film using a Polaron E5550 sputter coater (Polaron equipment Ltd, UK, now Quorum Technologies Ltd).

4.2.4 Digital processing

Images were edited using Paint.net v3.5.10 (dotPDN LLC, USA) and Power Point 2010 (Microsoft, USA). Distances and surfaces were measures in ImageJ 1.45s (National Institute of Health, USA). Photo-montages were performed in Photoshop CS2 (Adobe, USA).

4.3 Results

4.3.1 Semi-thin retinal sections

Semi-thin sections of retinal bio-hybrids were used to quantify the amount of physical coupling between the retinas and CNT islands. We have used two parameters to quantify coupling. One is the average number of islands adhering to each retinal explant (figure 4.7) and the other one is the distance between the external surface of each island and the retinal ILM (figure 4.6). The latter is calculated by dividing the surface between the two structures by the length of the island in that particular section (figure 4.5. Similar measurements were taken on all islands adhering to retinas for each particular time point.

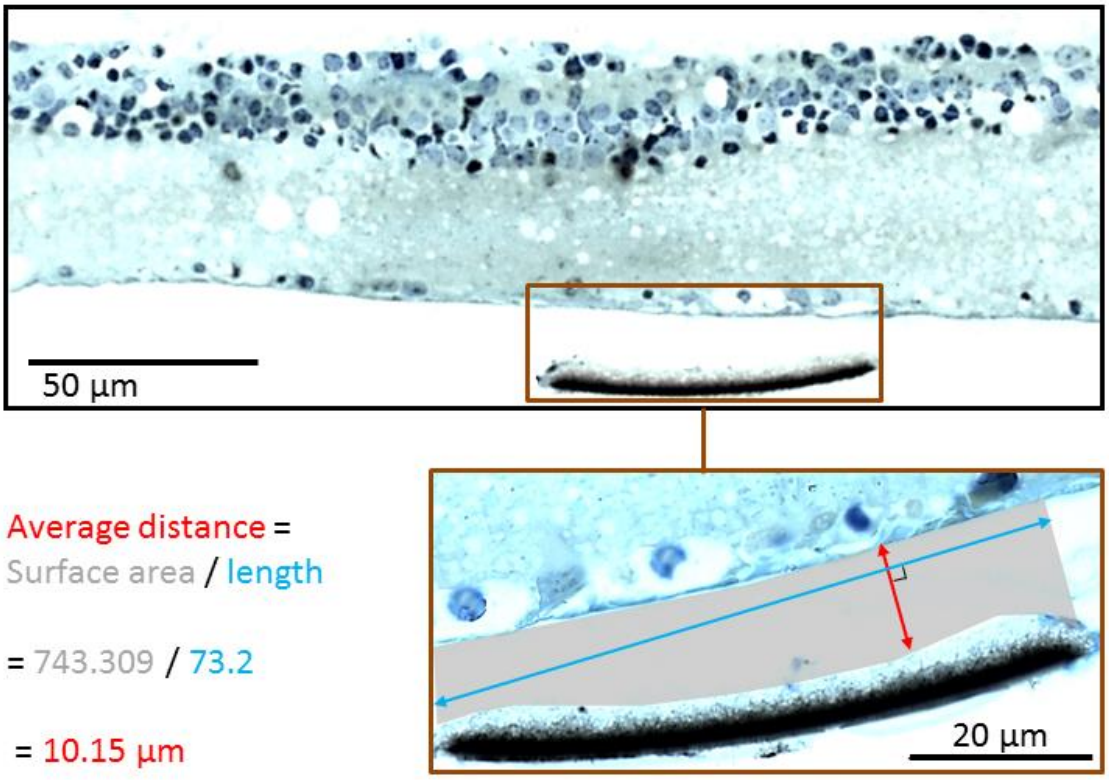

Figure 4.5: Illustration of the method for calculating average ILM-CNT distance. The average distance between a CNT island and the retinal ILM is calculated by dividing the area between the two structures by the length of the island. In this example, the retina has been in contact with CNT islands for 4 hours; the average distance is 10.15 µm.

The distance between ILM and CNT island surface decreases in a time-dependent fashion, providing anatomical evidence for an increase in coupling between the tissue and CNTs. Figure 4.6 A displays micrographs of semi-thin sections from retinas interfaced with CNT islands for 4, 12, 24 and 48 hours. The ILM-CNT distance clearly decreases with time until the island forms an integral part of the ILM at the 48 hour mark. Figure 4.6 B shows the average ILM-CNT distances in all samples, demonstrating gradual decrease from 11.5 µm to -1.40 µm between 4 and 48 hours. The value at 48 hours is negative because part of the island has been absorbed by the retina. It is worth noting that there are more data points for 48 hours than for earlier time points as there were more islands adhering to the retina then, as illustrated in figure 4.7. Hence, there were not enough data points to perform an adequate t-test between the pre- and post-48h groups (power = 0.417).

The average number of CNT islands adhering to the tissue increased with incubation time. Figure 4.7 illustrates this process with panel A showing a whole retina after 48 hours in contact with an array of loose CNT islands (in this example, the retina is being tested electrophysiologically on an MEA at the time of the photograph). Panel B shows a cross section of a retina with several CNT islands adhering to it after 48 hours. Panel C summarises the average number of islands adhering to retinal explants at different time points, clearly showing a gradual increase in the number of islands adhering to the tissue between 24 and 48 hours (0 to 6 islands for 24 hours and 2 to 20 islands for 48 hours). However, this difference is only marginally significant ($p = 0.052$, Mann-Whitney Rank Sum t-test) as the number of samples for the 24 hour time point is limited to 4 (as opposed to 9 for the 48 hour time point). The number of islands adhering to the tissue between 4 and 24 hours ranges from 0 and 6, totalling 9 different samples. The difference between these two groups is statistically significant ($p = 0.006$, t-test).

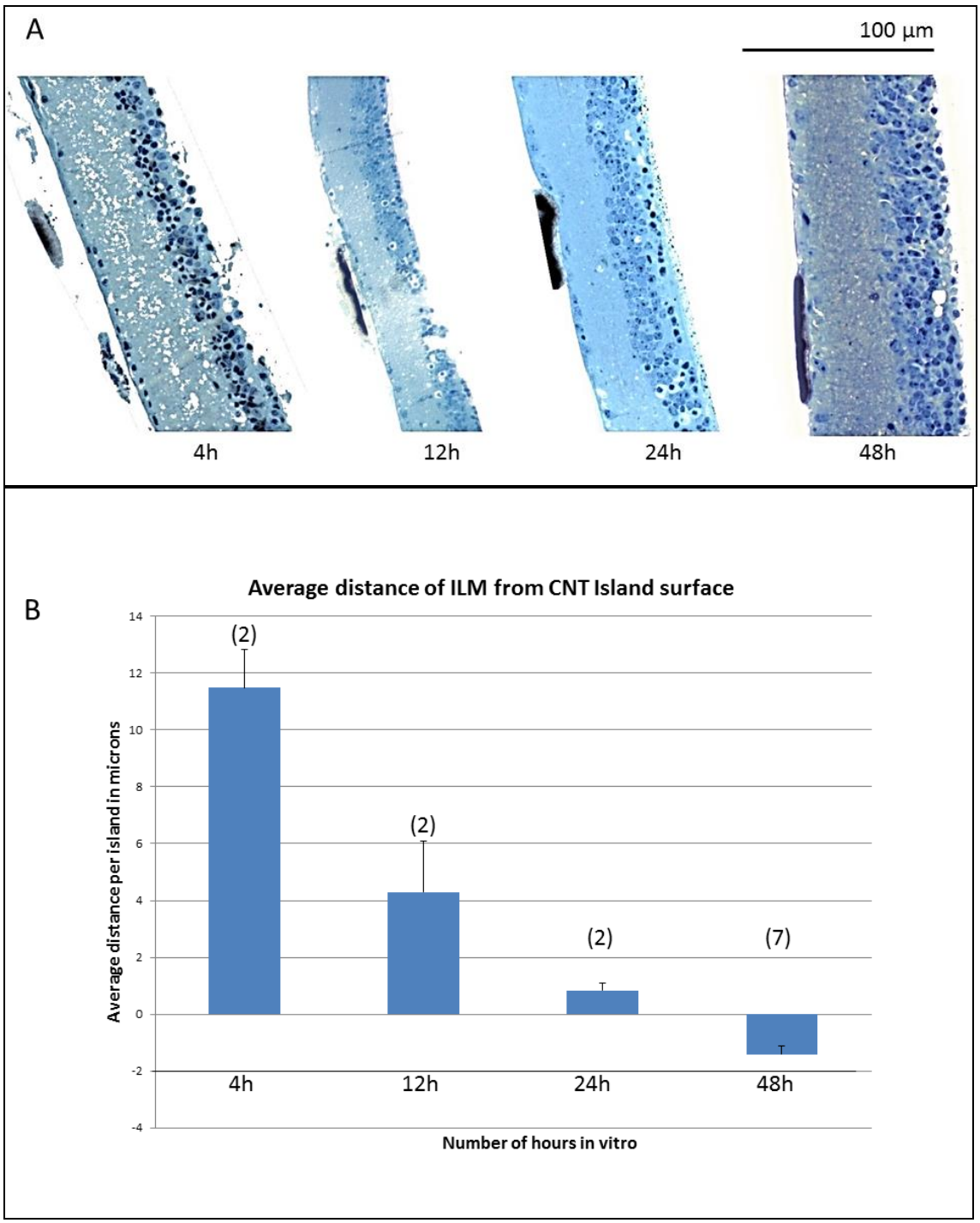

Figure 4.6: The average distance between ILM and CNT island decreases with time. A: 4 examples of Toluidine Blue stained semi-thin retinal sections interfaced with CNT islands for 4, 12, 24 and 48 hours incubation. B: Bar plot displaying average distance between island surface and retinal ILM, which decreases gradually from 11.5 µm to -1.40 µm between 4 and 48 hours. Error bars: SEM. Number of samples displayed above each bar in parentheses.

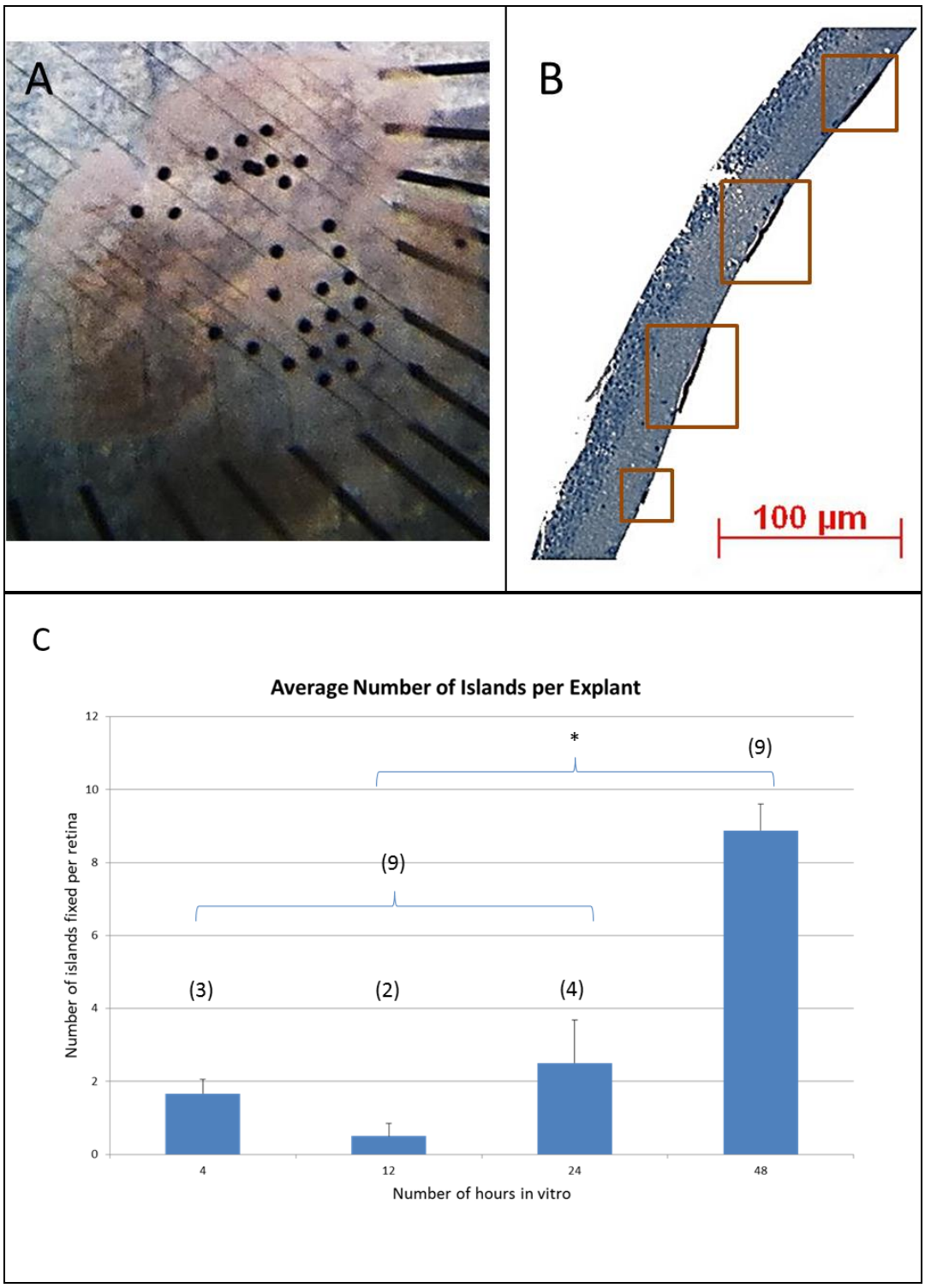

Figure 4.7: The number of islands adhering to an explant increases with the incubation time. A: Photograph of a live retina after 48 hours in contact with loose CNT islands, 30 of which ("large islands") adhered to it. B: Micrograph of Toluidine Blue stained semi-thin retinal section interfaced with CNT islands for 48 hours, showing 4 separate islands at the GCL. C: Bar graph of average number of adhering islands at 4, 12, 24 and 48 hours incubation. Error bars: SEM. Asterisk: statistical significance. Number of samples displayed above each bar in parentheses.

4.3.2 Transmission electron microscopy

TEM is a very powerful histological tool, which allows observation of ultrastructural details magnified up to 200,000 times. In this project, it allows the visualisation of individual CNTs and their interactions with the cellular and molecular components of the vitreo-retinal interface. In essence, it provides a window into the retinal response to the intrusion of CNT assemblies and the eventual juxtaposition of these two highly complex structures in the creation of bio-hybrid composites. The data is presented as a series of micrographs increasing in magnification and organised in a clockwise fashion. The border colour of each micrograph helps to determine the level of magnification within the set according to the following colour scheme: from lower to higher magnification, black, brown, blue, green, orange, yellow, white and red. The same colour scheme is used for arrows pointing to particular features in the set, going from high to low according to the size of the feature.

As a complement to the literature review presented in Chapter 1, TEM micrographs of an adult wild type mouse retina summarise features of the vitreo-retinal interface and its components. Despite thorough remodelling of the Crx neural retina, the vitreo-retinal interface is not fundamentally different from the wild type. However, introducing CNT assemblies triggers significant changes at the interface. The following sections present an account this response, as summarised in figure 4.8.

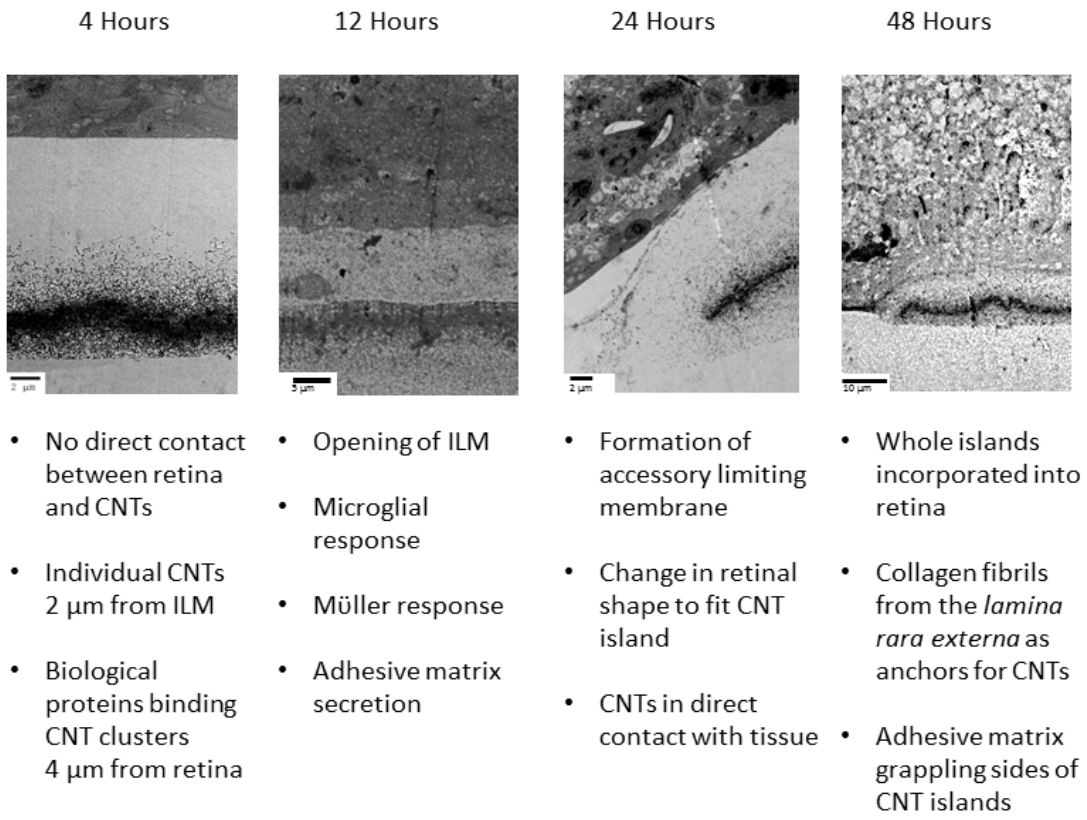

Figure 4.8: Chronological mosaic outlining the retina's response to the presence of CNT islands at its surface.

4.3.3 Ultrastructural characteristics of wild type versus CRX -/- retinas

Figure 4.9 presents an ultra-microscopic view of an adult wild type mouse retina with a focus on the GCL. Each panel provides a further magnified insight into the previous one. The black-lined (optic micrograph of semi-thin section) and brown-lined (TEM micrograph of ultra-thin section) panels show entire cross sections of the retina with each layer labelled in between both panels. The black arrows point to Müller cell end-feet, whose cytoplasmic membranes form the inner-most component of the ILM. As is typical for these radial glia, their cytoplasm is considerably more electron dense than their neural counterparts. This is due to the abundance of organelles, glycogen granules and cytoplasmic filaments supporting their many functions and hyper-productive metabolic demands (Magalhaes and Coimbra 1972; Rasmussen 1972). The brown circle highlights a capillary, completely surrounded by glial cell processes. The blue arrows point to RGC nuclei, the somata of which are enveloped in the dense

processes of astrocytes (green arrows) and even denser processes of Müller cells (orange arrows).

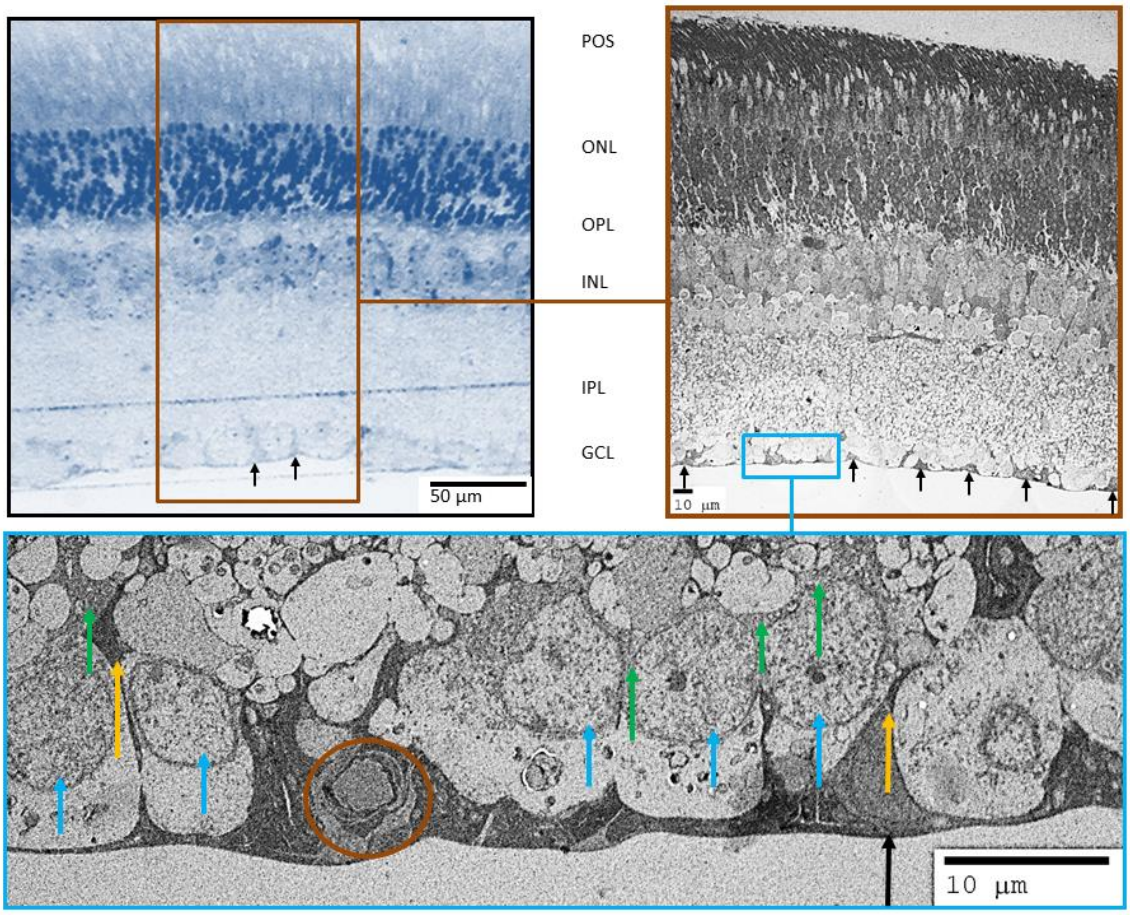

Figure 4.9: TEM of transverse section through a wild type adult mouse retina with focus on the GCL. The top panels display cross sections through the whole retina, with photoreceptor outer segments (POS), outer nuclear layer (ONL), outer plexiform layer (OPL), inner nuclear layer (INL), inner plexiform layer (IPL) and ganglion cell layer (GCL). The black arrows point to Müller cell end-feet. The blue-lined panel provides an ultrastructural view of the GCL, with RGC nuclei (blue arrows), astrocytic processes (green arrows) and Müller cell processes (orange arrows).

Figure 4.10 illustrates the vitreo-retinal interface of the wild type retina.

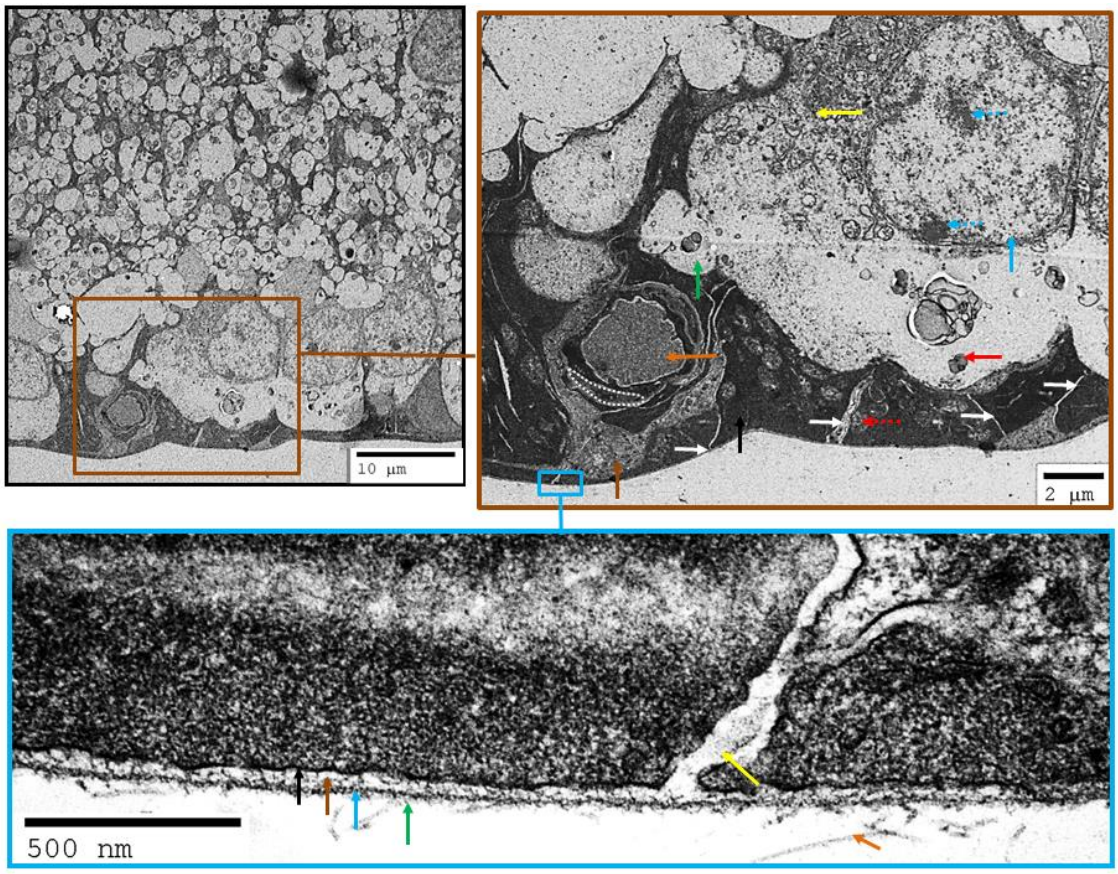

Figure 4.10: TEM of transverse section through a wild type adult mouse retina with focus on the ILM. Black-lined panel: Portion of the IPL and GCL encompassing Müller cell end-feet and a capillary. Brown-lined panel: area surrounding the capillary with arrows pointing to various cellular structures (vertical) and organelles (horizontal): black, Müller cell cytoplasm; brown, astrocytic cytoplasm; blue, RGC nucleus (dotted arrows point to the secondary nucleoli, typical in small neurons); green, axon; orange, capillary lumen; dotted white area, endothelial cell nucleus; yellow, rough endoplasmic reticulum; red, mitochondria (dotted arrow represents a Müller cell mitochondrion); white, interface between different glial processes. Blue-lined panel: ILM with a different set of arrows: black, cytoplasmic membrane of a Müller cell; brown, *lamina rara interna*; blue, *lamina densa*; green, *lamina rara externa*; yellow, interface between different glial processes; orange, collagen fibril.

Figure 4.11 displays an ultra-microscopic view of a P88 CRX mouse retina, with focus on the GCL (blue-lined panel). The black lined panel presents a Toluidine Blue stained semi-thin section, with black arrows pointing to two activated (hypertrophied) Müller cells. Photoreceptor cell death has prompted thorough remodelling in this retina, resulting in the six typical layers described above to be reduced to three: GCL (brown arrows), IPL (blue arrow) and INL (green arrow). The ONL and OPL are absent and synaptic rewiring in the IPL leads to microneuromas. As described in Chapter 1 (Jones,

Watt et al. 2003), microneuromas are aberrant synaptic connections reconstructed from serial ultra-thin sections. The Müller cell end-feet do not line the vitreo-retinal juncture. Indeed, the NFL (red arrow) is entombed in a glial seal, composed of atrophied and displaced Müller cells. The cytosol of these stressed Müller cells (white arrow) is not as dense as in wild type retinas or as dense as pyknotic RGCs (orange arrows) whose axon hillocks invest the hypertrophied NFL.

Figure 4.12 focuses on the GCL, NFL and ILM of the retina presented in figure 4.12. The black-lined panel is a higher magnification ultra-micrograph of the black box seen in the blue-lined panel of figure 4.12, focusing of the GCL. RGCs (green dotted area) have pyknotic nuclei (black arrows) and are heavily fasciculated by glial processes (blue arrows). A karyorrhexic RGC (brown arrow) has a fragmented nucleus leaking chromatin in its cytosol (dotted brown arrow). Karyorrhexis is the fragmentation of the nucleus of a dying cell (Zamzami and Kroemer 1999). The brown-lined panel focuses on the NFL which is populated by RGC axons (blue dotted area) containing mitochondria (brown arrows) and microtubules (blue arrows). Axon bundles are fasciculated in glial sheathes (black arrow). The ILM (blue-lined panel) presents the same basement membrane organisation as in a wild type retina with a *lamina rara interna* (blue arrow), *lamina densa* (green arrow) and *lamina rara externa* (orange arrow). The *lamina rara externa* is more sparsely populated in collagen fibrils and glycosaminoglycans granules, although the sparse presence of large vesicular elements (yellow arrow) is noteworthy. The Müller cell cytosol (black arrow) characterised by its electron-density and granular appearance is surrounded by its cytoplasmic membrane (brown arrow).

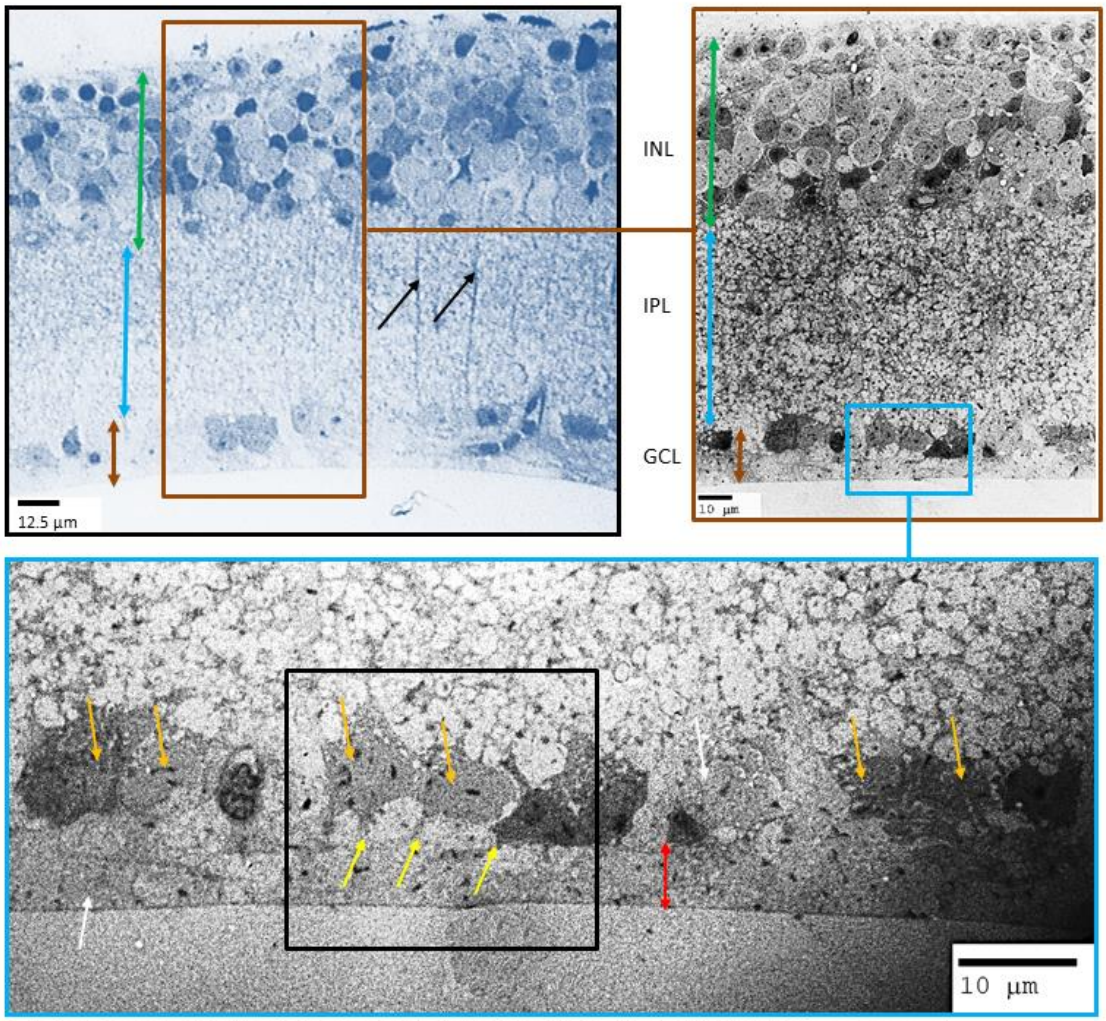

Figure 4.11: Ultrastructure of P88 CRX -/- retina with focus on the GCL. Black-lined panel: optical micrograph of a semi-thin section of a P90 CRX -/- retina showing activated Müller glia (black arrows) in an IPL (blue arrow) laminated by hypertrophied INL (green arrow) and GCL (brown arrow). Brown and blue-lined panels: increasingly high magnification TEM micrographs of ultra-thin sections of the same retina focusing on the GCL. Pyknotic RGCs (orange arrows) of the GCL invest their axon hillocks (yellow arrows) in a hypertrophied NFL (red arrow) entombed in Müller cell seals (white arrows).

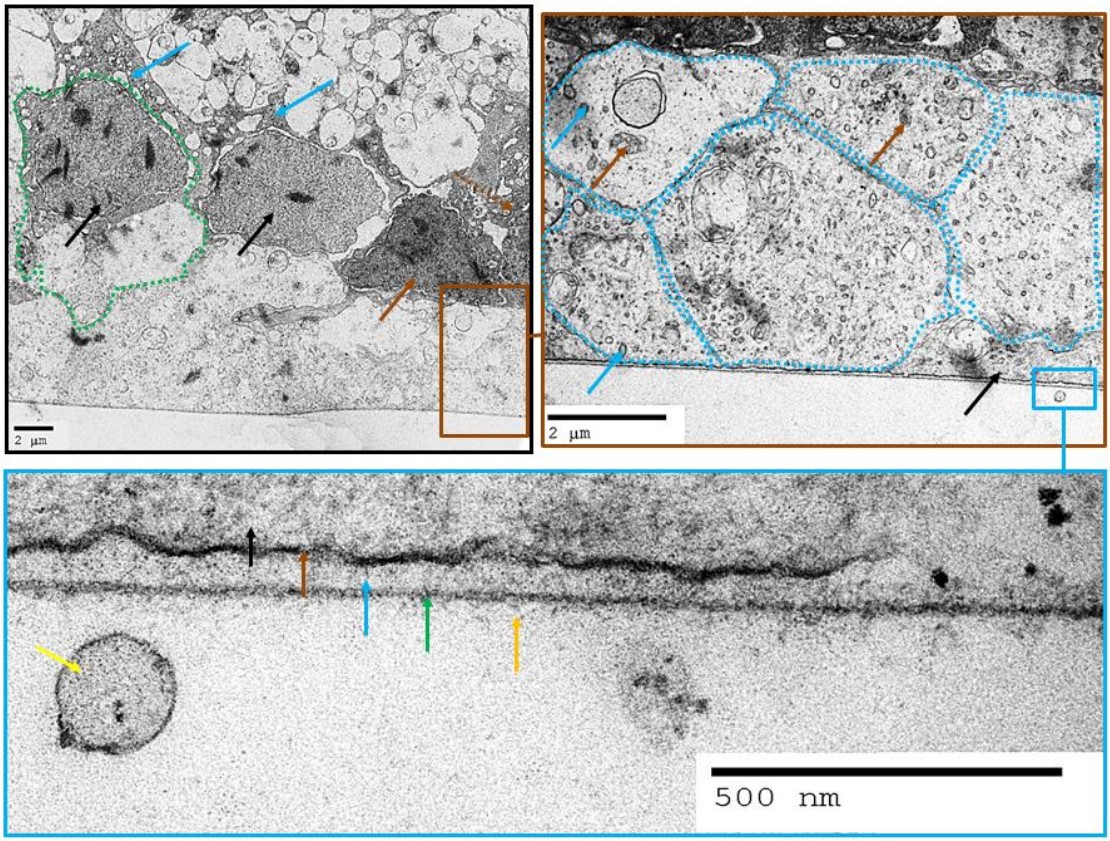

Figure 4.12: Ultrastructure of GCL, NFL and ILM of P88 CRX -/- retina. Black-lined panel: portion of the GCL extracted from the black box in figure 4.11 focusing on 2 RGCs with pyknotic nuclei (black arrows) and a completely degenerated cell (brown arrow) leaking chromatin in the cytosol (dotted brown arrow). These RGCs are heavily fasciculated by glial processes (blue arrows, either Müller or astrocytic). Brown-lined panel: focus on the NFL, with RGC axons (blue dotted areas) containing mitochondria (brown arrows) and microtubules (blue arrows). Axon bundles are fasciculated by Müller cell processes (black arrow). The blue-lined panel focuses on the ILM which shows a typical structure with a *lamina rara interna* (blue arrow), a *lamina densa* (green arrow) and a sparseness of extracellular matrix components in the *lamina rara externa* (orange arrow). The yellow arrow points to vesicular material at the vitreo-retinal juncture.

4.3.4 Initial reaction to CNT island presence: immune response and adhesive matrix production

Between four and twelve hours *in vitro*, the retina reacts to the presence of CNT islands.

The optical micrograph of the 12 h time point (figure 4.6) reveals two striking characteristics: the CNT island is surrounded by an amorphous substance as well as by multiple individual cells with large nuclei (larger than the other retinal cells present in that micrograph). These clearly originate from the retina and thus correspond to a biological response to the presence of the CNT island. Figures 4.13 to 4.16 show increasingly higher magnifications of individual events in this dramatic tableau, with figures 4.13 and 4.14 focusing on the cellular components and figures 4.15 and 4.16 focusing on the amorphous substance.

In figures 4.13 to 4.15, the black-lined panels correspond to a portion of the 12 h time point in figure 4.6. In the same set of figures, the brown-lined panel corresponds to a TEM zoom-in of the retina and CNT island.

In the brown lined panel of figure 4.13, the black arrows point to undulations in the ILM, features which are magnified in the blue-lined and green-lined panels. In the blue-lined panel, these ILM folds appear to become more prominent in the vicinity of the large cells found in the space between the island and the retina. The green-lined panel focuses further on such a fold, revealing an opening in the ILM l*amina densa* (black arrow), which is followed 2 µm along the right by a fold in the Müller cell (characterised by dense and granular cytosol) cytoplasmic membrane (brown arrow). This opening of the Müller cell cytoplasm into the ECM allows the release of vesicles (blue arrows). More vesicles are found in the vicinity (green arrows), perhaps primed to be docked at the membrane for release as well. The Müller cell processes (orange arrows) are overlapping each other and may be wrapping around cells as noted in “The Ultrastructure of Retinal Vessels III” (Hogan and Feeney 1963).

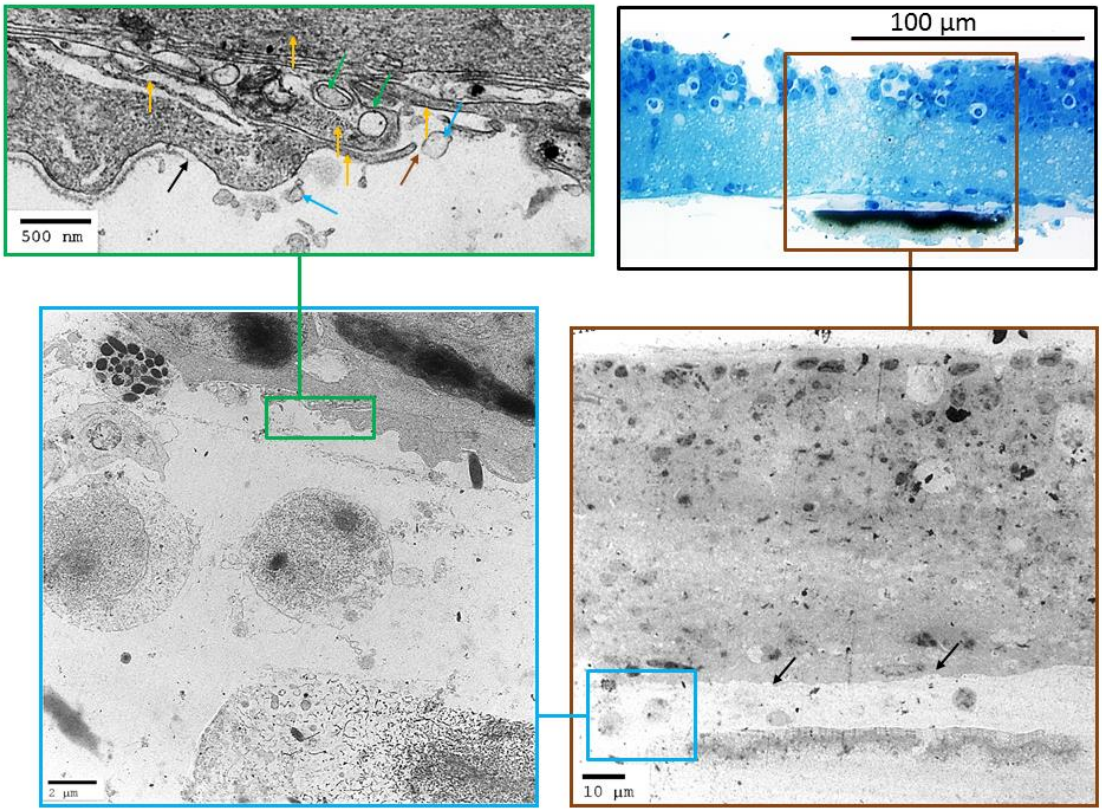

Figure 4.13: Release of vesicles by Müller cell end-feet after 12 hours. Black-lined panel: optical micrograph of a semi-thin section of a P90 CRX -/- retina interfaced with CNT islands for 12 hours. Brown, blue and green-lined panels: increasingly high magnification TEM micrographs of ultra-thin sections of the same retina focusing on undulations in the ILM (black arrows) opposite the CNT island (brown-lined panel). The level of undulation increases around large extra-retinal cells (blue-lined panel). Undulations in the ILM lead to a scission in the *lamina densa* (black arrow) and Müller cell cytoplasmic membrane (brown arrow) to allow the release of vesicles (blue and green arrows) into the extra-retinal space (green-lined panel). The orange arrows point to different Müller cell processes folded onto each other.

Figure 4.14 highlights the presence of individual cells (black arrows) whose pseudopodia (brown dotted outline) bind to the CNT assemblies. These cells present the amoeboid morphology of activated retinal microglia (Griffin, Illis et al. 1972; Stensaas 1977; Tseng, Ling et al. 1983; Banati, Egensperger et al. 2004; Bruban, Maoui et al. 2011), with irregular nuclei containing clumps of chromatin (green arrows), a dense ill-defined cytoplasmic membrane containing polyribosomes and dense granules (orange arrows), microvili and pseudopodia appearing as isolated vesicles and granules. The blue arrows in the orange-lined and blue-lined panels point to a hypertrophied basement membrane, which appears to be parallel to the plane of the retina, delimiting a barrier with the exposed Müller cell cytoplasm of figure 4.14. Note

the pigment granule within that membrane (yellow arrow, blue-lined panel). Such granules have been seen in dystrophic retinas by other research groups, and are thought to be ingested by RPE migrating to vessels in the inner retina (Dryja and Li 1995); ingested by retinal microglia (Szamier and Berson 1977); or ingested by Müller cells (Hogan and Feeney 1963). These granules also look like the product of non-specific esterase reactions as observed in activated microglial cells (Tseng, Ling et al. 1983).

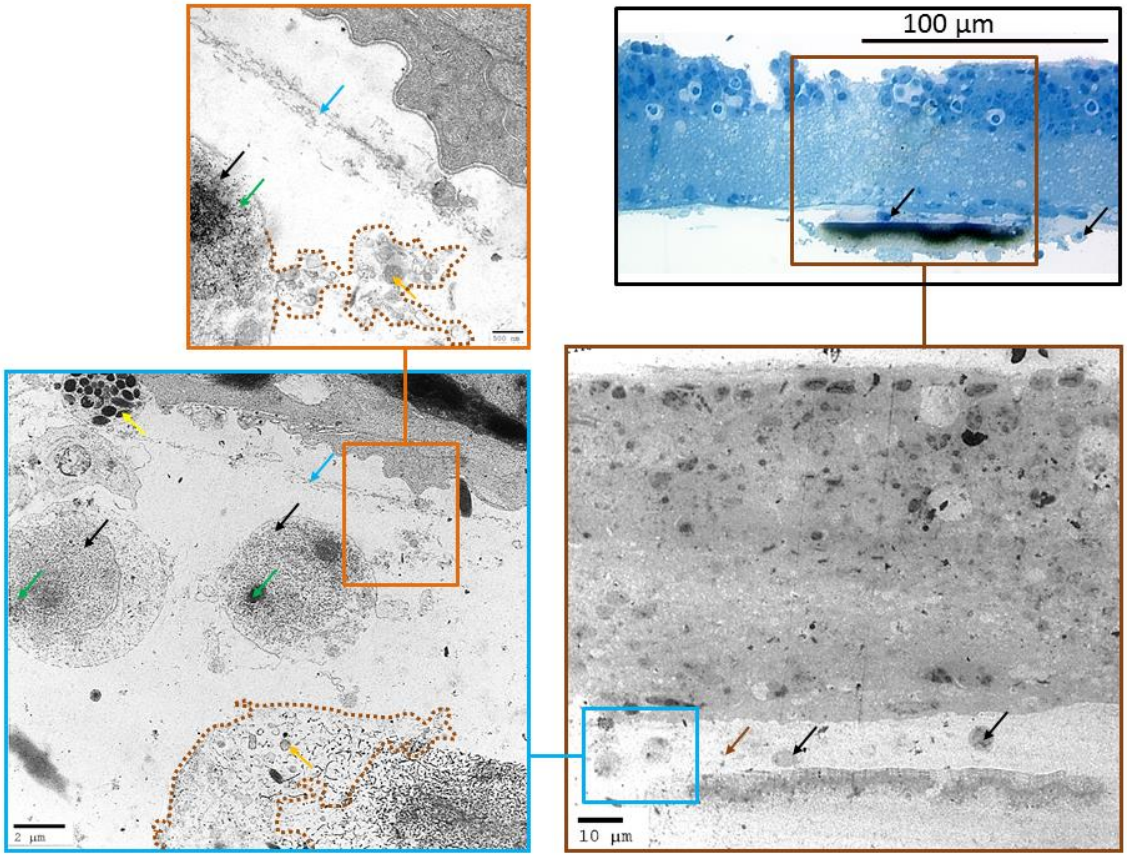

Figure 4.14: Attack on CNT island by activated microglia after 12 hours. Black-lined panel: optical micrograph of a semi-thin section of the same retina as figure 4.14. Brown, blue and orange-lined panels: increasingly high magnification TEM micrographs of ultra-thin sections of the same retina presenting higher magnifications of the extending pseudopodia (brown dotted outline) adhering to the CNTs. A distended membrane (blue arrow) creates a divide between Müller cell cytoplasm and extra-retinal space.

The two figures above point to attack of the CNT islands by two of the three different types of retinal glia. Indeed, figure 4.13 presents the release of cellular material by Müller cells whilst figure 4.14 presents the binding to CNT islands by activated

microglia. Both Müller cells and microglia have the capacity to phagocyte debris in the retina (Egensperger, Maslim et al. 1996), making the above interpretation plausible.

Although the high magnification TEM micrographs in figures 4.15 and 4.16 (blue, green and orange-lined) display a large amount of biological material in the space between retina and CNT island, that space is free of the amorphous substance observable in the optical micrograph of the black lined panel. TEM micrographs taken closer to the centre of the CNT island allow a highly magnified view of this substance. Figure 4.16 focuses on areas presenting this substance close to the CNT island (blue-lined panel) and close to the ILM (green-lined panel). In both panels, we can see that the substance contains globular material which is either uniform (brown arrows) for hundreds of square nano-meters or grainy (blue arrows). This substance appears to be emanating from pores in the ILM (green arrows). The presence of fibrous (orange arrows) and vesicular (yellow arrows) material are further indications that the amorphous substance is biological and thus secreted by the retina.

The presence of the amorphous substance in figure 4.15 but not 4.13 and 4.14 is intriguing, and can be explained by the fact that the areas shown in figures 4.13 and 14 have a larger retina-CNT distance. Figure 4.15 displays micrographs of the same retina as in the previous 2 figures, where there is a very clear shortening of the CNT-retina distance due to the angle of the CNT island. Indeed, the distance at the edge of the island (blue bar) is 15.6 µm whilst the distance at the right-hand edge of the micrograph (green bar) is 9.9 µm. The brown-lined panel indicates an area where a progressive change in the texture of the substance is readily observable. The blue box, located in an area at the middle of the micrograph shows the substance is a continuous matrix, with a regular globular appearance and polymorphous gaps of similar dimensions (black arrows). The green box, located at the right hand edge of the micrograph shows the substance to be almost solid with a decrease in the size and number of gaps in the matrix (brown arrows). Around the ILM, there are still fibrous elements whilst these are not present around the CNT island. This substance seems to fade out as the matrix thickens and the distance from the ILM increases.

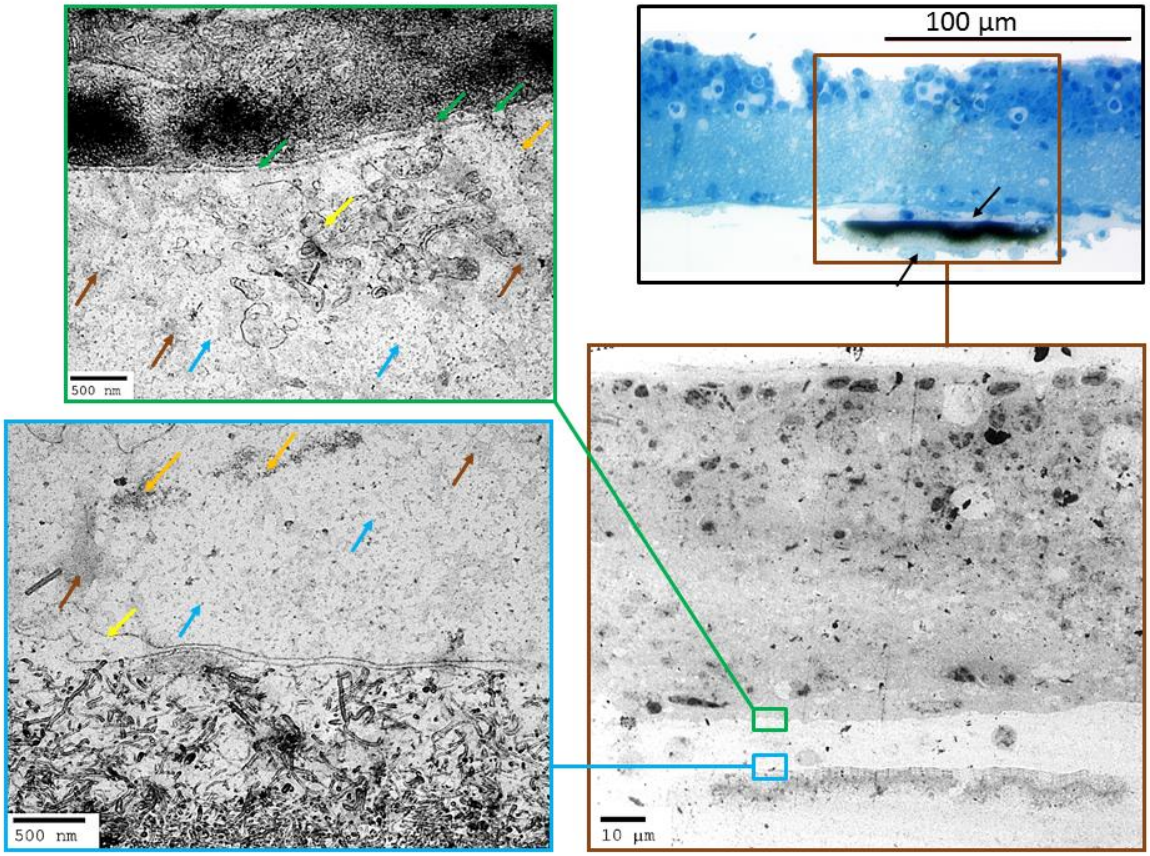

Figure 4.15: Secretion of globular substance by Müller cells after 12 hours. Black-lined panel: optical micrograph of a semi-thin section of the same retina as figure 4.14. Brown, blue and green-lined panels: increasingly high magnification TEM micrographs of ultra-thin sections of the same retina presenting higher magnifications of the grainy (blue arrows) and uniform (brown arrows) forms of the substance. Pores in the ILM (green arrows) indicate that the origin of this substance could be its secretion by Müller cells. The presence of both vesicular (yellow arrows) and fibrous (orange arrows) elements highlights the biological nature of the gel-like substance since they are not CNTs.

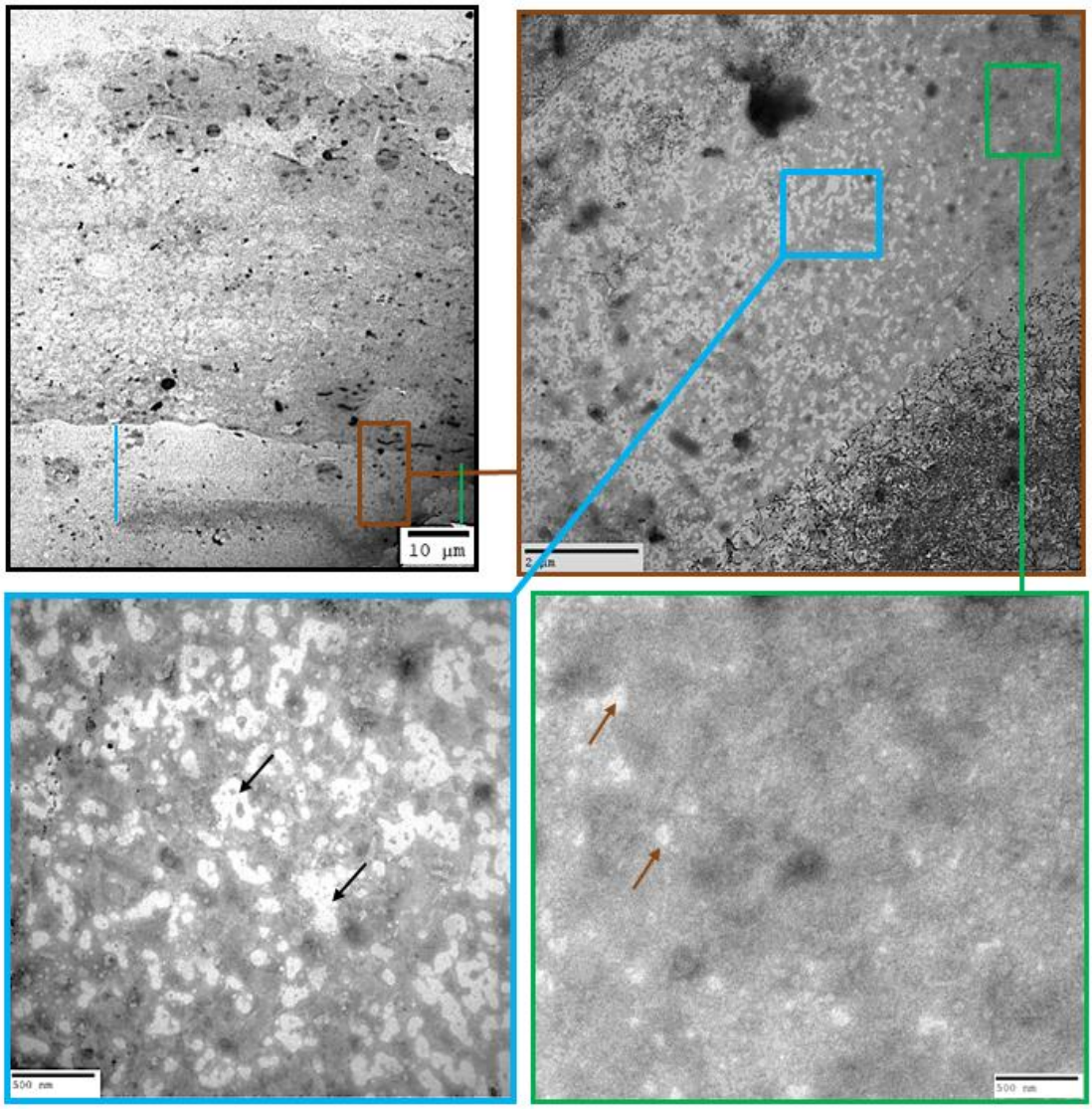

Figure 4.16: Thickening of globular substance as CNT island gets closer to the retina after 12 hours. TEM micrographs of the same retina as figure 4.14. Black-lined panel: the edge of the island is farther away from the retina (blue line, 15.6 µm) than the part close to the centre (green line, 9.9 µm). The globular substance becomes thicker and more homogenous as the distance between island and retina decreases, with a reduction in the number and area of gaps in the matrix. As such, black arrows in the blue-lined panel point to gaps larger than the ones pointed out in the green-lined panel by the brown arrows.

4.3.5 Structural incorporation of CNT islands

Between 12 and 24 hours, CNT islands get close enough for individual CNTs to penetrate the tissue, the retina starts to incorporate the islands within its structure. The optical micrograph of the 24 hour time point in figure 4.6 differs from that of the 12 hour time point in three fundamental ways. First, the retina and CNT island appear to be in direct contact, with the shape of the retina becoming modified to accommodate the island. In addition, both the amorphous matrix surrounding the island and the hypertrophied cells are no longer visible. Details of the interactions between the retina and CNTs at this time-point are revealed by TEM micrographs.

After 24 hours *in vitro*, the microglial component of the retinal response is no longer visible. However, the islands are encapsulated in biological material, adhering to the CNTs both above (interface with ILM) and below the islands. An accessory limiting membrane is formed to provide this encapsulation. Such membranes are seen in the brain and spinal cord following astrocytosis and encapsulation of foreign bodies (Fitch and Silver 2008). After 24 hours *in vitro*, individual CNTs are now close enough to penetrate the ILM.

Figure 4.17 displays a CNT island interfaced with a P90 CRX -/- retina for 24 hours *in vitro*. The island is broken at its mid-section (brown-lined panel, red double-arrow). There is biological material adhering to the CNTs at the top, bottom and sides of the island (brown arrows). On the left-hand side of the island (blue-lined panel), the CNTs are adhering to biological tissue from an opening in the retina (detailed in figure 4.18). There is no basement membrane and the CNT island has completely infiltrated the retinal tissue. On the right-hand side of the island (green-lined box) the ILM (black arrows) still presents a barrier to the CNTs. An accessory limiting membrane (blue arrow) encapsulates the CNT island from the bottom.

Figure 4.18 displays TEM micrographs of the same section as figure 4.17 with a focus on the opening in the ILM (blue-lined panel, blue arrow). The brown-lined panel displays an area where the ILM (black arrow) is intact with CNTs lodged in the *lamina rara externa* (brown arrows). The blue-lined panel displays an area where the ILM is no longer a barrier to CNTs which can now interact with vesicular material (green arrows).

The retinal tissue to the left of the blue-lined panel is completely integrated with the CNTs at the surface of the island (green-lined panel).

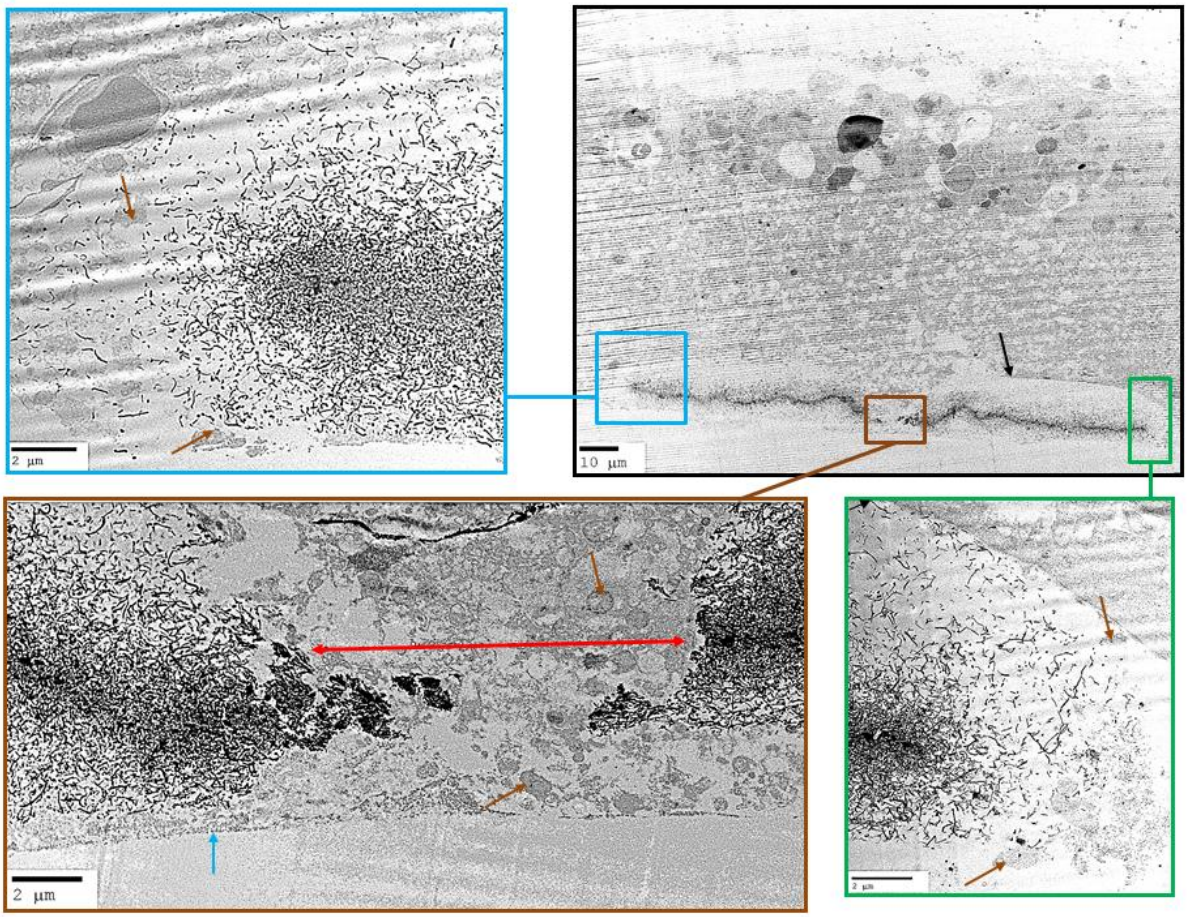

Figure 4.17: Encapsulation of CNT island after 24 hours. TEM micrographs of a P90 CRX -/- retina interfaced with a "large" CNT island for 24 hours. Blue-lined panel: biological tissue (brown arrows) is extruded from the left hand side of the island encapsulating it with a relatively straight accessory limiting membrane (blue arrow). Green-lined panel: on the right-hand side the ILM (black arrow) is still a barrier to the CNTs.

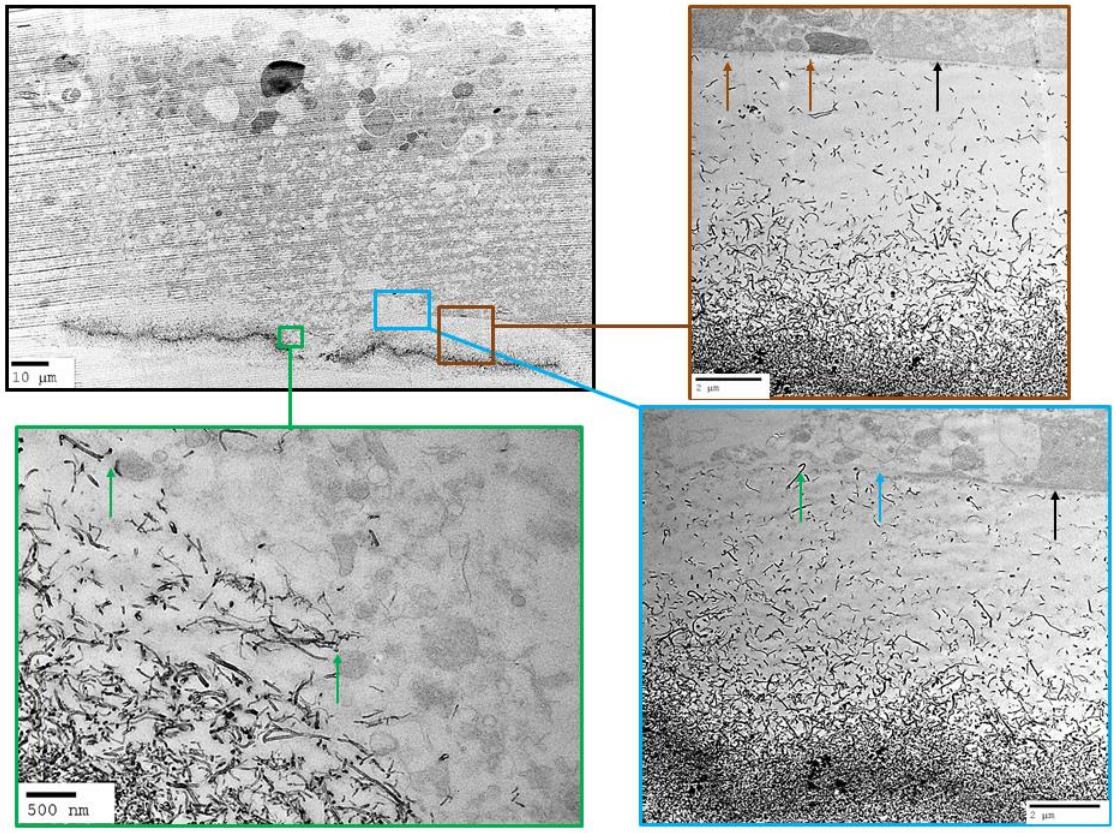

Figure 4.18: Break in ILM after 24 hours. TEM micrographs of the same section as figure 4.17. Brown-lined panel: ILM (black arrows) with CNTs in its *lamina rara externa* (brown arrows). Blue-lined panel: point where the ILM ceases to be a barrier (blue arrow) after which point CNTs interact with vesicular retinal tissue (green arrows, blue and green-lined panels).

In figure 4.19, the black-lined panel demonstrates the retina (black arrow) remodelling its shape drastically to accommodate the CNT island. Indeed, the retina is 76.4 µm thick before the island (blue arrow) and 61.65 µm thick at the apex of the island (dotted blue arrow). In the black-lined panel, the retinal tissue directly above the island appears darker than the surrounding tissue. This could be either biological or an acquisition artefact due to the contrast difference between island and retina. The brown-lined panel highlights the genesis of an accessory limiting membrane (brown arrow), which encapsulates the island with biological material (green arrow). The blue, green and orange-lined panels are high magnification micrographs focusing on a single CNT penetrating the ILM (orange arrow).

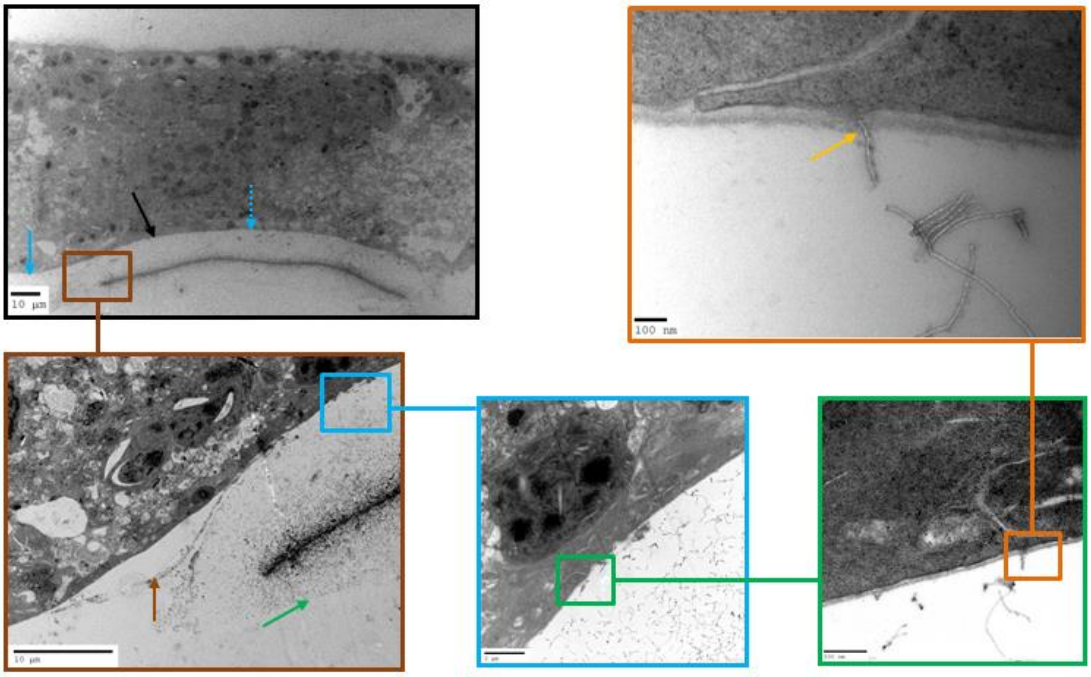

Figure 4.19: Genesis of accessory limiting membrane to encapsulate "large" CNT island after 24 hours. TEM micrographs of a P90 CRX -/- retina interfaced with a "large" CNT island for 24 hours. Black-lined panel: the retina dramatically adapts its shape to accommodate the CNT island. Brown-lined panel: additional element of this encapsulation is the genesis of an accessory limiting membrane (brown arrow). Blue, green and orange-lined panels: consecutive series of higher magnification micrographs allows the visualisation of a single CNT penetrating the ILM (orange arrow, orange lined-panel).

4.1.1 Adhesion of CNTs to inner retina

Optical micrographs of semi-thin retinal sections at the 48 hour time point indicate the CNT islands to be integrated within the retina, forming a bio-hybrid composite (figure 4.6). High magnification TEM micrographs reveal the presence of a homogenous matrix which completely encapsulates the edges of the CNT islands, making it continuous with the ILM. Figures 4.20 to 4.22 display the edges of the island at one of these bio-hybrid retinal composites, figure 4.22 shows the edges of the ILM at a point where one of the islands was ripped off. In all these figures, the black-lined panel shows the micrograph of a Toluidine Blue stained semi-thin retinal section and the brown-lined panel its TEM counterpart. Figures 22 and 23 display a "thin" CNT island which was integrated to the inner retina after only 24 hours.

Figure 4.20 displays the top edge of the interface between the retina and the CNT island at increasingly high magnifications. The globular matrix which first appeared at the 12 hour marker has now disappeared, replaced by a grainy homogenous substance (black arrows) which extends out of a dense network of collagen fibrils and glycosaminoglycans (green arrow). Vesicular elements (brown arrows) within this substance adhere to single CNTs (blue arrows).

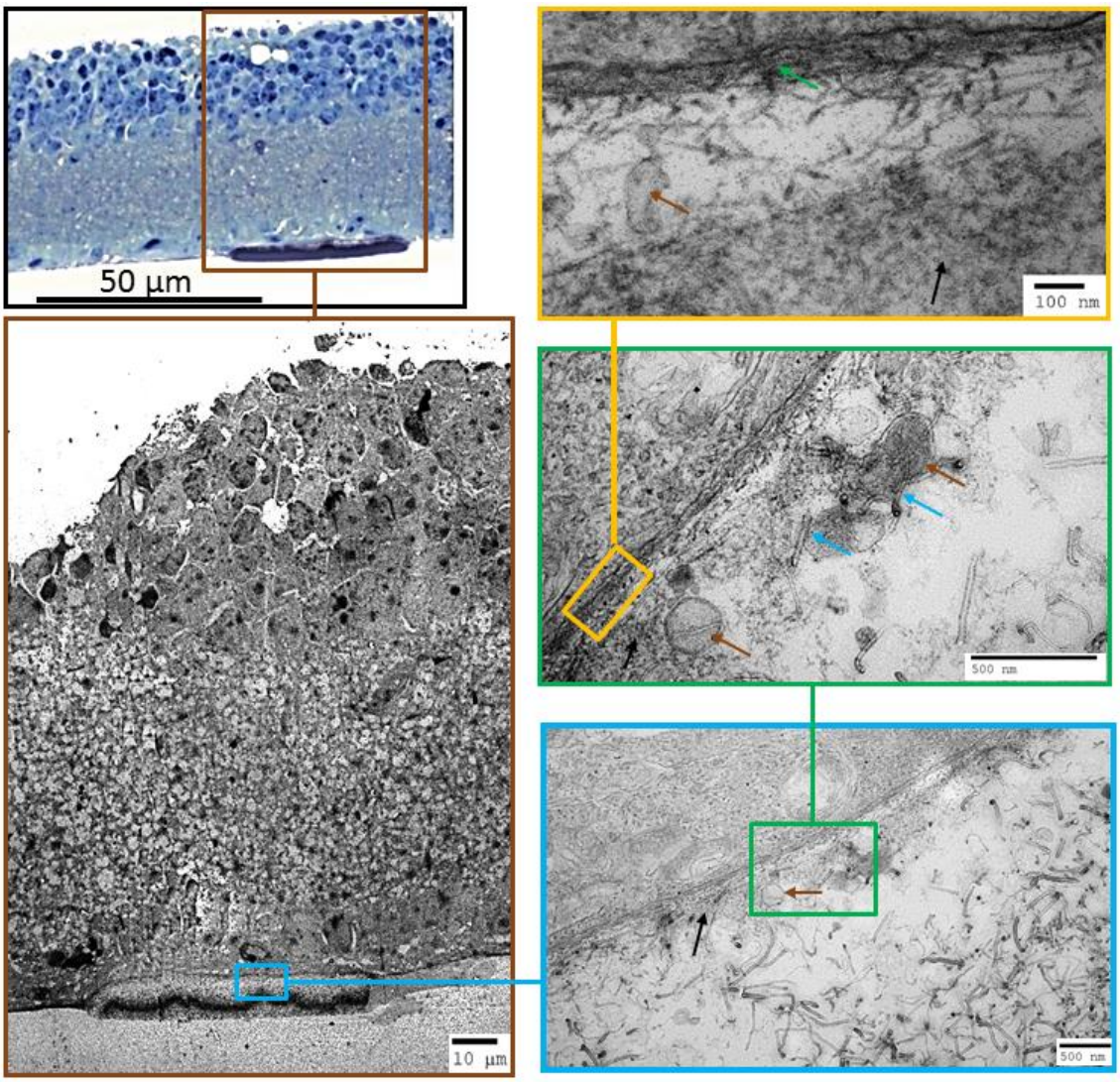

Figure 4.20: CNT island embedded in the ILM of a retina after 48 hours. Black-lined panel: optical micrograph of a semi-thin section of P90 CRX -/- retina interfaced with a CNT island for 48 hours. Brown, blue, green and orange-lined panels: increasingly high magnification TEM micrographs of ultra-thin sections of the same retina showing the island embedded in the ILM. A grainy substance (black arrows) emanates from the l*amina rara externa* where CNTs (blue arrows) adhere to vesicular material (brown arrows) and collagen fibrils (green arrow).

Figure 4.21 presents the homogenous matrix grappling the edge of a CNT island as it extends for over 24 µm to an invagination of the ILM (blue arrow). En route to this invagination, the matrix thins out progressively from 3.1 µm at the edge of the island to 294.5 nm, at a point of vesicular secretion (brown arrow) 9 µm further away, while getting progressively more electron-dense. A deeper invagination 3 µm away (black arrow) appears to secrete the *lamina rara externa* (green arrow). The green-lined panel highlights two of the multiple undulating points (orange arrows) in the ILM to accommodate the CNT island within the inner retina. On the right side of the island, the matrix appears to stop abruptly (brown-lined panels of figure 4.20), possibly due to a tear during processing.

Figure 4.22 presents the edge of a void where a large CNT-island has been ripped out. The brown-lined panel focuses on the homogenous matrix described above, pointing to clusters of CNTs (black arrows) embedded in this matrix. The blue lined panel focuses on the ILM, which presents a thick and dense *lamina rara interna* (brown arrow), a non-existent *lamina densa* and a thinly collagenous *lamina rara externa*. The green-lined panel displays the apex of the ripped-out island on the ILM, pointing to clusters of CNTs (black arrows) adhering to organelles (green arrow) and collagen fibrils (blue arrow).

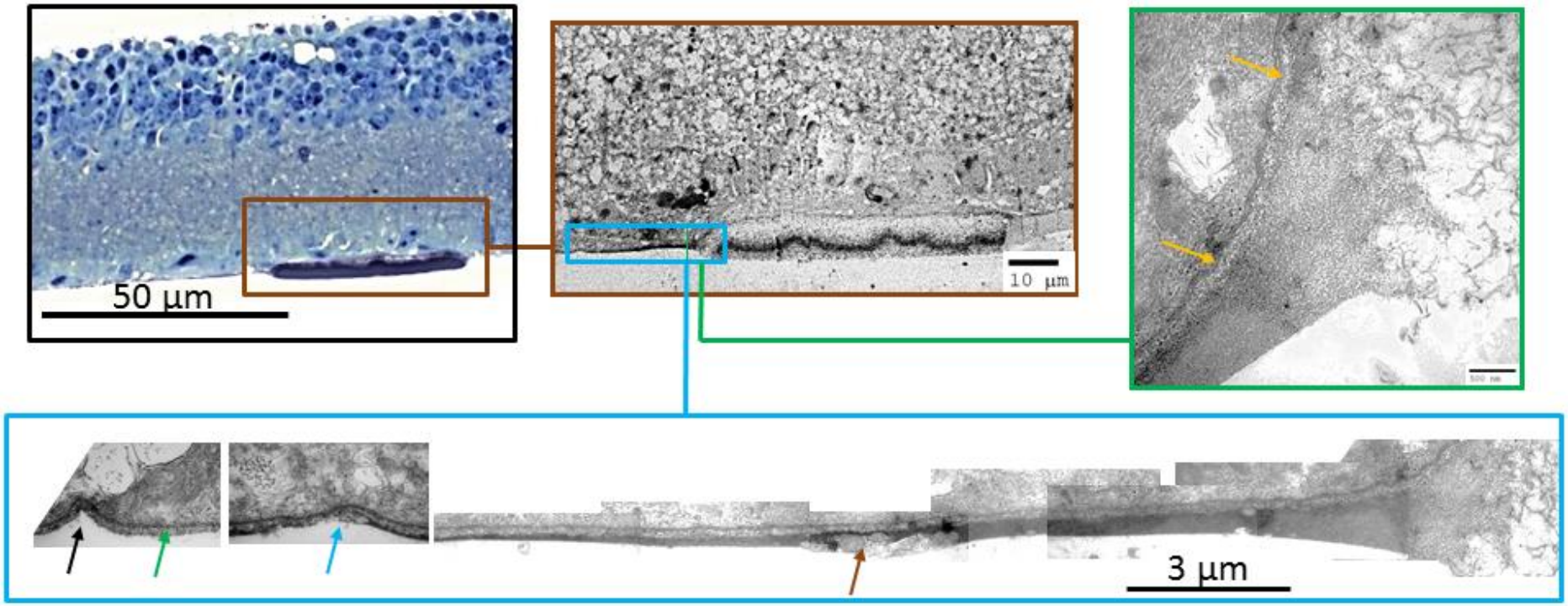

Figure 4.21: Homogenous matrix grappling edge of CNT island after 48 hours *in vitro* extends along the retina for over 24 µm. Black-lined panel: optical micrograph of the same section as figure 4.23. Brown, blue and green-lined panels: increasingly high magnification TEM micrographs from the same retina with the CNT island grappled by a long homogenous matrix (blue box). The blue-lined panel shows a photo-montage of 10 TEM micrographs which follow the matrix to an invagination in the ILM 23 µm away (blue arrow). The matrix becomes progressively thinner and denser as it approaches the invagination and passes an area of vesicular release (brown arrow). 4 µm further, a deeper invagination (black arrow) produces a fold in the ILM secreting *lamina rara externa* (green arrow). The green-lined panel displays a higher magnification micrograph showing the homogenous matrix grappling the edge of the CNT island. Here, the ILM is undulated at multiple locations (orange arrows) to accommodate the absorption of the CNT island within the innermost layers of the retina.

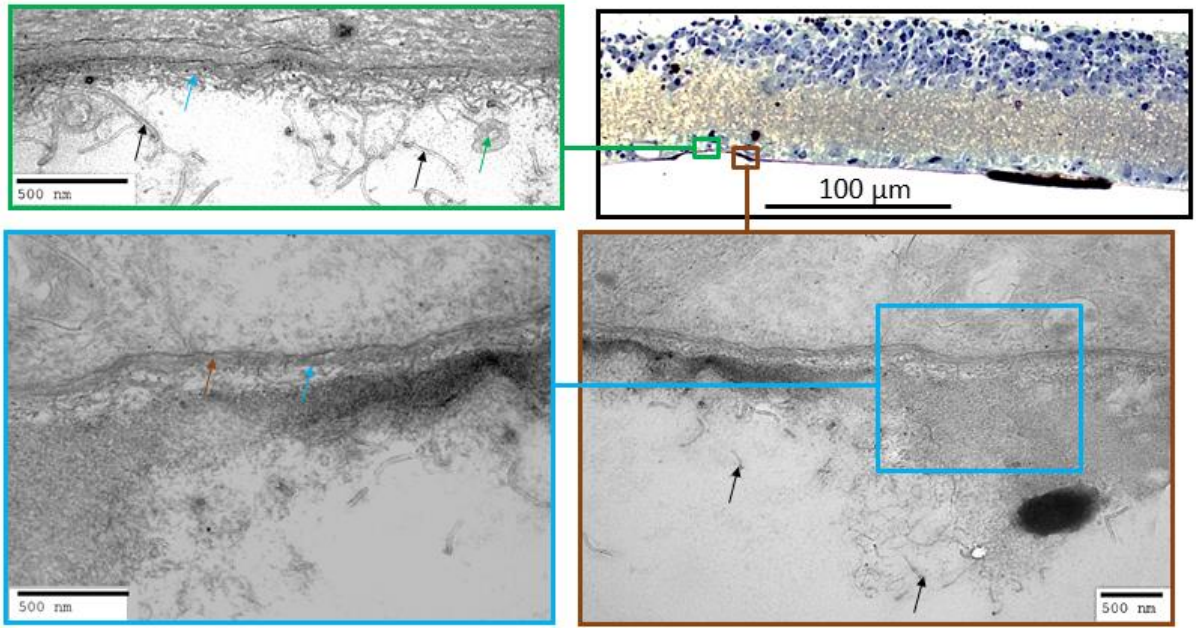

Figure 4.22: CNTs embedded in matrix following the ripping of island from ILM after 48 hours. Black-lined panel: optical micrograph of a semi-thin section of P90 CRX -/- retina interfaced with a CNT island for 48 hours. Brown and blue-lined panels: increasingly high magnification TEM micrographs of ultra-thin sections of the same retina focusing on the ILM, with the CNTs embedded in a homogenous matrix. The blue-lined panel focuses on a distended ILM which consists mostly of a dense *lamina rara interna* and a thin collagenous *lamina rara externa*, with virtually no *lamina densa*. The displaced island's apex is displayed in the green-lined panel, where individual CNTs (black arrows) are seen adhering to vesicular elements (green arrow) and collagen fibrils (blue arrow).

Figures 4.23 and 24 present the interfacing of a "thin" CNT island (black arrows) with a P90 CRX -/- retina after 24 hours *in vitro*. These images are very rare in our data set as thin CNT islands are difficult to detect with optical microscopy of Toluidine Blue stained semi-thin sections. The presence of these islands is an artefact of fabrication as islands are typically several microns thick whilst these are only about 1 µm thick. The brown-lined panel displays a portion of the island which was broken off during processing, emphasising the strength of adhesion between tissue and CNTs. As with the "large" islands described above, the biological material adheres to both sides of the island (brown arrows). The blue-lined panel displays the penetration of the ILM (green arrow) by individual CNTs (blue arrows). Here, the ILM is significantly thinner than in other micrographs, possibly explaining the ease of penetration for individual CNTs. Conversely, it might have become thinner as a result of 24 hours interfacing with these types of islands.

In figure 4.23, the black-lined panel displays tissue with its epi-retinal surface intruded with CNTs. The brown and blue-lined panels display higher magnifications views of CNTs (black arrows) interacting with retinal tissue (blue arrows), including large vesicular elements (brown arrow). In figure 4.24, the island was broken during tissue processing and retinal tissue binding the island has been ripped off the retina, illustrating the strength with which the CNTs bind to both sides of the retinal tissue (brown arrows).

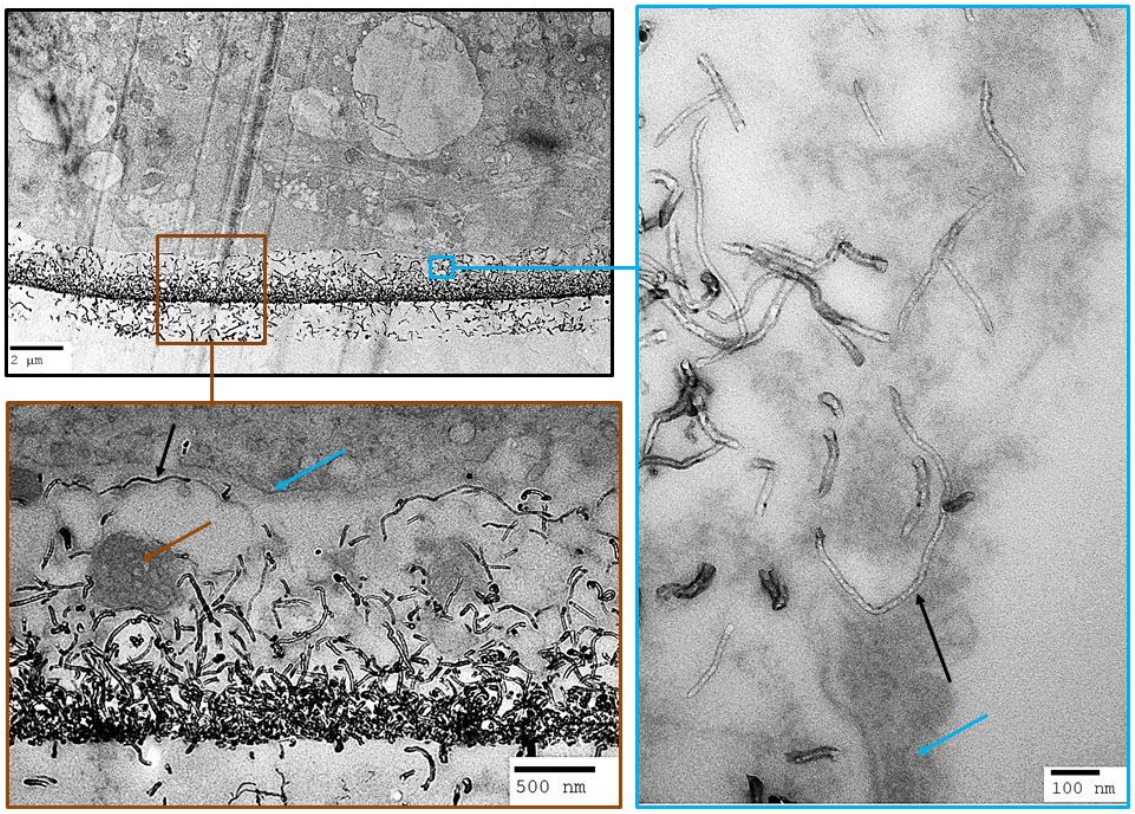

Figure 4.23: Interfacing of Crx retina with a thin CNT island after 24 hours. TEM micrographs of a P90 CRX-/- retina interfaced with a thin CNT island for 24 hours. Black-lined panel: innermost retinal layers in contact with a thin CNT island. Brown and blue-lined panels: higher magnification TEM micrographs allowing the resolution of individual CNTs (black arrows) binding to retinal tissue (blue arrows) including large vesicular elements (brown arrow).

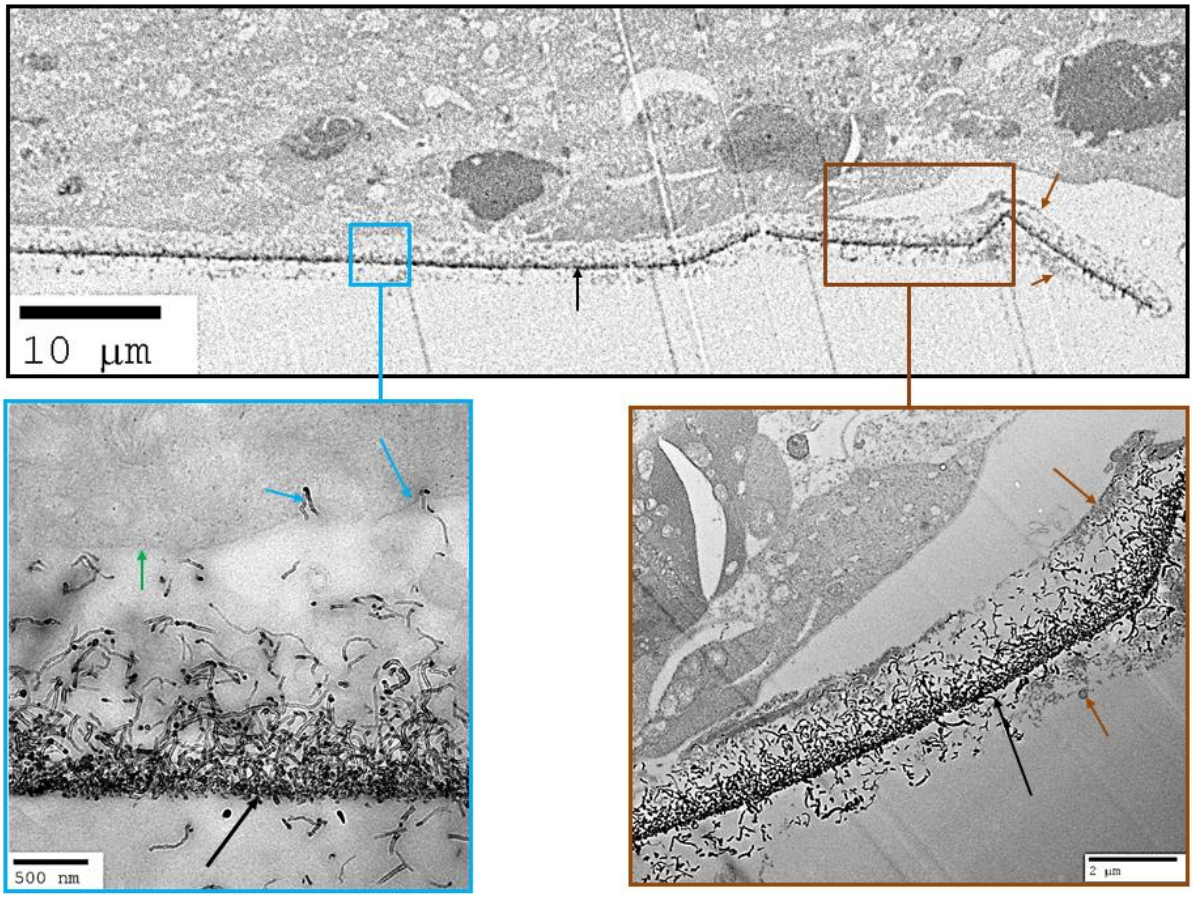

Figure 4.24: Interfacing of CRX retina with a broken thin CNT island after 24 hours *in vitro*. TEM micrographs of the same section as figure 4.21. Black-lined panel: the innermost retinal layers are in contact with a thin CNT island (black arrows). Brown-lined panel: island is shown to be encapsulated on both sides by biological material (brown arrows). Blue-lined panel: individual CNTs (blue arrows) penetrate the ILM (green arrow).

4.3.6 SEM control data

In order to characterise the interfacing of CRX -/- retinas with CNT islands, it is important to understand the topography of this tissue prior to neuro-engineering manipulations. Figure 4.25 displays SEM micrographs of half a P88 CRX retina with particular focus on the vitreo-retinal interface, which appears smooth, despite sub ILM elements affecting its topography such as axon fibre bundles (black arrows) and indentations, which could be blood vessels or glial endfeet (brown arrows) as well as remnants of the cortical vitreous (blue arrows). In contrast, the green-lined panel displays a portion of the retina's exterior limiting membrane, displaying chaotic evidence of dead photoreceptors in the outermost layer of these degenerated retinas. Incisions to planarize the explant were made post-fixation, to avoid reactive gliosis.

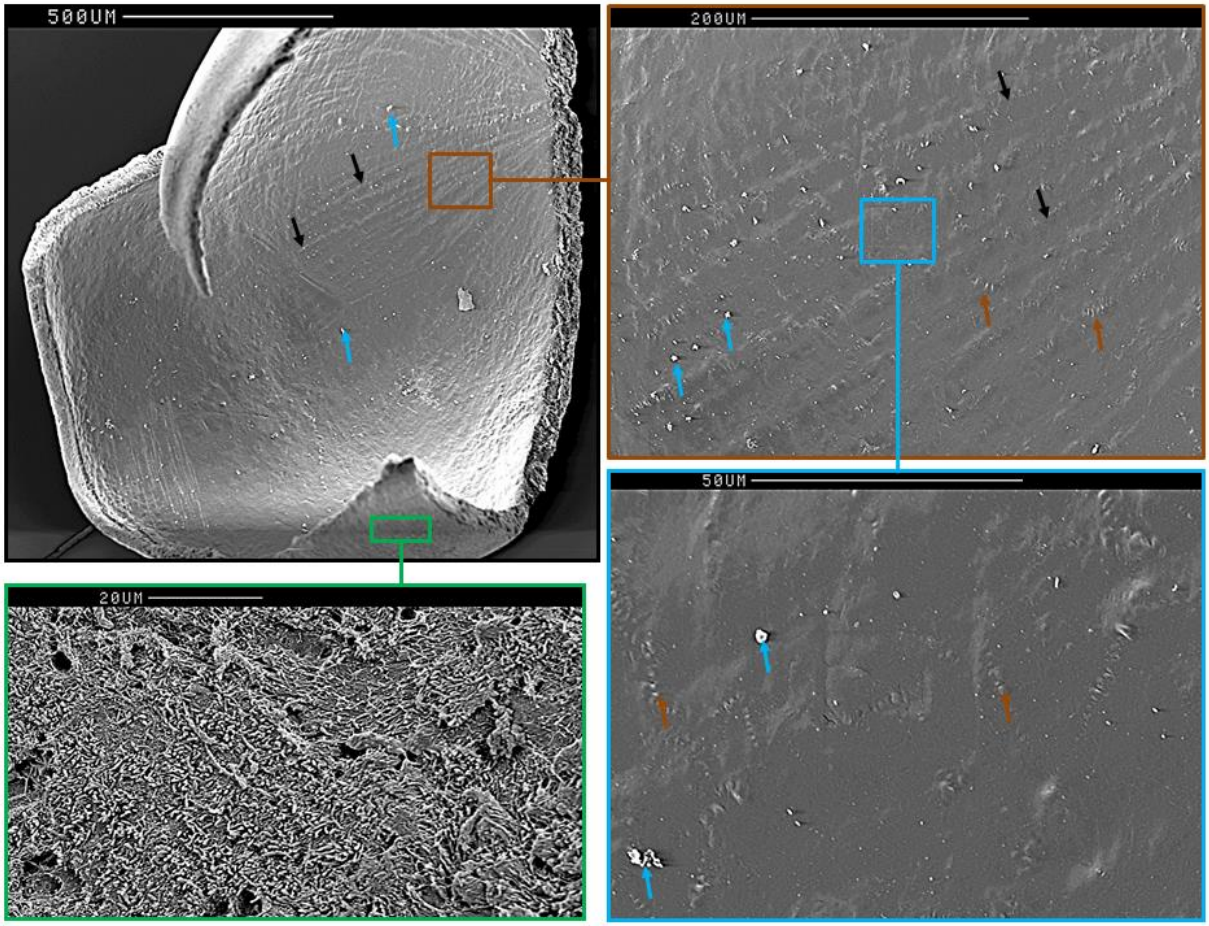

Figure 4.25: Smooth ILM on P88 CRX -/- retina. Increasingly high magnification SEM micrographs of a P88 CRX retina demonstrating the smoothness of the ILM (black, brown and blue-lined panels) compared to the roughness of its ELM (green-lined panel). Amid its bare surface, the ILM presents evidence of the structure's exterior (remnants of vitreous, blue arrows) and interior (axon bundles, black arrows; Müller cell end-feet, brown arrows) to it.

4.3.7 SEM large CNT islands

In this section, we present SEM micrographs of retinal explants which have been interfaced with “large” CNT islands for 48 hours *in vitro*. After dehydration in ethanol and critical point drying, the samples are very brittle, resulting in cracking along interesting features. Figure 4.26 presents a retinal explant with 10 CNT islands (black arrows) visible upon its surface. This explant surface (ILM, brown arrows) is smooth and representative of the typical retinal ILM in SEM micrographs (*c.f.* figure 4.25). The brown-lined panel focuses on one of the islands, exposing fibrous bundles (blue arrows) grappling the side of the island. The blue-lined panel focuses on part of the island periphery, which appears to be covered in an accessory limiting membrane (green arrows) approaching the texture of the ILM, with gaps in it (orange arrows) exposing the CNTs below (yellow arrows). The green-lined panel focuses on a CNT island which has been cracked following critical point drying (*cf.* methods). This allowed visualisation of biological bundles (as described above) infiltrating the CNT island throughout (blue arrow). These fibres cannot be the CNTs as TEM analysis has demonstrated that these are curled and disorganised whilst here, the fibres are aligned parallel to each other. A dotted white line continuous with the ILM reveals that half of the island volume is integrated in the retina.

As observed in figure 4.26, the CNT islands are not completely flat. Figure 4.27 displays SEM images of the retinal bio-hybrids with the ILM facing up allowing the visualisation of the topography below the CNT islands (black arrows). The black and brown-lined panels highlight invaginations (brown arrows) across the CNT islands. These appear to be the focus of grappling by fibrous bundles (green arrows), leaving the rest of the island surface encapsulated in the limiting membrane (orange arrows) mentioned above. CNTs (blue arrows) provide a solid and complex matrix of adhesion points for the bundles to grapple (green-lined panel). These invaginations possibly result from a break between islands and the substrate they were grown on, or from processing artefacts.

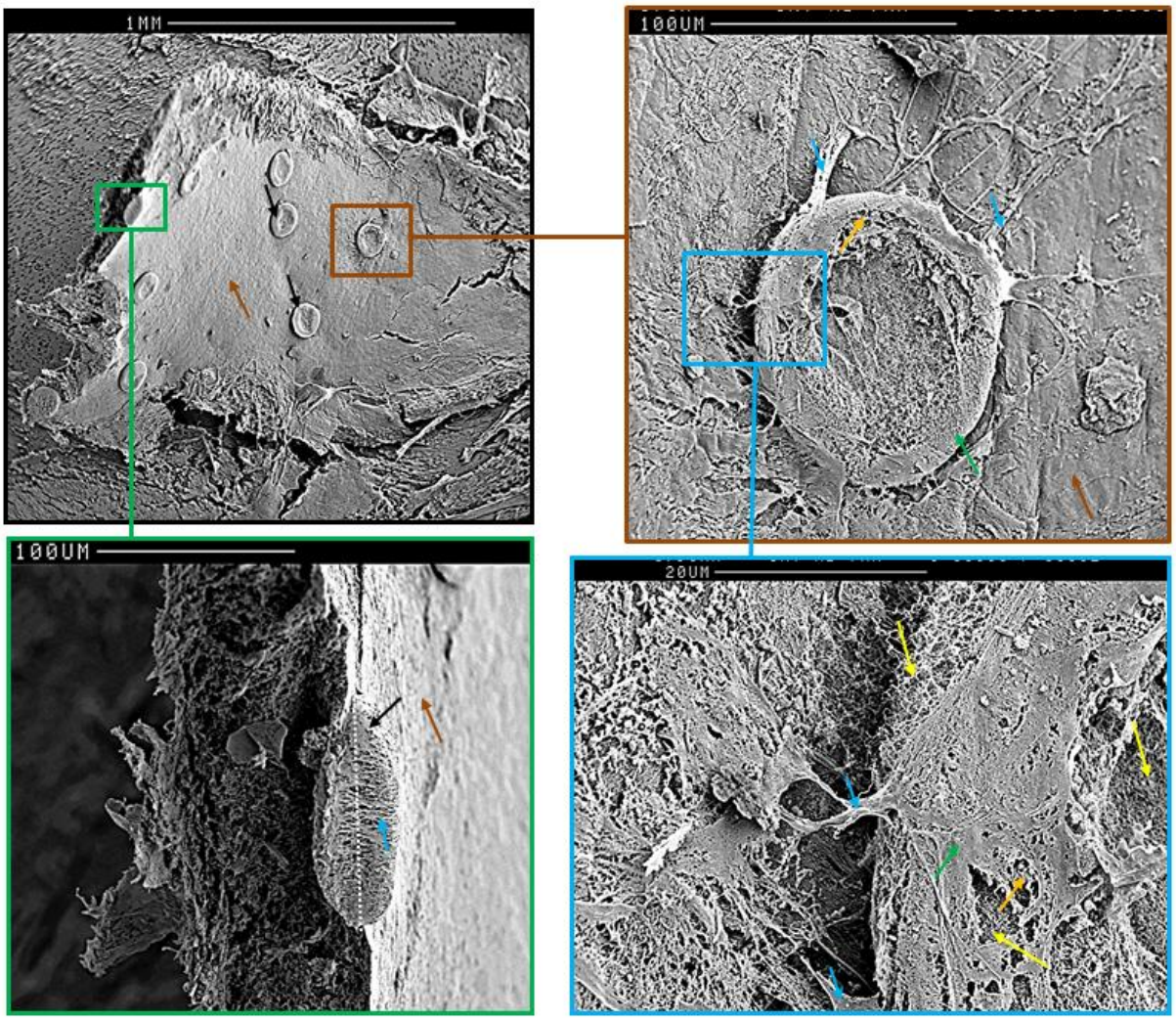

Figure 4.26: Grappling of CNT island by bundles issued from the ILM of a retinal explant after 48 hours. Increasingly higher magnification SEM micrographs of a P89 CRX -/- retina interfaced with CNT islands for 48 hours. Black-lined panel: explant with 10 islands (black arrows) adhering to its surface. Brown-lined panel: focus on one of these islands, revealing bundles of ILM fibres (blue arrows) grappling the side of the island and encapsulating it in an accessory limiting membrane (green arrows). Blue-lined panel: gaps exposing CNTs (yellow arrows) beneath the accessory limiting membrane. Green-lined panel: focus on one of the islands which has been cracked showing half of its volume (white dotted line) to be within the retina and parallel fibrous bundles (blue arrow) infiltrating it throughout.

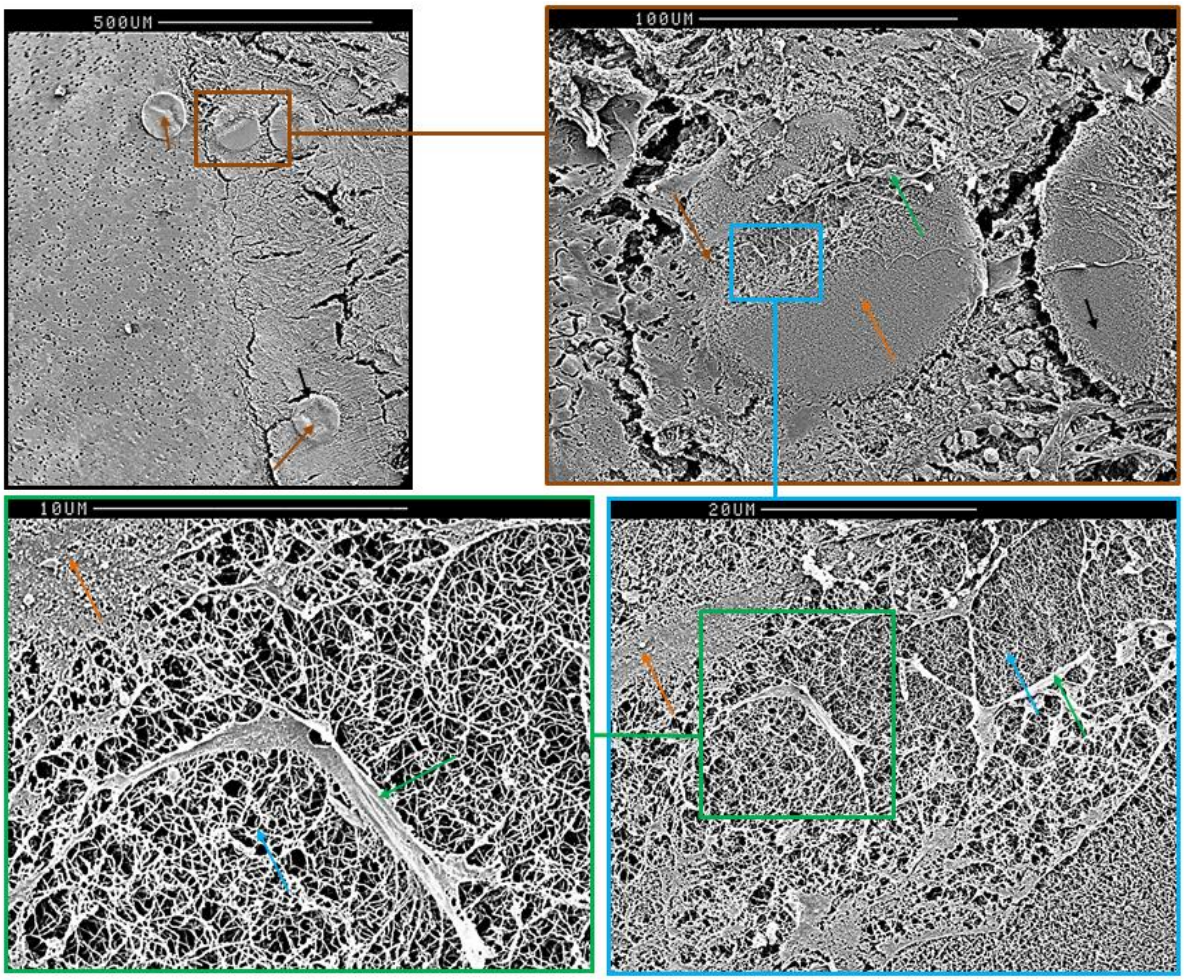

Figure 4.27: Invaginated topography of CNT island underside provides adhesion points for ILM fibrous bundles after 48 hours. Increasingly higher magnification SEM micrographs of a P89 CRX -/- retina interfaced with CNT islands for 48 hours. Black lined panel: 4 islands at the surface of the retina. Brown-lined panel: focus on one island. Blue-lined panel: focus on invaginations (brown arrows) in the CNT islands (black arrows) provide adhesion points for the fibrous bundles (green arrows) before their thickening into an encapsulating accessory limiting membrane (orange islands). Green-lined panel: focus on one of the fibrous bundles allowing resolution of individual CNTs.

4.3.8 SEM small CNT islands

The retinal explant in the black-lined panel of figure 4.28 presents at least 57 “small” CNT islands (black arrow) at its surface. Their precise number is difficult to estimate because some are deeply embedded within the accessory limiting membrane (brown arrow) and others are covered in a highly filamentous matrix (blue arrows) which appears to thicken (green arrows) before achieving the smooth texture of the ILM (orange arrow). The arrangement and pitch has changed radically from a gridline with 50 µm centre-to-centre pitch (green-lined panel) to a honeycomb arrangement with a 20 µm (the island diameter, meaning that the islands are touching each other) centre-to-centre pitch. This suggests that the encapsulation of the islands by the fibrous filaments of the ILM has displaced the islands together in a honeycomb cluster.

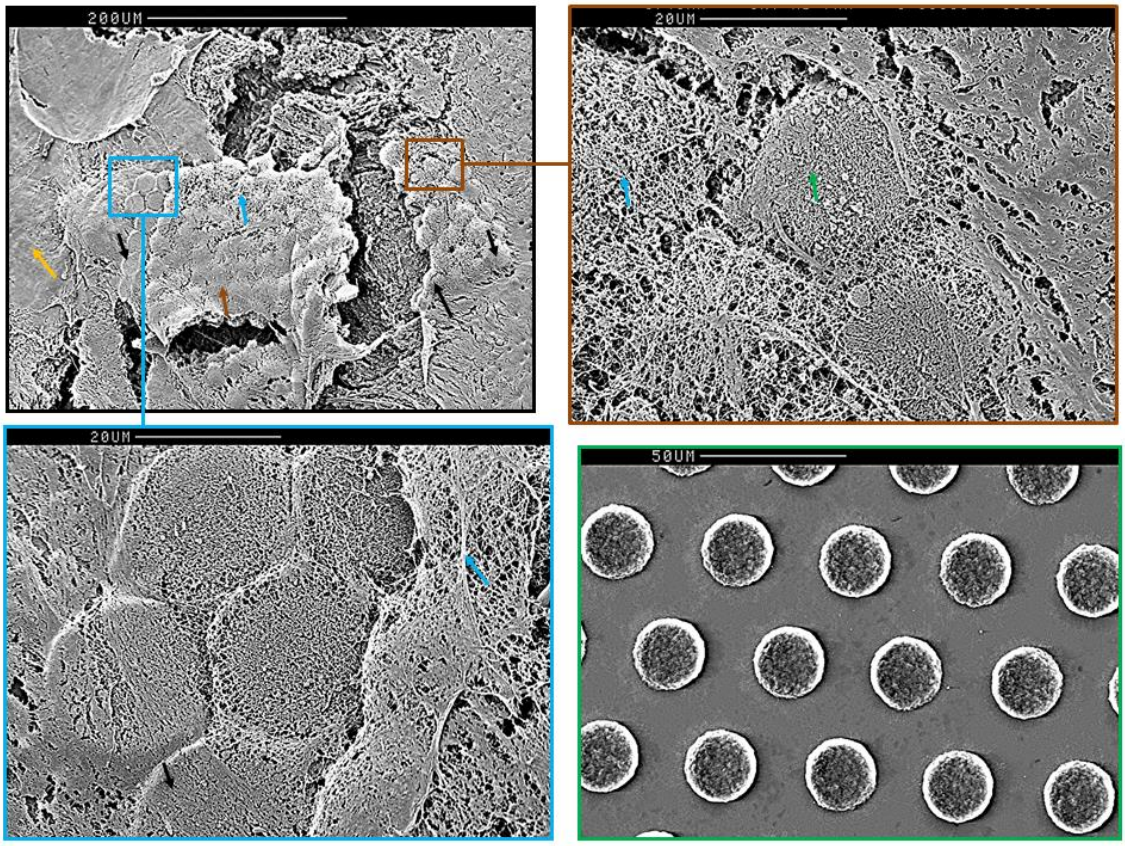

Figure 4.28: Encapsulation of small CNT islands into a honeycomb by filamentous fibres of the ILM after 48 hours. Increasingly higher magnification SEM micrographs of a P89 CRX explant interfaced with CNT islands for 48. Black-lined panel: retinal explant with over 50 islands (black arrows) embedded into the ILM (orange arrow) and clustered into a honeycomb structure. This structure differs substantially from the original orthogonal arrangement of “small” islands (green-lined panel). After grappling the CNTs, the fibrous material of the ILM (blue arrows) contracts and thickens into the smooth surface (brown arrow) continuous with the ILM (orange arrow).

4.4 Discussion

By combining the data obtained from optical, TEM and SEM, we can deduce a functional schematic for the integration of CNT islands within the CRX retinas during the penultimate degeneration stages (i.e. prior to phase 3, *cf.* Chapter 1). Interpretation of the biological events presented here is challenging. Indeed, the literature is abundant in ultrastructural description of normal (Hogan and Feeney 1963; Yoshimoto 1978) and dystrophic retinas, both in rodents (Jones, Watt et al. 2003; Jones and Marc 2005; Garcia and Koke 2009) and humans (Szamier and Berson 1977; Cotter and Noell 1984) but accounts of the ultrastructure of the CRX retina has been limited to the photoreceptor and plexiform layers (Morrow, Furukawa et al. 2005). The authors of the most comprehensive papers on retinal remodelling (Jones and Marc 2005) argue that remodelling occur in three distinct phases for all models of degeneration, the only variable being the speed at which the processes occur within each phase. We have thus extrapolated our observations from EM presented in the literature.

4.4.1 Incorporation of CNT islands within the retina

At the 4 hour time point, the CNTs do not appear to be in direct contact with the retina but rather approximately 10 µm away from the tissue. This could be due to a technical artefact occurring during one of the many steps involved in preparing resin blocks for TEM. Moreover, this time point does not reveal any morphological changes in retinal structure, indicating that the retina begins to "sense" the presence of the CNT island between 4 and 12 hours. This is counterintuitive as, during experimental preparation, the retina is flattened down onto the islands and appears to be in direct contact with them. Moreover, electrical recordings indicate changes in coupling within just a few hours (*cf.* Chapter 3 and Shoval *et al.* 2009) An extensive ultrastructural study of the carbohydrates of the mouse ILM (Rhodes 1982) reveals a labile component of the vitreo-retinal juncture composed of HA (figure 4.29) and only detectable after prolonged fixation in glutaraldhyde (192 hours). It is possible that this layer prevents the island from entering in direct contact with the retina, before dissolving several hours later.

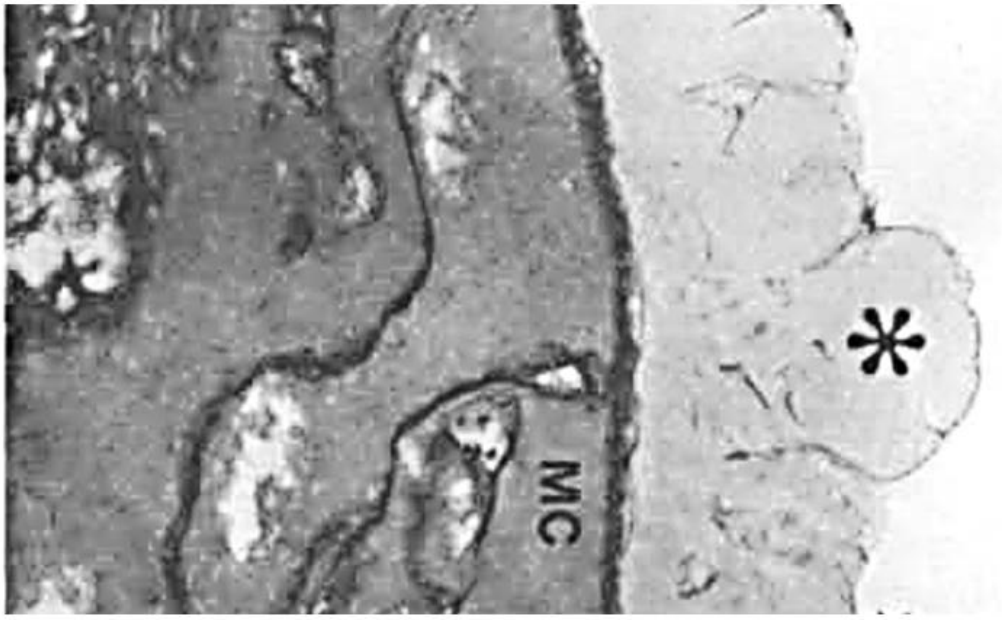

Figure 4.29: Hyaluronic component of the mouse retinal ILM. TEM micrograph of mouse ILM, highlighting its HA component (asterisk). Here, the tissue was fixed for 192 hours in glutaraldehyde and cetylpyridinium chloride, postfixed in osmium tetroxide and block-stained with ruthenium red. MC, Müller cell; x30,000; adapted from (Rhodes 1982).

A 12 months ultrastructural study on primate eyes following ILM removal assisted with indocyanine green (Nakamura, Murata et al. 2003) reveals extensive regeneration of Müller cell-end feet displaying a meshwork like configuration at 3 and 6 months. However, the ILM was still not fully regenerated after 12 months. This contradicts our assumption that the ILM has regenerated after 24 hours *in vitro* (*cf.* figure 4.19). We can argue that both the conditions and the animals are radically different to those of this paper, but this observation highlights the fact that in these figures, the ILM is still open at one end of the island; and in the 12 hour time point figures, it is only open in discrete areas. Thus, it is possible that not all of the ILM opens up to the CNT islands. The active removal of the ILM by indocyanine green is potentially much more severe than interfacing retinas with CNTs. Breaches of the ILM may be due to handling of the retina during dissection especially with stainless steel anchors pushing down upon it.

The accessory limiting membrane appearing at the 24 hour time-point and visible as a thick grainy matrix at the 48 hour time point appears to be an evolution of the globular matrix first seen at the 12 hour time point. The filamentous bundles grappling the sides of the large CNT island in SEM figures at the 48 hour time point present a

comparable morphology to the grainy matrix grappling the edge of CNT islands in the TEM figures of this time point. Indeed, both the fibres pointed out by blue arrows in the brown-lined panel of figure 4.31 measure 36 (left) and 49 μm (right), the same order of magnitude as the 24 μm long process of figure 4.21. From a morphological point of view, this substance is very similar to cartilage, which is illogical as there are no chondroblasts in the retina. However, cartilage is a ground substance containing elements known to be present in the ILM: collagen and proteoglycans. The secretion of these components by the retina is the first step in the incorporation of CNT islands into its inner layers, making them useful adjuncts in the field of epi-retinal prosthesis. The secretion of ECM by retinal astrocytes and Müller cells to fill the lumen of small capillaries has been observed in RP patients (Dryja and Li 1995).

The ILM's primary role is to provide an adhesive structure for the Collagen II containing vitreous humour. However, it is not adhesive enough to support epi-retinal prosthetic devices which currently require surgical tacks for securing electrodes to the tissue (Behrend, Ahuja et al. 2009), resulting in poor coupling between electrode and target neurons. According to our findings, using CNT electrodes (rather than more conventional materials such as platinum) would resolve this problem by ensuring a strong and biocompatible adhesion between the device and the retina.

As described in detail in Chapter 1, CNTs are a promising material exhibiting biocompatibility, strength and a surface roughness inductive to neural adhesion. Previous work from our collaborators in Tel Aviv, using similar CNT islands as the ones in this chapter have demonstrated strong entanglement of neural and glial processes to the islands (Shein, Greenbaum et al. 2009) as well as migration of dissociated neurons towards CNT islands, resulting in the formation of functional networks (Zuo, Ehmke et al. 2012). Combined with the superior electrochemical properties of CNTs, these findings suggest that CNT islands are an ideal substrate to be used in a neuro-prosthetic device. Our findings corroborate this suggestion by demonstrating the incorporation of CNT islands within the retina. Penetration of CNTs into the neural retina opens up the potential to further enhance the tissue electrode coupling in the generation of intracellular electrodes. The grappling of CNT islands by fibrous processes demonstrates that the retina actively incorporate the islands.

4.4.2 Immune response of the retina to the presence of CNT islands

Reaction of the retina at the 12 hour time-point is very pronounced, displaying a plethora of responses, including microglial activation and deployment, Müller cell activation, the production of a globular extracellular matrix and degradation of the ILM. Although more experiments at a finer timescale between 4 and 12 hours would provide an insight as to the sequence of these events, the existing literature allows us to provide an initial interpretation of these processes.

Microglial cells have a dynamic nature, with ramified processes constantly sensing the environment while the pseudopodia arbor remains symmetrical in uninjured tissue. These processes become polarized as the microglia migrate towards an injury. Using a time-lapse confocal microscope system, Lee and colleagues (Lee, Liang et al. 2008) monitored the response times of retinal microglia in $CX3CR1^{+/GFP}$ mice following focal laser induced burning. They determined the significant response time to a focal burn (50 µm spot size) of microglia in an area of 163,881 μm^2 (calculated from an image presented in the paper) to be 30 minutes. In a more complicated setup using a confocal scanning laser ophthalmoscope on the same transgenic mouse strain, Eter and colleagues (Eter, Engel et al. 2008) determined the *in vivo* deployment of microglia to the site of injury to be 1 hour, with cells persisting for up to 9 weeks at the site of repair. The presence of microglial cells after 12 hours *in vitro* in our hands concurs with these findings.

As they are stationary, Müller cells generally rely on microglia to sense an injury and become activated (Harada, Harada et al. 2002) through the production of neurotrophic factors. However, physical damage to Müller cell end feet has the potential to induce a non-specific glial response in the form of GFAP and vimentin up-regulation. As such, the removal of the ILM assisted by indocyanine green is a widely used surgical technique used to treat macular holes (Olsen, Sternberg et al. 1998; Gandorfer, Messmer et al. 2000; Smiddy, Feuer et al. 2001). The mechanisms following this surgery is not well understood, although a strong hypothesis is that damage to Müller cell endfeet initiates activation of these cells, resulting in trans-retinal gliosis promoting regeneration as opposed to appoptosis. The absence of microglial cells after 24 hours *in vitro* is intriguing, contradicting countless studies and established literature

indicating the survival of microglia at injury sites for months on end. Perhaps microglial cells get washed away through the perfusion as they would not be able to phagocyte a 100 µm diameter island.

4.4.3 Future work

The ultrastructural analysis of *in-vitro* interfacing of CNT islands with degenerated retinas is in no way exhaustive. Indeed, the time consuming and financial requirements of such a project heavily outclass those attributed to the third of a PhD studentship. Refinement of the techniques required to obtain the results for the TEM component of this chapter took 9 months alone. Moreover, the sectioning of each retinal explant (half a retina) averaged 12 full days of work. However, this study paves the way to understanding how the retinal ILM reacts to foreign bodies of different topography and morphology, thus furthering the development of novel epi-retinal electrodes.

In the set of experiments described in this chapter, TEM micrograph analyses relied on existing literature to identify the morphology of biological structures observed. Although this works for a number of different structures (e.g. glial cells have a denser cytosol than neurons), it still leaves a number of questions unanswered as to the exact nature of cells adhering to the CNT islands. The use of immunogold labelling is an established technique for the detection of different proteins in TEM micrographs (Nagelhus, Horio et al. 1999) and would be invaluable to further experiments for this project.

One of the most important questions to that aspect of the field is how electrodes interact within the retina on a 3D level. The TEM micrographs in this section only provide a 2D view of different points whilst SEM micrographs only provide a view of the surface of the retina-CNT bio-hybrid. The 3D EM approach used to characterise connectomes (Helmstaedter, Briggman et al. 2008) combines automated ultra-sectioning within SEM. The addition of energy dispersive x-ray spectrometry has been demonstrated for the detection of immunogold labelling (Scott 2011; Geerts, Zeuschner et al. 2012). Combining these techniques would allow a deep and comprehensive investigation of the structural changes occurring in CNT retinal bio-hybrids.

Chapter 5: General Discussion

5.1 Overview and conclusions

5.1.1 Summary of findings

In this body of work, I have presented anatomical and electrophysiological evidence for an increase in coupling between dystrophic retinas and CNT assemblies over 48 hours *in vitro*.

Anatomical findings show that the ILM undergoes remodelling to incorporate these foreign bodies, with very little evidence of an immune response. TEM analysis reveals that the incorporation of CNT assemblies within the tissue occurs between 24 and 48 hours. SEM imaging displays ECM processes extending from the ILM and grappling the side of CNT islands. Small islands are completely incorporated into the ILM and compressed into a hexagonal lattice. IHC analysis reveals statistically low-occurring astrocytic agglomeration on CNT islands as well as damage to the tissue during culture, but not to inner retinal vasculature.

Electrophysiological evidence is characterised by a time-dependent increase in signal amplitudes, lowering of stimulation thresholds and increase in cellular recruitment for the RGCs of retinas interfaced with CNT-MEAs. Investigation of different stimulation parameters confirmed the findings of other research groups concerning epi-retinal electrical stimulation. As such, cathodic-first asymmetrical current waveforms with a ratio of 2 (Figure 3.2 B) are optimal for the capacitive stimulation of RGCs.

5.1.2 Retinal adhesion of CNT electrodes

The incorporation of CNT assemblies into the retinal ILM has strong implication for the development of retinal prosthetic devices. One of the major challenges in the field is the adhesion of epi-retinal prosthetic devices to the retina. Current solutions include the use of surgical tacks which introduce a gap between the retina and stimulating electrodes, thus increasing the threshold of RGC activation (Behrend, Ahuja et al. 2009; Behrend, Ahuja et al. 2011). The use of CNT stimulating electrodes could potentially resolve this problem by ensuring a functional adhesion point at each stimulating electrode location, whilst providing intrinsically good coupling.

Retinal immune responses to the CNT assemblies could have negative implications for the long-term use of such devices for retinal stimulation. This may be reduced by

functionalizing CNTs with anti-mitotics to prevent proliferation (Boyden, Zhang et al. 2005) or by adding anti-bodies to allow CNT-bioconstructs to only bind certain types of cells (Guiseppi-Elie, Lei et al. 2002). This area of research is prolific yet still quite novel (Cui 2007). CNT assemblies as presented in this thesis could also be used as scaffolds to support the delivery of intra-retinal drugs, pluripotent cell based rescue strategies or intracellular nano-syringes (Kam, Liu et al. 2006). CNT islands could also be functionalised with photo-voltaic elements such as quantum dots, allowing high-resolution, wavelength-specific independent stimulating electrodes.

5.1.3 Electrical properties of CNT electrodes

I have demonstrated the capability of CNT electrodes to induce spiking in RGCs at least 200 µm away from the stimulation point with charge values as low as 0.4 nC. Thresholds are expected to be considerably lower when stimulating RGCs closer than 200 µm away. When developing retinal prosthetic devices, one would have to take into consideration electrode size as much as possible to ensure one-to-one interfacing between RGCs and electrodes. Delivery of 0.4 nC of charge through a 10 µm diameter MEA corresponds to a charge density of 0.51 mC/ cm^2, a value within the range of the charge injection limit of CNT electrodes developed by our collaborators in Tel-Aviv (unpublished data: 1.5-4 mC/ cm^2).

CNT electrodes incorporated into MEAs such as those used in this study provide a larger signal-to-noise ratio than commercial TiN MEAs (Shoval et al., 2009). Both commercial and CNT MEAs were susceptible to etching of the track passivation layer by repeated exposure to physiological solution and retinal tissue over the course of multiple experiments. However, CNT MEAs were also susceptible to a certain level of electrode surface degradation following 48 hour interfacing with the retinal ILM. Indeed, figures 4.25 and 5.1 D demonstrate the loss of CNTs to the ILM following removal of the retina from CNT assemblies. Thus, constant use of CNT MEAs in 3-Day experiments (as described in Chapter 3) would lead to a reduction in the signal-to-noise ratio. However, this should not impact permanently implanted devices. Figure 5.1 demonstrates this phenomenon in two different CNT MEAs which have been used in 3 to 8 experiments (A) and in over 10 experiments (B). The figure shows MC_Rack screenshots of blank recording (saline without retina in the MEA chamber) (A, B), SEM of damaged (C', F) and intact (C, E) electrodes as well as both light (D) and electron

micrographs (D') displaying CNTs embedded in the retinal ILM. Electrochemically, damage to the passivation layer is translated by completely saturated channels (green blocks filling the channel display; 3 in A and 14 in B). Damage to the electrode surface is translated by an increase in baseline noise as seen in 4 channels of (A) and 18 channels of (B).

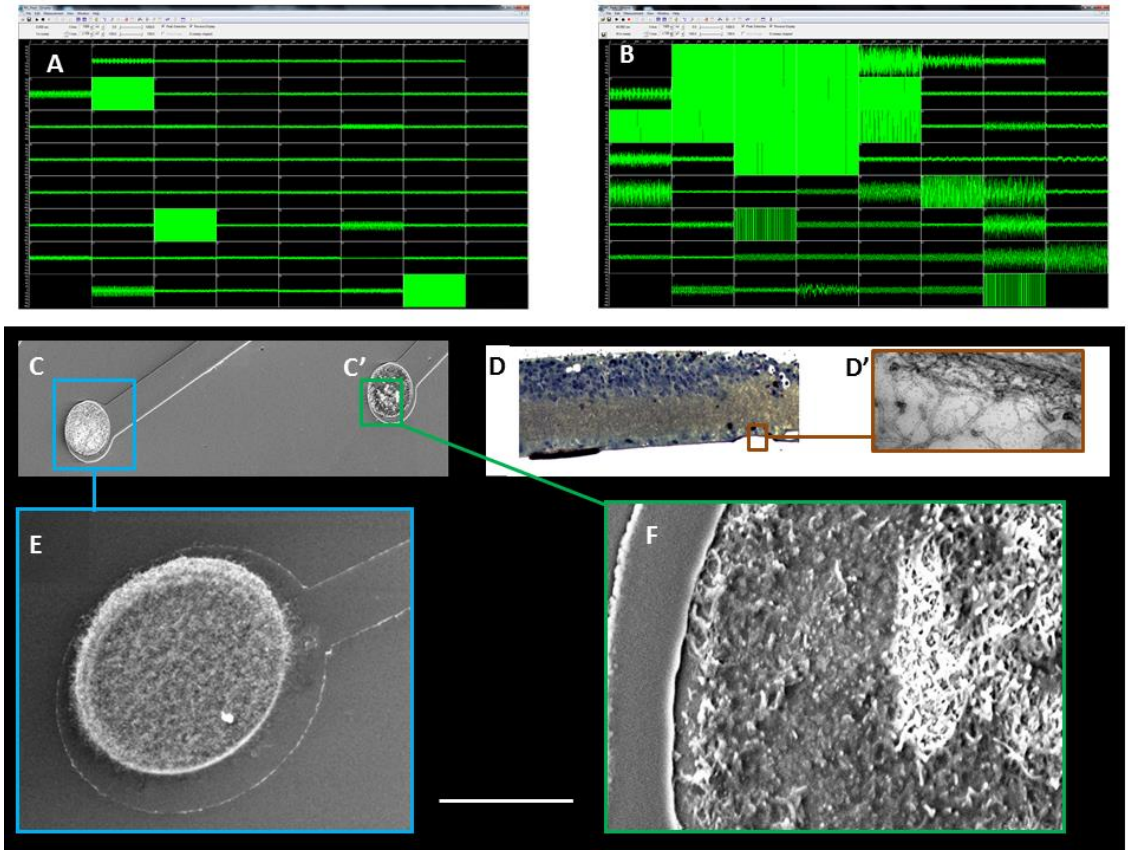

Figure 5.1: Damage to CNT MEA following repeated use leads to deterioration of electrochemical properties. A, B: MC_Rack screen shots of a fairly new (A) and very used (B) MEA displaying saturated channels and an increase in the baseline noise. C, E, F: SEM micrographs of intact (C, E) and damaged (C', F) CNT electrode surfaces. Optical micrograph (D) and TEM (D') of a retina exhibiting ripped CNTs in its ILM. Scale bar is 100 µm (C), 125 µm (D), 300 nm (D'), 5.7 µm (E) and 42.5 µm (F).

Further functionalization of CNT electrodes may lead to the fabrication of electrodes capable of interfacing on a one-to-one basis with target neurons, on a quasi-intracellular level, as achieved with micro gold-mushroom electrodes (Hai, Shappir et al. 2010).

Figure 5.2 displays a bar chart of the average impedance values recorded from a selection of MEAs, measured at 1 kHz. MVP36e and MVP36f are two CNT MEAs which were used heavily during the PhD. They display higher impedances than MVP20F and MVP39c which were used sporadically over a period of 6 years. An unfortunate lack of

foresight prevented the recording of a "freshly prepared" CNT MEA, although the "official" value is 10 kΩ (*cf.* table 5.1). As CNTs break off from the surface of electrodes (figure 5.1), the surface area is reduced, increasing the impedance value. TiN MEAs have an "official" impedance of 30 kΩ at 1 kHz, but we were unable to obtain values lower than 700 kΩ using brand new MEAs from Multi Channel Systems (Reutingen, Germany) which had been soaked for days in PBS (cf. Appendix D).

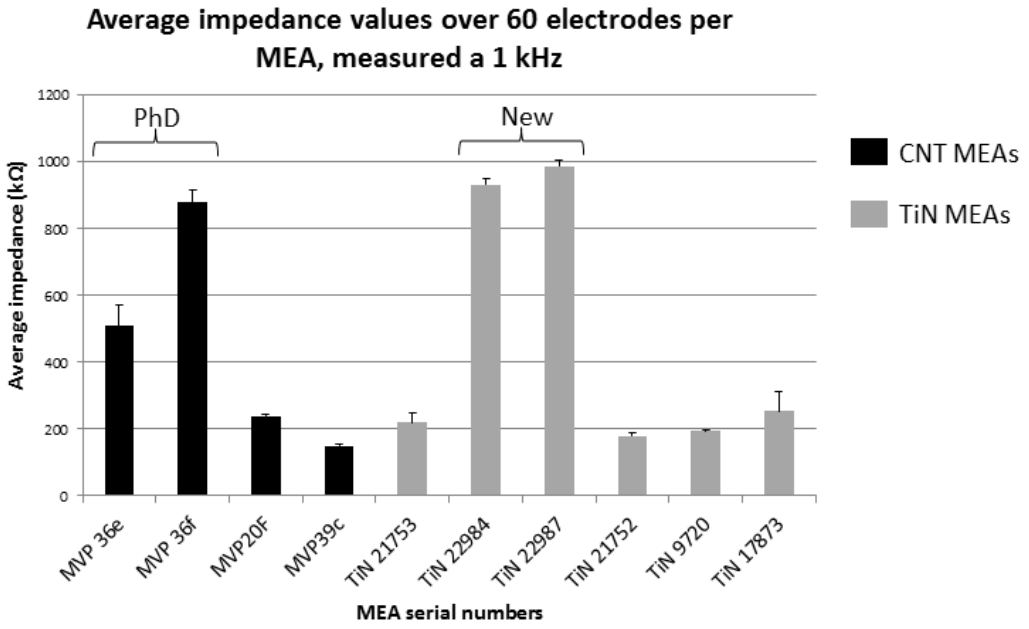

Figure 5.2: MEA impedances for CNT and TiN electrodes. Bar graph displaying the average impedance value, measured at 1 kHz for several CNT and TiN MEAs. Error bars: S.E.M. (Ravindran, Chaudhary et al. 2003)

5.1.4 Place of CNTs in the field of neuroprosthetics

CNTs are no doubt an interesting material with an exciting array of physical properties (*cf.* Chapter 1 and table 5.1). However, their use in biology remains controversial with the issue of toxicity which still remains to be solved. As nano-structures with impressive aspect ratios, CNTs in high enough concentrations can inflict damage both *in vivo* and *in vitro* (Foldvari and Bagonluri 2008). However, their use in new composite materials and their strong mechanical properties can insure the safety of the biological recipient. As neuro-stimulating electrodes, CNTs present an ideal surface area which is impeded by their unconventional electrical properties. Indeed, aligned CNTs have a ballistic conductivity matching that of IrO_2 but a poor surface area whilst "spaghetti-like" CNTs, as those used in this project have poor conduction with a high surface area. An electrode design concatenating both types of structures might provide an ideal

compromise. The ability to micro-manipulate CNT structures as well as functionalise them with biomolecules using covalent and non-covalent bonding (discussed in Chapter 1 and 2 as well as presented in table 5.1) remain in my opinion the most important properties of CNTs, and are ripe for exploiting in the field of neuro-prosthetic devices.

Table 5.1: Comparison of properties between MWCNTs, TiN and IrO_2

	MWCNTs	**TiN**	**IrO_2**
Conductivity (at physiological temperature, in Ωcm)	$2\ 10^{-6}$ **[10]**	$4.5\ 10^{-7}$ **[1]**	$3.7\ 10^{-6}$ **[13]**
Impedance (in kΩ, measured at 1 kHz)	10 **[1]** 100-1000 **[8]**	150 **[2]** 150-1200 **[8]** 30 **[9]**	100-750 **[2]** 73-210 **[11]**
Charge injection limit (in mC cm^{-2})	1.5-4 **[4]** 1-1.6 **[12]**	23 **[2]** 0.87 **[3]**	3.8-6.5 **[2]** 4 **[3]**
Biocompatibility	Attracts dissociated cells **[7]** Dose, size and shape-dependent toxicity **[14]**	Neurotoxic *in vitro* **[5]** FDA approved neuro-stimulators **[15]**	Delaminates at stimulation > 0.5 Hz **[6]** FDA approved neuro-stimulators **[15]**
Bio-functionalization	Non-covalent DNA binding **[16]** π – π stacking **[17]** Covalent bonding **[18]**		
Composite materials (number of hits for scientific publications in Google Scholar)	28900	7480	2380
Electrical stimulation	Capacitive	Capacitive	Faradaic

References:

[1] Gabay, Ben-David et al. 2007
[2] Janders, Egert et al. 1996
[3] Weiland, Anderson et al. 2002
[4] Unpublished data from Dr. Hanein's laboratory, Tel Aviv University
[5] Guenther, Troger et al. 1999
[6] Weiland and Anderson 2000
[7] Sorkin, Greenbaum et al. 2009
[8] PhD thesis, Cyril Eleftheriou
[9] Ti MEA manual, Multi Channel Systems)
[10] Berger, Yi et al. 2002
[11] Weiland and Anderson 2000
[12] Wang, Fishman et al. 2006
[13] Liu, Masumoto et al. 2004
[14] Foldvari and Bagonluri 2008
[15] Medtronic Inc, USA
[16] Clichici, Biris et al. 2013
[17] (Datir, Das et al. 2012
[18] Ravindran, Chaudhary et al. 2003

5.2 Future work

The relatively short lifetime of this project has resulted in a reliable set of results which could be further optimised using different strategies. Issues such as the exact time-point for the incorporation of CNT constructs within the ILM or the further investigation of indirect responses to different stimuli can be investigated with the tools and techniques developed in this thesis. In the following section, I explore the possible development of more advanced tools and methodologies to further the research and development in the field of epi-retinal prosthetics.

5.2.1 Optimal stimulation patterns

Although electrophysiological responses to electrical stimulation have been observed and characterised in our experiments, threshold for these stimulations were significantly higher than direct RGC activation. Other groups have investigated indirect responses according to stimulation shape and electrode size (Dorrell and Friedlander 2006; Margalit and Thoreson 2006; Garcia-Ayuso, Salinas-Navarro et al. 2010), finding that larger electrodes and longer pulses are most likely to target deeper tissue. This is relevant to a retinal prosthetic system designed to highjack BC and AC processing pathways. In light of the ever-changing nature of retinal remodelling in retinal dystrophies (Jones, Kondo et al. 2012) as well as the significant contribution of photoreceptor-originating glutamate in activation of ACs and BCs (Margalit, Babai et al. 2011), direct stimulation of RGCs is the most reliable pathway exploitable by a retinal prosthetic device, and therefore, efforts should be made to avoid BC and AC stimulation.

As discussed throughout this thesis, spontaneous activity in dystrophic retinas is characterised by slow oscillations and hyperactive spiking of RGCs (Stasheff 2008; Borowska, Trenholm et al. 2011; Menzler and Zeck 2011; Trenholm, Borowska et al. 2012). These aberrant signals possibly indicate survival strategies for deafferentated RGCs. They disappear following disabling of glutamate synaptic transmission of BCs and lateral gap-junction connectivity of ACs (Menzler and Zeck 2011). This activity would most likely create a strong barrier to the delivery of coherent input from a retinal prosthesis to visual centres in the brain. There does not appear to be any evidence suggesting that these would disappear following chronic stimulation of RGCs. A set of useful experiments to cancel such activity would aim to deliver chronic

electrical stimulation to dystrophic retinas and evaluate the persistence or fading of these signals. A possible strategy for abolishing the oscillations and bursting is the chronic delivery of glutamate receptor and gap junction blockers to the retina, possibly through hydrogels or a reservoir feeding to the choroid. Another possible option is the use of halorhodopsin transfected in RGC populations (Greenberg, Pham et al. 2011).

5.2.2 Multimodal electrophysiological characterisation of epi-retinal stimulation

As discussed in Chapter 3, we were unable to accurately monitor the direct activation of all RGCs by electrical stimulation because of electrode pitch and hardware limitations. Another research group has made use of MEAs with smaller, more closely spaced electrodes in order to have the smallest possible stimulation artefact and confirm the response of one RGC on multiple electrodes (Sekirnjak, Hottowy et al. 2008; Sekirnjak, Hulse et al. 2009). This group has further optimised their system to transiently disable acquisition whilst delivering stimulation pulses to present even smaller stimulation artefacts (Hottowy, Skoczen et al. 2012). Functionalising this system with CNTs may offer the best possible solution to observe direct responses in RGCs following incorporation of the protruding electrodes within the ILM.

Large scale / high density arrays such as the Active Pixel Sensor system (Imfeld, Garenne et al. 2007; Berdondini, Imfeld et al. 2009; Hennig, Maccione et al. 2011; Ferrea, Maccione et al. 2012), the Multi-Transistor Array (Lambacher, Jenkner et al. 2004; Menzler and Zeck 2011) or the 512-electrode array (Anishchenko, Greschner et al. 2010) allow the concurrent recording of thousands of RGCs with the use of 4096, 16284 and 512 electrodes respectively. These systems permit the characterisation of spontaneous activity during retinal degeneration (Sekirnjak, Hulse et al. 2009; Menzler and Zeck 2011) and development (Hennig, Maccione et al. 2011; Sernagor, Hennig et al. 2012) as well as the processing of visual stimuli (Anishchenko, Greschner et al. 2010) and electrical sub-retinal stimuli (Hottowy, Skoczen et al. 2012). However, these electrodes do not have the capacity to deliver electrical stimulation. Different types of high number and high density arrays for active photovoltaic (Kusnyerik, Resch et al. 2011), passive photovoltaic (Hottowy, Skoczen et al. 2012) or multi-capacitive stimulation (Eickenscheidt, Jenkner et al. 2012) have been tested on the retina without the possibility to record electrophysiological activity on the stimulating array. The

research group led by Luca Berdondini has developed the next generation of the Active Pixel Sensor which incorporates the ability to stimulate via 16 channels spread throughout the array (unpublished data).

Optogenetic approaches to retinal stimulation have been tested on commercial MEAs *in vitro* with low spatial resolution (Nirenberg and Pandarinath 2012) similar to the arrays used in our study, but not on large scale high-density recording systems. Planar electrode arrays allow the recording of RGC action potentials, giving us a limited insight into the physiological activity of interneurons and glial cells. Such cells do not fire action potentials, making their electrophysiological characterisation difficult. Retinal stimulation with MEAs has been combined with calcium imaging where retrograde labelling of salamander RGCs was achieved by incubating eyecups with the cut end of optic nerve exposed to a BAPTA calcium dye solution (Behrend, Ahuja et al. 2009; Behrend, Ahuja et al. 2011). Although it would be important to test this in degenerated retinas, the technique has not yet been perfected for mammalian retinas. By combining our *Free-float* system with this technique and mounting the MEA amplifier on an inverted microscope, experimentalists could observe calcium transients in whole RGC populations in response to electrical stimulation and compare it to electrophysiological signals from adjacent electrodes on the MEA.

An ideal scenario would be the monitoring of different cell populations in response to electrical stimulation. This could be achieved by using a confocal microscope focused at different depths within the retina, although this would require labelling of cells deep within the tissue which is not trivial. Another approach would be to genetically engineer a set of dystrophic retinal mouse models with different fluorescent protein tags for each of the different neuronal classes (Misteli and Spector 1997). For this approach to work, large populations of cells in the retina would have to be loaded with an intracellular calcium marker. This can be achieved by electroporation or incubating of retina with AM dyes prior to data acquisition (Newman and Zahs 1997). One major hurdle to these approaches would be the background fluorescence provided by Müller cells. Indeed, in degenerated retinas, these constitute the bulk of the retina and the calcium signal is likely to be noisier than in healthy retinas (Matsuda and Cepko 2004).

Bibliography

Adamis, A. P., L. P. Aiello, et al. (1999). "Angiogenesis and ophthalmic disease." Angiogenesis **3**(1): 9-14.

Adams, C., J. Simonotto, et al. (2008). "Multielectrode Array Recordings Of Neural Activity Patterns In The Developing Retina Of The Cone Rod Homeobox Knockout (Crx-/-) Mouse." 6th Int. Meeting on Substrate-Integrated Microelectrodes.

Ahnelt, P., C. Keri, et al. (1990). "Identification of pedicles of putative blue-sensitive cones in the human retina." Journal of Comparative Neurology **293**(1): 39-53.

Ahuja, A. K., J. D. Dorn, et al. (2011). "Blind subjects implanted with the Argus II retinal prosthesis are able to improve performance in a spatial-motor task." Br J Ophthalmol **95**(4): 539-543.

Ahuja, A. K., J. Yeoh, et al. (2013). "Factors Affecting Perceptual Threshold in Argus II Retinal Prosthesis Subjects." Translational Vision Science & Technology: 1.

Ames, A., Y. Y. Li, et al. (1992). "Energy-Metabolism of Rabbit Retina as Related to Function - High Cost of Na+ Transport." Journal of Neuroscience **12**(3): 840-853.

Amthor, F. R., E. S. Takahashi, et al. (1989). "Morphologies of rabbit retinal ganglion cells with complex receptive fields." Journal of Comparative Neurology **280**(1): 97-121.

Anderson, D. H., C. J. Guerin, et al. (1986). "Morphological recovery in the reattached retina." Invest Ophthalmol Vis Sci **27**(2): 168-183.

Anderson, J. R., B. W. Jones, et al. (2011). "Exploring the retinal connectome." Mol Vis **17**(41).

Anderson, J. R., B. W. Jones, et al. (2009). "A Computational Framework for Ultrastructural Mapping of Neural Circuitry." PLoS Biol **7**(3): 493-512.

Anishchenko, A., M. Greschner, et al. (2010). "Receptive field mosaics of retinal ganglion cells are established without visual experience." J Neurophysiol **103**(4): 1856-1864.

Antonetti, D. A., A. J. Barber, et al. (2006). "Diabetic retinopathy: seeing beyond glucose-induced microvascular disease." Diabetes **55**(9): 2401-2411.

Arshavsky, V. Y., T. D. Lamb, et al. (2002). "G proteins and phototransduction." Annu Rev Physiol **64**: 153-187.

Ashwell, K. (1990). "Microglia and Cell-Death in the Developing Mouse Cerebellum." Developmental Brain Research **55**(2): 219-230.

Banati, R. B., R. Egensperger, et al. (2004). "Mitochondria in activated microglia in vitro." J Neurocytol **33**(5): 535-541.

Behrend, M. R., A. K. Ahuja, et al. (2011). "Resolution of the epiretinal prosthesis is not limited by electrode size." IEEE Trans Neural Syst Rehabil Eng **19**(4): 436-442.

Behrend, M. R., A. K. Ahuja, et al. (2009). "Selective labeling of retinal ganglion cells with calcium indicators by retrograde loading in vitro." J Neurosci Methods **179**(2): 166-172.

Belanger, M. C. and Y. Marois (2001). "Hemocompatibility, biocompatibility, inflammatory and in vivo studies of primary reference materials low-density polyethylene and polydimethylsiloxane: a review." J Biomed Mater Res **58**(5): 467-477.

Berdichevsky, Y., H. Sabolek, et al. (2009). "Microfluidics and multielectrode array-compatible organotypic slice culture method." J Neurosci Methods **178**(1): 59-64.

Berdondini, L., K. Imfeld, et al. (2009). "Active pixel sensor array for high spatio-temporal resolution electrophysiological recordings from single cell to large scale neuronal networks." Lab Chip **9**(18): 2644-2651.
Blau, A., A. Murr, et al. (2011). "Flexible, all-polymer microelectrode arrays for the capture of cardiac and neuronal signals." Biomaterials **32**(7): 1778-1786.
Bogdanovich, A. E. and P. D. Bradford (2010). "Carbon nanotube yarn and 3-D braid composites. Part I: Tensile testing and mechanical properties analysis." Composites Part a-Applied Science and Manufacturing **41**(2): 230-237.
Boiko, T., A. Van Wart, et al. (2003). "Functional specialization of the axon initial segment by isoform-specific sodium channel targeting." Journal of Neuroscience **23**(6): 2306-2313.
Boos, R., H. Schneider, et al. (1993). "Voltage- and transmitter-gated currents of all-amacrine cells in a slice preparation of the rat retina." Journal of Neuroscience **13**(7): 2874-2888.
Borowska, J., S. Trenholm, et al. (2011). "An intrinsic neural oscillator in the degenerating mouse retina." Journal of Neuroscience **31**(13): 5000-5012.
Bowes, C., T. Li, et al. (1990). "Retinal degeneration in the rd mouse is caused by a defect in the beta subunit of rod cGMP-phosphodiesterase." Nature **347**(6294): 677-680.
Boyden, E. S., F. Zhang, et al. (2005). "Millisecond-timescale, genetically targeted optical control of neural activity." Nat Neurosci **8**(9): 1263-1268.
Bringmann, A., T. Pannicke, et al. (2006). "Muller cells in the healthy and diseased retina." Prog Retin Eye Res **25**(4): 397-424.
Bringmann, A. and A. Reichenbach (2001). "Role of Muller cells in retinal degenerations." Front Biosci **6**: E72-92.
Bruban, J., A. Maoui, et al. (2011). "CCR2/CCL2-mediated inflammation protects photoreceptor cells from amyloid-beta-induced apoptosis." Neurobiol Dis **42**(1): 55-72.
Brummer, S. B. and M. J. Turner (1977). "Electrical Stimulation with Pt Electrodes: II-Estimation of Maximum Surface Redox (Theoretical Non-Gassing) Limits." Biomedical Engineering, IEEE Transactions on **BME-24**(5): 440-443.
Bunt, A. H., A. E. Hendrickson, et al. (1975). "Monkey retinal ganglion cells: morphometric analysis and tracing of axonal projections, with a consideration of the peroxidase technique." J Comp Neurol **164**(3): 265-285.
Burke, J. M. and J. M. Smith (1981). "Retinal proliferation in response to vitreous hemoglobin or iron." Invest Ophthalmol Vis Sci **20**(5): 582-592.
Bussow, H. (1980). "The astrocytes in the retina and optic nerve head of mammals: a special glia for the ganglion cell axons." Cell Tissue Res **206**(3): 367-378.
Buzsaki, G., C. A. Anastassiou, et al. (2012). "The origin of extracellular fields and currents - EEG, ECoG, LFP and spikes." Nat Rev Neurosci **13**(6): 407-420.
Canton, I., D. M. Cole, et al. (2010). "Development of a 3D human in vitro skin co-culture model for detecting irritants in real-time." Biotechnol Bioeng **106**(5): 794-803.
Carroll, M. C. (2004). "The complement system in regulation of adaptive immunity." Nat Immunol **5**(10): 981-986.
Cartmell, S. (2009). "Controlled release scaffolds for bone tissue engineering." J Pharm Sci **98**(2): 430-441.
Cha, K., K. Horch, et al. (1992). "Simulation of a phosphene-based visual field: visual acuity in a pixelized vision system." Ann Biomed Eng **20**(4): 439-449.

Cha, K., K. W. Horch, et al. (1992). "Reading speed with a pixelized vision system." J Opt Soc Am A **9**(5): 673-677.
Chai, L. and J. E. Morris (1994). "Distribution of heparan sulfate proteoglycans in embryonic chicken neural retina and isolated inner limiting membrane." Curr Eye Res **13**(9): 669-677.
Chakrapani, N., B. Q. Wei, et al. (2004). "Capillarity-driven assembly of two-dimensional cellular carbon nanotube foams." Proc Natl Acad Sci U S A **101**(12): 4009-4012.
Chakravarthy, U., J. Evans, et al. (2010). "Age related macular degeneration." BMJ **340**: c981.
Chan-Ling, T., D. S. McLeod, et al. (2004). "Astrocyte-endothelial cell relationships during human retinal vascular development." Invest Ophthalmol Vis Sci **45**(6): 2020-2032.
Chan-Ling, T. and J. Stone (1992). "Degeneration of astrocytes in feline retinopathy of prematurity causes failure of the blood-retinal barrier." Invest Ophthalmol Vis Sci **33**(7): 2148-2159.
Charlier, J. C., X. Blase, et al. (2007). "Electronic and transport properties of nanotubes." Reviews of Modern Physics **79**(2): 677-732.
Chatterjee, S. and E. M. Callaway (2003). "Parallel colour-opponent pathways to primary visual cortex." Nature **426**(6967): 668-671.
Chen, L., P. Yang, et al. (2002). "Distribution, markers, and functions of retinal microglia." Ocul Immunol Inflamm **10**(1): 27-39.
Chen, S. J., M. Mahadevappa, et al. (2006). "Neural responses elicited by electrical stimulation of the retina." Trans Am Ophthalmol Soc **104**: 252-259.
Choi, Y. K. and K. W. Kim (2008). "Blood-neural barrier: its diversity and coordinated cell-to-cell communication." BMB Rep **41**(5): 345-352.
Cogan, S., D. Peramunage, et al. (2007). "Polyethylenedioxythiophene (PEDOT) coatings for neural stimulation and recording electrodes." Material Research Society meeting: Abstract QQ2.7.
Cogan, S. F. (2008). "Neural stimulation and recording electrodes." Annu Rev Biomed Eng **10**: 275-309.
Collin, S. P. (2008). "A web-based archive for topographic maps of retinal cell distribution in vertebrates." Clin Exp Optom **91**(1): 85-95.
Conway, B. E. (1990). Transition from `supercapacitor' to `battery' behavior in electrochemical energy storage. Power Sources Symposium, 1990., Proceedings of the 34th International.
Cotter, J. R. and W. K. Noell (1984). "Ultrastructure of remnant photoreceptors in advanced hereditary retinal degeneration." Invest Ophthalmol Vis Sci **25**(12): 1366-1375.
Cowey, A. and V. H. Perry (1979). "The projection of the temporal retina in rats, studied by retrograde transport of horseradish peroxidase." Exp Brain Res **35**(3): 457-464.
Cuenca, N., I. Pinilla, et al. (2004). "Regressive and reactive changes in the connectivity patterns of rod and cone pathways of P23H transgenic rat retina." Neuroscience **127**(2): 301-317.
Cui, D. X. (2007). "Advances and prospects on biomolecules functionalized carbon nanotubes." J Nanosci Nanotechnol **7**(4-5): 1298-1314.
Cui, X. Y., J. Wiler, et al. (2003). "In vivo studies of polypyrrole/peptide coated neural probes." Biomaterials **24**(5): 777-787.

Cunha-Vaz, J. G. (2004). "The blood-retinal barriers system. Basic concepts and clinical evaluation." Exp Eye Res **78**(3): 715-721.
Cunha-Vaz, J. G., M. Shakib, et al. (1966). "Studies on the permeability of the blood-retinal barrier. I. On the existence, development, and site of a blood-retinal barrier." Br J Ophthalmol **50**(8): 441-453.
Dacey, D. (2004). Origins of perception: retinal ganglion cell diversity and the creation of visual pathways. Cognitive Neurosciences. M. Gazzaniga. Cambridge, MA, MIT Press**:** 281-301.
Dacey, D. M. (2000). "Parallel pathways for spectral coding in primate retina." Annu Rev Neurosci **23**: 743-775.
Dacey, D. M. and B. B. Lee (1994). "The 'blue-on' opponent pathway in primate retina originates from a distinct bistratified ganglion cell type." Nature **367**(6465): 731-735.
Dai, H. J. (2002). "Carbon nanotubes: Synthesis, integration, and properties." Accounts of Chemical Research **35**(12): 1035-1044.
Darwin, R. W. and E. Darwin (1786). "New Experiments on the Ocular Spectra of Light and Colours. By Robert Waring Darwin, M. D.; Communicated by Erasmus Darwin, M. D. F. R. S." Philosophical Transactions of the Royal Society of London **76**(ArticleType: research-article / Full publication date: 1786 /): 313-348.
del Zoppo, G. J. and J. M. Hallenbeck (2000). "Advances in the vascular pathophysiology of ischemic stroke." Thromb Res **98**(3): 73-81.
Devries, S. H. and D. A. Baylor (1997). "Mosaic arrangement of ganglion cell receptive fields in rabbit retina." J Neurophysiol **78**(4): 2048-2060.
Dobelle, W. H. (2000). "Artificial vision for the blind by connecting a television camera to the visual cortex." ASAIO J **46**(1): 3-9.
Dorn, J. D., A. K. Ahuja, et al. (2012). "The Detection of Motion by Blind Subjects With the Epiretinal 60-Electrode (Argus II) Retinal Prosthesis." Arch Ophthalmol: 1-7.
Dorrell, M. I. and M. Friedlander (2006). "Mechanisms of endothelial cell guidance and vascular patterning in the developing mouse retina." Progress in Retinal and Eye Research **25**(3): 277-295.
Dowling, J. E. and B. Ehinger (1978). "Synaptic organization of the dopaminergic neurons in the rabbit retina." Journal of Comparative Neurology **180**(2): 203-220.
Drasdo, N. and C. W. Fowler (1974). "Non-linear projection of the retinal image in a wide-angle schematic eye." Br J Ophthalmol **58**(8): 709-714.
Dryja, T. P. and T. Li (1995). "Molecular genetics of retinitis pigmentosa." Hum Mol Genet **4 Spec No**: 1739-1743.
Duprey-Diaz, M. V., J. M. Blagburn, et al. (2012). "Changes in fibroblast growth factor-2 and FGF receptors in the frog visual system during optic nerve regeneration." J Chem Neuroanat.
Dyer, M. A. and C. L. Cepko (2000). "Control of Muller glial cell proliferation and activation following retinal injury." Nat Neurosci **3**(9): 873-880.
Edell, D. J., V. V. Toi, et al. (1992). "Factors Influencing the Biocompatibility of Insertable Silicon Microshafts in Cerebral-Cortex." Ieee Transactions on Biomedical Engineering **39**(6): 635-643.
Egensperger, R., J. Maslim, et al. (1996). "Fate of DNA from retinal cells dying during development: uptake by microglia and macroglia (Muller cells)." Brain Res Dev Brain Res **97**(1): 1-8.

Egert, U., B. Schlosshauer, et al. (1998). "A novel organotypic long-term culture of the rat hippocampus on substrate-integrated multielectrode arrays." Brain Res Brain Res Protoc **2**(4): 229-242.
Eggers, E. D. and P. D. Lukasiewicz (2011). "Multiple pathways of inhibition shape bipolar cell responses in the retina." Vis Neurosci **28**(1): 95-108.
Eickenscheidt, M., M. Jenkner, et al. (2012). "Electrical stimulation of retinal neurons in epiretinal and subretinal configuration using a multicapacitor array." J Neurophysiol **107**(10): 2742-2755.
Eiraku, M. and Y. Sasai (2011). "Self-organizing optic-cup morphogenesis in three-dimensional culture." Neuroscience Research **71**: E127-E128.
El Khakani, M. A. and M. Chaker (1998). "Reactive pulsed laser deposition of iridium oxide thin films." Thin Solid Films **335**(1-2): 6-12.
Eter, N., D. R. Engel, et al. (2008). "In vivo visualization of dendritic cells, macrophages, and microglial cells responding to laser-induced damage in the fundus of the eye." Invest Ophthalmol Vis Sci **49**(8): 3649-3658.
Falsini, B., M. Piccardi, et al. (2010). "Influence of saffron supplementation on retinal flicker sensitivity in early age-related macular degeneration." Invest Ophthalmol Vis Sci **51**(12): 6118-6124.
Famiglietti, E. V., Jr., A. Kaneko, et al. (1977). "Neuronal architecture of on and off pathways to ganglion cells in carp retina." Science **198**(4323): 1267-1269.
Fan, L., C. Feng, et al. (2012). "Directional Neurite Outgrowth on Superaligned Carbon Nanotube Yarn Patterned Substrate." Nano Lett **12**(7): 3668-3673.
Fendyur, A., N. Mazurski, et al. (2011). "Formation of Essential Ultrastructural Interface between Cultured Hippocampal Cells and Gold Mushroom-Shaped MEA-Toward "IN-CELL" Recordings from Vertebrate Neurons." Front Neuroeng **4**: 14.
Fendyur, A. and M. E. Spira (2012). "Toward on-chip, in-cell recordings from cultured cardiomyocytes by arrays of gold mushroom-shaped microelectrodes." Front Neuroeng **5**: 21.
Ferrea, E., A. Maccione, et al. (2012). "Large-scale, high-resolution electrophysiological imaging of field potentials in brain slices with microelectronic multielectrode arrays." Front Neural Circuits **6**: 80.
Field, G. D. and E. J. Chichilnisky (2007). "Information processing in the primate retina: Circuitry and coding." Annu Rev Neurosci **30**: 1-30.
Field, G. D., J. L. Gauthier, et al. (2010). "Functional connectivity in the retina at the resolution of photoreceptors." Nature **467**(7316): 673-677.
Fischer, F., M. Kneussel, et al. (2000). "Reduced synaptic clustering of GABA and glycine receptors in the retina of the gephyrin null mutant mouse." J Comp Neurol **427**(4): 634-648.
Fitch, M. T. and J. Silver (2008). "CNS injury, glial scars, and inflammation: Inhibitory extracellular matrices and regeneration failure." Exp Neurol **209**(2): 294-301.
Frautschy, S. A., F. S. Yang, et al. (1998). "Microglial response to amyloid plaques in APPsw transgenic mice." American Journal of Pathology **152**(1): 307-317.
Freund, C. L., C. Y. Gregory-Evans, et al. (1997). "Cone-rod dystrophy due to mutations in a novel photoreceptor-specific homeobox gene (CRX) essential for maintenance of the photoreceptor." Cell **91**(4): 543-553.
Fruttiger, M., A. R. Calver, et al. (1996). "PDGF mediates a neuron-astrocyte interaction in the developing retina." Neuron **17**(6): 1117-1131.
Fu, Y. and K. W. Yau (2007). "Phototransduction in mouse rods and cones." Pflugers Arch **454**(5): 805-819.

Fujii, G. Y., E. de Juan, et al. (2002). "Initial experience using the Transconjunctival Sutureless Vitrectomy System for vitreoretinal surgery." Ophthalmology **109**(10): 1814-1820.
Furukawa, T., E. M. Morrow, et al. (1997). "Crx, a novel otx-like homeobox gene, shows photoreceptor-specific expression and regulates photoreceptor differentiation." Cell **91**(4): 531-541.
Gabay, T., M. Ben-David, et al. (2007). "Electro-chemical and biological properties of carbon nanotube based multi-electrode arrays." Nanotechnology **18**(3): -.
Gabay, T., E. Jakobs, et al. (2005). "Engineered self-organization of neural networks using carbon nanotube clusters." Physica a-Statistical Mechanics and Its Applications **350**(2-4): 611-621.
Gabriel, G., R. Gomez, et al. (2009). "Easily made single-walled carbon nanotube surface microelectrodes for neuronal applications." Biosensors & Bioelectronics **24**(7): 1942-1948.
Gahwiler, B. H. (1988). "Organotypic cultures of neural tissue." Trends Neurosci **11**(11): 484-489.
Gahwiler, B. H., M. Capogna, et al. (1997). "Organotypic slice cultures: a technique has come of age." Trends Neurosci **20**(10): 471-477.
Gandorfer, A., E. M. Messmer, et al. (2000). "Resolution of diabetic macular edema after surgical removal of the posterior hyaloid and the inner limiting membrane." Retina **20**(2): 126-133.
Gandorfer, A., M. Ulbig, et al. (2002). "Plasmin-assisted vitrectomy eliminates cortical vitreous remnants." Eye (Lond) **16**(1): 95-97.
Garcia-Ayuso, D., M. Salinas-Navarro, et al. (2010). "Retinal ganglion cell numbers and delayed retinal ganglion cell death in the P23H rat retina." Exp Eye Res **91**(6): 800-810.
Garcia, D. M. and J. R. Koke (2009). "Astrocytes as gate-keepers in optic nerve regeneration--a mini-review." Comp Biochem Physiol A Mol Integr Physiol **152**(2): 135-138.
Geerts, W. J. C., D. Zeuschner, et al. (2012). "3D Electron Tomography and EDX:

high-resolution imaging tools for cell biological applications."
Gehrig, A., T. Langmann, et al. (2007). "Genome-wide expression profiling of the retinoschisin-deficient retina in early postnatal mouse development." Invest Ophthalmol Vis Sci **48**(2): 891-900.
Gehrmann, J. (1996). "Microglia: a sensor to threats in the nervous system?" Res Virol **147**(2-3): 79-88.
Gerhardt, H., M. Golding, et al. (2003). "VEGF guides angiogenic sprouting utilizing endothelial tip cell filopodia." J Cell Biol **161**(6): 1163-1177.
Ghosh, K. K., S. Bujan, et al. (2004). "Types of bipolar cells in the mouse retina." Journal of Comparative Neurology **469**(1): 70-82.
Gold, C., D. A. Henze, et al. (2006). "On the origin of the extracellular action potential waveform: A modeling study." J Neurophysiol **95**(5): 3113-3128.
Golgi, C. (1903). Opera Omnia. Milan, Hoepli Editore.
Gollisch, T. and M. Meister (2010). "Eye smarter than scientists believed: neural computations in circuits of the retina." Neuron **65**(2): 150-164.
Goureau, O., F. Regnier-Ricard, et al. (1999). "Requirement for nitric oxide in retinal neuronal cell death induced by activated Muller glial cells." J Neurochem **72**(6): 2506-2515.

Greenberg, K. P., A. Pham, et al. (2011). "Differential targeting of optical neuromodulators to ganglion cell soma and dendrites allows dynamic control of center-surround antagonism." Neuron **69**(4): 713-720.
Greenberg, R. J., T. J. Velte, et al. (1999). "A computational model of electrical stimulation of the retinal ganglion cell." IEEE Trans Biomed Eng **46**(5): 505-514.
Greene, A. S., J. H. Lombard, et al. (1990). "Microvessel Changes in Hypertension Measured by Griffonia-Simplicifolia I-Lectin." Hypertension **15**(6): 779-783.
Griffin, R., L. S. Illis, et al. (1972). "Identification of neuroglia by light and electronmicroscopy." Acta Neuropathol **22**(1): 7-12.
Grossman, N., V. Poher, et al. (2010). "Multi-site optical excitation using ChR2 and micro-LED array." Journal of Neural Engineering **7**(1): 16004.
Guenther, E., B. Troger, et al. (1999). "Long-term survival of retinal cell cultures on retinal implant materials." Vision Res **39**(24): 3988-3994.
Guiseppi-Elie, A., C. H. Lei, et al. (2002). "Direct electron transfer of glucose oxidase on carbon nanotubes." Nanotechnology **13**(5): 559-564.
Gunning, D. E., J. M. Beggs, et al. (2013). "Dense arrays of micro-needles for recording and electrical stimulation of neural activity in acute brain slices." Journal of Neural Engineering **10**(1).
Gunning, D. E., C. J. Kenney, et al. (2009). "High spatial resolution probes for neurobiology applications." Nuclear Instruments & Methods in Physics Research Section a-Accelerators Spectrometers Detectors and Associated Equipment **604**(1-2): 104-107.
Hai, A., A. Dormann, et al. (2009). "Spine-shaped gold protrusions improve the adherence and electrical coupling of neurons with the surface of micro-electronic devices." J R Soc Interface **6**(41): 1153-1165.
Hai, A., J. Shappir, et al. (2010). "Long-term, multisite, parallel, in-cell recording and stimulation by an array of extracellular microelectrodes." J Neurophysiol **104**(1): 559-568.
Hai, A. and M. E. Spira (2012). "On-chip electroporation, membrane repair dynamics and transient in-cell recordings by arrays of gold mushroom-shaped microelectrodes." Lab Chip **12**(16): 2865-2873.
Harada, T., C. Harada, et al. (2002). "Microglia-Muller glia cell interactions control neurotrophic factor production during light-induced retinal degeneration." J Neurosci **22**(21): 9228-9236.
Harder, D. R., N. J. Alkayed, et al. (1998). "Functional hyperemia in the brain: hypothesis for astrocyte-derived vasodilator metabolites." Stroke **29**(1): 229-234.
Hartline, H. (1938). "THE RESPONSE OF SINGLE OPTIC NERVE FIBERS OF THE VERTEBRATE EYE TO ILLUMINATION OF THE RETINA." American Journal of Physiology **121**: 400-415.
Hartong, D. T., E. L. Berson, et al. (2006). "Retinitis pigmentosa." Lancet **368**(9549): 1795-1809.
Haskal, Z. J. and L. H. Brennecke (1999). "Transjugular intrahepatic portosystemic shunts formed with polyethylene terephthalate-covered stents: Experimental evaluation in pigs." Radiology **213**(3): 853-859.
Hattar, S., H. W. Liao, et al. (2002). "Melanopsin-containing retinal. ganglion cells: Architecture, projections, and intrinsic photosensitivity." Science **295**(5557): 1065-1070.
Hatten, M. E., R. K. Liem, et al. (1991). "Astroglia in CNS injury." Glia **4**(2): 233-243.

Haverkamp, S. and H. Wassle (2000). "Immunocytochemical analysis of the mouse retina." Journal of Comparative Neurology **424**(1): 1-23.
Hecht, S., S. Shlaer, et al. (1942). "Energy, Quanta, and Vision." J Gen Physiol **25**(6): 819-840.
Heegaard, S., O. A. Jensen, et al. (1986). "Structure and composition of the inner limiting membrane of the retina. SEM on frozen resin-cracked and enzyme-digested retinas of Macaca mulatta." Graefes Arch Clin Exp Ophthalmol **224**(4): 355-360.
Helmstaedter, M., K. L. Briggman, et al. (2008). "3D structural imaging of the brain with photons and electrons." Current Opinion in Neurobiology **18**(6): 633-641.
Hennig, M., A. Maccione, et al. (2011). "Analysis of simultaneous multielectrode recordings with 4,096 channels: changing dynamics of spontaneous activity in the developing retina." BMC Neuroscience 2011(12(Suppl 1):P296).
Hennig, M. H., K. Funke, et al. (2002). "The influence of different retinal subcircuits on the nonlinearity of ganglion cell behavior." Journal of Neuroscience **22**(19): 8726-8738.
Henze, D. A., Z. Borhegyi, et al. (2000). "Intracellular features predicted by extracellular recordings in the hippocampus in vivo." J Neurophysiol **84**(1): 390-400.
Hodgkin, A. L. and A. F. Huxley (1952). "A quantitative description of membrane current and its application to conduction and excitation in nerve." J Physiol **117**(4): 500-544.
Hogan, M. J. and L. Feeney (1963). "The Ultrastructure of the Retinal Vessels. Iii. Vascular-Glial Relationships." J Ultrastruct Res **49**: 47-64.
Hogue, M. J. (1947). "Human fetal brain cells in tissue cultures; their identification and motility." J Exp Zool **106**(1): 85-107.
Hottowy, P., A. Skoczen, et al. (2012). "Properties and application of a multichannel integrated circuit for low-artifact, patterned electrical stimulation of neural tissue." Journal of Neural Engineering **9**(6): 066005.
Hottowy, P., A. Skoczen, et al. (2012). "Properties and application of a multichannel integrated circuit for low-artifact, patterned electrical stimulation of neural tissue." J Neural Eng **9**(6): 066005.
Hu, H., Y. C. Ni, et al. (2005). "Polyethyleneimine functionalized single-walled carbon nanotubes as a substrate for neuronal growth." Journal of Physical Chemistry B **109**(10): 4285-4289.
Hu, H., Y. C. Ni, et al. (2004). "Chemically functionalized carbon nanotubes as substrates for neuronal growth." Nano Lett **4**(3): 507-511.
Hu, L. B., D. S. Hecht, et al. (2009). "Infrared transparent carbon nanotube thin films." Applied Physics Letters **94**(8): -.
Humayun, M., R. Propst, et al. (1994). "Bipolar surface electrical stimulation of the vertebrate retina." Arch Ophthalmol **112**(1): 110-116.
Humayun, M. S., J. D. Weiland, et al. (2003). "Visual perception in a blind subject with a chronic microelectronic retinal prosthesis." Vision Res **43**(24): 2573-2581.
Iandiev, I., O. Uckermann, et al. (2006). "Glial cell reactivity in a porcine model of retinal detachment." Invest Ophthalmol Vis Sci **47**(5): 2161-2171.
Imfeld, K., A. Garenne, et al. (2007). "High-resolution MEA platform for in-vitro electrogenic cell networks imaging." Conf Proc IEEE Eng Med Biol Soc **2007**: 6086-6089.
Janders, M., U. Egert, et al. (1996). Novel thin film titanium nitride micro-electrodes with excellent charge transfer capability for cell stimulation and sensing

applications. Engineering in Medicine and Biology Society, 1996. Bridging Disciplines for Biomedicine. Proceedings of the 18th Annual International Conference of the IEEE.

Jensen, R. J., J. F. Rizzo, 3rd, et al. (2003). "Thresholds for activation of rabbit retinal ganglion cells with an ultrafine, extracellular microelectrode." Invest Ophthalmol Vis Sci **44**(8): 3533-3543.

Jensen, R. J., O. R. Ziv, et al. (2005). "Thresholds for activation of rabbit retinal ganglion cells with relatively large, extracellular microelectrodes." Invest Ophthalmol Vis Sci **46**(4): 1486-1496.

Jensen, R. J., O. R. Ziv, et al. (2009). "Spatiotemporal aspects of pulsed electrical stimuli on the responses of rabbit retinal ganglion cells." Exp Eye Res **89**(6): 972-979.

Jones, B. W., M. Kondo, et al. (2012). "Retinal remodeling." Jpn J Ophthalmol **56**(4): 289-306.

Jones, B. W., M. Kondo, et al. (2011). "Retinal remodeling in the Tg P347L rabbit, a large-eye model of retinal degeneration." Journal of Comparative Neurology **519**(14): 2713-2733.

Jones, B. W. and R. E. Marc (2005). "Retinal remodeling during retinal degeneration." Exp Eye Res **81**(2): 123-137.

Jones, B. W., R. E. Marc, et al. (2011). "Chapter 3: Retinal remodeling and visual prosthetics." **Visual Prosthetics: Physiology, Bioengineering, Rehabilitation**.

Jones, B. W., R. E. Marc, et al. (2006). "Neural plasticity revealed by light-induced photoreceptor lesions." Retinal Degenerative Diseases **572**: 405-410.

Jones, B. W., C. B. Watt, et al. (2003). "Retinal remodeling triggered by photoreceptor degenerations." Journal of Comparative Neurology **464**(1): 1-16.

Journet, C. and P. Bernier (1998). "Production of carbon nanotubes." Applied Physics a-Materials Science & Processing **67**(1): 1-9.

Jurrus, E., R. Whitaker, et al. (2008). "An Optimal-Path Approach for Neural Circuit Reconstruction." Proc IEEE Int Symp Biomed Imaging **2008**(4541320): 1609-1612.

Jusuf, P. R., S. Haverkamp, et al. (2005). "Localization of glycine receptor alpha subunits on bipolar and amacrine cells in primate retina." Journal of Comparative Neurology **488**(2): 113-128.

Kam, N. W. S., Z. A. Liu, et al. (2006). "Carbon nanotubes as intracellular transporters for proteins and DNA: An investigation of the uptake mechanism and pathway." Angewandte Chemie-International Edition **45**(4): 577-581.

Kandel, E. R., J. H. Schwartz, et al. (2000). Principles of Neural Science, McGraw Hill.

Kass, M. A., D. K. Heuer, et al. (2002). "The Ocular Hypertension Treatment Study: a randomized trial determines that topical ocular hypotensive medication delays or prevents the onset of primary open-angle glaucoma." Arch Ophthalmol **120**(6): 701-713; discussion 829-730.

Kawano, T., T. Harimoto, et al. (2010). "Electrical interfacing between neurons and electronics via vertically integrated sub-4 mu m-diameter silicon probe arrays fabricated by vapor-liquid-solid growth." Biosensors & Bioelectronics **25**(7): 1809-1815.

Keirstead, S. A. and R. F. Miller (1995). "Calcium Waves in Dissociated Retinal Glial (Muller) Cells Are Evoked by Release of Calcium from Intracellular Stores." Glia **14**(1): 14-22.

Kesler, A. and P. Pianka (2003). "Toxic optic neuropathy." Curr Neurol Neurosci Rep **3**(5): 410-414.

Khawly, J. A., J. D. Matthews, et al. (1999). "Appearance and rapid growth of retinal tumor (reactive astrocytic hyperplasia?)." Graefes Arch Clin Exp Ophthalmol **237**(1): 78-81.
Kim, D. H., N. Lu, et al. (2011). "Materials for multifunctional balloon catheters with capabilities in cardiac electrophysiological mapping and ablation therapy." Nat Mater **10**(4): 316-323.
Kim, I. J., Y. Zhang, et al. (2008). "Molecular identification of a retinal cell type that responds to upward motion." Nature **452**(7186): 478-482.
Klier, E. M. and D. E. Angelaki (2008). "Spatial Updating and the Maintenance of Visual Constancy." Neuroscience **156**(4): 801-818.
Koeberle, P. D. and A. K. Ball (1999). "Nitric oxide synthase inhibition delays axonal degeneration and promotes the survival of axotomized retinal ganglion cells." Exp Neurol **158**(2): 366-381.
Koehler, R. C., R. J. Roman, et al. (2009). "Astrocytes and the regulation of cerebral blood flow." Trends Neurosci **32**(3): 160-169.
Kohler, K. L., H. Schmid, et al. (2005). "Implanting Electrical Devices Into the Eye: Evaluation of Long-Term Tolerance and Pathological Thresholds of Electrical Stimuli to the Retina." Invest. Ophthalmol. Vis. Sci. **46**(5): 1525-.
Koizumi, A. and H. Jouhou (2009). "Organotypic culture of adult rodent retina." Neuroscience Research **65**: S172-S172.
Koizumi, A., G. Zeck, et al. (2007). "Organotypic Culture of Physiologically Functional Adult Mammalian Retinas." Plos One **2**(2).
Kolb, H. (1970). "Organization of the outer plexiform layer of the primate retina: electron microscopy of Golgi-impregnated cells." Philos Trans R Soc Lond B Biol Sci **258**(823): 261-283.
Kolb, H. (1977). "The organization of the outer plexiform layer in the retina of the cat: electron microscopic observations." Journal of Neurocytology **6**(2): 131-153.
Kolb, H. and E. V. Famiglietti (1974). "Rod and cone pathways in the inner plexiform layer of cat retina." Science **186**(4158): 47-49.
Kolb, H., R. Nelson, et al. (1981). "Amacrine cells, bipolar cells and ganglion cells of the cat retina: a Golgi study." Vision Res **21**(7): 1081-1114.
Koós, A. A., R. J. Nicholls, et al. (2012). "Tailoring gas sensing properties of multi-walled carbon nanotubes by in situ modification with Si, P, and N." Carbon **50**(8): 2816-2823.
Koriyama, Y., K. Sugitani, et al. (2012). "An application for mammalian optic nerve repair by fish regeneration-associated genes." Adv Exp Med Biol **723**: 161-166.
Koroleva, A., A. A. Gill, et al. (2012). "Two-photon polymerization-generated and micromolding-replicated 3D scaffolds for peripheral neural tissue engineering applications." Biofabrication **4**(2): 025005.
Kuffler, S. W. (1953). "Discharge patterns and functional organization of mammalian retina." J Neurophysiol **16**(1): 37-68.
Kusnyerik, A., M. Resch, et al. (2011). "[Vision restoration with implants in retinal degenerations]." Orv Hetil **152**(14): 537-545.
Lambacher, A., M. Jenkner, et al. (2004). "Electrical imaging of neuronal activity by multi-transistor-array (MTA) recording at 7.8 mu m resolution." Applied Physics a-Materials Science & Processing **79**(7): 1607-1611.
Langmann, T. (2007). "Microglia activation in retinal degeneration." J Leukoc Biol **81**(6): 1345-1351.

LaVail, M. M., K. Unoki, et al. (1992). "Multiple growth factors, cytokines, and neurotrophins rescue photoreceptors from the damaging effects of constant light." Proc Natl Acad Sci U S A **89**(23): 11249-11253.

LaVail, M. M., D. Yasumura, et al. (1998). "Protection of mouse photoreceptors by survival factors in retinal degenerations." Invest Ophthalmol Vis Sci **39**(3): 592-602.

Lee, J. E., K. J. Liang, et al. (2008). "Ex vivo dynamic imaging of retinal microglia using time-lapse confocal microscopy." Invest Ophthalmol Vis Sci **49**(9): 4169-4176.

Lesny, P., J. De Croos, et al. (2002). "Polymer hydrogels usable for nervous tissue repair." J Chem Neuroanat **23**(4): 243-247.

Leventhal, A. G., J. Keens, et al. (1980). "The Afferent Ganglion-Cells and Cortical Projections of the Retinal Recipient Zone (Rrz) of the Cats Pulvinar Complex." Journal of Comparative Neurology **194**(3): 535-554.

Lewis, G. P. and S. K. Fisher (2000). "Muller cell outgrowth after retinal detachment: association with cone photoreceptors." Invest Ophthalmol Vis Sci **41**(6): 1542-1545.

Lewis, G. P., K. A. Linberg, et al. (1999). "Effects of the neurotrophin brain-derived neurotrophic factor in an experimental model of retinal detachment." Invest Ophthalmol Vis Sci **40**(7): 1530-1544.

Li, G., B. De La Garza, et al. (2012). "Layer-specific blood-flow MRI of retinitis pigmentosa in RCS rats." Exp Eye Res **101**: 90-96.

Lin, B., R. H. Masland, et al. (2009). "Remodeling of cone photoreceptor cells after rod degeneration in rd mice." Exp Eye Res **88**(3): 589-599.

Lin, C. M., Y. T. Lee, et al. (2009). "Flexible carbon nanotubes electrode for neural recording." Biosensors & Bioelectronics **24**(9): 2791-2797.

Linberg, K. A., G. P. Lewis, et al. (2006). "Immunocytochemical evidence that rod-connected horizontal cell axon terminals remodel in response to experimental retinal detachment in the cat." Mol Vis **12**: 1674-1686.

Liu, B. and A. H. Neufeld (2001). "Nitric oxide synthase-2 in human optic nerve head astrocytes induced by elevated pressure in vitro." Arch Ophthalmol **119**(2): 240-245.

Los, L. I., M. J. A. van Luyn, et al. (1999). "Organization of the rabbit vitreous body: Lamellae, Cloquet's channel and a novel structure, the 'alae canalis Cloqueti'." Exp Eye Res **69**(3): 343-350.

Lyubarsky, A. L., B. Falsini, et al. (1999). "UV- and midwave-sensitive cone-driven retinal responses of the mouse: a possible phenotype for coexpression of cone photopigments." Journal of Neuroscience **19**(1): 442-455.

Maccarone, R., S. Di Marco, et al. (2008). "Saffron supplement maintains morphology and function after exposure to damaging light in mammalian retina." Invest Ophthalmol Vis Sci **49**(3): 1254-1261.

Machida, S., D. Raz-Prag, et al. (2008). "Photopic ERG negative response from amacrine cell signaling in RCS rat retinal degeneration." Invest Ophthalmol Vis Sci **49**(1): 442-452.

MacNeil, M. A., J. K. Heussy, et al. (2004). "The population of bipolar cells in the rabbit retina." J Comp Neurol **472**(1): 73-86.

MacNeil, M. A. and R. H. Masland (1998). "Extreme diversity among amacrine cells: implications for function." Neuron **20**(5): 971-982.

Magalhaes, M. M. and A. Coimbra (1972). "The rabbit retina Muller cell. A fine structural and cytochemical study." J Ultrastruct Res **39**(3): 310-326.

Maguire, A. M., F. Simonelli, et al. (2008). "Safety and efficacy of gene transfer for Leber's congenital amaurosis." N Engl J Med **358**(21): 2240-2248.
Mahadevappa, M., J. D. Weiland, et al. (2005). "Perceptual thresholds and electrode impedance in three retinal prosthesis subjects." IEEE Trans Neural Syst Rehabil Eng **13**(2): 201-206.
Malecaze, F., C. Caratero, et al. (1985). "Some Ultrastructural Aspects of the Vitreoretinal Juncture." Ophthalmologica **191**(1): 22-28.
Mandel, Y., G. Goetz, et al. (2013). "Cortical responses elicited by photovoltaic subretinal prostheses exhibit similarities to visually evoked potentials." Nat Commun **4**.
Marc, R. E. (2009). Functional Neuroanatomy of the retina. Duane's Ophthalmology 2009 Edition. W. J. Tasman, Edward A., Lippincott Williams & Wilkins (LWW).
Marc, R. E. (2010). Injury and Repair: Retinal Remodeling. Enceclopedia of the Eye. D. A. Dartt, Elsevier.
Marc, R. E. and B. W. Jones (2003). "Retinal remodeling in inherited photoreceptor degenerations." Mol Neurobiol **28**(2): 139-147.
Marc, R. E., B. W. Jones, et al. (2007). "Neural reprogramming in retinal degeneration." Invest Ophthalmol Vis Sci **48**(7): 3364-3371.
Marc, R. E., B. W. Jones, et al. (2012). "Building retinal connectomes." Curr Opin Neurobiol **22**(4): 568-574.
Marc, R. E., B. W. Jones, et al. (2003). "Neural remodeling in retinal degeneration." Prog Retin Eye Res **22**(5): 607-655.
Marc, R. E., B. W. Jones, et al. (2008). "Extreme retinal remodeling triggered by light damage: implications for age related macular degeneration." Mol Vis **14**: 782-806.
Margalit, E., N. Babai, et al. (2011). "Inner and outer retinal mechanisms engaged by epiretinal stimulation in normal and rd mice." Vis Neurosci **28**(2): 145-154.
Margalit, E., M. Maia, et al. (2002). "Retinal prosthesis for the blind." Surv Ophthalmol **47**(4): 335-356.
Margalit, E. and W. B. Thoreson (2006). "Inner retinal mechanisms engaged by retinal electrical stimulation." Invest Ophthalmol Vis Sci **47**(6): 2606-2612.
Margolis, D. J., G. Newkirk, et al. (2008). "Functional stability of retinal ganglion cells after degeneration-induced changes in synaptic input." Journal of Neuroscience **28**(25): 6526-6536.
Masland, R. H. (2001). "The fundamental plan of the retina." Nat Neurosci **4**(9): 877-886.
Masland, R. H. (2001). "Neuronal diversity in the retina." Curr Opin Neurobiol **11**(4): 431-436.
Masland, R. H. (2012). "The neuronal organization of the retina." Neuron **76**(2): 266-280.
Masland, R. H. (2012). "The tasks of amacrine cells." Vis Neurosci **29**(1): 3-9.
Mathieson, K., J. Loudin, et al. (2012). "Photovoltaic retinal prosthesis with high pixel density." Nature Photonics **6**(6): 391-397.
Matsuda, T. and C. L. Cepko (2004). "Electroporation and RNA interference in the rodent retina in vivo and in vitro." Proc Natl Acad Sci U S A **101**(1): 16-22.
Matsumoto, B., J. C. Blanks, et al. (1984). "Topographic variations in the rabbit and primate internal limiting membrane." Invest Ophthalmol Vis Sci **25**(1): 71-82.

Matsumoto, K., C. Sato, et al. (2007). "Neurite outgrowths of neurons with neurotrophin-coated carbon nanotubes." Journal of Bioscience and Bioengineering **103**(3): 216-220.
McCreery, D. B., W. F. Agnew, et al. (1990). "Charge density and charge per phase as cofactors in neural injury induced by electrical stimulation." IEEE Trans Biomed Eng **37**(10): 996-1001.
McGovern, B., R. B. Palmini, et al. (2010). "A New Individually Addressable Micro-LED Array for Photogenetic Neural Stimulation." Ieee Transactions on Biomedical Circuits and Systems **4**(6): 469-476.
Medana, I. M., T. Chan-Ling, et al. (1996). "Redistribution and degeneration of retinal astrocytes in experimental murine cerebral malaria: relationship to disruption of the blood-retinal barrier." Glia **16**(1): 51-64.
Medana, I. M., N. H. Hunt, et al. (1997). "Early activation of microglia in the pathogenesis of fatal murine cerebral malaria." Glia **19**(2): 91-103.
Meier, R., U. Egert, et al. (2008). "FIND--a unified framework for neural data analysis." Neural Netw **21**(8): 1085-1093.
Menzler, J. and G. Zeck (2011). "Network oscillations in rod-degenerated mouse retinas." Journal of Neuroscience **31**(6): 2280-2291.
Mills, S. L. and S. C. Massey (1994). "Distribution and Coverage of a-Type and B-Type Horizontal Cells Stained with Neurobiotin in the Rabbit Retina." Vis Neurosci **11**(3): 549-560.
Misteli, T. and D. L. Spector (1997). "Applications of the green fluorescent protein in cell biology and biotechnology." Nat Biotechnol **15**(10): 961-964.
Miyata, T., N. Asami, et al. (1999). "A reversibly antigen-responsive hydrogel." Nature **399**(6738): 766-769.
Morgans, C. W., J. M. Zhang, et al. (2009). "TRPM1 is required for the depolarizing light response in retinal ON-bipolar cells." Proc Natl Acad Sci U S A **106**(45): 19174-19178.
Moritoh, S., K. F. Tanaka, et al. (2010). "Organotypic tissue culture of adult rodent retina followed by particle-mediated acute gene transfer in vitro." Plos One **5**(9): e12917.
Morrow, E. M., T. Furukawa, et al. (2005). "Synaptogenesis and outer segment formation are perturbed in the neural retina of Crx mutant mice." BMC Neurosci **6**: 5.
Moshfeghi, D. M. (2006). "Presumed transient reactive astrocytic hyperplasia in immature retina." Retina **26**(7 Suppl): S69-73.
Nagashima, M., H. Sakurai, et al. (2009). "Involvement of retinoic acid signaling in goldfish optic nerve regeneration." Neurochem Int **54**(3-4): 229-236.
Nagelhus, E. A., Y. Horio, et al. (1999). "Immunogold evidence suggests that coupling of K+ siphoning and water transport in rat retinal Muller cells is mediated by a coenrichment of Kir4.1 and AQP4 in specific membrane domains." Glia **26**(1): 47-54.
Nakamura, T., T. Murata, et al. (2003). "Ultrastructure of the vitreoretinal interface following the removal of the internal limiting membrane using indocyanine green." Curr Eye Res **27**(6): 395-399.
Nakazawa, T., A. Matsubara, et al. (2006). "Characterization of cytokine responses to retinal detachment in rats." Molecular Vision **12**(97-98): 867-878.

Nash, M. S. and N. N. Osborne (1999). "Assessment of Thy-1 mRNA levels as an index of retinal ganglion cell damage." Investigative Ophthalmology & Visual Science **40**(6): 1293-1298.
Natoli, R., Y. Zhu, et al. (2010). "Gene and noncoding RNA regulation underlying photoreceptor protection: microarray study of dietary antioxidant saffron and photobiomodulation in rat retina." Mol Vis **16**: 1801-1822.
Nelson, R., E. V. Famiglietti, Jr., et al. (1978). "Intracellular staining reveals different levels of stratification for on- and off-center ganglion cells in cat retina." J Neurophysiol **41**(2): 472-483.
Neufeld, A. H. (1999). "Nitric oxide: a potential mediator of retinal ganglion cell damage in glaucoma." Surv Ophthalmol **43 Suppl 1**: S129-135.
Newman, E. A. (2001). "Propagation of intercellular calcium waves in retinal astrocytes and Muller cells." Journal of Neuroscience **21**(7): 2215-2223.
Newman, E. A. and K. R. Zahs (1997). "Calcium waves in retinal glial cells." Science **275**(5301): 844-847.
Newman, N. J. (1993). "Leber's hereditary optic neuropathy. New genetic considerations." Arch Neurol **50**(5): 540-548.
Nimmerjahn, A., F. Kirchhoff, et al. (2005). "Resting microglial cells are highly dynamic surveillants of brain parenchyma in vivo." Science **308**(5726): 1314-1318.
Nirenberg, S. and C. Pandarinath (2012). "Retinal prosthetic strategy with the capacity to restore normal vision." Proc Natl Acad Sci U S A **109**(37): 15012-15017.
Nishihara, H. (1991). "[Studies on the ultrastructure of the inner limiting membrane of the retina--distribution of anionic sites in the inner limiting membrane of the retina]." Nihon Ganka Gakkai Zasshi **95**(10): 951-958.
Nissl, F. (1894). "Ueber eine neue Untersuchungsmethode des Centralorgans zur Feststellung der Localisation der Nervenzellen." Neurologisches Centralblatt(13): 507-508.
Norenberg, M. D. (1994). "Astrocyte responses to CNS injury." J Neuropathol Exp Neurol **53**(3): 213-220.
O'Hearn, T. M., S. R. Sadda, et al. (2006). "Electrical stimulation in normal and retinal degeneration (rd1) isolated mouse retina." Vision Res **46**(19): 3198-3204.
Ogden, T. E. (1978). "Nerve fiber layer astrocytes of the primate retina: morphology, distribution, and density." Invest Ophthalmol Vis Sci **17**(6): 499-510.
Ogilvie, J. M., J. D. Speck, et al. (1999). "A reliable method for organ culture of neonatal mouse retina with long-term survival." J Neurosci Methods **87**(1): 57-65.
Olsen, T. W., P. Sternberg, Jr., et al. (1998). "Macular hole surgery using thrombin-activated fibrinogen and selective removal of the internal limiting membrane." Retina **18**(4): 322-329.
Otani, A., K. Kinder, et al. (2002). "Bone marrow-derived stem cells target retinal astrocytes and can promote or inhibit retinal angiogenesis." Nat Med **8**(9): 1004-1010.
Otto, W. R., J. Nanchahal, et al. (1995). "Survival of allogeneic cells in cultured organotypic skin grafts." Plast Reconstr Surg **96**(1): 166-176.
Oyster, C. W., J. I. Simpson, et al. (1980). "Retinal Ganglion-Cells Projecting to the Rabbit Accessory Optic-System." Journal of Comparative Neurology **190**(1): 49-61.
Parpura, V., V. Grubisic, et al. (2011). "Ca(2+) sources for the exocytotic release of glutamate from astrocytes." Biochim Biophys Acta **1813**(5): 984-991.

Parpura, V. and A. Verkhratsky (2012). "The astrocyte excitability brief: from receptors to gliotransmission." Neurochem Int **61**(4): 610-621.
Pavlidis, M., D. Fischer, et al. (2000). "Photoreceptor degeneration in the RCS rat attenuates dendritic transport and axonal regeneration of ganglion cells." Invest Ophthalmol Vis Sci **41**(8): 2318-2328.
Pedler, C. (1961). "The Inner Limiting Membrane of the Retina." Br J Ophthalmol **45**(6): 423-438.
Pellegrini, G., C. E. Traverso, et al. (1997). "Long-term restoration of damaged corneal surfaces with autologous cultivated corneal epithelium." Lancet **349**(9057): 990-993.
Perrault, I., J. M. Rozet, et al. (1999). "Leber congenital amaurosis." Mol Genet Metab **68**(2): 200-208.
Perry, V. H. and A. Cowey (1984). "Retinal Ganglion-Cells That Project to the Superior Colliculus and Pretectum in the Macaque Monkey." Neuroscience **12**(4): 1125-1137.
Perry, V. H., D. A. Hume, et al. (1985). "Immunohistochemical localization of macrophages and microglia in the adult and developing mouse brain." Neuroscience **15**(2): 313-326.
Perry, V. H., R. Oehler, et al. (1984). "Retinal Ganglion-Cells That Project to the Dorsal Lateral Geniculate-Nucleus in the Macaque Monkey." Neuroscience **12**(4): 1101-1123.
Piccardi, M., D. Marangoni, et al. (2012). "A longitudinal follow-up study of saffron supplementation in early age-related macular degeneration: sustained benefits to central retinal function." Evid Based Complement Alternat Med **2012**: 429124.
Pignatelli, V., C. L. Cepko, et al. (2004). "Inner retinal abnormalities in a mouse model of Leber's congenital amaurosis." Journal of Comparative Neurology **469**(3): 351-359.
Pinilla, I., R. D. Lund, et al. (2005). "Enhanced cone dysfunction in rats homozygous for the P23H rhodopsin mutation." Neurosci Lett **382**(1-2): 16-21.
Poitry-Yamate, C. L., S. Poitry, et al. (1995). "Lactate released by Muller glial cells is metabolized by photoreceptors from mammalian retina." Journal of Neuroscience **15**(7 Pt 2): 5179-5191.
Polyak, S. L. (1941). The Retina. Chicago, University of Chicago Press.
Provis, J. M. (2001). "Development of the primate retinal vasculature." Prog Retin Eye Res **20**(6): 799-821.
Quiroga, R. Q., Z. Nadasdy, et al. (2004). "Unsupervised spike detection and sorting with wavelets and superparamagnetic clustering." Neural Comput **16**(8): 1661-1687.
Radushkevich, L. and V. Lukyanovich (1952). "O strukture ugleroda, obrazujucegosja pri termiceskom razlozenii okisi ugleroda na zeleznom kontakte." Zurn Fisic Chim.(26): 88–95.
Ramon y Cajal, S. (1911). Histology of the Nervous System New York.
Ranck, J. B., Jr. (1975). "Which elements are excited in electrical stimulation of mammalian central nervous system: a review." Brain Res **98**(3): 417-440.
Rasmussen, K. E. (1972). "A morphometric study of the Muller cell cytoplasm in the rat retina." J Ultrastruct Res **39**(5): 413-429.

Ravindran, S., S. Chaudhary, et al. (2003). "Covalent Coupling of Quantum Dots to Multiwalled Carbon Nanotubes for Electronic Device Applications." Nano Lett **3**(4): 447-453.

Raviola, E. and N. B. Gilula (1975). "Intramembrane organization of specialized contacts in the outer plexiform layer of the retina. A freeze-fracture study in monkeys and rabbits." J Cell Biol **65**(1): 192-222.

Reese, B. E., P. W. Keeley, et al. (2011). "Developmental plasticity of dendritic morphology and the establishment of coverage and connectivity in the outer retina." Dev Neurobiol.

Reilly, R. M. (2007). "Carbon nanotubes: potential benefits and risks of nanotechnology in nuclear medicine." J Nucl Med **48**(7): 1039-1042.

Rhodes, R. H. (1982). "An Ultrastructural-Study of the Complex Carbohydrates of the Mouse Posterior Vitreoretinal Juncture." Invest Ophthalmol Vis Sci **22**(4): 460-477.

Rio-Hortega, P. D. (1932). "Microglia." Cytology and cellular pathology of the nervous system: 481–534.

Rio, J. P., J. Reperant, et al. (1989). "A preliminary description of the regeneration of optic nerve fibers in a reptile, Vipera aspis." Brain Res **479**(1): 151-156.

Rivolta, C., D. Sharon, et al. (2002). "Retinitis pigmentosa and allied diseases: numerous diseases, genes, and inheritance patterns." Hum Mol Genet **11**(10): 1219-1227.

Rockhill, R. L., T. Euler, et al. (2000). "Spatial order within but not between types of retinal neurons." Proc Natl Acad Sci U S A **97**(5): 2303-2307.

Rohrer, B. and J. M. Ogilvie (2003). "Retarded outer segment development in TrkB knockout mouse retina organ culture." Mol Vis **9**: 18-23.

Ross, J. W., J. P. Fernandez de Castro, et al. (2012). "Generation of an inbred miniature pig model of retinitis pigmentosa." Invest Ophthalmol Vis Sci **53**(1): 501-507.

Rothermel, A., L. Liu, et al. (2009). "A CMOS Chip With Active Pixel Array and Specific Test Features for Subretinal Implantation." Ieee Journal of Solid-State Circuits **44**(1): 290-300.

Rungger-Brandle, E., A. A. Dosso, et al. (2000). "Glial reactivity, an early feature of diabetic retinopathy." Invest Ophthalmol Vis Sci **41**(7): 1971-1980.

Russell, S. R., J. D. Shepherd, et al. (1991). "Distribution of glycoconjugates in the human retinal internal limiting membrane." Invest Ophthalmol Vis Sci **32**(7): 1986-1995.

Saito, T., K. Matsushige, et al. (2002). "Chemical treatment and modification of multi-walled carbon nanotubes." Physica B-Condensed Matter **323**(1-4): 280-283.

Sakimoto, S., H. Kidoya, et al. (2012). "A role for endothelial cells in promoting the maturation of astrocytes through the apelin/APJ system in mice." Development **139**(7): 1327-1335.

Schiefer, M. A. and W. M. Grill (2006). "Sites of neuronal excitation by epiretinal electrical stimulation." IEEE Trans Neural Syst Rehabil Eng **14**(1): 5-13.

Schiller, P. H. and N. K. Logothetis (1990). "The color-opponent and broad-band channels of the primate visual system." Trends Neurosci **13**(10): 392-398.

Schnapf, J. L., T. W. Kraft, et al. (1988). "Spectral sensitivity of primate photoreceptors." Vis Neurosci **1**(3): 255-261.

Schuettler, M. (2007). "Electrochemical properties of platinum electrodes in vitro: comparison of six different surface qualities." Conf Proc IEEE Eng Med Biol Soc **2007**: 186-189.

Schuetz, E. and S. Thanos (2004). "Microglia-targeted pharmacotherapy in retinal neurodegenerative diseases." Curr Drug Targets **5**(7): 619-627.
Schultze, M. (1866). Zur Anatomie und Physiologie der Retina Bonn

Cohen.
Scott, K. (2011). "3D elemental and structural analysis of biological specimens using electrons and ions." Journal of Microscopy **242**(1): 86-93.
Sekirnjak, C., P. Hottowy, et al. (2006). "Electrical stimulation of mammalian retinal ganglion cells with multielectrode arrays." J Neurophysiol **95**(6): 3311-3327.
Sekirnjak, C., P. Hottowy, et al. (2008). "High-resolution electrical stimulation of primate retina for epiretinal implant design." Journal of Neuroscience **28**(17): 4446-4456.
Sekirnjak, C., C. Hulse, et al. (2009). "Loss of responses to visual but not electrical stimulation in ganglion cells of rats with severe photoreceptor degeneration." J Neurophysiol **102**(6): 3260-3269.
Sernagor, E., M. Hennig, et al. (2012). Following The Assembly Of Functional Circuitry: High Resolution Large-Scale Population Neuronal Dynamics In The Neonatal Mouse Retina In Health And Disease. 8th Int. Meeting on Substrate-Integrated Microelectrodes, BIOPRO Baden-Württemberg GmbH.
Shein, M., A. Greenbaum, et al. (2009). "Engineered neuronal circuits shaped and interfaced with carbon nanotube microelectrode arrays." Biomedical Microdevices **11**(2): 495-501.
Shen, Y., J. A. Heimel, et al. (2009). "A Transient Receptor Potential-Like Channel Mediates Synaptic Transmission in Rod Bipolar Cells." Journal of Neuroscience **29**(19): 6088-6093.
Shi, J., H. Y. Zhang, et al. (2012). "An aqueous media based approach for the preparation of a biosensor platform composed of graphene oxide and Pt-black." Biosensors & Bioelectronics **38**(1): 314-320.
Shire, D. B., S. K. Kelly, et al. (2009). "Development and Implantation of a Minimally Invasive Wireless Subretinal Neurostimulator." Ieee Transactions on Biomedical Engineering **56**(10): 2502-2511.
Shoval, A., C. Adams, et al. (2009). "Carbon nanotube electrodes for effective interfacing with retinal tissue." Front Neuroengineering **2**: 4.
Sigelman, J., V. Ozanics, et al. (1982). Ocular Anatomy, Embryology and Teratology Lippincott Williams and Wilkins
Smiddy, W. E., W. Feuer, et al. (2001). "Internal limiting membrane peeling in macular hole surgery." Ophthalmology **108**(8): 1471-1476; discussion 1477-1478.
Smith, W., J. Assink, et al. (2001). "Risk factors for age-related macular degeneration: Pooled findings from three continents." Ophthalmology **108**(4): 697-704.
Sorkin, R., A. Greenbaum, et al. (2009). "Process entanglement as a neuronal anchorage mechanism to rough surfaces." Nanotechnology **20**(1): 015101.
Spira, M., D. Kamber, et al. (2007). "Improved neuronal adhesion to the surface of electronic device by engulfment of protruding micro-nails fabricated on the chip surface." The 14th International Conference on Solid-State Sensors, Actuators and Microsystems, Lyon, France,.
Stasheff, S. F. (2008). "Emergence of sustained spontaneous hyperactivity and temporary preservation of OFF responses in ganglion cells of the retinal degeneration (rd1) mouse." J Neurophysiol **99**(3): 1408-1421.

Stensaas, L. J. (1977). "The ultrastructure of astrocytes, oligodendrocytes, and microglia in the optic nerve of urodele amphibians (A. punctatum, T. pyrrhogaster, T. viridescens)." J Neurocytol **6**(3): 269-286.
Stone, J. and Z. Dreher (1987). "Relationship between astrocytes, ganglion cells and vasculature of the retina." Journal of Comparative Neurology **255**(1): 35-49.
Stone, J., J. Leicester, et al. (1973). "The naso-temporal division of the monkey's retina." Journal of Comparative Neurology **150**(3): 333-348.
Stoppini, L., P. A. Buchs, et al. (1991). "A simple method for organotypic cultures of nervous tissue." J Neurosci Methods **37**(2): 173-182.
Streit, W. J., S. A. Walter, et al. (1999). "Reactive microgliosis." Prog Neurobiol **57**(6): 563-581.
Strettoi, E., V. Pignatelli, et al. (2003). "Remodeling of second-order neurons in the retina of rd/rd mutant mice." Vision Res **43**(8): 867-877.
Strettoi, E., V. Porciatti, et al. (2002). "Morphological and functional abnormalities in the inner retina of the rd/rd mouse." Journal of Neuroscience **22**(13): 5492-5504.
Strettoi, E., E. Raviola, et al. (1992). "Synaptic connections of the narrow-field, bistratified rod amacrine cell (AII) in the rabbit retina." Journal of Comparative Neurology **325**(2): 152-168.
Sullivan, R., P. Penfold, et al. (2003). "Neuronal migration and glial remodeling in degenerating retinas of aged rats and in nonneovascular AMD." Invest Ophthalmol Vis Sci **44**(2): 856-865.
Suzuki, S., M. S. Humayun, et al. (2004). "Comparison of electrical stimulation thresholds in normal and retinal degenerated mouse retina." Jpn J Ophthalmol **48**(4): 345-349.
Suzumura, A., S. G. E. Mezitis, et al. (1987). "Mhc Antigen Expression on Bulk Isolated Macrophage-Microglia from Newborn Mouse-Brain - Induction of Ia-Antigen Expression by Gamma-Interferon." J Neuroimmunol **15**(3): 263-278.
Swann, D. A. and I. J. Constable (1972). "Vitreous structure. I. Distribution of hyaluronate and protein." Invest Ophthalmol **11**(3): 159-163.
Szamier, R. B. and E. L. Berson (1977). "Retinal ultrastructure in advanced retinitis pigmentosa." Invest Ophthalmol Vis Sci **16**(10): 947-962.
Szel, A., P. Rohlich, et al. (1992). "Unique topographic separation of two spectral classes of cones in the mouse retina." J Comp Neurol **325**(3): 327-342.
Tailoi, C. L., S. Tout, et al. (1992). "Vascular Changes and Their Mechanisms in the Feline Model of Retinopathy of Prematurity." Invest Ophthalmol Vis Sci **33**(7): 2128-2147.
Takesue, I., J. Haruyama, et al. (2006). "Superconductivity in entirely end-bonded multiwalled carbon nanotubes." Phys Rev Lett **96**(5): 057001.
Tang, Z. K., L. Y. Zhang, et al. (2001). "Superconductivity in 4 angstrom single-walled carbon nanotubes." Science **292**(5526): 2462-2465.
Tassicker, G. E. (1956). Retinal Stimulator. USA. .
Thanos, S., J. Mey, et al. (1993). "Treatment of the Adult Retina with Microglia-Suppressing Factors Retards Axotomy-Induced Neuronal Degradation and Enhances Axonal Regeneration Invivo and Invitro." Journal of Neuroscience **13**(2): 455-466.
Thiebaud, P., N. F. de Rooij, et al. (1997). "Microelectrode arrays for electrophysiological monitoring of hippocampal organotypic slice cultures." IEEE Trans Biomed Eng **44**(11): 1159-1163.

Trenholm, S., J. Borowska, et al. (2012). "Intrinsic oscillatory activity arising within the electrically coupled AII amacrine-ON cone bipolar cell network is driven by voltage-gated Na+ channels." J Physiol **590**(Pt 10): 2501-2517.
Tseng, C. Y., E. A. Ling, et al. (1983). "Light and electron microscopic and cytochemical identification of amoeboid microglial cells in the brain of prenatal rats." J Anat **136**(Pt 4): 837-849.
Turner, J. N., W. Shain, et al. (1999). "Cerebral astrocyte response to micromachined silicon implants." Experimental Neurology **156**(1): 33-49.
Uga, S. and Smelser (1973). "Comparative study of the fine structure of retinal Muller cells in various vertebrates." Invest Ophthalmol **12**(6): 434-448.
Vaney, D. I. (1986). "Morphological identification of serotonin-accumulating neurons in the living retina." Science **233**(4762): 444-446.
Vaney, D. I., I. C. Gynther, et al. (1991). "Rod-signal interneurons in the rabbit retina: 2. AII amacrine cells." Journal of Comparative Neurology **310**(2): 154-169.
Volgyi, B., D. Xin, et al. (2001). "Morphology and physiology of the polyaxonal amacrine cells in the rabbit retina." Journal of Comparative Neurology **440**(1): 109-125.
Wagenaar, D. A., J. Pine, et al. (2004). "Effective parameters for stimulation of dissociated cultures using multi-electrode arrays." J Neurosci Methods **138**(1-2): 27-37.
Wagenaar, D. A. and S. M. Potter (2002). "Real-time multi-channel stimulus artifact suppression by local curve fitting." J Neurosci Methods **120**(2): 113-120.
Wang, B. H., B. C. Robertson, et al. (2001). "Traumatic optic neuropathy: a review of 61 patients." Plast Reconstr Surg **107**(7): 1655-1664.
Wang, K., H. A. Fishman, et al. (2006). "Neural stimulation with a carbon nanotube microelectrode array." Nano Lett **6**(9): 2043-2048.
Wang, K., D. Loftus, et al. (2003). "Carbon nanotubes as microelectrodes for a retinal prosthesis." Invest Ophthalmol Vis Sci **44**: U702-U702.
Wang, L., K. Mathieson, et al. (2012). "Photovoltaic retinal prosthesis: implant fabrication and performance." Journal of Neural Engineering **9**(4): 046014.
Wang, L. L., K. Mathieson, et al. (2012). "Photovoltaic retinal prosthesis: implant fabrication and performance." Journal of Neural Engineering **9**(4).
Wassle, H., C. Puller, et al. (2009). "Cone contacts, mosaics, and territories of bipolar cells in the mouse retina." Journal of Neuroscience **29**(1): 106-117.
Watanabe, T. and M. C. Raff (1988). "Retinal astrocytes are immigrants from the optic nerve." Nature **332**(6167): 834-837.
Weiland, J. D. and D. J. Anderson (2000). "Chronic neural stimulation with thin-film, iridium oxide electrodes." Ieee Transactions on Biomedical Engineering **47**(7): 911-918.
Weiland, J. D., D. J. Anderson, et al. (2002). "In vitro electrical properties for iridium oxide versus titanium nitride stimulating electrodes." IEEE Trans Biomed Eng **49**(12 Pt 2): 1574-1579.
Werblin, F. S. (2011). "The retinal hypercircuit: a repeating synaptic interactive motif underlying visual function." J Physiol **589**(Pt 15): 3691-3702.
Werblin, F. S. and J. E. Dowling (1969). "Organization of the retina of the mudpuppy, Necturus maculosus. II. Intracellular recording." J Neurophysiol **32**(3): 339-355.
Wilke, R., V. P. Gabel, et al. (2011). "Spatial resolution and perception of patterns mediated by a subretinal 16-electrode array in patients blinded by hereditary retinal dystrophies." Invest Ophthalmol Vis Sci **52**(8): 5995-6003.
Williams, P. (1995). Gray's Anatomy. New York, Churchill Livingstone.

Winkler, B. S., M. J. Arnold, et al. (2000). "Energy metabolism in human retinal Muller cells." Invest Ophthalmol Vis Sci **41**(10): 3183-3190.
Wojtkowski, M., V. Srinivasan, et al. (2005). "Three-dimensional retinal imaging with high-speed ultrahigh-resolution optical coherence tomography." Ophthalmology **112**(10): 1734-1746.
Wong-Riley, M. (1979). "Changes in the visual system of monocularly sutured or enucleated cats demonstrable with cytochrome oxidase histochemistry." Brain Res **171**(1): 11-28.
Wu, S. M., F. Gao, et al. (2001). "Integration and segregation of visual signals by bipolar cells in the tiger salamander retina." Progress in Brain Research **131**: 125-143.
Xin, H., J. A. Yannazzo, et al. (2007). "A novel organotypic culture model of the postnatal mouse retina allows the study of glutamate-mediated excitotoxicity." J Neurosci Methods **159**(1): 35-42.
Ye, J. H., K. H. Kim, et al. (2008). "Comparison of electrically-evoked ganglion cell responses in normal and degenerate retina." Conf Proc IEEE Eng Med Biol Soc **2008**: 2465-2468.
Ye, J. H., S. B. Ryu, et al. (2010). "Retinal ganglion cell (RGC) responses to different voltage stimulation parameters in rd1 mouse retina." Conf Proc IEEE Eng Med Biol Soc **2010**: 6761-6764.
Yoshimoto, H. (1978). "[Ultrastructure of the intercellular junction between the endothelial cells of retinal blood vessels in spontaneously hypertensive rate (SHR) (author's transl)]." Nihon Ganka Gakkai Zasshi **82**(11): 798-809.
Yu, D. Y. and S. J. Cringle (2001). "Oxygen distribution and consumption within the retina in vascularised and avascular retinas and in animal models of retinal disease." Prog Retin Eye Res **20**(2): 175-208.
Zamzami, N. and G. Kroemer (1999). "Apoptosis - Condensed matter in cell death." Nature **401**(6749): 127-128.
Zayed, M. A., W. Yuan, et al. (2007). "CIB1 regulates endothelial cells and ischemia-induced pathological and adaptive angiogenesis." Circ Res **101**(11): 1185-1193.
Zeiss, C. J. and E. A. Johnson (2004). "Proliferation of microglia, but not photoreceptors, in the outer nuclear layer of the rd-1 mouse." Invest Ophthalmol Vis Sci **45**(3): 971-976.
Zeiss, C. J. and E. A. Johnson (2004). "Proliferation of microglia, but not photoreceptors, the outer nuclear layer of the rd-1 mouse." Invest Ophthalmol Vis Sci **45**(3): 971-976.
Zeng, H. Y., X. A. Zhu, et al. (2005). "Identification of sequential events and factors associated with microglial activation, migration, and cytotoxicity in retinal degeneration in rd mice." Invest Ophthalmol Vis Sci **46**(8): 2992-2999.
Zhou, R. P., Z. M. Zhang, et al. (2012). "Establishing a disc degeneration model using computed tomography-guided percutaneous puncture technique in the rabbit." J Surg Res.
Zimmermann, J. (2009). Restoring Function to the Spinal Cord and Retina Using Electrical Stimulation. MRes in Medical and Molecular Biosciences: 2008/2009 Masters, Newcastle University.
Zrenner, E., K. U. Bartz-Schmidt, et al. (2011). "Subretinal electronic chips allow blind patients to read letters and combine them to words." Proc Biol Sci **278**(1711): 1489-1497.
Zuo, X. N., R. Ehmke, et al. (2012). "Network centrality in the human functional connectome." Cereb Cortex **22**(8): 1862-1875.

Appendices

Appendix A: Matlab Scripts

1. Scripts used in Chapter 1

```
function thresh2Dense(diam,thr)

% this function provides the charge density in mC/cm2 according to
% electrode diameter (diam) in um and threshold (thr) in nC

d = diam * (10^-4);
A = (d/2)*(d/2) * pi;
T = thr * (10^-6);

CD = T/A
```

```
function Dense2thresh(diam,dense)

% this function provides the charge threshold according to
% electrode diameter (diam) in um and charge density (dense) in mC/cm2

d = diam * (10^-4);
A = (d/2)*(d/2) * pi;
D = dense * (10^6);
 Thr = A*D
```

2. Scripts used in Chapter 2

```
function pixnum(a)

% Reads in 8 bit image, makes it binary and calculates the number of pixels
% in it

I = imread(a);
Ic = double (I);
Ib = logical(Ic);
num_1 = length(find(Ib==1))
num_0 = length(find(Ib==0))
num_all = numel(Ib)
```

3. Scripts used in Chapter 3

```
function  peak2peaxAll(expnum,stimnum,in,days)
% This function runs through spikes extracted by wave_clus from a 60 channel mcd file
and saved as channeldata.spikes.mat,
% extracts the peak-to-peak value between 20 and 100 ms and organises them
% into histograms with blue (day 1), red (day 2) and green (day 3)

% Variables
% Input variables:
% expnum:.....the value of the experiment's name. i.e. 29 for CE0029
% stimnum:.....the value of the stimulating electrode investigated
% in:.....the index-1 of the first of three directories
% days:.....how many days to look at
 % Constants
% electlist.....Organisation of channels from MC Rac to Natlab
% Xavs: .....The average peak-to-peak value for all spikes

eleclist = [12 13 14 15 16 17 21 22 23 24 25 26 27 28 31 32 33 34 35 36 37 38 41 42 43
44 45 46 47 48 51 52 53 54 55 56 57 58 61 62 63 64 65 66 67 68 71 72 73 74 75 76 77
78 81 82 83 84 85 86 87];

 a = num2str(expnum);
c = num2str(stimnum);

Xmins = zeros(60,days);       % initiates the Xmin variable, generally a 60 by 3 matrix
Xavs = zeros(60,days);        % initiates the Xavs variable, generally a 60 by 3 matrix
Xall = cell(days,1);

maxNSpikes = -Inf;
for j = 1:days

   t = num2str(j);
   tt = num2str(in + j);                    % as the index increases by one with each
day, this is why in = index-1
   b = sprintf('CE00%s_Stim%s_e%s_*spikes.mat',a,t,c);     % finds directory where
spikes are saved according to input values

%if j == 3
 %  b = sprintf('CE00%s_Stim%s_e%s_*spikes.mat',a,t,c);      %Add these lines in for
dealing with CE0017.
                                        %Also add an_ on line 36 CE0017_Stim_1
%end
% if j == 1
%     b = sprintf('CE00%s_Stim_e%s_*spikes.mat',a,c);
% end
```

```
   if in<8                                  % These if statements are there because
depending on the index size, there are either one or 2
      cd(  sprintf('00%s_CE00%s_Stim%s_e%s',tt,a,t,c));   % zeros in the directory name
   end
   if in>8
      cd(  sprintf('0%s_CE00%s_Stim%s_e%s',tt,a,t,c));
   end

   skip = find(eleclist == stimnum);

   datas = dir(b);                          % datas is the spikes extracted for all channels
   d = length(datas);                       % There are generally 60 channels


   All1 = [];
   for i = [1:skip-1 skip+1:d]              % This loops runs through all the channels to
extract the largest or average spike value
    % for i = 1:d
      file =  datas(i).name;
      load(file)                            % loads file that contains the spikes for that
channel
      %peax = zeros(length(spikes),1);      % initializes the peax variable
      peaxAll = zeros(length(spikes),1);


      peax = range(spikes(:,10:45),2);%-min(spikes(k,10:45));      % loads peak-to-peak
value for each spike between 20 and 40 ms
      chl(i)= str2num(file(end-12:end-11));

      TF = isempty(peax);                   % Sometimes you get files missing, so this adds
the value "x" to the Avs or mins variable if the file
      if  TF == 1                           % is missing
         Avs(i) = 'x';
         mins(i) = 'x';
         All1 = [All1; nan];
      end
      if TF == 0
      mins(i) = max(peax);                  % records the largest spike over all 60
channels
      Avs(i) = mean(peax);                  % records the average spike value over all 60
channels
      %All(i) = peax;                       % records all the spikes
      All1 = [All1; peax];
      end
      clear channelData
   end

 %   Xavs(1:g,j) = XY;
   maxNSpikes = max(maxNSpikes,length(All1));
```

```
    Xall{j} = All1;
    Xmins(1:length(mins),j) = mins;
    cd ..

end

Xall2 = zeros(maxNSpikes,days);

for j = 1:days
    all = Xall{j};
    Xall2(1:length(all),j) = all;
end

filename = [ 'Xmins' num2str(expnum) '_e' num2str(stimnum)]; % generates name of
excel file according to name of experiment and stim electrode
filenamea = [ 'Xavs' num2str(expnum) '_e' num2str(stimnum)];
filenameb = [ 'Xall' num2str(expnum) '_e' num2str(stimnum)];

if days > 2

    C1 = Xall2(:,1);
    C1 = C1(C1~=0);
    C2 = Xall2(:,2);
    C2 = C2(C2~=0);
    C3 = Xall2(:,3);
    C3 = C3(C3~=0);

    c1 = length(C1);
    c2 = length(C2);
    c3 = length(C3);
    c4 = [c1 c2 c3];
    c5 = max(c4);
    c6 = min(c4);

    C1 = C1(1:c6);
    C2 = C2(1:c6);
    C3 = C3(1:c6);

    L2 = [C1 C2 C3];
    max(L2);

end


if days == 2

    C1 = Xall2(:,1);
    C1 = C1(C1~=0);
    C2 = Xall2(:,2);
```

```
    C2 = C2(C2~=0);

    c1 = length(C1);
    c2 = length(C2);

    c4 = [c1 c2];
    c6 = min(c4);

    C1 = C1(1:c6);
    C2 = C2(1:c6);

    L2 = [C1 C2];

end
%figure
nat = [0:30:300];
xt = 1:length(nat);
natc = num2cell(nat);
natcn = cellfun(@num2str,natc,'Uni',0);
tal = histc(L2,nat);
bar(tal)

set(gca,'Yscale','log')
set(gca,'XTick',[xt],'XTickLabel',natcn);;

h = findobj(gca,'Type','patch');
set(h(1),'FaceColor','g','EdgeColor','w');
set(h(2),'FaceColor','r','EdgeColor','w');
if days > 2
   set(h(3),'FaceColor','b','EdgeColor','w');
end
% Create xlabel
xlabel('Spike size in micro-Volts');

% Create ylabel
ylabel('Number of spikes per bin');

title(['Number of spikes according to size (all) for CE00' a '_ e' c ],'FontWeight','bold')
```

4. Scripts used in Chapter 5

```
function conHexa(diam1, diam2, diam3, diam4)

% This function returns the surface area of a set of 3 concentric hexagons
% with diam1 providing the diameter of the most internal hexagon


Surfa1 = diam1*diam1*(3*sqrt(3/2))
```

Surfa2 = ((diam2*diam2)*(3*sqrt(3/2))) - Surfa1
Surfa3 = ((diam3*diam3)*(3*sqrt(3/2))) - (Surfa2 + Surfa1)

Appendix B: Sigma Plot reports

1. **Statistical tests from Chapter 2**

Astrocytic density of clusters

One Way Analysis of Variance

Normality Test: Passed (P = 0.835)

Equal Variance Test: Passed (P = 0.799)

Group Name	N	Missing	Mean	Std Dev	SEM
Col 1	6	0	6.142	0.441	0.180
Col 2	6	0	8.561	0.411	0.168
Col 3	6	0	2.739	0.310	0.126

Source of Variation	DF	SS	MS	F	P
Between Groups	2	102.657	51.328	334.757	<0.001
Residual	15	2.300	0.153		
Total	17	104.957			

The differences in the mean values among the treatment groups are greater than would be expected by chance; there is a statistically significant difference (P = <0.001).

Power of performed test with alpha = 0.050: 1.000

All Pairwise Multiple Comparison Procedures (Holm-Sidak method):
Overall significance level = 0.05

Comparisons for factor:

Comparison	Diff of Means	t	Unadjusted P	Critical Level	Significant?
Col 2 vs. Col 3	5.822	25.753	<0.001	0.017	Yes
Col 1 vs. Col 3	3.403	15.054	<0.001	0.025	Yes
Col 2 vs. Col 1	2.419	10.699	<0.001	0.050	Yes

2. **Statistical test from Chapter 3**

Section 3.3.3. Figure 3.4

Pooled percentage of oscillating electrodes

One Way Analysis of Variance

Normality Test: Passed (P = 0.083)

Equal Variance Test: Passed (P = 0.398)

Group Name	N	Missing	Mean	Std Dev	SEM
Col 1	14	0	65.374	24.200	6.468
Col 2	14	0	65.239	30.269	8.090
Col 3	14	0	55.322	23.681	6.329
Col 4	14	0	43.229	28.350	7.577
Col 5	14	1	18.556	15.946	4.423
Col 6	14	4	22.117	20.814	6.582

Source of Variation	DF	SS	MS	F	P
Between Groups	5	27239.551	5447.910	8.995	<0.001
Residual	73	44213.223	605.661		
Total	78	71452.774			

The differences in the mean values among the treatment groups are greater than would be expected by chance; there is a statistically significant difference (P = <0.001).

Power of performed test with alpha = 0.050: 1.000

Multiple Comparisons versus Control Group (Holm-Sidak method):
Overall significance level = 0.05

Comparisons for factor:

Comparison	Diff of Means	t	Unadjusted P	Critical Level	Significant?
Col 1 vs. Col 5	46.819	4.939	<0.001	0.010	Yes
Col 1 vs. Col 6	43.257	4.245	<0.001	0.013	Yes
Col 1 vs. Col 4	22.145	2.381	0.020	0.017	No
Col 1 vs. Col 3	10.052	1.081	0.283	0.025	No
Col 1 vs. Col 2	0.135	0.0145	0.988	0.050	No

Pooled percentage of active electrodes

Kruskal-Wallis One Way Analysis of Variance on Ranks

Data source: Data 1 in Notebook4

Group	N	Missing	Median	25%	75%
Col 1	14	0	61.474	37.736	75.000
Col 2	14	0	73.125	41.509	78.431
Col 3	14	0	52.512	36.538	70.000
Col 4	14	0	58.013	38.182	72.340
Col 5	14	1	41.509	25.581	61.498
Col 6	14	4	39.108	23.077	53.846

H = 8.552 with 5 degrees of freedom. (P = 0.128)

The differences in the median values among the treatment groups are not great enough to exclude the possibility that the difference is due to random sampling variability; there is not a statistically significant difference (P = 0.128)

Section 3.3.4. Figure 3.6

Average number of electrodes with inverted spikes per retina for days 1, 2 ,3

Group	N	Missing	Median	25%	75%
Col 1	13	0	0.000	0.000	1.750
Col 2	13	0	3.000	2.000	5.250
Col 3	13	0	1.000	0.000	1.250

H = 12.555 with 2 degrees of freedom. (P = 0.002)

The differences in the median values among the treatment groups are greater than would be expected by chance; there is a statistically significant difference (P = 0.002)

To isolate the group or groups that differ from the others use a multiple comparison procedure.
All Pairwise Multiple Comparison Procedures (Tukey Test):

Comparison	Diff of Ranks	q	P<0.05
Col 2 vs Col 3	174.500	4.245	Yes
Col 2 vs Col 1	173.500	4.220	Yes
Col 1 vs Col 3	1.000	0.0243	No

Note: The multiple comparisons on ranks do not include an adjustment for ties.

Day 2 CNT v TiN inverted spikes

t-test
Normality Test: Passed (P = 0.170)
Equal Variance Test: Passed (P = 0.317)

Group Name	N	Missing	Mean	Std Dev	SEM
Col 1	10	0	3.200	1.619	0.512
Col 2	2	0	4.000	2.828	2.000

Difference -0.800

t = -0.581 with 10 degrees of freedom. (P = 0.574)

95 percent confidence interval for difference of means: -3.868 to 2.268

The difference in the mean values of the two groups is not great enough to reject the possibility that the difference is due to random sampling variability. There is not a statistically significant difference between the input groups (P = 0.574).

Power of performed test with alpha = 0.050: 0.050

The power of the performed test (0.050) is below the desired power of 0.800.
Less than desired power indicates you are less likely to detect a difference when one actually exists. Negative results should be interpreted cautiously.

Day 3 CNT v TiN inverted spikes

Mann-Whitney Rank Sum Test

Group	N	Missing	Median	25%	75%
Col 4	10	0	0.000	0.000	1.000
Col 5	2	0	1.500	1.000	2.000

Mann-Whitney U Statistic= 3.500

T = 19.500 n(small)= 2 n(big)= 10 (P = 0.160)

The difference in the median values between the two groups is not great enough to exclude the possibility that the difference is due to random sampling variability; there is not a statistically significant difference (P = 0.160)

Section3.3.10

Direct response thresholds overall

All CNT vs TiN thresholds
t-test

Normality Test: Failed (P < 0.050)
Test execution ended by user request, Rank Sum Test begun

Mann-Whitney Rank Sum Test Friday, April 20, 2012, 02:01:24

Data source: Data 1 in Notebook1

Group	N	Missing	Median	25%	75%
Col 1	364	141	1.800	1.300	2.400
Col 2	1627	841	1.500	1.125	2.000

Mann-Whitney U Statistic= 62481.500

T = 137772.500 n(small)= 223 n(big)= 786 (P = <0.001)

The difference in the median values between the two groups is greater than would be expected by chance; there is a statistically significant difference (P = <0.001)CNT vs TiN

CNT thresholds for Day 1, Day 2 and Day 3: Figure 3.19

Kruskal-Wallis One Way Analysis of Variance on Ranks

Group	N	Missing	Median	25%	75%
Col 1	539	298	1.750	1.200	2.400
Col 2	544	155	1.250	0.990	1.880
Col 3	543	387	1.200	0.900	1.800

H = 45.626 with 2 degrees of freedom. (P = <0.001)

The differences in the median values among the treatment groups are greater than would be expected by chance; there is a statistically significant difference (P = <0.001)

To isolate the group or groups that differ from the others use a multiple comparison procedure.

All Pairwise Multiple Comparison Procedures (Dunn's Method) :

Comparison	Diff of Ranks	Q	P<0.05
Col 1 vs Col 3	147.133	6.306	Yes
Col 1 vs Col 2	95.585	5.136	Yes
Col 2 vs Col 3	51.548	2.396	Yes

Note: The multiple comparisons on ranks do not include an adjustment for ties.

TiN thresholds for Day 1, Day 2 and Day 3: Figure 3.19

Kruskal-Wallis One Way Analysis of Variance on Ranks

Group	N	Missing	Median	25%	75%
Col 1	145	62	1.800	1.600	2.400
Col 2	159	63	1.800	1.200	2.000
Col 3	123	73	1.800	1.600	3.000

H = 5.340 with 2 degrees of freedom. (P = 0.069)

The differences in the median values among the treatment groups are not great enough to exclude the possibility that the difference is due to random sampling variability; there is not a statistically significant difference (P = 0.069)

Direct responses per retina

CNT early number of responses per retina : Figure 3.20

One Way Repeated Measures Analysis of Variance

Normality Test: Passed (P = 0.127)

Equal Variance Test: Passed (P = 0.537)

Treatment Name	N	Missing	Mean	Std Dev	SEM
Col 1	11	0	21.909	14.909	4.495
Col 2	11	0	35.091	30.772	9.278
Col 3	11	0	13.818	13.385	4.036

Source of Variation	DF	SS	MS	F	P
Between Subjects	10	7853.212	785.321		
Between Treatments	2	2536.424	1268.212	4.505	0.024
Residual	20	5630.242	281.512		
Total	32	16019.879			

The differences in the mean values among the treatment groups are greater than would be expected by chance; there is a statistically significant difference (P = 0.024). To isolate the group or groups that differ from the others use a multiple comparison procedure.

Power of performed test with alpha = 0.050: 0.582

All Pairwise Multiple Comparison Procedures (Tukey Test):

Comparisons for factor:

Comparison	Diff of Means	p	q	P	P<0.050	
Col 2 vs. Col 3	21.273	3	4.205	0.020	Yes	
Col 2 vs. Col 1	13.182	3	2.606	0.182	No	
Col 1 vs. Col 3	8.091	3	1.599	0.507		No

TiN early number of responses per retina: Figure 3.20
Friedman Repeated Measures Analysis of Variance on Ranks

Group	N	Missing	Median	25%	75%
Col 1	2	0	41.500	41.000	42.000
Col 2	2	0	48.000	39.000	57.000
Col 3	2	0	25.000	24.000	26.000

Chi-square= 3.000 with 2 degrees of freedom. P(est.)= 0.223 P(exact)= 0.500

The differences in the median values among the treatment groups are not great enough to exclude the possibility that the difference is due to random sampling variability; there is not a statistically significant difference (P = 0.500)

Average early CNT threshold per explant: Figure 3.20

One Way Repeated Measures Analysis of Variance
Equal Variance Test: Passed (P = 0.350)

Treatment Name	N	Missing	Mean	Std Dev	SEM
Col 1	11	0	1.767	0.635	0.191
Col 2	11	0	1.516	0.401	0.121
Col 3	11	1	1.623	0.746	0.236

Source of Variation	DF	SS	MS	F	P
Between Subjects	10	8.898	0.890		
Between Treatments	2	0.347	0.174	1.896	0.178
Residual	19	1.740	0.0916		
Total	31	10.987	0.354		

The differences in the mean values among the treatment groups are not great enough to exclude the possibility that the difference is due to random sampling variability; there is not a statistically significant difference (P = 0.178).

Power of performed test with alpha = 0.050: 0.175

The power of the performed test (0.175) is below the desired power of 0.800.
Less than desired power indicates you are less likely to detect a difference when one actually exists. Negative results should be interpreted cautiously.

Expected Mean Squares:
Approximate DF Residual = 19.000
Expected MS(Subj) = var(res) + 2.900 var(Subj)
Expected MS(Treatment) = var(res) + var(Treatment)
Expected MS(Residual) = var(res)

Average Early TiN threshold per explant: Figure 3.20

Kruskal-Wallis One Way Analysis of Variance on Ranks

Group	N	Missing	Median	25%	75%
Col 1	2	0	2.019	1.986	2.051
Col 2	2	0	1.785	1.715	1.854
Col 3	2	0	1.971	1.960	1.983

H = 4.571 with 2 degrees of freedom. P(est.)= 0.102 P(exact)= 0.067

The differences in the median values among the treatment groups are not great enough to exclude the possibility that the difference is due to random sampling variability; there is not a statistically significant difference (P = 0.067)

Average threshold value for all CNT retinas: Figure 3.21

CE0017

Kruskal-Wallis One Way Analysis of Variance on Ranks

Group	N	Missing	Median	25%	75%
Col 1	46	1	2.100	1.750	3.000
Col 2	99	1	1.600	1.200	2.100
Col 3	7	1	1.500	0.900	1.800

H = 20.621 with 2 degrees of freedom. (P = <0.001)

The differences in the median values among the treatment groups are greater than would be expected by chance; there is a statistically significant difference (P = <0.001)

To isolate the group or groups that differ from the others use a multiple comparison procedure.

All Pairwise Multiple Comparison Procedures (Dunn's Method) :

Comparison	Diff of Ranks	Q	P<0.05
Col 1 vs Col 3	52.133	2.779	Yes
Col 1 vs Col 2	32.740	4.213	Yes

Col 2 vs Col 3	19.393	1.068	No

Note: The multiple comparisons on ranks do not include an adjustment for ties.
CE0018

Kruskal-Wallis One Way Analysis of Variance on Ranks

Group	N	Missing	Median	25%	75%
Col 1	46	1	1.400	1.200	1.600
Col 2	93	1	1.200	0.600	1.450
Col 3	35	1	1.400	1.200	1.800

H = 26.922 with 2 degrees of freedom. (P = <0.001)

The differences in the median values among the treatment groups are greater than would be expected by chance; there is a statistically significant difference (P = <0.001)

To isolate the group or groups that differ from the others use a multiple comparison procedure.

All Pairwise Multiple Comparison Procedures (Dunn's Method) :

Comparison	Diff of Ranks	Q	P<0.05
Col 3 vs Col 2	44.233	4.452	Yes
Col 3 vs Col 1	11.050	0.982	No
Col 1 vs Col 2	33.183	3.685	Yes

Note: The multiple comparisons on ranks do not include an adjustment for ties.

CE0019

Kruskal-Wallis One Way Analysis of Variance on Ranks

Group	N	Missing	Median	25%	75%
Col 1	41	1	2.325	1.800	2.400
Col 2	36	1	1.800	1.435	2.400
Col 3	6	1	2.400	1.925	2.900

H = 4.144 with 2 degrees of freedom. (P = 0.126)

The differences in the median values among the treatment groups are not great enough to exclude the possibility that the difference is due to random sampling variability; there is not a statistically significant difference (P = 0.126)

CE0020

Kruskal-Wallis One Way Analysis of Variance on Ranks

Group Name	N	Missing	Mean	Std Dev	SEM
Col 1	13	1	3.100	0.736	0.212
Col 2	20	1	2.263	1.108	0.254
Col 3	7	1	3.333	0.816	0.333

Source of Variation	DF	SS	MS	F	P
Between Groups	2	7.950	3.975	4.307	0.022
Residual	34	31.378	0.923		
Total	36	39.328			

The differences in the mean values among the treatment groups are greater than would be expected by chance; there is a statistically significant difference (P = 0.022).

Power of performed test with alpha = 0.050: 0.583

All Pairwise Multiple Comparison Procedures (Holm-Sidak method):
Overall significance level = 0.05

Comparisons for factor:

Comparison	Diff of Means	t	Unadjusted P	Critical Level	Significant?
Col 3 vs. Col 2	1.070	2.379	0.023	0.017	No
Col 1 vs. Col 2	0.837	2.362	0.024	0.025	Yes
Col 3 vs. Col 1	0.233	0.486	0.630	0.050	No

CE0021

t-test

Normality Test: Failed (P < 0.050)

Test execution ended by user request, Rank Sum Test begun

Mann-Whitney Rank Sum Test

Data source: Data 1 in Notebook11

Group	N	Missing	Median	25%	75%
Col 1	24	1	2.000	1.500	2.750
Col 2	32	1	1.760	1.680	2.200

Mann-Whitney U Statistic= 290.000

T = 699.000 n(small)= 23 n(big)= 31 (P = 0.246)

The difference in the median values between the two groups is not great enough to exclude the possibility that the difference is due to random sampling variability; there is not a statistically significant difference (P = 0.246)

CE0024

Kruskal-Wallis One Way Analysis of Variance on Ranks

Group	N	Missing	Median	25%	75%
Col 1	16	1	1.800	1.800	2.000
Col 2	23	1	1.600	1.200	1.880
Col 3	28	1	1.600	0.510	1.950

H = 7.668 with 2 degrees of freedom. (P = 0.022)

The differences in the median values among the treatment groups are greater than would be expected by chance; there is a statistically significant difference (P = 0.022)

To isolate the group or groups that differ from the others use a multiple comparison procedure.

All Pairwise Multiple Comparison Procedures (Dunn's Method) :

Comparison	Diff of Ranks	Q	P<0.05
Col 1 vs Col 3	16.326	2.723	Yes
Col 1 vs Col 2	9.248	1.483	No
Col 2 vs Col 3	7.077	1.323	No

Note: The multiple comparisons on ranks do not include an adjustment for ties.

CE0025

Kruskal-Wallis One Way Analysis of Variance on Ranks

Group	N	Missing	Median	25%	75%
Col 1	12	1	0.900	0.675	1.125
Col 2	31	1	0.900	0.800	1.200
Col 3	38	1	0.900	0.800	0.900

H = 1.871 with 2 degrees of freedom. (P = 0.392)

The differences in the median values among the treatment groups are not great enough to exclude the possibility that the difference is due to random sampling variability; there is not a statistically significant difference (P = 0.392)

CE0026

Kruskal-Wallis One Way Analysis of Variance on Ranks

Group	N	Missing	Median	25%	75%
Col 1	14	1	1.200	1.050	1.600
Col 2	16	1	1.200	0.600	1.200
Col 3	5	1	1.600	1.600	1.600

H = 9.238 with 2 degrees of freedom. (P = 0.010)

The differences in the median values among the treatment groups are greater than would be expected by chance; there is a statistically significant difference (P = 0.010)

To isolate the group or groups that differ from the others use a multiple comparison procedure.

All Pairwise Multiple Comparison Procedures (Dunn's Method) :

Comparison	Diff of Ranks	Q	P<0.05
Col 3 vs Col 2	15.067	2.854	Yes
Col 3 vs Col 1	10.923	2.036	No
Col 1 vs Col 2	4.144	1.166	No

Note: The multiple comparisons on ranks do not include an adjustment for ties.

CE0027

Kruskal-Wallis One Way Analysis of Variance on Ranks

Group	N	Missing	Median	25%	75%
Col 1	25	1	1.200	0.800	1.350
Col 2	22	1	1.200	1.150	1.650
Col 3	12	1	0.600	0.600	1.050

H = 10.275 with 2 degrees of freedom. (P = 0.006)

The differences in the median values among the treatment groups are greater than would be expected by chance; there is a statistically significant difference (P = 0.006)

To isolate the group or groups that differ from the others use a multiple comparison procedure.

All Pairwise Multiple Comparison Procedures (Dunn's Method) :

Comparison	Diff of Ranks	Q	P<0.05
Col 2 vs Col 3	18.970	3.125	Yes
Col 2 vs Col 1	6.083	1.248	No
Col 1 vs Col 3	12.886	2.170	No

Note: The multiple comparisons on ranks do not include an adjustment for ties.

CE0028

Kruskal-Wallis One Way Analysis of Variance on Ranks

Equal Variance Test: Failed (P < 0.050)

Group	N	Missing	Median	25%	75%
Col 1	6	1	1.800	1.600	2.400
Col 2	6	1	1.600	1.400	1.600
Col 3	3	1	1.600	1.600	1.600

H = 5.090 with 2 degrees of freedom. P(est.)= 0.078 P(exact)= 0.181

The differences in the median values among the treatment groups are not great enough to exclude the possibility that the difference is due to random sampling variability; there is not a statistically significant difference (P = 0.181)

CE0029

Kruskal-Wallis One Way Analysis of Variance on Ranks

Group	N	Missing	Median	25%	75%
Col 1	9	1	1.200	1.200	1.800
Col 2	19	1	1.600	1.200	1.800
Col 3	21	1	1.800	1.200	1.800

H = 0.798 with 2 degrees of freedom. (P = 0.671)

The differences in the median values among the treatment groups are not great enough to exclude the possibility that the difference is due to random sampling variability; there is not a statistically significant difference (P = 0.671)

Average threshold value for all TiN retinas: Figure 3.23

CE0032

One Way Analysis of Variance

Normality Test: Passed (P = 0.325)

Equal Variance Test: Passed (P = 0.174)

Group Name	N	Missing	Mean	Std Dev	SEM
Col 1	4	0	1.986	0.629	0.314
Col 2	4	0	1.715	0.0959	0.0480
Col 3	4	0	1.960	0.482	0.241

Source of Variation	DF	SS	MS	F	P
Between Groups	2	0.178	0.0892	0.420	0.669
Residual	9	1.909	0.212		
Total	11	2.088			

The differences in the mean values among the treatment groups are not great enough to exclude the possibility that the difference is due to random sampling variability; there is not a statistically significant difference (P = 0.669).

Power of performed test with alpha = 0.050: 0.050

The power of the performed test (0.050) is below the desired power of 0.800.
Less than desired power indicates you are less likely to detect a difference when one actually exists. Negative results should be interpreted cautiously.

CE0034

One Way Analysis of Variance

Normality Test: Passed (P = 0.439)

Equal Variance Test: Passed (P = 0.654)

Group Name	N	Missing	Mean	Std Dev	SEM
Col 1	4	0	2.051	0.380	0.190
Col 2	4	0	1.854	0.227	0.114
Col 3	4	1	1.983	0.306	0.176

Source of Variation	DF	SS	MS	F	P
Between Groups	2	0.0792	0.0396	0.408	0.678
Residual	8	0.776	0.0969		
Total	10	0.855			

The differences in the mean values among the treatment groups are not great enough to exclude the possibility that the difference is due to random sampling variability; there is not a statistically significant difference (P = 0.678).

Power of performed test with alpha = 0.050: 0.050

The power of the performed test (0.050) is below the desired power of 0.800.
Less than desired power indicates you are less likely to detect a difference when one actually exists. Negative results should be interpreted cautiously.

Indirect response thresholds overall

CNT vs TiN

Mann-Whitney Rank Sum Test

Group	N	Missing	Median	25%	75%
Col 1	476	205	1.400	1.200	1.800
Col 2	164	52	1.600	1.200	1.800

Mann-Whitney U Statistic= 13922.500

T = 22757.500 n(small)= 112 n(big)= 271 (P = 0.198)

The difference in the median values between the two groups is not great enough to exclude the possibility that the difference is due to random sampling variability; there is not a statistically significant difference (P = 0.198)

Indirect average response thresholds per day

CNT average late threshold total per day: Figure 3.27

Kruskal-Wallis One Way Analysis of Variance on Ranks Sunday, April 22, 2012, 18:25:50

Group	N	Missing	Median	25%	75%
Col 1	242	162	1.500	1.200	2.100
Col 2	254	138	1.500	1.200	1.800
Col 3	254	179	1.200	0.975	1.800

H = 3.031 with 2 degrees of freedom. (P = 0.220)

The differences in the median values among the treatment groups are not great enough to exclude the possibility that the difference is due to random sampling variability; there is not a statistically significant difference (P = 0.220)

TiN average late threshold total per day: Figure 3.27

Kruskal-Wallis One Way Analysis of Variance on Ranks

Group	N	Missing	Median	25%	75%
Col 1	60	12	1.600	1.200	1.700
Col 2	74	29	1.600	1.200	1.800
Col 3	69	49	1.800	1.200	1.800

H = 4.946 with 2 degrees of freedom. (P = 0.084)

The differences in the median values among the treatment groups are not great enough to exclude the possibility that the difference is due to random sampling variability; there is not a statistically significant difference (P = 0.084)

Indirect response thresholds per retina

Average late CNT numbers per retina: Figure 3.28

Friedman Repeated Measures Analysis of Variance on Ranks

Group	N	Missing	Median	25%	75%
Col 1	10	0	5.500	3.000	13.000
Col 2	10	0	8.000	2.000	15.000
Col 3	10	0	3.500	1.000	8.000

Chi-square= 1.077 with 2 degrees of freedom. (P = 0.584)

The differences in the median values among the treatment groups are not great enough to exclude the possibility that the difference is due to random sampling variability; there is not a statistically significant difference (P = 0.584)

Average late CNT Thresholds per retina: Figure 3.28

One Way Repeated Measures Analysis of Variance

Normality Test: Passed (P = 0.051)

Equal Variance Test: Passed (P = 0.788)

Treatment Name	N	Missing	Mean	Std Dev	SEM
Col 1	12	0	1.938	1.297	0.375
Col 2	12	0	2.917	2.257	0.652
Col 3	12	0	1.771	2.593	0.748

Source of Variation	DF	SS	MS	F	P
Between Subjects	11	89.762	8.160		
Between Treatments	2	9.198	4.599	1.722	0.202
Residual	22	58.742	2.670		
Total	35	157.701			

The differences in the mean values among the treatment groups are not great enough to exclude the possibility that the difference is due to random sampling variability; there is not a statistically significant difference (P = 0.202).

Power of performed test with alpha = 0.050: 0.151

The power of the performed test (0.151) is below the desired power of 0.800.
Less than desired power indicates you are less likely to detect a difference when one actually exists. Negative results should be interpreted cautiously.

Average late TiN numbers per retina: Figure 3.28

Friedman Repeated Measures Analysis of Variance on Ranks

Group	N	Missing	Median	25%	75%
Col 1	2	0	31.000	27.000	35.000
Col 2	2	0	30.500	25.000	36.000
Col 3	2	0	16.500	8.000	25.000

Chi-square= 3.000 with 2 degrees of freedom. P(est.)= 0.223 P(exact)= 0.500

The differences in the median values among the treatment groups are not great enough to exclude the possibility that the difference is due to random sampling variability; there is not a statistically significant difference (P = 0.500)

Average late TiN Thresholds per retina: Figure 3.28

Friedman Repeated Measures Analysis of Variance on Ranks

Group	N	Missing	Median	25%	75%
Col 1	2	0	1.483	1.471	1.495
Col 2	2	0	1.617	1.603	1.631
Col 3	2	0	1.663	1.467	1.860

Chi-square= 1.000 with 2 degrees of freedom. P(est.)= 0.607 P(exact)= 0.833

The differences in the median values among the treatment groups are not great enough to exclude the possibility that the difference is due to random sampling variability; there is not a statistically significant difference (P = 0.833)

Average late CNT thresholds per retina: Figure 3.29

CE0018

Kruskal-Wallis One Way Analysis of Variance on Ranks

Group	N	Missing	Median	25%	75%
Col 1	31	18	1.200	1.200	1.450
Col 2	31	19	1.200	1.200	1.550
Col 3	19	5	1.400	1.200	1.800

H = 1.358 with 2 degrees of freedom. (P = 0.507)

The differences in the median values among the treatment groups are not great enough to exclude the possibility that the difference is due to random sampling variability; there is not a statistically significant difference (P = 0.507)

CE0019

t-test

Normality Test: Passed (P = 0.518)

Equal Variance Test: Passed (P = 0.075)

Group Name N Missing Mean Std Dev SEM

Col 5	24	8	1.866	0.706	0.176
Col 6	22	13	1.963	0.964	0.321

Difference -0.0977

t = -0.291 with 23 degrees of freedom. (P = 0.773)

95 percent confidence interval for difference of means: -0.792 to 0.596

The difference in the mean values of the two groups is not great enough to reject the possibility that the difference is due to random sampling variability. There is not a statistically significant difference between the input groups (P = 0.773).

Power of performed test with alpha = 0.050: 0.050

The power of the performed test (0.050) is below the desired power of 0.800.
Less than desired power indicates you are less likely to detect a difference when one actually exists. Negative results should be interpreted cautiously.

CE0020

One Way Analysis of Variance
Normality Test: Passed (P = 0.255)
Equal Variance Test: Passed (P = 0.272)

Group Name	**N**	**Missing**	**Mean**	**Std Dev**	**SEM**
Col 9	10	4	3.133	0.882	0.360
Col 10	17	2	2.627	1.090	0.281
Col 11	8	0	3.350	1.041	0.368

Source of Variation	**DF**	**SS**	**MS**	**F**	**P**
Between Groups	2	3.039	1.520	1.406	0.263
Residual	26	28.103	1.081		
Total	28	31.142			

The differences in the mean values among the treatment groups are not great enough to exclude the possibility that the difference is due to random sampling variability; there is not a statistically significant difference (P = 0.263).

Power of performed test with alpha = 0.050: 0.105

The power of the performed test (0.105) is below the desired power of 0.800.
Less than desired power indicates you are less likely to detect a difference when one actually exists. Negative results should be interpreted cautiously.

CE0025

Mann-Whitney Rank Sum Test

Group	N	Missing	Median	25%	75%
Col 14	12	5	0.900	0.825	1.200
Col 15	12	6	0.800	0.600	0.900

Mann-Whitney U Statistic= 11.000

T = 32.000 n(small)= 6 n(big)= 7 P(est.)= 0.163 P(exact)= 0.181

The difference in the median values between the two groups is not great enough to exclude the possibility that the difference is due to random sampling variability; there is not a statistically significant difference (P = 0.181)

CE0027

One Way Analysis of Variance

Normality Test: Passed (P = 0.167)

Equal Variance Test: Passed (P = 0.059)

Group Name	N	Missing	Mean	Std Dev	SEM
Col 18	28	11	1.371	0.452	0.110
Col 19	25	8	1.359	0.528	0.128
Col 20	13	8	1.000	0.548	0.245

Source of Variation	DF	SS	MS	F	P
Between Groups	2	0.581	0.290	1.170	0.322
Residual	36	8.936	0.248		
Total	38	9.517			

The differences in the mean values among the treatment groups are not great enough to exclude the possibility that the difference is due to random sampling variability; there is not a statistically significant difference (P = 0.322).

Power of performed test with alpha = 0.050: 0.072

The power of the performed test (0.072) is below the desired power of 0.800.
Less than desired power indicates you are less likely to detect a difference when one actually exists. Negative results should be interpreted cautiously.

CE0029

Kruskal-Wallis One Way Analysis of Variance on Ranks

Group	N	Missing	Median	25%	75%
Col 23	36	31	1.800	1.650	1.800
Col 24	48	21	1.600	1.200	1.800
Col 25	48	12	1.200	1.200	1.800

H = 5.603 with 2 degrees of freedom. (P = 0.061)

The differences in the median values among the treatment groups are not great enough to exclude the possibility that the difference is due to random sampling variability; there is not a statistically significant difference (P = 0.061).

Aerage late threshold for each TiN retina: Figure 3.30

CE0032

Kruskal-Wallis One Way Analysis of Variance on Ranks

Group	N	Missing	Median	25%	75%
Col 1	38	3	1.600	1.200	1.600
Col 2	32	9	1.600	1.050	1.800
Col 3	11	5	1.800	1.200	2.400

H = 2.246 with 2 degrees of freedom. (P = 0.325)

The differences in the median values among the treatment groups are not great enough to exclude the possibility that the difference is due to random sampling variability; there is not a statistically significant difference (P = 0.325)

CE0034

Kruskal-Wallis One Way Analysis of Variance on Ranks

Group	N	Missing	Median	25%	75%
Col 6	28	9	1.200	1.200	1.800
Col 7	23	5	1.500	1.200	1.800
Col 8	17	5	1.800	1.500	1.800

H = 2.610 with 2 degrees of freedom. (P = 0.271)

The differences in the median values among the treatment groups are not great enough to exclude the possibility that the difference is due to random sampling variability; there is not a statistically significant difference (P = 0.271)

Section 3.4.3

Early vs Late CNT average thresholds: Figure 3.31

Mann-Whitney Rank Sum Test Monday, May 21, 2012, 19:08:43

Group	N	Missing	Median	25%	75%
Col 1	1262	481	1.500	1.000	2.000
Col 2	476	205	1.400	1.200	1.800

Mann-Whitney U Statistic= 105711.500

T = 142795.500 n(small)= 271 n(big)= 781 (P = 0.979)

The difference in the median values between the two groups is not great enough to exclude the possibility that the difference is due to random sampling variability; there is not a statistically significant difference (P = 0.979)

Early vs Late TiN average thresholds: Figure 3.31

Mann-Whitney Rank Sum Test

Data source: Data 1 in Notebook3

Group	N	Missing	Median	25%	75%
Col 1	364	141	1.800	1.300	2.400
Col 2	164	52	1.600	1.200	1.800

Mann-Whitney U Statistic= 8871.000

T = 15199.000 n(small)= 112 n(big)= 223 (P = <0.001)

The difference in the median values between the two groups is greater than would be expected by chance; there is a statistically significant difference (P = <0.001)

3. Statistical tests from Chapter 4

Island distance Pre vs Post 48 hours

t-test

Normality Test: Passed (P = 0.597)

Equal Variance Test: Passed (P = 0.140)

Group Name	N	Missing	Mean	Std Dev	SEM
Col 1	6	0	5.540	5.069	2.069
Col 2	3	0	-1.406	0.848	0.490

Difference 6.946

t = 2.280 with 7 degrees of freedom. (P = 0.057)

95 percent confidence interval for difference of means: -0.258 to 14.149

The difference in the mean values of the two groups is not great enough to reject the possibility that the difference is due to random sampling variability. There is not a statistically significant difference between the input groups (P = 0.057).

Power of performed test with alpha = 0.050: 0.417

The power of the performed test (0.417) is below the desired power of 0.800.
Less than desired power indicates you are less likely to detect a difference when one actually exists. Negative results should be interpreted cautiously.

Island numbers 24h vs 48h

Mann-Whitney Rank Sum Test

Equal Variance Test: Failed (P < 0.050)

Group	N	Missing	Median	25%	75%
Col 1	8	4	1.500	1.000	4.000
Col 2	9	0	8.000	3.500	14.500

Mann-Whitney U Statistic= 5.000

T = 15.000 n(small)= 4 n(big)= 9 (P = 0.052)

The difference in the median values between the two groups is not great enough to exclude the possibility that the difference is due to random sampling variability; there is not a statistically significant difference (P = 0.052)

Island numbers Pre vs post 48h

t-test
Normality Test: Passed (P = 0.139)

Equal Variance Test: Passed (P = 0.083)

Group Name	N	Missing	Mean	Std Dev	SEM
Col 1	9	0	1.778	1.787	0.596
Col 2	9	0	8.889	6.470	2.157

Difference -7.111

t = -3.178 with 16 degrees of freedom. (P = 0.006)

95 percent confidence interval for difference of means: -11.854 to -2.368

The difference in the mean values of the two groups is greater than would be expected by chance; there is a statistically significant difference between the input groups (P = 0.006).

Power of performed test with alpha = 0.050: 0.821

Appendix C: Experimental Protocols

Retina-CNT Biohybrid PROTOCOL

Chamber fabrication

Ingredients

- Pyrex petri dish
- Sylgard 184 Silicone Elastomer Kit
- Chamber ring (Inner diameter: 18.4mm, Outer diameter: 25 mm, Height: 6 mm)

Utensils

- Forceps
- Heating surface

Method

1. Prepare Sylgard kit at 10/1 weight ratio (base/curing agent)
2. Vacuum off bubbles from Sylgard mixture
3. Dip chamber rings in sylgard mixture
4. Apply chamber rings to bottom of petri dish
5. Cure on heating plate at 50°C for 24 hours

Retina-CNT Biohybrid PROTOCOL

Artificial Cerebro Spinal Fluid - 2L preparation

Ingredients

- Glucose (MW 180.2)
- $NaHC0_3$ (MW 84.01)
- $CaCl_2$ 1M stock solution
- NaCl (MW 58.44)
- $MgCl_2x6H_2O$ (MW 203.3)
- $NaH_2PO_4x2H_2O$ (MW 156.01)
- KCl (MW, 74.55)
- Penicilin-Strptomycin-Neomicin (Sigma P4083)

Utensils

- Pyrex glassware
- Stirring plate/stirrer

Method

A. Make stock solution from 1 L Di H_2O (18.2 MΩ/cm)

	MW	conc (mM)	stock (10x/1liter) (grams)
NaCl	58.44	118	68.95
KCl	74.55	3	2.2365
$MgCl_2x6H_2O$	203.3	1	2.03
$NaH2PO_4x2H_2O$	156.01	1	1.56

B. Prepare final solution on day of experiment

1. Take 200ml from the 10x stock and add 1800ml Di H_2O (18.2 MΩ/cm)
2. Add $NaHCO_3$ (MW 84.01) 25mM: 4.2 g
3. Add glucose (MW 180.2) 10mM: 3.6g
4. Add L-Glutamine (MW 146.14) 0.5mM: 0.1461g
4. Add 4ml CaCl2 from a 1M stock solution
5. Add 2.5 ml Penicilin Streptomycin Neomycin

Retina-CNT Biohybrid PROTOCOL

Biohybrid-Incubation

Ingredients

- aCSF
- Carboxygen
- Mouse

Utensils

- Dissection kit (forceps, micro scissors, micro-scalpel)
- Peristaltic pump
- Incubation chamber
- Polyester membrane filter (8 µm pores, ~9 mm^2 pieces)
- Stainless steel anchors (7 mm inner Ø, 12 mm outer Ø, // capillaries)
- CNT islands on $SiSiO_2$ substrate
- Fine paint brush

Method

6. Dissect retina in best aseptic conditions possible in carboxygenated aCSF
7. Apply surface of retina to CNT islands
8. Submerge membrane filter and push down on retina with paint brush (fig 1)
9. Secure retina with two anchors (fig 2)
10. Incubate for 48 hours with air-stone bubbling in the incubation chamber and perfusing with peristaltic pump at 1.2 ml/min (fig 3)
11. Remove anchors off retina.
12. Use another filter paper as a shovel to dissociate retina from $SiSiO_2$ substrate
13. Record electrophysiological activity on MEA to test viability (figure 4)

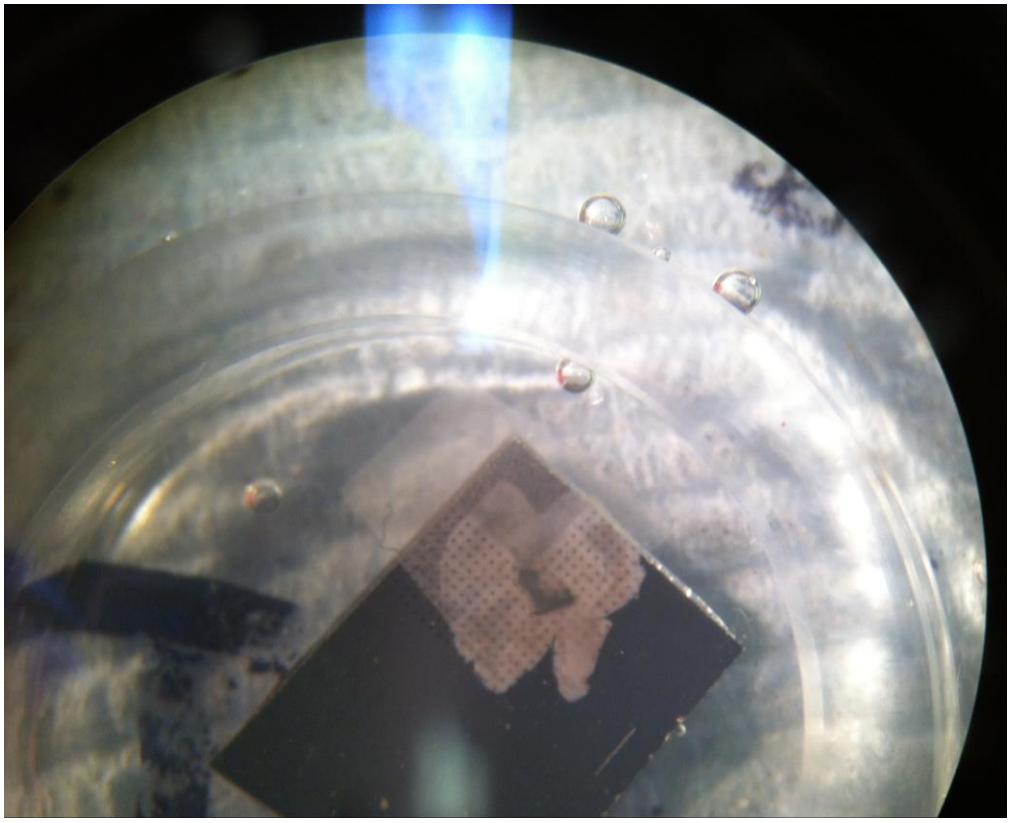

Figure 1: Retina on SiSiO2 substrate-CNT islands

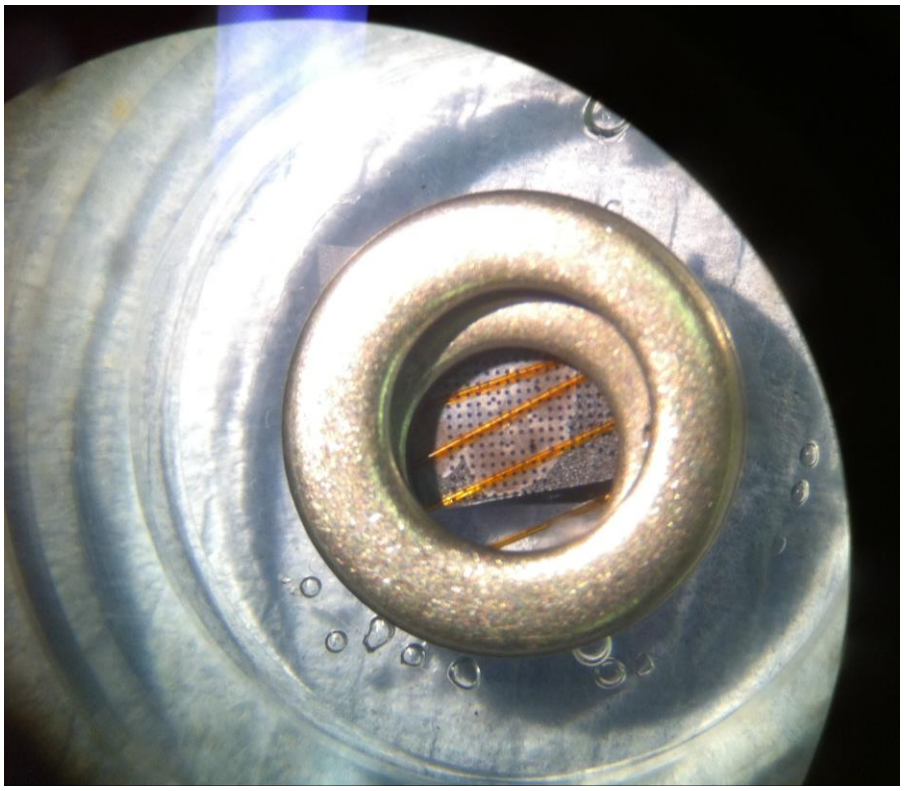

Figure 2: Retina secured below two anchors

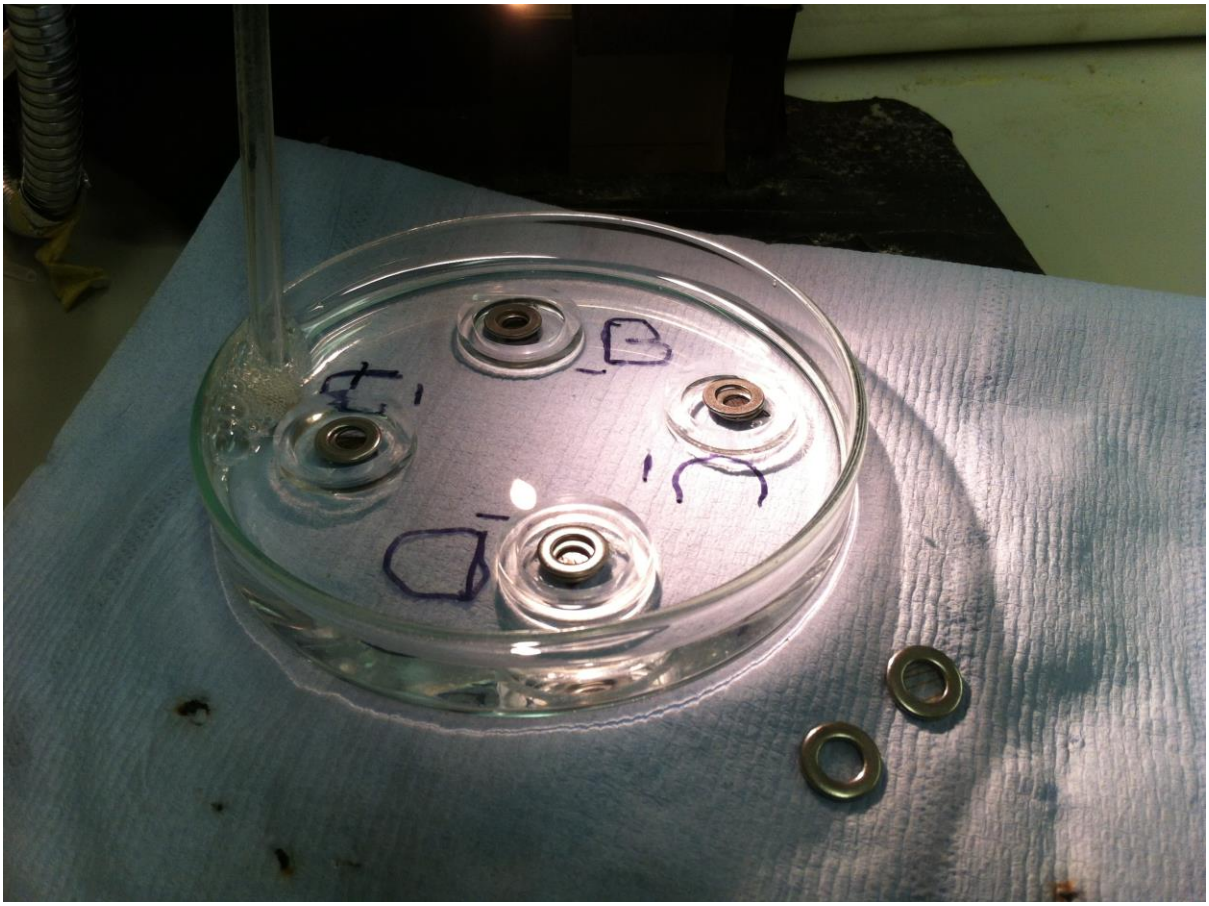

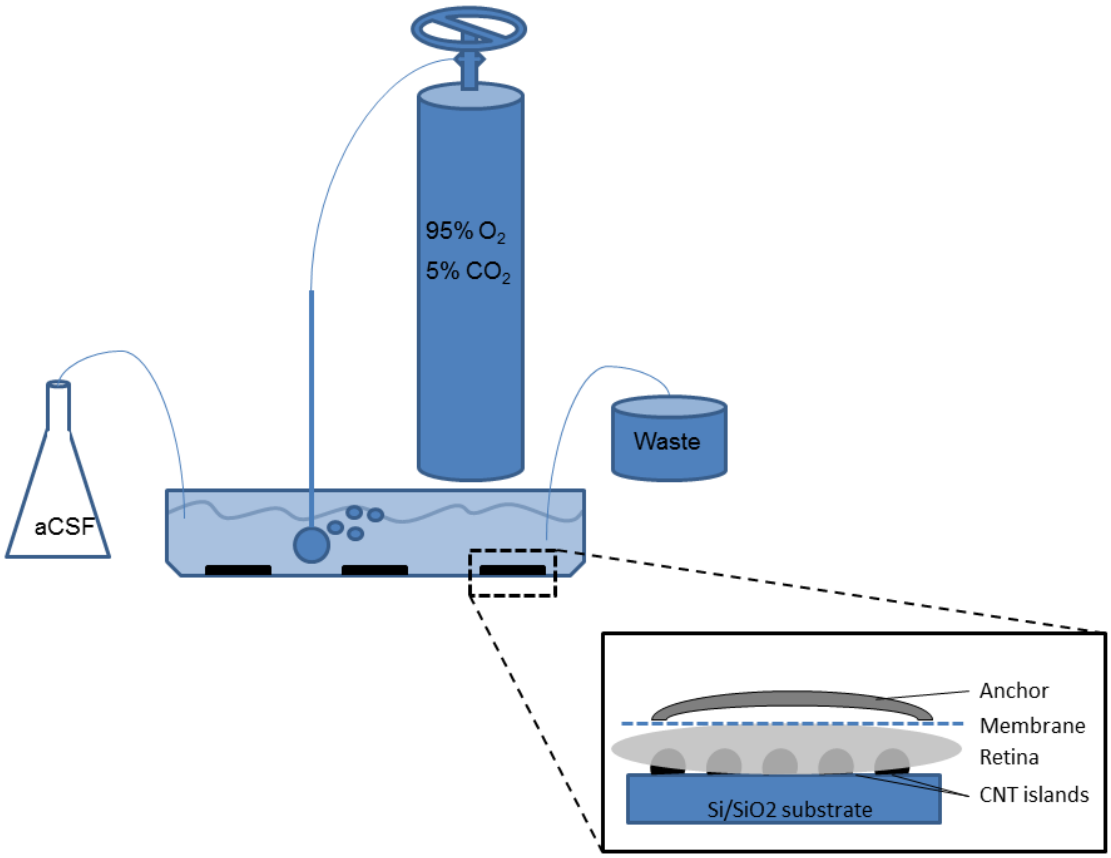

Figure 3: Retinas in chamber of oxygenated aCSF

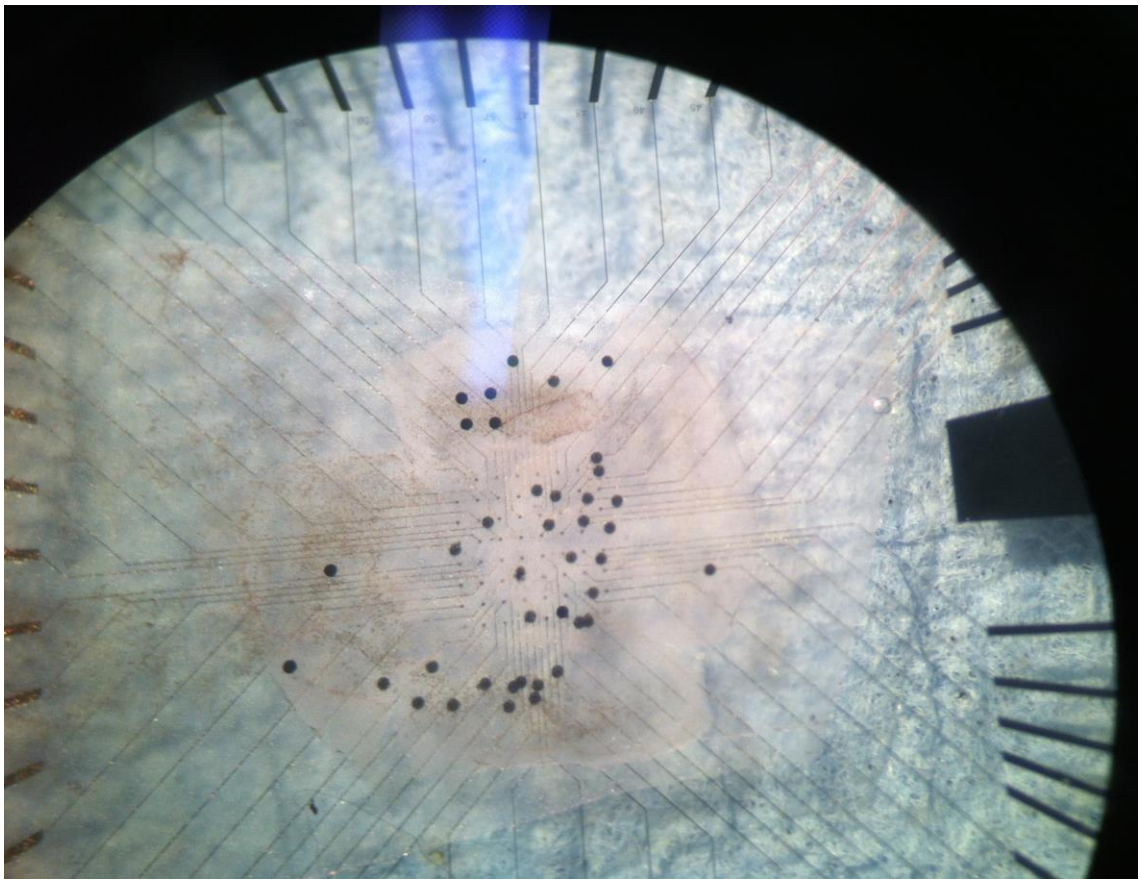

Figure 4: Retina-CNT Biohybrid on MEA contacts

TEM solutions

Cacodylate buffer stock

Stock Solution A: 0.2M Sodium cacodylate. Assuming MWT 214

- 21.4g sodium cacodylate in 500mls distilled water

Solution B: 0.2N HCl

- 1.7mls HCl in 100mls distilled water

To make up a 0.1M solution pH 7.4. mix together

- 100mls of solution A with 5mls solution B made up to 200mls with distilled water. Check ph.
- Filter using Nalgene poral filter and vacuum pump.

Sorenson's Phosphate Buffer (pH 7.3) 0.1M

Solution A: Potassium dihydrogen orthophosphate (mw 136.09)

- 1.36 grms KH_2PO_4 in 100 mls distilled water

Solution B: di- Sodium hydrogen orthophosphate (mw 177.99)

- 8.895 grams $Na_2HPO_4.2H_2O$ in 500mls distilled water.

To make up, mix together:

- 28.5 mls Solution A with 71.5 mls Solution B, check pH (store at 4°C)

2% Gluteraldehyde in buffer for storage

- 20 mls 25% Gluteraldehyde (**EM Grade**) plus 230 mls of either cacodylate or phosphate buffer. Mix well. Decant into universals or bijou tubes.
  Stored frozen and labelled .

1 % Osmium Tetraoxide

- 5ml of 2% Osmium Tetraoxide (stored in vials) plus 5mls D. water.
  Use new bottle each time to avoid contamination

  Dispose of waste solution in container provided.

  Rinse contaminated items in alcohol before disposal

Resin

TAAB premix resin kits. Follow supplier's instructions.

Store for short periods in desiccator longer periods -

at 4°C. Bring to room temp in desiccator.

Polymerise all waste in 60ºC oven before disposal

Gluteraldehyde supplied by TAAB

Retina-CNT Biohybrid PROTOCOL

Resin block embedding for TEM

- Fix in 2% gluteraldehyde in cacodylate buffer for 24 hours.
- Rinse in cacodylate buffer 3 x 30mins or 3 changes over several hours.
- Leave in buffer overnight. Next day rinse in D. water 2x 15 mins.
- Post fix in 1% osmium tetroxide in deionised water - 1 hr
  Dispose of waste in container provided in fume hood

- Rinse in deionised water minimum 2 x 15 mins
- Dehydration

25% acetone	30 mins
50% acetone	30 mins
75% acetone	30 mins

From this point on, use acetone stored in desiccator (not from wash bottles)

100% acetone	1 hr
100% acetone	1 hr

Using TAAB epoxy resin kit, mixed to manufacturers specification- mix well.

- Impregnate with

25% resin in acetone	1 hr
50% resin in acetone	1 hr
75% resin in acetone	1 hr
100% resin	1 hr

(Can be left overnight on rotator at this stage)

Store the liquid resin in the desiccator

100% resin	1 hr
100% resin	1 hr
100% resin	at least 3 hrs

- Embed in fresh 100% resin at 60° C for 24 hrs
  Polymerise all items contaminated with resin in 60ºC oven overnight before appropriate disposal

Grid coating for TEM

Ingredients

- Pyroform
- Copper grids (50 mesh)
- De-ionised water (18.2 MΩ. cm)
- Parafilm M

Utensils

- Forceps
- Microscope slide
- Scalpel
- Bowl of water
- Glass or pyrex beaker

Method

14. Dip microscope slide in Pyroform beaker for 2 seconds (figure 1)
15. Angle slide within beaker for 16 seconds (figure 2)
16. Rest slide on top of beaker for 25 seconds (figure 3)
17. Scratch surface of slide that was facing down inside beaker with scalpel in oblong shape
18. Dip slide at an obtuse angle in water bowl to have Pyroform film float at surface
19. Place grids on surface of film
20. Place oblong of Parafilm onto Pyroform film, remove from water with forceps
21. Dry before use
22. Cut out grids with forceps

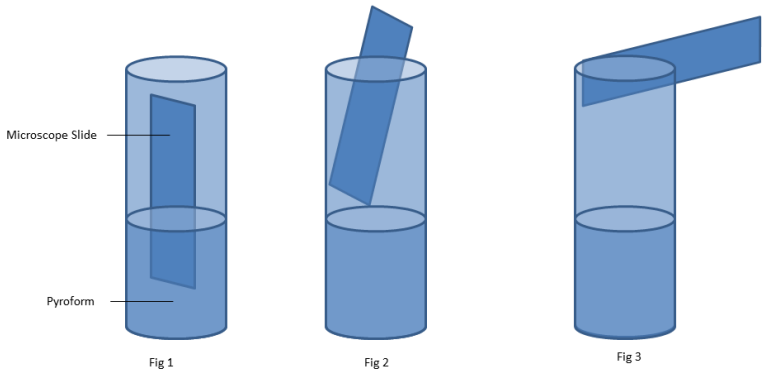

Toluidine Blue Staining

For staining semi-thin resin sections dried onto a glass slide on a hot plate

Preparation of solutions :

- Dissolve 2.5 grms Borax (di-sodium tetraborate) in 500mls distilled water (ie. 0.5%)
- Add 5grms Toluidine Blue, leave to mature, filter before use.

To stain sections:

- Ensure sections are completely dry before staining
- Cover section with stain, heat on a hot plate for approx 1 min
- Rinse with water.
- Overstaining can be rectified by rinsing in 1% acid/alcohol

TEM grid staining

Preparation.

Grids are stained in Petri dishes on parafilm and transferred between solutions with forceps. Washes are carried by holding the grid in forceps and dipping it in and out of distilled water contained in small beakers. Wear gloves and work in positive flow.

Stain 1 (2% aqueous Uranyl Acetate) stored in sealed containers at 4˚C

Spin before use. Take up stain in pipette from the surface of the solution. Avoid disturbing any sediment

Stain 2 (Lead Citrate) supplied by Leica UK in sealed bag.

As Lead citrate has a high affinity for atmospheric carbon dioxide, which results in the formation of insoluble lead carbonate precipitating onto the surface of the section, it is not advisable to stain more than 3 grids at any one time and Petri dish must contain wet pellets of sodium hydroxide**.**

Staining Procedure

Stain 1

- Place one drop of stain per grid into petri dish.
- Place grid, section side down, onto drop of stain. Cover lid with circle of black plastic and heat using anglepoise lamp (approx two inches away). Stain for **30 mins.**
- Remove grids from stain 1 and wash in 3 separate distilled water rinses.
- Blot dry with grade 50 filter paper.
- Dry thoroughly under lamp. This stops lead deposit
- Place grids back into grid box.

Stain 2

- Prepare a second Petri dish with parafilm and add 2 pellets of sodium hydroxide,add a few drops of water to the pellets . Place appropriate number of drops of stain 2 in dish two, ***taking care not to allow fresh air into Petri dish by raising dish lid only enough to allow access.***
- Place grid on drop of stain 2, section side down, for **30 mins.**
- Remove the grids from the stain and wash in 3 separate distilled water rinses.
- Blot the grids dry with grade 50 filter paper and store

Appendix D: Designs

1. Optimisation of *Submerged* incubation systems

Submerged incubation systems allowed the careful and consistent monitoring of neural activity in individual retinas (*Submerged on-substrate* system) or the sparse and unreliable monitoring of multiple retinas (*Free-float* system). The fundamental advantage of the *Submerged on-substrate* incubation system over other systems recording from MEAs directly is the steady perfusion of carboxygenated aCSF, without recycling, which evacuates noxious secretions from the retina. A limitation of the *submerged* systems was their susceptibility to bacterial infection (figure 2.17). An ideal system would allow the careful monitoring of fluorescence and/or electrophysiological activity of multiple retinas for as long as possible. I propose the design of a simple bioreactor allowing the concurrent culture of multiple retinas onto MEAs whilst maintaining rigorous aseptic conditions (figure 2.19). Reducing the risk of bacterial infection and limiting physical manipulation is likely to increase the lifetime of retinal explants.

The proposed device is an oblong container separated into different compartments which can be individually portioned from one another. The use of a single container is useful here as it limits the number of interactions required by the experimentalist to maintain several explants concurrently. Other bioreactors use parallel peristaltic pump systems to supply multiple explants (Cui 2007). Each chamber can be interfaced with the culture chamber of an MEA to allow the flow of carboxygenated aCSF across a submerged retina. This chamber can also be partitioned from the rest of the device when an MEA must be removed from the device to record activity. A thread (or screw mechanism) on the culture chambers of MEAs and its counterpart on the chamber interface allows water-tight coupling between MEA chambers and the device. Partitions are allowed to slide in and out of the device and maintain a good coupling via the use of Neodymium magnets etched or machined into L-shapes embedded within strategic locations of both device and partitions (figure 2.19, C and D). To facilitate fabrication, the device is divided into two main interlocking units, the base (figure 2.19, C) and the shell (figure 2.19, D).

In an effort to maintain aseptic conditions, the aCSF should be prepared with autoclaved water and the supply bottle (figure 2.19, B) should have sealing gaskets in the cap allowing the penetration of tubing and air-stone for the pumping of aCSF and the bubbling of carboxygen, respectively. Optic nerve astrocytes orchestrate the degeneration of RGCs in response to optic nerve severing (Garcia and Koke 2009). Supplementing the aCSF with appropriate growth factors or completely removing the post laminar optic nerve might promote RGC survival. As in typical organotypic culture preparations, dissections would be executed in a laminar flow hood with sterile instruments, glassware and protective clothing. The diagrams in figure 2.19 illustrate a 5-chamber device as an example. Naturally, this could be made longer with more chambers to accommodate more retinas. Coating the partitions in a flexible polymer would ensure the device stays water-tight.

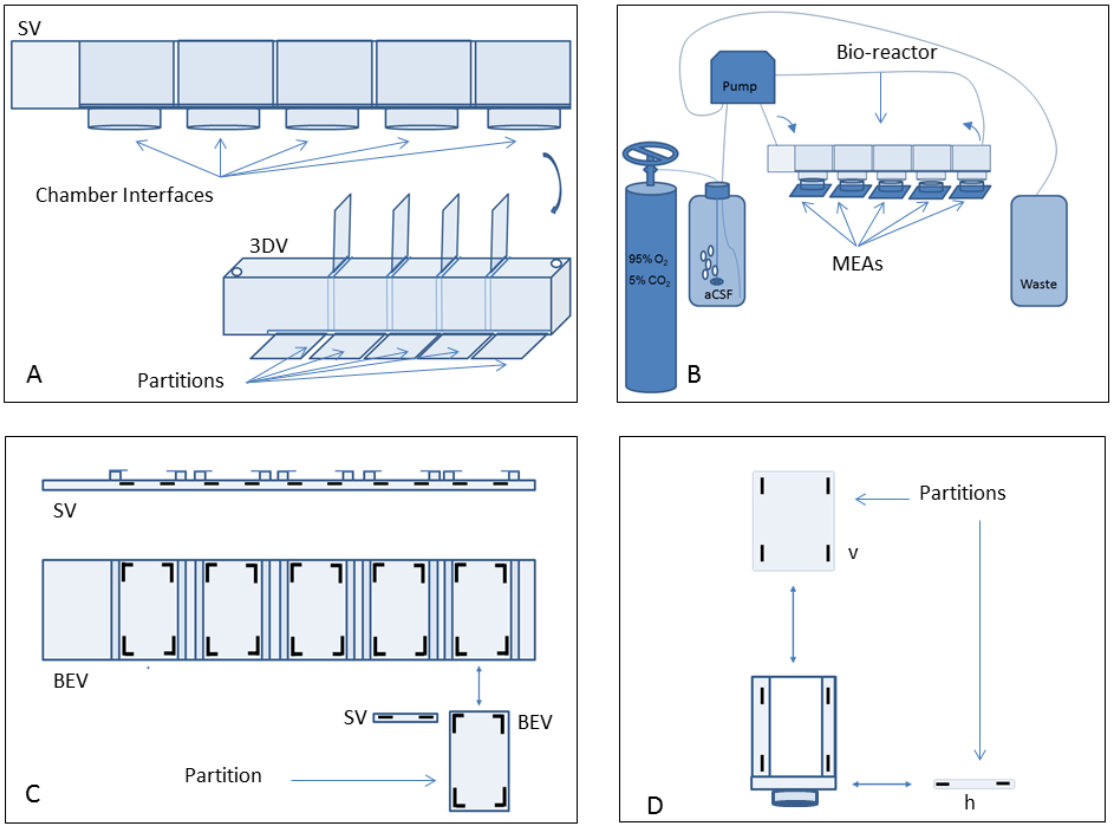

Figure 2.19: Plans for bulk *Submerged on-substrate* culture system. Diagrams outlining preliminary design plans for a bioreactor allowing the concurrent culture of retinas under *Submerged on-substrate* conditions. Panels A and B display a fully constructed version of the device whilst panels C and D display its base and shell, respectively. A: side-view (SV) and 3D view (3DV) of the device highlighting removable partitions between compartments in the device as well as parts to interface MEA chamber rings with the compartments. B: side-view of the device interfaced with 5 MEAs whilst a peristaltic pump maintains a flow of carboxygenated aCSF across the chambers. Arrows display the flow of aCSF in and out of the device. C: bird's eye views

(BEV) and side-views (SV) of the device's base and one of the partitions. The black elements are magnets embedded into the base and partition. Thus, when a partition is slid into the base, it is held firmly against it, keeping it water-tight. A latch located at the edge of each partition would prevent it from escaping the device completely. D: cross section of the bioreactor, demonstrating the vertical (v) and horizontal (h) partitioning of compartments.

2. Design for CNT-based epi-retinal implant

Based on extensive research in the literature of retinal prosthetic devices and on the outcome from my work, I have developed the conceptual design for an epi-retinal MPDA highlighting the most important characteristics required for such a device. The device I propose accommodates the shape of the retina, it does not require an external power source and makes use of the natural affinity between CNTs and retinal tissue, as demonstrated in this thesis. Similar to the sub-retinal NIR MPDA discussed in Chapter 1 (Mathieson, Loudin et al. 2012), my design relies on focused light to create photovoltaic charging of stimulating electrodes. Protruding CNT electrodes incorporate the ILM, to achieve the best possible coupling with target RGCs.

With a flexible polymer as a base (possibly PDMS), my suggested device consists of a set of interconnected hexagonal and pentagonal units, allowing a tiling of the inner retinal surface in a manner similar to the carbon faces on a buckminsterfullerene, or the stitching on a football. In order to provide embedded centre-surround inhibition, each of the hexagonal units would be equipped with integrated logic consisting of a 6 input NAND (negated AND) gate provided by a transistor on each side and connecting to the adjacent pixel through a flexible conductor. Gold has been demonstrated as an ideal material for such applications (Kim, Lu et al. 2011). Concentric rings of increasingly larger units would compensate for the increase in RGC receptive field proportional to retinal eccentricity. Numerous limitations include the inability to activate ON-centre Off-surround pathways, the complex variation in receptive field size and chromatic vision encoding.

Figure 5.2 A displays a bird's eye view of 6 interconnected elements of the device, with details of the components of each element's retinal and vitreal side as well as the integrated logic. Here, I propose initial (conservatively small as RGC somata are generally several times larger than 4 μm) values for the size of each element and its

constituents which fit with both the biological and technological constraints. As such, a 4 µm diameter CNT stimulating electrode would have a charge injection limit of 0.18 to 0.37 nC. A concentric TiN return electrode of 12 µm diameter would have a surface area (minus the surface of the integrated logic) of 40.41 μm^2 and a charge injection limit of 0.94 nC (Margalit, Maia et al. 2002). The integrated logic consists of 6 transistors on 354.86 μm^2, which is several orders of magnitude larger than the smallest commercialised transistors. Figure 5.2 B provides a side view of the device, detailing the morphology of each constituent. As such, CNT stimulating electrodes protrude in a mushroom shape allowing the ILM to encapsulate it whilst embedding the insulating shaft in ECM. Thus, the device would be secured at the vitreo-retinal juncture whilst providing the best possible coupling between RGC and stimulating electrode. The flexible PDMS base would allow the implant to fit the curvature of the eye. Figure 5.3 displays two examples of centre surround inhibition by the integrated NAND gate on a surface of 41 interconnected elements. Any 6 concentric elements of the MPDA stimulated concurrently would disable the central stimulating electrode.

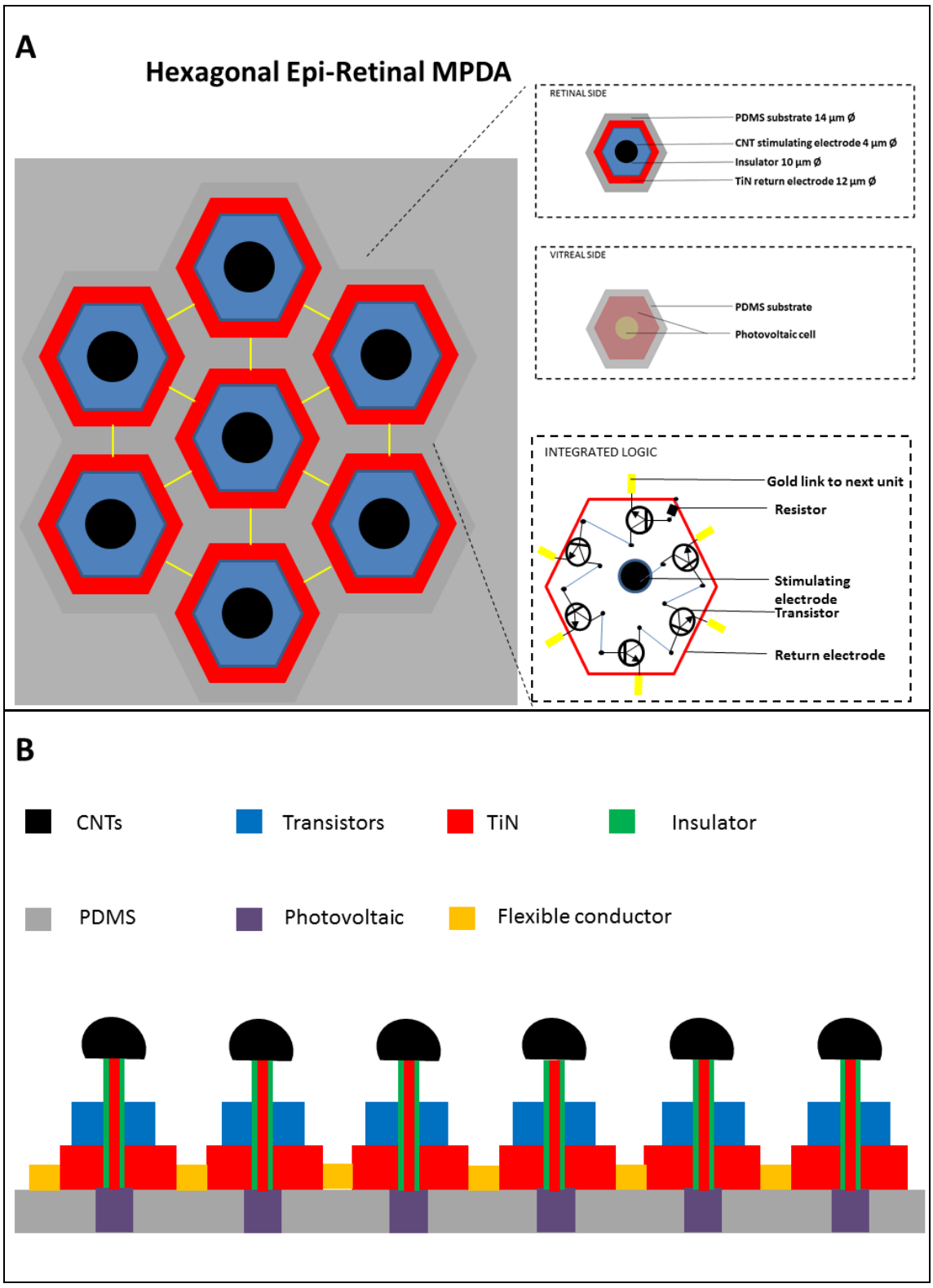

Figure 5.2: Photovoltaic CNT MPDA design. A: Bird's eye view of 6 elements of the device detailing vitreal and retinal architecture as well as integrated logic circuit. B: side view of the device, detailing morphological characteristics of 6 elements.

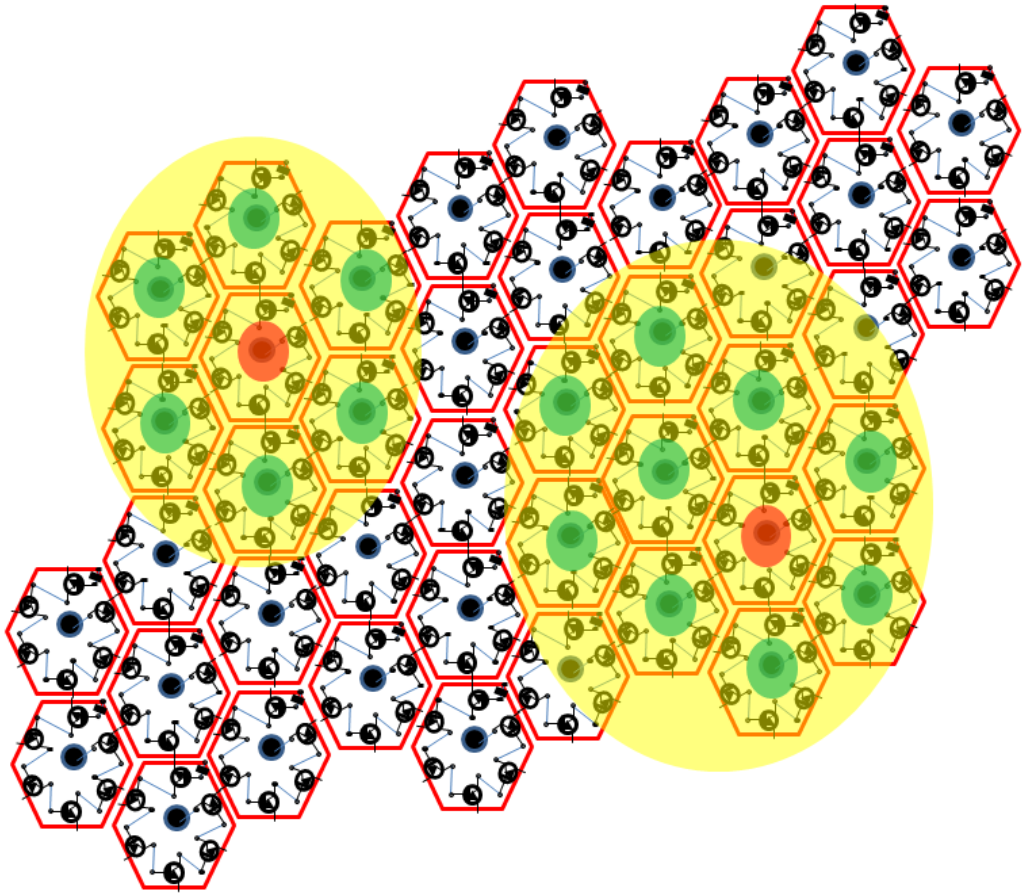

Figure 5.3: Centre-surround inhibition provided by integrated logic. Bird's eye view of 41 interconnected elements displaying the integrated logic circuit of 6 transistors in series. If 6 elements are activated in a circular fashion, the central element is inactivated. Light stimulation is displayed as a yellow circle, stimulating electrode activation is displayed as a green circle and electrode inactivation is displayed as a red circle.

Appendix E: MEA Impedances

Impedances measured at 1 kHz, in kΩ with an IMP-1 (BAK Electronics Inc, Florida, USA)

MVP 36e CNT, used loads, tested on 24/01/2012

450	340	250	400	310	340	290	350	390	320
410	360	310	360	5	340	500	240	500	480
440	340	260	460	380	550	440	500	1800	3200
2100	410	460	490	390	390	7	300	390	400
480	400	550	360	490	5	500	460	350	500
570	390	460	380	500	290	310	500	310	6

MVP36f CNT, used loads, tested on 24/01/2012

900	600	800	500	600	600	700	700	1000	600
800	800	900	1000	5	1000	900	1100	600	700
1000	6	900	800	900	800	700	700	900	700
500	500	500	600	800	1200	7	900	800	800
1000	1500	900	800	7	900	800	800	800	800
900	900	1000	1400	1600	1200	1800	1200	1200	600

MVP20F CNT, never used, received 09/052013, tested 15/05/2013

24	240	250	250	250	270	290	270	260	270
260	29	300	310	300	300	290	240	230	260
250	240	220	3	210	210	210	230	250	210
210	230	240	210	240	210	240	240	240	240
3	200	210	240	240	210	230	220	240	240
200	200	210	200	210	240	240	24	220	240

MVP39c CNT, used many times before, tested 15/05/2013

35	150	110	110	150	160	130	200	160	150
120	110	150	110	150	160	140	120	150	160
110	200	190	180	190	10	110	200	110	150
170	190	180	160	140	120	110	190	130	150
170	9	11	Inf	100	120	160	200	180	140
190	170	110	130	150	170	160	140	120	8

TiN 21753, used a few times, received from MCS on 29/01/2013, tested 20/05/2013

750	150	600	140	140	130	1	150	150	150
150	150	150	150	150	1200	150	150	150	150
150	150	150	150	1000	150	150	150	150	700
140	140	140	750	140	140	140	160	170	140
140	150	150	150	160	170	140	140	150	150
150	150	130	140	140	450	100	100	100	150

TiN 22984, never used, received from MCS on 22/03/2013, tested 20/05/2013

1100	1000	1000	900	800	800	1	700	700	700
700	700	1000	1000	900	900	900	900	900	900
900	900	900	900	900	900	900	900	900	900
1000	1000	1000	900	900	900	900	800	900	1000
1100	1100	800	1000	900	800	1100	900	1100	800
1100	1200	1100	1100	1100	1100	1000	1000	1000	900

TiN 22987, never used, received from MCS on 22/03/2013, tested 21/05/2013

1000	1000	1000	1000	1000	700	900	1	900	900
900	900	1000	1000	1000	1100	1000	1000	1000	900
900	900	1000	1000	1000	1000	1000	900	900	1100
1200	1300	1300	1200	1300	900	900	900	900	900
900	900	900	900	900	1300	1300	1200	900	900
900	900	900	1000	900	1000	900	1000	900	1000

TiN 21752, used a few times, received from MCS on 17/01/2012, tested 21/05/2013

170	160	180	170	160	1	150	150	170	160
160	170	180	170	250	170	160	160	170	180
170	160	170	180	170	160	170	180	210	160
180	600	160	160	170	180	200	180	180	160
180	160	170	180	170	160	170	180	180	180
160	170	180	160	170	180	160	170	180	170

TiN 9720, used loads, tested 21/05/2013

190	180	180	190	170	180	180	180	170	190
170	180	160	160	170	220	210	230	180	210
250	230	230	210	280	210	230	220	210	200
200	200	200	200	200	200	200	200	200	200
260	180	170	170	190	200	170	210	180	190
170	180	190	170	190	180	200	1	170	160

TiN 17873, used loads, tested 21/05/2013

170	170	200	190	120	190	1	160	160	150
600	160	190	180	150	150	130	300	320	140
130	130	140	230	110	120	140	130	150	160
140	120	160	120	140	120	160	160	2000	120
120	110	320	150	350	140	140	320	140	160
3000	140	130	130	140	230	120	120	320	110